



HAL
open science

Synthèse et caractérisations de matériaux moléculaires magnétiques

Jürgen Feuersenger

► **To cite this version:**

Jürgen Feuersenger. Synthèse et caractérisations de matériaux moléculaires magnétiques. Matériaux. Université Sciences et Technologies - Bordeaux I, 2010. Français. NNT : . tel-00755137

HAL Id: tel-00755137

<https://theses.hal.science/tel-00755137>

Submitted on 20 Nov 2012

HAL is a multi-disciplinary open access archive for the deposit and dissemination of scientific research documents, whether they are published or not. The documents may come from teaching and research institutions in France or abroad, or from public or private research centers.

L'archive ouverte pluridisciplinaire **HAL**, est destinée au dépôt et à la diffusion de documents scientifiques de niveau recherche, publiés ou non, émanant des établissements d'enseignement et de recherche français ou étrangers, des laboratoires publics ou privés.

N° d'ordre:

THÈSE

présentée à

L'UNIVERSITÉ DE BORDEAUX 1

ÉCOLE DOCTORALE DES SCIENCES CHIMIQUES

par **JÜRGEN FEUERSENGER**

POUR OBTENIR LE GRADE DE

DOCTEUR

SPÉCIALITÉ : Physico-Chimie de la Matière Condensée

SYNTHESIS AND CHARACTERISATION OF $3d$ - $4f$ -COMPLEXES
AND THEIR MAGNETIC PROPERTIES

Soutenu le 20 décembre 2010

Après avis de :

M. YVES JOURNAUX	Directeur de Recherche au CNRS	Rapporteur
M. JEAN-PASCAL SUTTER	Directeur de Recherche au CNRS	Rapporteur

Devant la commission d'examen formée de :

M ^{me} . CORINE MATHONIÈRE	Professeur, Université Bordeaux 1	Présidente
M. YVES JOURNAUX	Directeur de Recherche au CNRS	Rapporteurs
M. JEAN-PASCAL SUTTER	Directeur de Recherche au CNRS	
M ^{me} . ANNIE K. POWELL	Professeur, Karlsruhe Institute of Technology (KIT)	Examineurs
M. RODOLPHE CLÉRAC	Chargé de Recherche au CNRS	
M. PHILIPPE RICHETTI	Directeur de Recherche au CNRS	

Directeur de thèse :

M. RODOLPHE CLÉRAC ET M. PHILIPPE RICHETTI

Résumé:

Ce travail de thèse décrit (i) la synthèse de complexes hétérométalliques d'ions 3*d* et 4*f* à partir de précurseurs de Mn, Fe et Co, de sels de lanthanides et de ligands organiques et (ii) l'étude de leurs structures et propriétés. 41 complexes polynucléaires ont été synthétisés dans le cadre de ce travail. Les structures moléculaires de tous les composés ont été déterminées par diffraction des rayons X. Les propriétés magnétiques de 22 complexes ont été étudiées, dont quatre montrent une relaxation lente de leur aimantation considérée comme la signature d'un comportement de molécule-aimant. L'activité catalytique du complexe {Mn₄Dy₆Li₂} calciné a aussi été étudiée et s'est avérée efficace pour l'oxydation du monoxyde de carbone. L'étude systématique de complexes isostructuraux de lanthanides a montré que l'incorporation d'ions 4*f* peut introduire de l'anisotropie magnétique et que l'ion Dy^{III} est généralement le meilleur candidat pour le ciblage de molécules-aimants hétérométalliques 3*d*-4*f*.

Mots clés :

- Aimants moléculaires
- Single-Molecule Magnet
- Effet tunnel quantique
- Relaxation lente de l'aimantation

Abstract:

This dissertation describes the syntheses of 3*d*-4*f*-metal complexes starting from preformed compounds of Mn, Fe and Co, lanthanide salts and organic ligands and also the investigation of their structures and properties. 41 new polynuclear heterometallic metal complexes were synthesised in the course of this work with different interesting properties.

The structures of all obtained compounds have been confirmed using X-ray diffraction. The magnetic properties of 22 complexes were studied, of which four show frequency dependent out-of-phase signals as expected for SMMs. The catalytic activity of calcinated {Mn₄Dy₆Li₂} was investigated and proved effective for the oxidation of CO.

It was established, that the use of precursors leads to new families of compounds. Moreover the study of isostructural compounds across the lanthanide series showed 1) that the incorporation of 4*f* ions introduces magnetic anisotropy and 2) Dy^{III} is usually the best candidate for targeting 3*d*-4*f*-SMMs.

Keywords:

- Single-Molecule Magnet
- Quantum tunnelling of magnetisation (QTM)
- 3*d*-4*f* complexes
- Slow relaxation of magnetisation

Table of contents

1	Introduction	1
1.1	General introduction	1
1.2	Magnetic susceptibility	2
1.3	Basic principles of magnetism	2
1.3.1	Diamagnetism	3
1.3.2	Paramagnetism	3
1.3.3	Curie paramagnetism	4
1.3.4	Curie-Weiss paramagnetism	6
1.3.5	Ferromagnetism	8
1.3.6	Antiferromagnetism	9
1.3.7		9
1.3.8	Ferrimagnetism	10
1.3.9	Interaction types	10
1.3.9.1	Direct interaction exchange	11
1.3.9.2	Superexchange	12
1.3.9.3	RKKY-exchange	12
1.3.9.4	Double-exchange	13
1.4	Single molecule magnets (SMMs)	14
1.4.1	The role of the spin ground state for SMM's	19
1.4.2	Synthetic approaches for isolating polynuclear complexes	20
1.5	Introduction to manganese chemistry	22
1.6	Introduction to iron chemistry	23
1.7	Introduction to cobalt chemistry	23
1.8	Introduction to rare-earth metal chemistry	24
1.9	Introduction to 3d-4f complexes	25
1.10	Ligand selection	27
1.11	Co-ligand selection	29
1.12	Precursors as starting materials	30
1.12.1	$[\text{Mn}^{\text{II}}_4\text{Mn}^{\text{III}}_2\text{O}_2(\text{O}_2\text{CCMe}_3)_{10}(\text{py})_{2.5}] \cdot (\text{HO}_2\text{CCMe}_3)_{1.5}$ (1)	30
1.12.2	$[\text{Mn}^{\text{III}}_8\text{Mn}^{\text{IV}}_4\text{O}_{12}(\text{CH}_3\text{COO})_{12}(\text{CHCl}_2\text{COO})_4] \cdot 4\text{H}_2\text{O}$ (3)	31
1.12.3	$[\text{Co}^{\text{II}}_2(\mu\text{-OH}_2)(\text{O}_2\text{CCMe}_3)_4(\text{HO}_2\text{CCMe}_3)_4]$ (4)	33
1.12.4	$[\text{Co}^{\text{III}}_3(\mu_3\text{-O})(\text{O}_2\text{CCMe}_3)_6(\text{py})_3] \cdot \text{O}_2\text{CCMe}_3 \cdot \text{H}_2\text{O} \cdot 3.5\text{HO}_2\text{CCMe}_3$ (5)	33
1.12.5	$[\text{Fe}^{\text{III}}_3\text{O}(\text{O}_2\text{CCMe}_3)_6(\text{H}_2\text{O})_3] \cdot \text{O}_2\text{CCMe}_3 \cdot 2\text{HO}_2\text{CCMe}_3$ (6)	34
1.12.6	$[(\text{Fe}^{\text{III}}_3\text{O})_2(\text{O})_2(\text{O}_2\text{CCMe}_3)_{12}(\text{HO}_2\text{CCMe}_3)_2]$ (7)	35
1.12.7	$[\text{Dy}_2(\text{O}_2\text{CCMe}_3)_6(\text{HO}_2\text{CCMe}_3)_6] \cdot \text{HO}_2\text{CCMe}_3$ (8)	35
1.13	Crystallisation methods	36
1.13.1	Evaporation	39
1.13.2	Vapour and Liquid Diffusion	39

TABLE OF CONTENTS

1.13.3	Thermal Gradient	40
2	Structure and magnetic properties of manganese-lanthanide aggregates	41
2.1	Structure of tetranuclear complexes	41
2.1.1	Structure of $[\text{Mn}^{\text{III}}_2\text{La}^{\text{III}}_2(\text{hmp})_6(\text{piv})_2(\text{NO}_3)_4]$ (9)	41
2.2	Structure and magnetic properties of hexanuclear complexes	43
2.2.1	Structure of $\text{Mn}^{\text{III}}_4\text{La}^{\text{III}}_2(\mu_4\text{-O})(\mu_3\text{-O})(\text{hmp})_7(\text{O}_2\text{CMe})(\text{O}_2\text{CCHCl}_2)(\text{NO}_3)_5(\text{OH}_2)_{0.5}] \cdot 3\text{acetone}$ (10)	43
2.2.2	Magnetic properties of $[\text{Mn}^{\text{III}}_4\text{La}^{\text{III}}_2(\mu_4\text{-O})(\mu_3\text{-O})(\text{hmp})_7(\text{OAc})_2(\text{NO}_3)_5]$	47
2.2.3	Structure of $[\text{Mn}^{\text{III}}_2\text{Dy}^{\text{III}}_4(\mu_4\text{-O})_2(\text{hmp})_4(\text{pic})_2(\text{piv})_6(\mu\text{-N}_3)_2] \cdot 4\text{CH}_3\text{CN}$ (14)	51
2.2.4	Magnetic properties of $[\text{Mn}^{\text{III}}_2\text{Ln}^{\text{III}}_4(\mu_4\text{-O})_2(\text{hmp})_4(\text{pic})_2(\text{piv})_6(\mu\text{-N}_3)_2] \cdot 4\text{CH}_3\text{CN}$	56
2.3	Structure and magnetic properties of heptanuclear complexes	60
2.3.1	Structure of $[\text{Mn}^{\text{II}}\text{Mn}^{\text{III}}_2\text{Mn}^{\text{IV}}\text{Ho}^{\text{III}}_3(\mu_4\text{-O})(\mu_3\text{-OH})_2(\text{n-bdea})_3(\text{piv})_9(\text{N}_3)(\text{NO}_3)] \cdot \text{MeCN}$ (19)	60
2.3.2	Magnetic properties of $[\text{Mn}^{\text{II}}\text{Mn}^{\text{III}}_2\text{Mn}^{\text{IV}}\text{Ln}^{\text{III}}_3(\mu_4\text{-O})(\mu_3\text{-OH})_2(\text{n-bdea})_3(\text{piv})_9(\text{N}_3)(\text{NO}_3)] \cdot \text{MeCN}$	65
2.4	Structure and magnetic properties of dodecanuclear complexes	68
2.4.1	Structure of $[\text{Mn}^{3.5}_4\text{Gd}^{\text{III}}_6\text{Li}_2(\mu_3\text{-O})_2(\mu_5\text{-CO}_3)_2(\text{n-bdea})_6(\text{piv})_{12}(\text{NO}_3)_2] \cdot 3\text{CH}_3\text{CN}$ (25)	68
2.4.2	Magnetic properties of $[\text{Mn}^{3.5}_4\text{Ln}^{\text{III}}_6\text{Li}_2(\mu_3\text{-O})_2(\mu_5\text{-CO}_3)_2(\text{n-bdea})_6(\text{piv})_{12}(\text{NO}_3)_2] \cdot 3\text{CH}_3\text{CN}$	77
2.4.3	Catalytic Oxidation properties of calcinated $[\text{Mn}^{\text{IV}}_2\text{Mn}^{\text{III}}_2\text{Dy}^{\text{III}}_6\text{Li}_2(\mu_3\text{-O})_2(\mu_5\text{-CO}_3)_2(\text{n-bdea})_6(\text{piv})_{12}(\text{NO}_3)_2] \cdot 3\text{CH}_3\text{CN}$	84
3	Structure and magnetic properties of iron-lanthanide aggregates	86
3.1	Structure and magnetic properties of hexanuclear complexes	86
3.1.1	Structure of $[\text{Fe}^{\text{III}}_4\text{Pr}^{\text{III}}_2(\mu_4\text{-O})_2(\text{n-bdea})_4(\text{piv})_4(\text{NO}_3)_2(\text{H}_2\text{O})_2] \cdot \text{MeCN}$ (30)	86
3.1.2	Magnetic properties of $[\text{Fe}^{\text{III}}_4\text{Ln}^{\text{III}}_2(\mu_4\text{-O})_2(\text{n-bdea})_4(\text{piv})_4(\text{NO}_3)_2(\text{H}_2\text{O})_2]$	93
3.1.3	Mössbauer measurement on $[\text{Fe}^{\text{III}}_4\text{Pr}^{\text{III}}_2(\mu_4\text{-O})_2(\text{n-bdea})_4(\text{piv})_4(\text{NO}_3)_2(\text{H}_2\text{O})_2]$	97
3.2	Structure and magnetic properties of hexanuclear Fe(III) complexes	98
3.2.1	Structure of $[\text{Fe}^{\text{III}}_6(\mu_3\text{-O})_2(\text{hmp})_6(\text{piv})_6]^{2+}[\text{Gd}(\text{NO}_3)_5]^{2-}$ (37)	98
3.2.2	Magnetic properties of $[\text{Fe}^{\text{III}}_6(\mu_3\text{-O})_2(\text{hmp})_6(\text{piv})_6]^{2+}[\text{Ln}(\text{NO}_3)_5]^{2-}$	101
4	Structure and magnetic properties of cobalt-lanthanide aggregates	105
4.1	Structure and magnetic properties of hexanuclear complexes	105
4.1.1	Structure of $[\text{Co}^{\text{II}}_2\text{Dy}^{\text{III}}_4(\mu_3\text{-OH})_2(\text{hmp})_4(\text{piv})_8(\text{N}_3)_2(\text{NO}_3)_2] \cdot 2\text{CH}_3\text{CN}$ (46)	105
4.1.2	Magnetic properties of $[\text{Co}^{\text{II}}_2\text{Ln}^{\text{III}}_4(\mu_3\text{-OH})_2(\text{hmp})_4(\text{piv})_8(\text{N}_3)_2(\text{NO}_3)_2] \cdot 2\text{CH}_3\text{CN}$	113
5	Summary	121
6	Conclusion	123
7	Experimental section	124
7.1	Elemental analysis	124

TABLE OF CONTENTS

7.2	Fourier-Transform-Infrared-Spectroscopy (FT-IR) _____	124
7.3	X-ray diffraction on single crystals _____	124
7.4	X-ray Powder diffraction _____	126
7.5	Magnetic measurements _____	126
7.6	Mößbauer spectroscopy _____	127
7.7	Some magnetic parameters for lanthanides ions _____	127
7.8	Synthetic approach _____	128
7.9	Synthesis of precursor compounds _____	128
7.9.1	Manganese Precursor Compounds _____	128
7.9.1.1	[Mn ^{III} ₂ Mn ^{IV} ₄ O ₂ (O ₂ CCMe ₃) ₁₀ (py) _{2.5}]·(HO ₂ CCMe ₃) _{1.5} (1) _____	128
7.9.1.2	Mn ^{II} (CHCl ₂ COO) ₃ ·4H ₂ O (2) _____	129
7.9.1.3	[Mn ^{III} ₈ Mn ^{IV} ₄ O ₁₂ (CH ₃ COO) ₁₂ (CHCl ₂ COO) ₄]·4H ₂ O (3) _____	129
7.9.2	Cobalt Precursor Compounds _____	129
7.9.2.1	[Co ^{II} ₂ (μ-OH ₂)(O ₂ CCMe ₃) ₄ (HO ₂ CCMe ₃) ₄] (4) _____	129
7.9.2.2	[Co ^{III} ₃ (μ ₃ -O)(O ₂ CCMe ₃) ₆ (py) ₃]·O ₂ CCMe ₃ ·H ₂ O·3.5HO ₂ CCMe ₃ (5) _____	130
7.9.3	Iron Precursor Compounds _____	130
7.9.3.1	[Fe ^{III} ₃ O(O ₂ CCMe ₃) ₆ (H ₂ O) ₃] ⁺ [O ₂ CCMe ₃] ⁻ ·2HO ₂ CCMe ₃ (6) _____	130
7.9.3.2	[Fe ₆ (O ₂)(O ₂)(O ₂ CCMe ₃) ₁₂ (HO ₂ CCMe ₃) ₂] (7) _____	130
7.9.4	Lanthanide Precursor Compounds _____	131
7.9.4.1	[Dy ₂ (O ₂ CCMe ₃) ₆ (HO ₂ CCMe ₃) ₆]·HO ₂ CCMe ₃ (8) _____	131
7.10	Synthetic procedure for the described compounds _____	131
7.10.1	[Mn ^{II} ₂ La ^{III} ₂ (hmp) ₆ (piv) ₂ (NO ₃) ₄]·2acetone (9) _____	131
7.10.2	Mn ^{III} ₄ La ^{III} ₂ (μ ₄ -O)(μ ₃ -O)(hmp) ₇ (OAc)(DCAc)(NO ₃) ₅ (OH ₂) _{0.5}]·3acetone (10) _____	132
7.10.3	[Mn ^{III} ₂ Eu ^{III} ₄ (μ ₄ -O) ₂ (hmp) ₄ (pic) ₂ (piv) ₆ (μ-N ₃) ₂]·2CH ₃ CN (11) _____	132
7.10.4	[Mn ^{III} ₂ Gd ^{III} ₄ (μ ₄ -O) ₂ (hmp) ₄ (pic) ₂ (piv) ₆ (μ-N ₃) ₂]·2CH ₃ CN (12) _____	133
7.10.5	[Mn ^{III} ₂ Tb ^{III} ₄ (μ ₄ -O) ₂ (hmp) ₄ (pic) ₂ (piv) ₆ (μ-N ₃) ₂]·4CH ₃ CN (13) _____	133
7.10.6	[Mn ^{III} ₂ Dy ^{III} ₄ (μ ₄ -O) ₂ (hmp) ₄ (pic) ₂ (piv) ₆ (μ-N ₃) ₂]·4CH ₃ CN (14) _____	134
7.10.7	[Mn ^{III} ₂ Ho ^{III} ₄ (μ ₄ -O) ₂ (hmp) ₄ (pic) ₂ (piv) ₆ (μ-N ₃) ₂]·4CH ₃ CN (15) _____	135
7.10.8	[Mn ^{III} ₂ Er ^{III} ₄ (μ ₄ -O) ₂ (hmp) ₄ (pic) ₂ (piv) ₆ (μ-N ₃) ₂]·4CH ₃ CN (16) _____	135
7.10.9	[Mn ^{II} Mn ^{III} ₂ Mn ^{IV} Gd ^{III} ₃ (μ ₄ -O)(μ ₃ -OH) ₂ (n-bdea) ₃ (piv) ₉ (N ₃)(NO ₃)]·MeCN (17) _____	136
7.10.10	[Mn ^{II} Mn ^{III} ₂ Mn ^{IV} Dy ^{III} ₃ (μ ₄ -O)(μ ₃ -OH) ₂ (n-bdea) ₃ (piv) ₉ (N ₃)(NO ₃)]·MeCN (18) _____	136
7.10.11	[Mn ^{II} Mn ^{III} ₂ Mn ^{IV} Ho ^{III} ₃ (μ ₄ -O)(μ ₃ -OH) ₂ (n-bdea) ₃ (piv) ₉ (N ₃)(NO ₃)]·MeCN (19) _____	137
7.10.12	Mn ^{II} Mn ^{III} ₂ Mn ^{IV} Er ^{III} ₃ (μ ₄ -O)(μ ₃ -OH) ₂ (n-bdea) ₃ (piv) ₉ (N ₃)(NO ₃)]·MeCN (20) _____	137
7.10.13	[Mn ^{3.5} ₄ Pr ^{III} ₆ Li ₂ (μ ₃ -O) ₂ (μ ₅ -CO ₃) ₂ (n-bdea) ₆ (piv) ₁₂ (NO ₃) ₂]·4CH ₃ CN (21) _____	137
7.10.14	[Mn ^{3.5} ₄ Nd ^{III} ₆ Li ₂ (μ ₃ -O) ₂ (μ ₅ -CO ₃) ₂ (n-bdea) ₆ (piv) ₁₂ (NO ₃) ₂]·3CH ₃ CN (22) _____	138
7.10.15	Mn ^{3.5} ₄ Sm ^{III} ₆ Li ₂ (μ ₃ -O) ₂ (μ ₅ -CO ₃) ₂ (n-bdea) ₆ (piv) ₁₂ (NO ₃) ₂]·3CH ₃ CN (23) _____	138
7.10.16	[Mn ^{3.5} ₄ Eu ^{III} ₆ Li ₂ (μ ₃ -O) ₂ (μ ₅ -CO ₃) ₂ (n-bdea) ₆ (piv) ₁₂ (NO ₃) ₂]·3CH ₃ CN (24) _____	139
7.10.17	[Mn ^{3.5} ₄ Gd ^{III} ₆ Li ₂ (μ ₃ -O) ₂ (μ ₅ -CO ₃) ₂ (n-bdea) ₆ (piv) ₁₂ (NO ₃) ₂]·3CH ₃ CN (25) _____	139
7.10.18	[Mn ^{3.5} ₄ Tb ^{III} ₆ Li ₂ (μ ₃ -O) ₂ (μ ₅ -CO ₃) ₂ (n-bdea) ₆ (piv) ₁₂ (NO ₃) ₂]·3CH ₃ CN (26) _____	140
7.10.19	[Mn ^{3.5} ₄ Dy ^{III} ₆ Li ₂ (μ ₃ -O) ₂ (μ ₅ -CO ₃) ₂ (n-bdea) ₆ (piv) ₁₂ (NO ₃) ₂]·3CH ₃ CN (27) _____	140

TABLE OF CONTENTS

7.10.20	[Mn ^{3.5} ₄ Ho ^{III} ₆ Li ₂ (μ ₃ -O) ₂ (μ ₅ -CO ₃) ₂ (n-bdea) ₆ (piv) ₁₂ (NO ₃) ₂]·8CH ₃ CN (28)	140
7.10.21	[Mn ^{3.5} ₄ Y ^{III} ₆ Li ₂ (μ ₃ -O) ₂ (μ ₅ -CO ₃) ₂ (n-bdea) ₆ (piv) ₁₂ (NO ₃) ₂]·8CH ₃ CN (29)	141
7.10.22	[Fe ^{III} ₄ Pr ^{III} ₂ (μ ₄ -O) ₂ (n-bdea) ₄ (piv) ₄ (NO ₃) ₂ (H ₂ O) ₂]·MeCN (30)	141
7.10.23	[Fe ^{III} ₄ Nd ^{III} ₂ (μ ₄ -O) ₂ (n-bdea) ₄ (piv) ₄ (NO ₃) ₂ (H ₂ O) ₂]·acetone (31)	142
7.10.24	[Fe ^{III} ₄ Sm ^{III} ₂ (μ ₄ -O) ₂ (n-bdea) ₄ (piv) ₄ (NO ₃) ₂ (H ₂ O) ₂]·acetone (32)	142
7.10.25	[Fe ^{III} ₄ Eu ^{III} ₂ (μ ₄ -O) ₂ (n-bdea) ₄ (piv) ₄ (NO ₃) ₂ (H ₂ O) ₂]·acetone (33)	143
7.10.26	[Fe ^{III} ₄ Gd ^{III} ₂ (μ ₄ -O) ₂ (n-bdea) ₄ (piv) ₄ (NO ₃) ₂ (H ₂ O) ₂]·acetone (34)	143
7.10.27	[Fe ^{III} ₄ Y ^{III} ₂ (μ ₄ -O) ₂ (n-bdea) ₄ (piv) ₄ (NO ₃) ₂ (H ₂ O) ₂]·acetone (35)	144
7.10.28	[Fe ^{III} ₆ (μ ₃ -O) ₂ (hmp) ₆ (piv) ₆] ²⁺ [Eu ^{III} (NO ₃) ₅] ²⁻ ·2acetone (36)	144
7.10.29	[Fe ^{III} ₆ (μ ₃ -O) ₂ (hmp) ₆ (piv) ₆] ²⁺ [Gd ^{III} (NO ₃) ₅] ²⁻ ·2acetone (37)	144
7.10.30	[Fe ^{III} ₆ (μ ₃ -O) ₂ (hmp) ₆ (piv) ₆] ²⁺ [Dy ^{III} (NO ₃) ₅] ²⁻ ·2acetone (38)	145
7.10.31	[Fe ^{III} ₆ (μ ₃ -O) ₂ (hmp) ₆ (piv) ₆] ²⁺ [Ho ^{III} (NO ₃) ₅] ²⁻ ·2acetone (39)	145
7.10.32	[Fe ^{III} ₆ (μ ₃ -O) ₂ (hmp) ₆ (piv) ₆] ²⁺ [Er ^{III} (NO ₃) ₅] ²⁻ ·2acetone (40)	146
7.10.33	[Co ^{III} ₂ Pr ^{III} ₄ (μ ₃ -OH) ₂ (hmp) ₄ (piv) ₈ (μ-N ₃) ₂ (NO ₃) ₂]·2CH ₃ CN (41)	146
7.10.34	[Co ^{III} ₂ Sm ^{III} ₄ (μ ₃ -OH) ₂ (hmp) ₄ (piv) ₈ (μ-N ₃) ₂ (NO ₃) ₂]·2CH ₃ CN (42)	147
7.10.35	[Co ^{III} ₂ Eu ^{III} ₄ (μ ₃ -OH) ₂ (hmp) ₄ (piv) ₈ (μ-N ₃) ₂ (NO ₃) ₂]·2CH ₃ CN (43)	147
7.10.36	[Co ^{III} ₂ Gd ^{III} ₄ (μ ₃ -OH) ₂ (hmp) ₄ (piv) ₈ (μ-N ₃) ₂ (NO ₃) ₂]·2CH ₃ CN (44)	147
7.10.37	[Co ^{III} ₂ Tb ^{III} ₄ (μ ₃ -OH) ₂ (hmp) ₄ (piv) ₈ (μ-N ₃) ₂ (NO ₃) ₂]·2CH ₃ CN (45)	148
7.10.38	[Co ^{III} ₂ Dy ^{III} ₄ (μ ₃ -OH) ₂ (hmp) ₄ (piv) ₈ (μ-N ₃) ₂ (NO ₃) ₂]·2CH ₃ CN (46)	148
7.10.39	[Co ^{III} ₂ Ho ^{III} ₄ (μ ₃ -OH) ₂ (hmp) ₄ (piv) ₈ (μ-N ₃) ₂ (NO ₃) ₂]·2CH ₃ CN (47)	149
7.10.40	[Co ^{III} ₂ Er ^{III} ₄ (μ ₃ -OH) ₂ (hmp) ₄ (piv) ₈ (μ-N ₃) ₂ (NO ₃) ₂]·2CH ₃ CN (48)	149
8	Crystal structure data	151
9	Bibliography	167
10	Affix	182
10.1	List of Abbreviations	182
10.2	List of figures	183
10.3	List of tables	187
11	Acknowledgments	189
12	Conference contributions	191

1 Introduction

1.1 General introduction

Historically, magnetism is an effect recognised for thousands of years. A first account is by the Greek Thales of Miletus (about 585 B.C.) who said loadstone (a form of magnetite, Fe_3O_4) attracts iron. Later in the 11th century, this phenomenon was used by the Chinese to create the floating compass (Verschuur, 1993). In 1269 Petrus Peregrinus de Maricourt identified that magnets have poles called North and South magnetic poles. He noted that opposite poles attracted while similar magnetic poles repelled and that also breaking a magnet was not destructive. Years later, in the 16th century, William Gilbert created a new synthetic magnetic-iron that lost its magnetic force on heating and regained upon cooling. In the 19th century, additional key developments occurred and the understanding of the phenomenon of magnetism was greatly influenced by pivotal contributions. Hans Christian Oersted observed in 1819 that electricity affected magnets (Oersted 1820: 273ff). In 1823 Michael Faraday invented the electromagnet (Kloss, 1994), and the use of magnets enabled the production of low-cost electricity with the help of generators or transformers. Heinrich Rudolf Hertz clarified and expanded in 1885 the electromagnetic theory of light that had been put forward by Maxwell. In 1907 the french physicist, Pierre-Ernest Weiss, developed the theory of ferromagnetism based on the assumption that the interaction between magnetic molecules could be described empirically considering an internal molecular field. Niels Bohr identified in 1913 the underlying physics from which magnetism results, i.e. the minute spin associated with an unpaired electron (Morrish, 1965).

In 1935, AEG put the first magnetic tape recorder on the market. The development of magnetic information storage for computer technology started in the 1930s with the magnetic drum memory machine invented by Gustav Tauschek, which was used in a range of computers (Tauschek, 1933). Since then, memory storage devices have become smaller and smaller, so that nowadays ever larger amounts of information can be stored on hard disks, cash cards or flash memories. The need for memory capacity is still growing continuously, but the downsizing of the size of a bit represented by a certain number of spin carriers has a lower physical limit (Wengenmayr 2002: 24ff), so that new types of materials for the storing of information are required. One of these new materials could be Single Molecule Magnets (SMMs). Since their discovery in the 1990s, their synthesis and characterisation, the improvement of their magnetic properties and their understanding has become the subject of much research.

Conventional magnetic materials are prepared at high temperatures using metallurgical methodologies. These materials are atom-based magnets which means that their active spins are located in the atomic orbitals of the constituent metal ions (Miller, 2000: 4392ff). These classical magnets are two- or three-dimensional arrays of inorganic atoms, transition metals and/or lanthanide metals, providing spin units (Pilawa, 1999: 191ff).

Later on further development to design molecule-based magnets with bulk magnetism led to a new field called Molecular Magnetism (Miller, 1994: 385ff). These magnetic materials can no longer be synthesised in the metallurgical manner because molecular magnets comprise purely organic and organic/inorganic hybrid materials for which high temperature conditions usually inhibit their formation. Thus they are prepared using conventional organic and inorganic synthetic methodologies. Molecular magnetism has been promoted mostly by the discovery of Single Molecule Magnet (SMM) behaviour first reported in 1991 (Caneschi, 1991: 5873ff). It was discovered that the $[\text{Mn}_{12}\text{O}_{12}(\text{O}_2\text{CMe})_{16}(\text{H}_2\text{O})_4]$ complex (Mn_{12}Ac) first synthesised in 1980 (Lis, 1980: 2042ff) exhibits slow relaxation of magnetisation of purely molecular origin at low temperatures and thus represents a molecular approach to nanomagnets. These molecules possess a spin ground state (S), where $S \geq \frac{1}{2}$ and a uniaxial magnetoanisotropy, $D < 0$. The combination of these properties can lead to an energy barrier to the thermal relaxation of magnetisation. The magnetic bistability arising from this energy barrier indicates potential applications for these materials in information storage devices, whereby a single molecule could act as the smallest possible unit of magnetic memory. They have many important advantages over conventional nanoscale magnetic particles composed of metal, metal alloys and metal oxides because of their uniform size, solubility in organic solvents and readily alterable peripheral ligands. In order to obtain new SMMs, polynuclear metal compounds which contain interacting metal centres held together by bridging units, such as oxygen atoms derived from oxides, hydroxide, alkoxide and carboxylates, have been synthesised. Extended networks of magnetically coupled SMMs can lead to new magnetic behaviour induced by the intrinsic properties of the magnetic units, such as the high-spin state, the Ising-type anisotropy and quantum effects (Lecren, 2005: 11311ff).

1.2 Magnetic susceptibility

In electromagnetism the magnetic susceptibility is the degree of magnetisation of a substance in response to an applied magnetic field. Magnetic measurements can give information about the electronic structure and the magnetic exchange interactions and stereochemistry of transition metal complexes. This section should give an overview of how magnetic measurements can be applied to this area of inorganic chemistry. For more detailed information literature from (Carlin, 1986), (Mabbs, 1973), (O'Connor, 1982), (Kahn, 1993) and (Kittel, 1953) are recommended.

1.3 Basic principles of magnetism

To understand the following sections on molecular magnetism, it is useful to give a brief overview of the basic principles of magnetism. Broadly speaking, substances can be classed as diamagnetic (containing no unpaired electrons) or paramagnetic (with unpaired electrons). Diamagnetic substances are repelled by an applied magnetic field, whereas paramagnetic materials are attracted into an externally applied magnetic field.

The magnetic susceptibility, χ_m , is used to describe this behaviour of a substance, in an applied magnetic field H:

$$\chi_m = \frac{\partial M}{\partial H} \quad (1.1)$$

M constitutes the additional magnetisation from the sample to the external magnetic field H, where M is defined as the magnetic moment per unit volume. Thus, the magnetic susceptibility characterises the interaction of a substance with an external applied field (Gade, 1998: 307ff). In terms of a quantum description, it is the interaction of the external applied field H_0 with the total angular momenta of the occupied states.

The more commonly used molecular susceptibility, χ_{mol} , is defined as

$$\chi_{mol} = \frac{M_{mol}}{H} = \mu_0 \frac{N_A \mu_r \mu^2}{3k_B T} \quad (1.2)$$

Generally χ is the algebraic sum of two contributions:

$$\chi = \chi^D + \chi^P \quad (1.3)$$

where χ^D and χ^P represent the diamagnetic and paramagnetic susceptibilities, respectively.

If a substance is paramagnetic, the magnetic field lines will be drawn into it, reinforcing the field and M_p is positive giving a positive value for the susceptibility ($\chi > 0$). The opposite is found for diamagnetic substances and $\chi < 0$.

1.3.1 Diamagnetism

Diamagnetism is a fundamental property of matter which is always present, even when it is masked by the often stronger paramagnetism. It is due to the interaction of the magnetic field with the motion of electrons in their orbitals. Diamagnetic susceptibility, χ^D , is usually independent of the temperature and the strength of the applied field. When this is the only response, these substances are composed of atoms which have no net magnetic moments because all the orbitals are filled with electrons, which, as a result of the Pauli exclusion principle, must have different spin directions. When a magnetic field is applied, a negative magnetisation is produced and the susceptibility is negative.

1.3.2 Paramagnetism

Any atom, ion or molecule, which has one or more unpaired electrons, is paramagnetic and thus possesses a net magnetic moment. On applying an external field, it becomes energetically favourable for the individual magnetic moments to align parallel to the external magnetic field, thereby reinforcing it. Hence, these substances are attracted into a magnetic field resulting in positive magnetisation and a positive value for the magnetic susceptibility.

Paramagnetic substances do not retain any magnetisation in the absence of an externally applied magnetic field, because thermal motion causes the spins to become randomly oriented. Thus, the total magnetisation will become zero when the applied field is removed.

Typical values for the susceptibility χ are shown in Table 1:

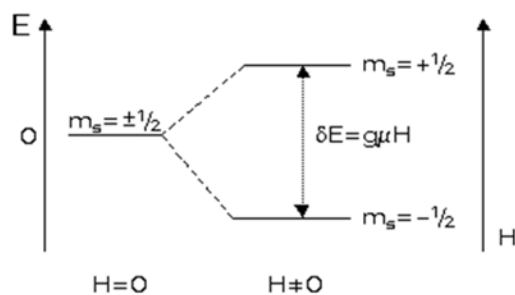
Kind of magnetism	specific susceptibility χ_{mol}	temperature dependence
Diamagnetism	$-1 \cdot 10^{-6} - -10^{-4} \text{ cm}^3 \cdot \text{mol}^{-1}$	none
Pauli-Paramagnetism	$1 \cdot 10^{-5} - 10^{-3} \text{ cm}^3 \cdot \text{mol}^{-1}$	$1/T$
Curie-Paramagnetism	$1 \cdot 10^{-6} - 10^{-1} \text{ cm}^3 \cdot \text{mol}^{-1}$	$1/T$ or complex
Ferromagnetism	$1 \cdot 10^{-2} - 10^6 \text{ cm}^3 \cdot \text{mol}^{-1}$	complex
Antiferromagnetism	$1 \cdot 10^{-7} - 1 \cdot 10^{-5} \text{ cm}^3 \cdot \text{mol}^{-1}$	complex

Table 1: Typical ranges for χ (Riedel, 2007: 243).

However, the diamagnetic effect is still present for all substances and the measured data for any paramagnetic substance should be corrected to take account of the diamagnetism.

1.3.3 Curie paramagnetism

The temperature dependence of the susceptibility of paramagnetic substances was discovered by Pierre Curie in 1895 (Huheey, 2003: 534ff). He found that the magnetic susceptibility is inversely proportional to the temperature, which can be shown using the following example of an isolated $S=1/2$ spin.



Scheme 1: Energy diagram of a spin, $S = 1/2$ system with and without a magnetic field

For one mole of $S = 1/2$ particles in zero field ($H = 0$) the two levels $m_s = \pm 1/2$ are degenerate. If a magnetic field is applied, the two levels split into two energetically different levels as shown in Scheme 1. The energy of each level is then given by

$$E = m_s g \mu_B H \quad (1.4)$$

where m_s is the spin quantum number, g the g -factor and μ_B the Bohr magneton.

Hence, the energies for the upper and lower levels are $1/2 g \mu_B H$ and $-1/2 g \mu_B H$, respectively. The energy difference between the two levels is therefore $\Delta E = g \mu_B H$, which for $g = 2$ corresponds to approximately 1 cm^{-1} at 1 Tesla field strength.

The molar macroscopic moment of the electron is summed according to a Boltzmann distribution (Carlin, 1986: 8f) which is given as follows:

$$M = N \sum_n \mu_n P_n = N(\mu_{1/2} P_{1/2} + \mu_{-1/2} P_{-1/2}) \quad (1.5)$$

$$\mu_n = -m_s g \mu_B, P_n = \frac{N_n}{N} \text{ with } N = \sum_n N_n \quad (1.6)$$

$$P_{1/2} = \frac{\exp\left(\frac{1/2 g \mu_B H}{k_B T}\right)}{\exp\left(\frac{1/2 g \mu_B H}{k_B T}\right) + \exp\left(-\frac{1/2 g \mu_B H}{k_B T}\right)} \quad (1.7)$$

$$P_{-1/2} = \frac{\exp\left(-\frac{1/2 g \mu_B H}{k_B T}\right)}{\exp\left(\frac{1/2 g \mu_B H}{k_B T}\right) + \exp\left(-\frac{1/2 g \mu_B H}{k_B T}\right)} \quad (1.8)$$

Substituting for $P_{1/2}$ and $P_{-1/2}$ one obtains the Brillouin function:

$$M = 1/2 N g \mu_B \frac{\exp\left(\frac{1/2 g \mu_B H}{k_B T}\right) - \exp\left(-\frac{1/2 g \mu_B H}{k_B T}\right)}{\exp\left(\frac{1/2 g \mu_B H}{k_B T}\right) + \exp\left(-\frac{1/2 g \mu_B H}{k_B T}\right)} \quad (1.9)$$

$$M = 1/2 N g \mu_B \tanh\left(\frac{g \mu_B H}{2 k_B T}\right) \quad (1.10)$$

For moderate fields and temperatures, with $\frac{g \mu_B H}{2 k_B T} \ll 1$, $\tanh\left(\frac{g \mu_B H}{2 k_B T}\right) \approx \left(\frac{g \mu_B H}{2 k_B T}\right)$; M thus becomes:

$$M = 1/2 N g \mu_B \left(\frac{g \mu_B H}{2 k_B T}\right) = \frac{N g^2 \mu_B^2 H}{4 k_B T} = \frac{C H}{T} \quad (1.11)$$

where C is the Curie constant specific to the given substance.

As the magnetic susceptibility is defined as $\chi = \frac{M}{H}$ the susceptibility for an isolated magnetic spin is as follows:

$$\chi = \frac{C}{T} \quad (1.12)$$

This equation is known as Curie's law.

However, Curie's law can only be used for substances in which the paramagnetic centres are isolated from each other by diamagnetic atoms, such as free atoms and ions. In addition it is not valid at high fields and low temperature.

In 1932 Van Vleck translated the temperature dependency of the paramagnetic susceptibility into the language of quantum mechanics with the Van Vleck formula:

$$\chi = \frac{N \sum_n \left(\frac{E_n^{(1)2}}{k_B T} - 2E_n^{(2)} \right) \exp\left(-\frac{E_n^{(0)}}{kT}\right)}{\sum_n \exp\left(-\frac{E_n^{(0)}}{kT}\right)} \quad (1.13)$$

where $E_n^{(0)}$ is the energy of level n in zero field and $E_n^{(1)}$ and $E_n^{(2)}$ are called first- and second-order Zeemann coefficients, respectively (Kahn, 1993: 5ff).

1.3.4 Curie-Weiss paramagnetism

In some cases where paramagnetic atoms or ions interact, Curie's law is no longer valid and the magnetic exchange between spin carriers needs to be included in the model. As a result, in ferromagnets and antiferromagnets the Curie-Weiss law is applicable, which is:

$$M = C \frac{H}{T - \theta} \quad \text{with } C = \frac{N \beta^2 g^2 a^2 S(S+1)}{3k_B} \quad \text{and } \theta = \frac{zJS(S+1)}{3k_B} \quad (1.14)$$

and the magnetic susceptibility becomes:

$$\chi = \frac{C}{(T - \theta)} \quad (1.15)$$

where θ is the Weiss-constant ($[\theta] = T$). This equation is known as the Curie-Weiss law.

If $\theta > 0$, ferromagnetic effects predominate and if $\theta < 0$, ferrimagnetic behaviour or antiferromagnetic interactions predominate.

We define J as the total angular momentum, resulting from the coupling of L , the orbital angular momentum with S , the spin angular momentum: $J = L + S$.

The Curie constant C also includes the Landé g -factor:

$$C = \frac{N_A \cdot \mu^2}{3k_B} = \frac{N_A g^2 J(J+1) \mu_B^2}{3k_B} \quad (1.16)$$

as it describes the relation between the magnetic moment μ of a particle and its total angular momentum.

$$g = 1 + \frac{J(J+1) + S(S+1) - L(L+1)}{2J(J+1)} \quad (1.17)$$

For isotropic systems and systems without spin-orbit coupling, g is approximately 2. For systems with spin-orbit coupling the value for g can be different, as these systems can show magnetic anisotropy. If so, one has to consider a specific Spin-Hamiltonian, where g is a generalised g tensor.

$$\hat{H}_{\text{eff}} = \mu_B \vec{B} \cdot \vec{g} \cdot \vec{S} \quad (1.18)$$

where \hbar is the reduced Planck constant and B is defined as $B = \mu_0 H$.

Experimentally, the presence of magnetic anisotropy can be verified by plotting the reduced magnetisation (M vs. H/T). In isotropic systems the isothermal lines are superposed while in anisotropic systems the isothermal lines no longer superpose.

Depending on the relative arrangement of the magnetic moments, substances can be described as showing ferromagnetism, antiferromagnetism or ferrimagnetism (Figure 1). In all three cases, spins are cooperatively coupled and for ferro- and ferrimagnetic materials, a spontaneous magnetisation can arise and the materials used in magnetic devices.

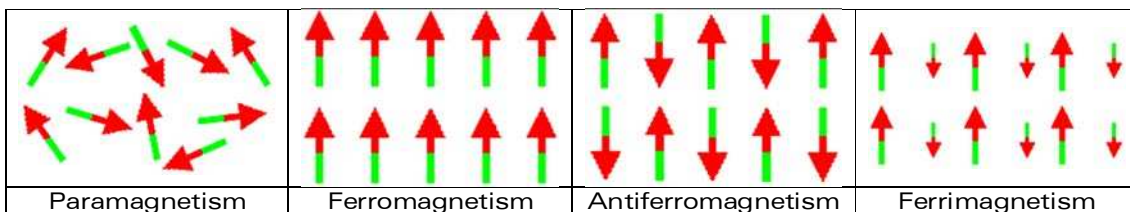


Figure 1: Overview of possible spin arrangements

1.3.5 Ferromagnetism

In ferromagnetic materials, within so-called "Weiss-domains" all spins are aligned parallel, but the domains themselves are arranged in such a way that they effectively cancel each other. Thus no overall magnetisation is observed (Figure 2). These domains are separated by "Bloch-walls", which minimises the total free energy of the system.

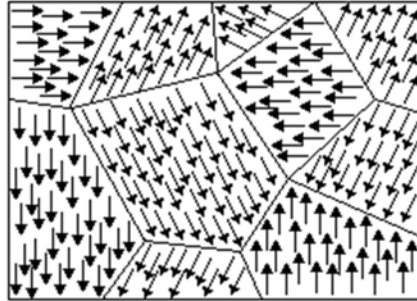


Figure 2: Weiss-domains with Bloch-walls

On applying an external magnetic field, providing it remains below the critical temperature, the Curie temperature T_C , the Bloch-walls move in order to increase the size of the domain with the magnetisation parallel to the applied field and thus the material has all spins pointing in the direction of the external magnetic field, at the saturation magnetisation. Above T_C , the thermal motion of the particles increases sufficiently for the spin ordering to break down and the magnetic moments show overall again in all directions and cancel each other thus showing paramagnetic behaviour (Figure 3).

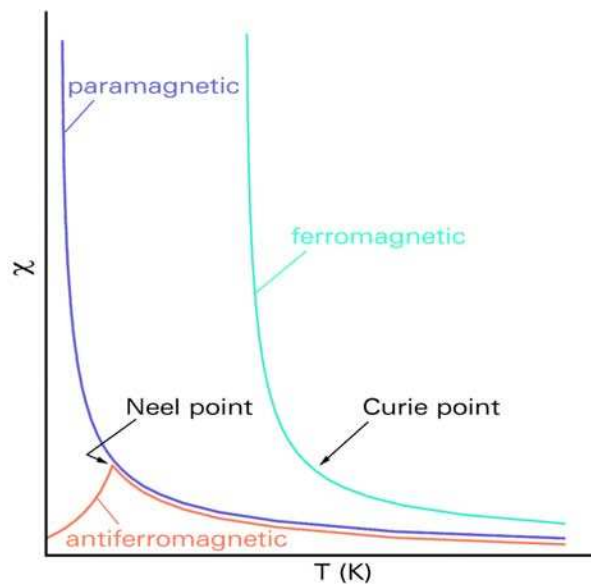


Figure 3: The plot of magnetic susceptibility as a function of temperature for paramagnetic, ferromagnetic and antiferromagnetic materials.

Two different types of ferromagnets can be distinguished on the basis of their hysteresis loops (Figure 4). Hard ferromagnets possess a broad loop and M is large, when the applied field is reduced to zero. This makes them suitable for use as permanent magnets. Soft ferromagnets, on the contrary, show a narrow loop, so they are much more responsive to the change of the applied field.

This behaviour makes them suitable for the use in transformers, where a fast response to rapidly oscillating fields is required (Shriver, 2006: 606).

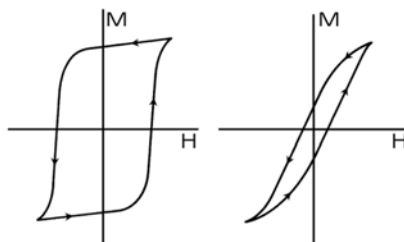


Figure 4: Hysteresis loop of a hard (left) and a soft (right) ferromagnet with the hysteresis measured using the same sweep rate.

1.3.6 Antiferromagnetism

In antiferromagnetic substances the spins are aligned antiparallel. The temperature below which cooperative coupling operates is known as the Néel temperature, T_N . From 0 K up to this temperature, the susceptibility increases continuously since the increase in temperature facilitates the breakdown in the antiparallel alignment of the moments in the external magnetic field and on reaching this temperature the system becomes paramagnetic.

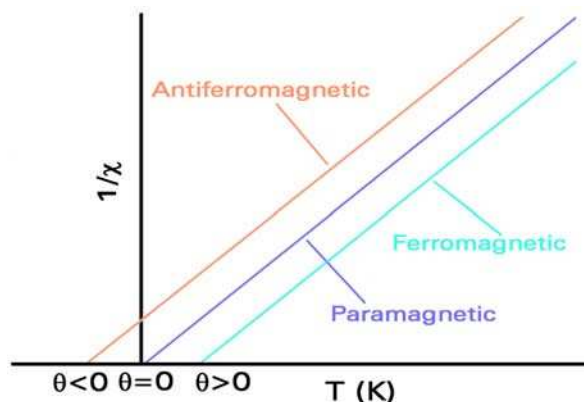


Figure 5: The plot of $1/\chi$ as a function of temperature for paramagnetic, ferromagnetic and antiferromagnetic materials.

1.3.7

1.3.8 Ferrimagnetism

Ferrimagnetism is a third type of collective magnetic behaviour (Figure 6). It shows some similarities to both the previously described magnetic behaviours. Ferrimagnetic substances are divided into Weiss-domains and show a magnetic order below T_c like ferromagnetic substances. However, the alignments of the moments are antiparallel. In contrast to antiferromagnetism, the different magnitudes of the individual spin moments cancel incompletely, so that an uncompensated magnetic moment remains and a spontaneous magnetisation is observed. This magnetisation is therefore significantly weaker than in the case of ferromagnetism.

A well-known example of a ferrimagnetic substance is magnetite (Fe_3O_4), which was originally classified as a ferromagnet before L. Néel discovered the phenomenon of ferrimagnetism (Néel, 1948: 137ff).

However, there are further possibilities for the spin alignment in addition to those described here, e.g. *spin frustration* (Manson, 2000: 1135ff; Zheng, 2006: 165ff), *spin canting* (Riedel, 1975: 413ff; Morales, 1997: 5461ff) and *helical spin* (Uchida, 2006: 359ff; Binz, 2006: 207202), and spin canting (weak ferromagnetism) for which the cited literature can be consulted.

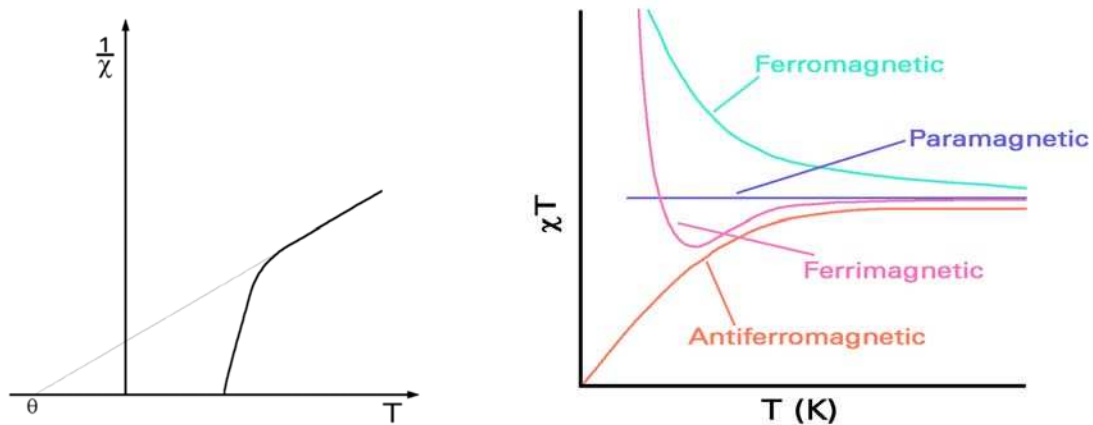


Figure 6: Magnetic characteristic of an ideal ferrimagnet (left) and the plot of χT as a function of temperature for paramagnetic, ferromagnetic, antiferromagnetic and ferrimagnetic materials (right).

1.3.9 Interaction types

In the following the microscopic causes of the spontaneous alignment of magnetic moments in the magnetically ordered state should be discussed. In contrary to diamagnetism or paramagnetism one needs a description of the interaction between the magnetic moments is needed, as the formation of magnetic order is a collective phenomenon.

Although the dipole-dipole-interaction plays an important role in the formation of magnetic domains, the interaction energy is much too low and thus it is not responsible for the formation of the magnetic order in a material. Also the spin-orbit-interaction can be excluded as a significant reason. However, it is causing an anisotropy of the magnetic interaction.

A main reason for magnetic order is the exchange interaction. The exchange interaction has a purely electrostatic origin and can only be explained with the help of quantum mechanics. There are different types of exchange interactions: direct and indirect interaction exchange.

1.3.9.1 *Direct interaction exchange*

Direct interaction exchange occurs between magnetic moments when the lattice atoms are close enough that their wave functions can overlap sufficiently. Indeed the coupling is strong, but decreases rapidly as the ions are separated.

If one imagines two atoms with one electron each, the electrons will localise mainly between the nuclei, as the Coulomb interaction is then minimal.

As the electrons are then at the same place in space at the same time, the Pauli exclusion principle dictates that both electrons will align in antiparallel directions, therefore giving a negative exchange coupling resulting to antiferromagnetic coupling.

If the nuclei are separated, the electrons will act correspondingly in order to minimise the electron-electron repulsion. This leads to a parallel alignment of the spins and so to a positive exchange interaction and thus ferromagnetic coupling.

The magnitude of direct exchange as a function of interatomic distance is represented by the Bethe-Slater curve (Figure 7) (Slater, 1930: 509ff).

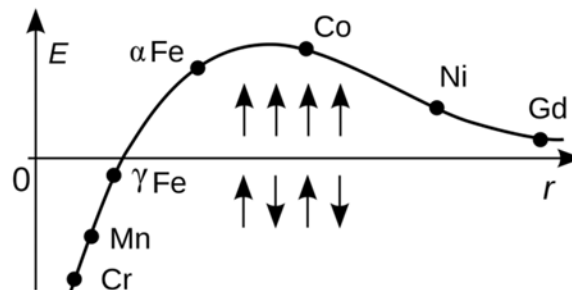


Figure 7: Bethe-Slater curve

The direct interaction exchange is in contrary to the indirect interaction exchange fairly short-ranged and thus the indirect interaction exchange is more often realised. Examples for indirect interaction exchange are the superexchange, the RKKY-exchange and the double-exchange.

1.3.9.2 *Superexchange*

Superexchange is, in contrast to direct exchange, an indirect exchange since spin-coupling is mediated via an extra atom (Figure 8).

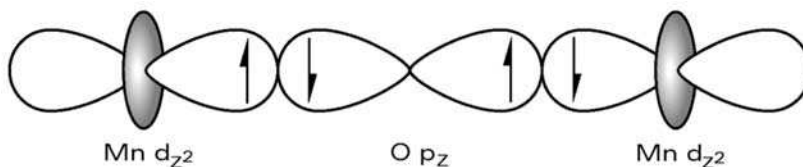


Figure 8: super exchange using the example of MnO

In this case the spin of one metal atom (left Mn(II)) couples with the electron spin of the other metal atom (right Mn(II)) through a third diamagnetic centre, here an oxide ion. It is energetically favourable to have the electron spins of the manganese atoms in this arrangement coupled antiparallel instead of parallel. The more the orbitals overlap, the stronger this interaction becomes and the higher the Néel temperature, which is e.g. 122K for MnO and 523K for NiO as a result of the smaller ionic radius for nickel. In molecular complexes, the coupling indeed often takes place through intervening ligands instead of a simple oxide ion.

1.3.9.3 *RKKY-exchange*

The RKKY-exchange, named after M.A. Rudermann, C. Kittel, T. Kasuya and K. Yosida, describes the indirect exchange between the magnetic moments of the metal atoms. The coupling of the magnetic moments is hereby arranged by the spin polarisation of the itinerant electrons in the metal. The RKKY exchange coefficient j oscillates from positive to negative as the separation of the ion changes, which means that, depending on the distance between the atoms in the solid state the coupling is ferromagnetic or antiferromagnetic (Figure 9).

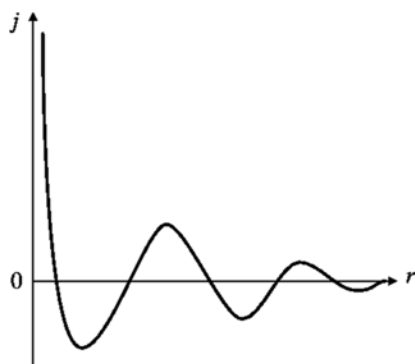


Figure 9: Variation of the indirect exchange coupling constant, j , of a free electron gas in the neighbourhood point magnetic moment at the origin $r=0$.

In particular in the rare-earth metals, direct Heisenberg exchange interaction is not possible, due to the evanescent overlap of the wave functions. This is because the magnetic electrons in the 4*f* shell are shielded by the 5*s* and 5*p* electrons, so that the magnetic order is takes place via the conduction electrons (Rudermann, 1954: 99ff; Kasuya, 1956: 45ff; Yosida, 1957: 893ff).

1.3.9.4 Double-exchange

The semiconductor LaMnO₃ (perovskite type) containing the magnetically active Mn^{III} shows antiferromagnetic behaviour. However, La_{1-x}A_xMnO₃-phases, where some of the La³⁺ ions are substituted by an alkaline earth metal ion A²⁺, show electronic conductivity and ferromagnetic behaviour.

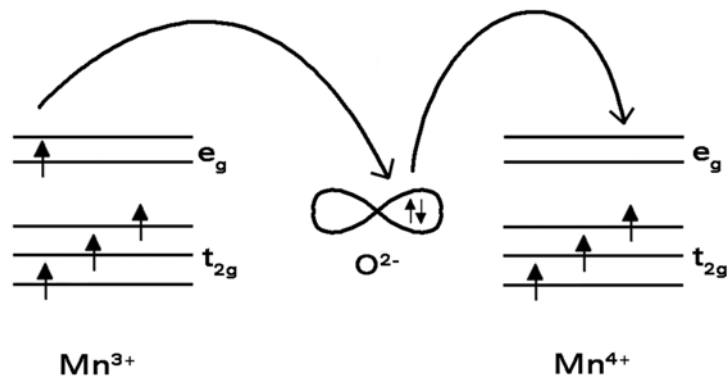


Figure 10: Double-exchange of the d-electron of Mn^{III}

Here, Mn exists in two oxidation states (Mn^{III} and Mn^{IV}) and the electronic conductivity is due to the electron transfer from the Mn^{III} to the Mn^{IV} ion in conjunction with an O²⁻ ion between the two Mn ions.

The mechanism of double-exchange (Figure 10) was first proposed in 1951 by C. Zener (Zener, 1951: 403ff). In order to obey Hund's rule the spin of the electron transferred to the Mn^{IV} ion must be the same as the spin of the electron transferred to the O²⁻ ion and thus the behaviour is ferromagnetic.

1.4 Single molecule magnets (SMMs)

A single molecule magnet (SMM) is a molecule that shows slow relaxation of the magnetisation of purely molecular origin. It is a molecule that can be magnetised. Below the blocking temperature it will remain magnetised for a certain time (in the range of seconds up to several months) even after switching off the external magnetic field (Sessoli, 2003: 278ff). This is a property of the molecule itself. No interaction between the molecules is necessary for this phenomenon to occur. This makes SMMs fundamentally different from traditional bulk magnets. SMMs can be dissolved in a solvent or put in some other matrix, like a polymer, and will still show this property. The prerequisites for such a system are

- a high-spin ground state (S)
- a negative uniaxial zero-field splitting D (due to high magnetic anisotropy) and
- a negligible magnetic interaction between molecules.

The combination of these properties can lead to an energy barrier so that at low enough temperatures the system can be trapped at the bottom of one of two high-spin energy wells (Figure 12). The anisotropy leads to an energy barrier which the spins must overcome when they switch from an "all up" alignment to an "all down" alignment.

This barrier (U) is defined as

$$U = |D|S^2 \quad (1.19)$$

where S is the dimensionless total spin state and D is the zero-field splitting parameter in cm^{-1} or K. The selection rule $\Delta M_S = \pm 1$ for an allowed spin transition (Haken, 2006: 280ff), results in energy barrier U which separates the two lowest energy levels of $M_S = \pm S$. A positive D value would result in the $M_S = 0$ level being lowest in energy. This means that for a molecule to behave as an SMM, it should have a negative D value. Theoretically the higher the barrier the longer a material remains magnetised, and a high barrier is obtained when the molecule contains many unpaired electrons and also when its zero-field splitting value is large.

An example is the $\{\text{Mn}_{12}\text{-Ac}\}$ (Lis, 1980: 2042ff) cluster (Figure 11) which is composed of a central $\{\text{Mn}^{\text{IV}}_4\text{O}_4\}$ cube surrounded by a ring of 8 Mn^{III} ions connected through bridging oxo ligands. The molecule has a spin state of 10 (involving 20 unpaired electrons) and $D = -0.5 \text{ cm}^{-1}$ resulting in a barrier of 50 cm^{-1} (Figure 12).

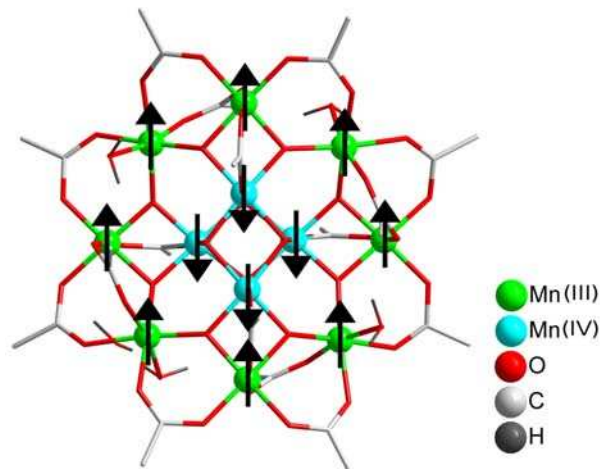


Figure 11: Spin alignment in $[\text{Mn}_{12}\text{O}_{12}(\text{CH}_3\text{COO})_{16}(\text{H}_2\text{O})_4]$ (Caneschi, 1991: 5873ff).

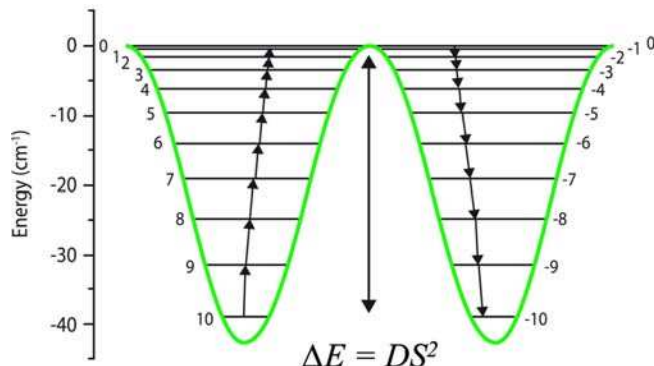


Figure 12: Two potential diagram showing the relative positions of the zero-field split M_S levels of an $S_T = 10$ system and the energy barrier separating the $M_S = +10$ and the $M_S = -10$ states.

SMM behaviour is characterised by a hysteresis, which appears when magnetisation is measured in a magnetic field sweep: on lowering the magnetic field again after reaching the maximum magnetisation, the magnetisation remains at high levels and it requires a reversed field to bring magnetisation back to zero (Figure 13). It has been reported that the energy barrier U is apparently dependent on $\{\text{Mn}_{12}\text{-Ac}\}$ crystal size/morphology. In addition, it was found that the magnetisation relaxation times vary as a function of particle size and size distribution (Munto, 2006: 2612ff).

The series of steps, observed in Figure 13, are induced by resonant quantum tunnelling (Sessoli, 1993: 141ff).

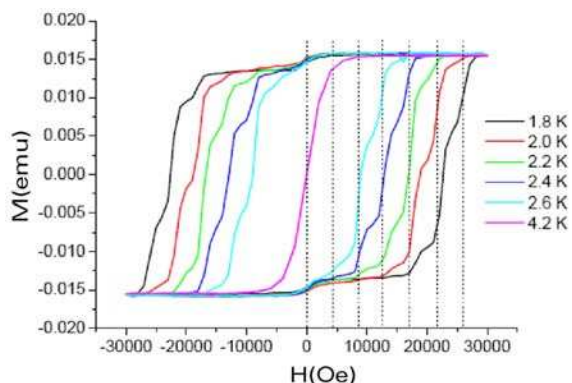


Figure 13: The magnetic hysteresis loops of Mn_{12} -Ac are shown at the indicated temperatures at a scan rate of 0.025 T/10 s (Thomas, 1996:145ff).

The effect of single molecule magnetism is readily probed through ac magnetic susceptibility measurements, which provide a direct means of gauging the relaxation rate. Here the magnetic susceptibility of a sample is measured using a weak magnetic field that switches direction at a fixed frequency. If the effective barrier to magnetisation relaxation is significant in comparison to the thermal energy, then the measured susceptibility referred to as the in-phase (real component (χ')) of the ac susceptibility begins to diminish in comparison to the out-of-phase signal (χ''). Accordingly, the portion of the susceptibility that cannot keep up with the switching field, the out-of-phase (imaginary component of the ac susceptibility, χ'') increases and thus the ration between the in-phase and out-of-phase signal becomes bigger. When a magnetisation reversal barrier exists, then χ' and χ'' are also frequency-dependent. If the net magnetisation relaxes fast enough to keep up with the oscillating ac field, then there is no imaginary (out-of-phase) susceptibility (χ'') and the real (in-phase) susceptibility (χ') is equal to the dc susceptibility (Figure 14).

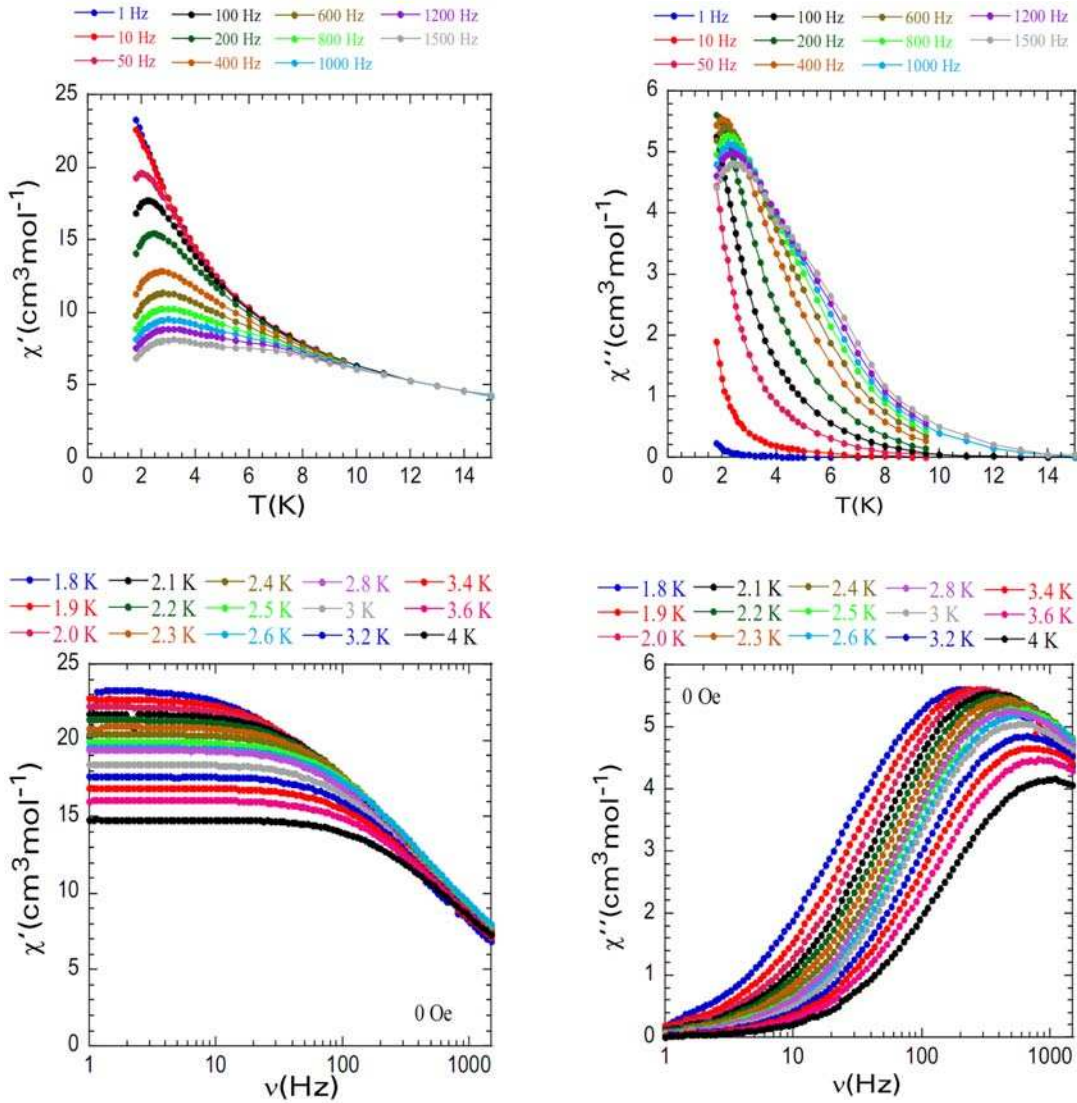


Figure 14: An example of ac susceptibility measurements as a function of temperature at different frequencies, and as a function of frequency at different temperatures: (a, c) in-phase and (b, d) out-of-phase signals of a Dy_4 compound (Abbas, 2010: 8067ff).

If just a single relaxation process is operational, then each plot of χ'' versus frequency at different temperatures will display a peak at the temperature where the switching of the magnetic field matches the relaxation rate, $1/\tau$. Furthermore, since $1/\tau$ increases with temperature, this peak should shift to higher temperatures when the switching frequency is increased. The relaxation time for the magnetisation in a single molecule magnet can be thus expressed by the Arrhenius relationship

$$\tau = \tau_0 e^{\left(\frac{U_{\text{eff}}}{k_B T}\right)} \quad (1.20)$$

where τ_0 is the pre-exponential factor and U_{eff} the effective energy barrier.

A plot of $\ln(\tau)$ versus $1/T$ should be linear, with the slope and intercept permitting evaluation of U_{eff} and τ_0 respectively (Figure 15).

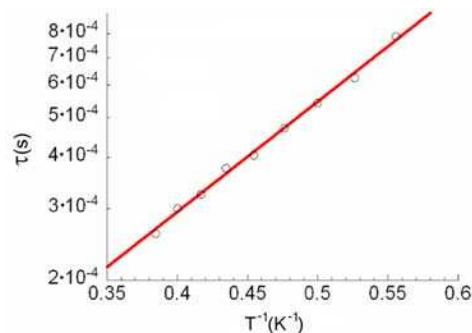


Figure 15: An example of τ versus $1/T$ plot obtained from both temperature and frequency dependent ac susceptibility measurements under zero dc field of a Dy_4 compound (Abbas, 2010: 8067ff).

It has also been recognised that there can be additional influences on the SMM behaviour such as quantum tunnelling (Sessoli, 1993: 141ff) or inter-complex magnetic interactions (Wernsdorfer 2002: 416ff). Indeed at low enough temperature, quantum tunnelling of the magnetisation can be experimentally observed as it becomes faster than the thermally activated relaxation involving U_{eff} . When two M_S microstates on either side of the energy barrier have similar energies, then there is an increased probability of quantum tunnelling of the magnetisation (QTM). SMM complexes appear to be unique systems for studying fundamental phenomenon such as quantum spin tunnelling. These may find uses in future applications in molecular electronics such as quantum computing. The quantum-mechanical approach is based on the Schrodinger equation, a differential equation for the wave function Ψ , which indicates where a particle can be. This wave function is also in the "forbidden" region, e.g. within or beyond a barrier, nowhere zero, but abate there exponentially with increasing penetration depth. Even at the end of the forbidden area, its value is unequal zero. Since the magnitude square of the wave function $|\Psi|^2$ is interpreted as the probability density for the position of a particle, there is a nonzero probability for the particles to appear on the other side of the barrier.

The naming of tunnel effect reflects the fact that the particles cannot overcome classical the barrier if the energy is not higher than the potential barrier. Thus the effect can be rather seen as a "tunneling" through the barrier.

The interested reader is referred to literature such as (Leggett, 1987: 1ff), (Enz, 1986: 1765ff) or (Chudnovsky, 1988: 661ff).

1.4.1 The role of the spin ground state for SMM's

In many of the previously synthesised SMMs particular attention was paid to the synthesis of clusters with as large a spin ground state as possible. This is easy to comprehend, if one considers the equation to estimate the energy barrier in a SMM:

$$\Delta E \propto |D| \cdot S^2 \quad (1.21)$$

Thus, an increase of ΔE can be achieved by an increase of $|D|$ and S . Ideally, both factors, S and $|D|$, should be controlled, which in reality is synthetically very difficult. Initially researchers concentrated first on controlling one parameter. As spin S enters into Equation (1.21) as a squared contribution, the increase of S held the promise of achieving an increase in ΔE more easily than trying to control the parameter D and therefore it seemed to be logical to focus on S to obtain new SMMs with larger energy barriers and, as a consequence of this, also longer relaxation times. Therefore the most promising way forward in the early days of SMM research seemed simply to try to increase S in order to improve the SMM behaviour. Successful attempts to increase S are described in numerous publications. In 2004 Murugesu et. al. could synthesise a Mn_{25} -cluster with a total spin of $51/2$ (Murugesu, 2004: 4766f) and two years later Ako et. al. obtained a Mn_{19} -cluster with a total spin of $83/2$ (Ako, 2006: 4926ff), which is still the compound with the largest spin ever. In contrast to the Mn_{25} , where some of the spin moments are arranged antiparallel and cancel each other, all spins in the Mn_{19} molecule are aligned parallel leading to the maximum possible spin ground state of $S=83/2$. Thus, the synthesis of molecules, where the spin moments within the molecule are arranged completely parallel remains a major objective and challenge of SMM research. Since there is a parallel arrangement of spins in the case of Mn_{19} , a significant improvement in SMM behaviour in terms of operating temperature might be expected for this molecule. However, magnetic measurements showed that despite the large spin ground state the Mn_{19} molecule does not show SMM behaviour, since D is close to zero and slightly positive (Ako, 2006: 4926ff). Hence, an energy barrier which prevents the rapid relaxation of the spins does not exist and thus the idea that a high S value will give access automatically to interesting SMM behaviour is an oversimplification. Based on these findings, a detailed theoretical study of the relationships between ΔE , $|D|$ and S was needed and led to calculations that show that in many cases it is found that the anisotropy barrier does not increase with S as S^2 but as S^0 in equation (1.21) (Waldmann, 2007: 10035ff; Ruiz, 2008: 52ff). This and successful improvements of SMM behaviour by focussing on parameter $|D|$ (Yang, 2007: 456f; Ishikawa, 2005: 2931ff; Milios, 2007: 2754f) led in fact to the thought that the focus should be put on the anisotropy. One example is the $Mn_{18}Dy$ cluster (Ako, 2009: 544ff) in which the central manganese ion of the Mn_{19} cluster is substituted with a dysprosium ion. Although this reduces the spin ground state, $Mn_{18}Dy$ shows SMM behaviour resulting from the anisotropy of the dysprosium ion.

Finally it is important to mention, that neither the first simplification for S nor the new calculations are universally valid. Which correlation is finally found to exist between ΔE and S must be investigated theoretically for each particular case, but it seems to be proven, that a complex requires both large S and $|D|$ values to show SMM behaviour and the larger these values are, the higher will be the temperature, where this behaviour can be observed.

1.4.2 Synthetic approaches for isolating polynuclear complexes

Several synthetic routes are being pursued to construct new magnetic materials that, ideally, satisfy the criteria for SMMs. It is difficult to achieve a rational synthesis of a high-spin species from simple reagents, and even then there is the danger that the anisotropy will be too low to either give an SMM, or to give one with a reasonable barrier (Murugesu, 2004: 4766f; Stamatatos, 2006: 4134ff; Ako, 2006: 4926ff). An alternative approach to new high-spin molecules is to start with a preformed molecule, which already provide a certain nuclearity and spin ground state, respectively, and then perturb it in some way, without major structural change, in order to modify the constituent exchange parameters and possibly alter the ground state to a larger value rather than a smaller one. An early synthetic success using this approach was the formation of an undecanuclear iron complex made by Lippard et al. (Gorun, 1987: 3337ff).

Among the various Mn^{III} sources which have been explored in the past are $\{Mn_3O\}^{6+/7+}$ and $\{Mn^{III}_4O_2\}^{8+}$. They have provided useful routes to a variety of higher nuclearity complexes (Mishra, 2005: 54ff; Mishra, 2008: 1940ff). However, there are only a few examples where $[Mn_6O_2(piv)_{10}(py)_{2.5}]$ has been used as a source for new manganese clusters (Mereacre, 2010: 4918ff). The tridentate chelating ligands which have been used have been fairly flexible ones, such as deprotonated *N*-butyldiethanolamine (*N*-n-bdeaH₂), allowing the alkoxide arms to bind and bridge with little structural restriction, thus giving a variety of products (Heroux, 2009: 3541ff; Akhtar, 2009: 3502ff).

The second strategy can be termed as self- or serendipitous assembly. A prerequisite for the successful application of self-assembly is to take into account the impossibility of fully understanding the influence of all factors involved in a reaction on the resulting product (Galloway, 2008: 7438). Therefore a wide range of conditions for any specific reaction is explored. The substitution pattern of the ligand or ligands, the metal salt, the metal:ligand ratio, the crystallisation solvent, the solution concentration and the crystallisation temperature may all play a role in the formation of a complex. Although this synthetic approach produces unpredictable results, minor variations in the ligands may influence the structure and solubility. The use of mixtures of organic ligands can, for example, form complexes of higher nuclearities (Scott, 2005: 6540ff). Another approach is to use co-ligands having carboxylate or hydroxyl groups to construct large polynuclear clusters. The functional groups can coordinate to more than one metal centre. In order to have N-donor and O-donor atoms, several co-ligands such as pivalic acid or other carboxylic acids and azide were used along with the *N*-n-butyldiethanolamine (*n*-bdeaH₂) ligand.

Varying the co-ligand by increasing the number of donor groups might lead to the incorporation of more metal centres. When alcohol-based solvents (ROH or H₂O) are employed, solvolysis reactions can occur, forming hydroxyl, alkoxy or oxo bridges. Heterometallic complexes can be obtained by using two types of metal ions along with co-ligands. The presence of two different metal centres can give rise to interesting magnetic properties and can allow further investigations of the exchange interaction between two different metal ions. This can involve using two different transition metals or a combination of transition and lanthanide metal ions. The lanthanides behave as hard acids preferring O- rather than N-donors, while transition metal ions have the tendency to coordinate to N-donors as well as O-donors. Consequently, a typical approach to construct 3d-4f complexes is by self-assembly of different metal ions with ligands containing both, O- and N-donors. This need is fulfilled with the use of derivatives of diethanolamine ligands and hydroxymethyl- and hydroxyethylpyridine, respectively.

Furthermore, it seems, that the environment of the lanthanide ion is of extraordinary importance. Basically, the ground state of a lanthanide ion (e.g. ⁷F₆ for Tb^{III}) is made up of a series of sublevels $|J, J_z\rangle$, with $J_z = \pm J, \pm(J-1), \dots, 0$, e.g. $|6, J_z\rangle$, with $J_z = \pm 6, \pm 5, \dots, 0$ for the ⁷F₆ ground state of Tb^{III}. These sublevels split in a ligand field.

For uniaxial anisotropy, the levels with the highest $|J_z|$ (i.e. ± 6 for Tb^{III}) are needed to be the most stable, i.e. lowest in energy (Kajiwara, 2011: 196ff).

For Tb^{III}, Dy^{III} and to a lesser extent also Ho^{III}, these sublevels have an oblate profile, while for Er^{III} it is prolate. To minimise the destabilisation of these from the negatively-charged ligand field, the ligand field needs to have the opposite geometry so that concentrations of electron density in the ligand field are kept as far away from the electron distribution in the sublevel.

Therefore for Tb^{III}, Dy^{III} and Ho^{III} to show uniaxial anisotropy, a ligand field is needed which is prolate or predominantly axial in nature, with the harder more negatively charged ligand atoms concentrated on opposite sides of the ion. This is why the (Phth)₂Tb and (Phth)₂Dy sandwiches, with the coordinating atoms forming an axially-extended square antiprism, work so well as Single-Ion Magnets, for example.

By contrast, Er^{III} requires an oblate ligand field in order to have axial anisotropy. So for an Er^{III}-based SMM a ligand geometry with harder atoms concentrated in a "belt" or equatorial plane around the Er^{III} ion is needed.

It seems as if one is better at generating lanthanide complexes in which the Ln^{III} ion has an axial/prolate ligand field, which is why usually the Dy and Tb analogues are found to show the most favourable magnetic behaviour and thus represent the most interesting SMMs, with Ho^{III} is being worse and Er^{III} being even useless! Therefore, if a Dy compound is not showing SMM behaviour, it is worth to look at the Er analogue, rather than assuming that this will be even worse.

1.5 Introduction to manganese chemistry

Manganese is quite common on earth with about the same relative abundance as carbon. Major sources of the metal are Braunstein (MnO_2) in the form of e.g. Pyrolusite ($\text{MnO}_{1.7-2}$), Braunit (Mn_2O_3) which is isostructural to $\alpha\text{-Fe}_2\text{O}_3$ and the corresponding hydroxide Manganite ($\text{MnO}(\text{OH})$), Hausmannite (Mn_3O_4) and the carbonate Rhodochrosite (MnCO_3).

Manganese lies at the top of group 7 in the periodic table and occurs mainly in the oxidation states +2, +3, +4 and +7, but several oxidation states from -3 to +7 are known. The most stable oxidation state is +2, as the d -shell is then half-filled. The electronic configuration of Mn^0 is $[\text{Ar}] 4s^2 3d^5$.

Mn^{II} mostly adopts the coordination numbers 5, 6 or 7 and rarely even 8 (Ako, 2006: 5048ff), while Mn^{III} is most commonly penta and hexa-coordinate. Mn^{II} is quite resistant towards oxidation and reduction due to the half-filled d -orbital set mentioned above. For the high spin configuration there is no crystal field stabilisation energy (CFSE). Mn^{II} forms mostly high-spin complexes. Only very strong-field ligands like CN or CNR lead to low-spin complexes (Wiberg, 2007).

Mn^{III} has four d -electrons and tends to favour the high-spin configuration (Figure 16). In this case the fourth electron can fill the $d_{x^2-y^2}$ or the degenerate d_{z^2} orbital which causes the so called Jahn-Teller distortion that is often observed for Mn^{III} (Jahn, 1937: 220ff). The Jahn-Teller effect describes the geometrical distortion of non-linear molecules, which have an electronically degenerate ground-state. The molecule or ion will distort to remove the degeneracy and thus to prevent the instability. The effect of the Jahn-Teller distortion is particularly obvious in systems with d^4 high-spin configuration (Mn^{III}), d^7 low-spin configuration (Co^{II}) and d^9 configuration (Cu^{II}) octahedral complexes, respectively.

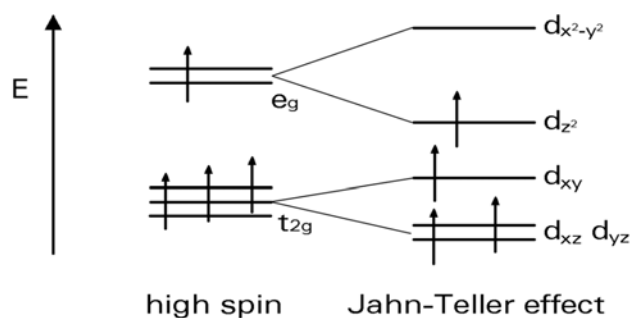


Figure 16: d^4 high-spin Mn^{III} configuration leading to Jahn-Teller distortion

1.6 Introduction to iron chemistry

Iron is one of the essential elements necessary for living organisms and it is found in the earth's core as an abundant transition metal in different types of ore in sufficient quantity to be converted into iron metal. Iron is widely distributed in the earth's crystals rocks as oxide and oxhydroxide minerals such as hematite (Fe_2O_3), the mixture of hydrated Fe^{III} oxide-hydroxide of varying composition, limonite ($\text{FeO}(\text{OH}) \cdot n\text{H}_2\text{O}$), magnetite ($\text{FeO} \cdot \text{Fe}_2\text{O}_3$), goethite ($\text{FeO}(\text{OH})$), lepidocrocite ($\gamma\text{-FeO}(\text{OH})$), akaganeite ($\beta\text{-Fe}(\text{O},\text{OH},\text{Cl})$) and also as the carbonate siderite (FeCO_3). Also sulphur containing minerals occur in form of e.g. pyrite (FeS_2) and α -metavoltine (Jambor, 1998: 2549ff). The importance of iron in environmental, geological, industrial and biological fields makes the understanding of iron chemistry of great significance.

One of the most characteristic features of Fe^{III} chemistry is its hydrolysis to form rust ($\text{Fe}(\text{OH})_3$), which is also formed as the result of an electrochemical oxidation process on the metal in the presence of water, an electrolyte and oxygen (De Sa, 1991: 55). Iron lies at the top of Group 8 in the periodic table and occurs mainly in the oxidation states +2 and +3. Fe^{III} has the electronic configuration $[\text{Ar}]3d^54s^0$ and its compounds are usually high-spin d^5 unless a strong field ligand is present and the d orbitals are well-separated to give a low spin configuration, as it is the case in $[\text{Fe}(\text{CN})_6]^{3-}$ (Cotton, 1972: 185ff).

Most Fe^{III} complexes are octahedral but are nearly always distorted from ideal octahedral geometry. The two possible arrangements of the five d -orbitals for the octahedral case are shown below (Figure 17).

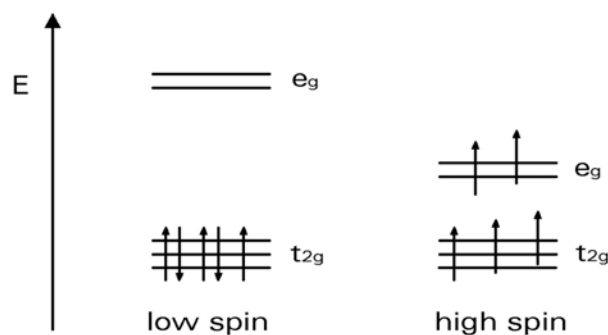


Figure 17: Two possible arrangements of five electrons in octahedral environment

1.7 Introduction to cobalt chemistry

Cobalt is an essential metal for the human body to form e.g. vitamin B_{12} and naturally it is mostly found in form of different cobalt ores like Smaltite (CoAs_{2-3}), Cobaltite (CoAsS) and Linnaeite (Co_3S_4).

Cobalt occurs in oxidation states from -1 to +5, but the main oxidation states are +2 and +3. Co^{II} is mostly tetra, penta- or hexa-coordinate, while Co^{III} is almost exclusively hexa-coordinate. Normally Co^{III} forms octahedral low-spin complexes with t_{2g}^6 configuration and with no unpaired electrons, so diamagnetic behaviour.

The contrary is true for Co^{II} , where the low-spin configuration is an exception and only very strong donors like cyano ligands will give low-spin complexes, e.g. paramagnetic $[\text{Co}(\text{CN})_5]^{3-}$ (Wiberg, 2007). However, there are also spin-crossover complexes known, where Co^{II} is switching under certain conditions between high-spin and low-spin configuration (Brooker, 2002: 2080ff; Faus, 1994: 5535ff).

Because of the paramagnetic characteristics of Co^{II} , it is magnetically much more interesting than Co^{III} as it provides three unpaired electrons, no matter if tetrahedral or octahedral high-spin complexes are formed.

1.8 Introduction to rare-earth metal chemistry

The lanthanides (Ln) are unusual in that they are all found together in natural ores. The most common ores are Bastnasite (LnCO_3F) and Monazite (LnPO_4). In both ores, two general observations can be made about relative abundance. The abundance of the even atomic-numbered elements is about ten times greater than the odd atomic-numbered elements (Harkins rule) and the abundance decreases with increasing atomic number, odd or even. The rare-earth metals are all electropositive with a remarkable uniformity of chemical properties. Frequently the only significant difference between two lanthanides is their size. The ability to choose a rare-earth metal of a particular size often leads to the possibility to “tune” the properties of their compounds. The elements favour the oxidation state +3 with a uniformity that is unprecedented in the periodic table. Other properties vary significantly e.g. the radii of the Ln^{3+} ions contract steadily from 116 pm for La^{3+} to 98 pm for Lu^{3+} . The decrease in ionic radius is attributed in part to the increase in Z_{eff} as electrons are added to the 4f subshell, but detailed calculations indicate that subtle relativistic effects also make a significant contribution. A Ln^{3+} ion is a hard Lewis acid, as indicated by its preference for F^- and oxygen-containing ligands and its occurrence with PO_4^{3-} in minerals as mentioned above. The relatively large Ln^{3+} ions can have high coordination numbers and a variety of coordination environments in the solid state which are also observed in solution. The spatially shielded f electrons have no significant stereochemical influence and consequently ligands adopt positions that minimise the ligand-ligand repulsions. The study of the coordination chemistry of lanthanide elements is a rapidly growing area of interest because of the potential applications of their complexes as magnetic resonance imaging (MRI) contrast agents (Aime, 1998: 19ff), as catalysts in organic synthesis (Bao, 2007: 2333ff), as molecular magnetic materials (Ishikawa, 2005: 3650f), as luminescent species (Liu, 2004: 2280f) and as single molecule magnets (Tang, 2006: 1729ff). In comparison to the advances in the synthesis and study of the magnetic properties of polynuclear complexes of the d-block metals (Stamatatos, 2010; Tasiopoulos, 2004: 2117ff; Abu-Nawwas, 2008: 198ff) rather little attention has been dedicated to exploring the systematic synthesis and study of the magnetic properties of 4f- (Thiakou, 2006: 2869ff; Eliseeva, 2006: 4809ff; John, 2005: 4486ff) and 3d-4f-metal complexes (Mereacre, 2010: 5293ff; Xiang, 2010: 4737ff; Baskar, 2010: 4747ff).

In the lanthanide series, the inner $4f$ electron shell is filled from lanthanum to lutetium. Lanthanides have the advantages that they can have a large number of unpaired f -electrons and considerable single-ion anisotropy. The origin of SMM behaviour in lanthanide containing compounds is, however, more complicated than that of most d -block transition metal ions since there is likely to be a significant orbital component. The effect of spin-orbit coupling increases as the atomic number increases, with the exception of the $4f^7$ configuration of gadolinium, which has no first order angular momentum. As a result it is useful to synthesise Gd^{III} analogues of Ln^{III} complexes in order to interpret the magnetic properties. However, this is only possible, if the system is not too complicated. The limited magnetic investigations have focussed on $Gd(III)$ - $Gd(III)$ coupling because of the relative simplicity as compared to the rest of the Ln^{III} ions where both orbital and crystal field effects have to be considered in the interpretation of results. In general, the complexity of lanthanide systems is based on the characteristics of the magnetic centres and the type of structural links between them. The magnetic interactions between paramagnetic centres can take place not only through single atoms but also through multi-atomic bridges such as those provided by carboxylato and other O-C-O ligands. The latter have been proved to be effective for the transmission of magnetic information through a variety of bridging conformations e.g. bidentate or tridentate bridging. Usually, when the lanthanide centres are functionalised with these kinds of ligands the resulting structural motifs are complicated. However they present potentially interesting magnetic properties (Yi, 1998: 2243ff). According to the literature, weak ferromagnetic (Baggio, 2005: 8979ff; Costes, 2002: 323ff) or weak antiferromagnetic (Rohde, 2003: 2069ff; Lam, 2003: 149ff) interactions can be found in pure polynuclear Ln^{III} clusters and $3d$ - $4f$ -compounds (Wang, 2010: 7276ff; Zhao, 2010: 4911ff), respectively ($3d$ -metal=Mn, Co). High-nuclearity clusters of paramagnetic metal ions are of the interest in view of the fact that they can exhibit SMM phenomenon (Aubin 1996: 7746ff).

1.9 Introduction to $3d$ - $4f$ complexes

Using a lanthanide element in permanent magnets is hardly a new concept. The first work in this area was published in 1935, when Urbain, et al. reported that gadolinium is ferromagnetic (Urbain, 1935: 2132). Some of the lanthanides have record magnetic moments, but unfortunately their Curie temperatures lie far below room temperature. In the 1940's, scientists and engineers had access to reasonable quantities of high purity lanthanide elements and have systematically studied the many unique properties, not just magnetic, of these elements and their alloys. The magnetic properties of the binary lanthanide-iron alloy compounds, including Nd-Fe, were examined at about the same time as the lanthanide-cobalt systems in the 1960's and early 1970's. However, all the binary lanthanide-iron alloys have at least one of the following problems, making them unsuitable as permanent magnets:

1. A Curie temperature near or below room temperature,
2. Unfavourable anisotropy, usually an easy cone or an easy plane and
3. Antiferromagnetic coupling between the lanthanide and the iron magnetic moments, resulting in low saturation magnetisation.

However, it should be noted, that in the case of lanthanide ions, spin-orbit coupling also plays a role, making it difficult to estimate the real antiferromagnetic interaction due to the lack of a model for the anisotropy.

Lanthanide ions have radii that vary between 116 and 98 pm. By comparison, high spin Fe^{3+} has an ionic radius of 65 pm. Thus the volume occupied by a Ln^{3+} ion is typically five to ten times greater than that occupied by a 3*d*-metal ion. Unlike the 3*d*-metal atoms, which rarely exceed a coordination number of 6, compounds of lanthanide ions often have high coordination numbers and a wide variety of coordination environments. In contrast to lanthanide-transition metal alloys, SMMs, which are molecular superparamagnets, derive their properties from the combination of a large ground state spin value *S* respectively *J* for lanthanide ions and a large and negative magnetoanisotropy (negative zero-field splitting parameter, *D*). In the case of mixed metal 3*d*-4*f* systems, the presence of lanthanide ions provides for some of the lanthanide ions both, large spin and considerable magnetic anisotropy. As reflected in the large *D* values, these systems could generate SMMs with properties significantly different from those of pure transition metal SMMs (Zaleski, 2004: 3912ff; Mori, 2005:2588ff). This combination results in a significant energy barrier to magnetisation reversal and hence slow relaxation of the magnetisation is observed at low temperatures. The latter can either be detected as frequency-dependent signals in ac susceptibility measurements or as hysteresis in magnetisation versus applied dc field sweeps (Scheurer, 2010: 4784ff). There are now many homometallic SMMs, most of them manganese or iron species (Saalfrank, 2001: 2765ff) and new approaches aimed at producing heterometallic species have been more recently explored as a route to distinctly different properties. As a result of such work, some mixed transition metal/lanthanide SMMs have recently been reported (Mereacre, 2008: 3577ff; Chen, 2009: 808ff; Schray, 2010: 5185ff). However, a goal of this research is to understand the chemistry of such 3*d*-4*f*-systems and to elucidate their magnetochemistry. Therefore it is necessary to study new compounds comprising mixed 3*d*-4*f* clusters. The exploration of new 3*d*-4*f* compounds with manganese, iron and cobalt as transition metals hence seemed timely.

Nevertheless, the inherent anisotropy of most lanthanide ions and the difficulty in analysing the magnetic properties of 3*d*-4*f* couples makes the description of their magnetic properties challenging. This often makes identifying the origin of the SMM behaviour in such compounds more complicated than is the case for coordination clusters based solely on 3*d* metal ions. However, the use of lanthanide ions is appealing since there is the possibility of combining large spin states with the highly anisotropic nature of most of the single ions. Furthermore, the systematic study of a family 3*d*-4*f* compounds can lead to insights regarding the contributions to the overall magnetic behaviour provided by a given lanthanide ion. For example, the Tb^{III} ion is a source of six electrons and significant anisotropy. Replacement of Tb^{III} with Gd^{III} can add an additional electron, but largely switch off the Ln^{III} spin-orbit coupling effects and anisotropy. Introducing diamagnetic rare earths such as La^{III} , Y^{III} or Lu^{III} can switch off the contribution from unpaired *f*-electrons altogether. However, a fundamental problem in much of the work reported on 3*d*-4*f* systems is the lack of systematic magnetic studies on a family of isostructural aggregates in which the 4*f* ion is varied across the series.

Such an investigation could help provide answers to questions concerning, for example, the relative contributions of the $3d$ - and $4f$ ions to the magnetic properties of the molecule. It should also be possible to estimate how significant the interactions between the $3d$ - and $4f$ ions are or, indeed, whether these contributions to the overall magnetic behaviour are largely independent. It should also be possible to discover the rules to help choose the best lanthanide to optimize the magnetic properties of a cluster. Thus, to fulfil this concept a number of compounds will be presented within this thesis with isostructural families running across the lanthanide series in a large range in order to address these issues.

1.10 Ligand selection

All ligands used in this thesis provide mixed oxygen (O) and nitrogen (N) donor sets and are potentially multidentate.

N-n-butyl-diethanolamine (n-bdeaH₂) has been reported in reaction systems with $3d$ transition metal elements, such as manganese (Ako, 2006: 2579ff; Malaestean, 2010: 1990ff), iron (Ako, 2007: 756ff), cobalt (Scheurer, 2010: 4784ff) and copper (Gruenwald, 2009: 2109ff), but the intersection of $3d$ transition metal elements and lanthanides is a burgeoning field of chemical research requiring more attention. As a result, the n-bdeaH₂ ligand was selected in order to explore the range of accessible $3d$ - $4f$ mixed metal complexes and correlate their structures and properties. Coordination complexes containing the n-bdeaH₂ ligand along with different co-ligands (e.g. pivalic acid) will be presented in the forthcoming chapters.

In the following figure, all the known coordination modes of this ligand are depicted and it is obvious that *n*-bdeaH₂ is a very useful means to build high-nuclearity clusters as a result of the manifold bridging modes available (Figure 18).

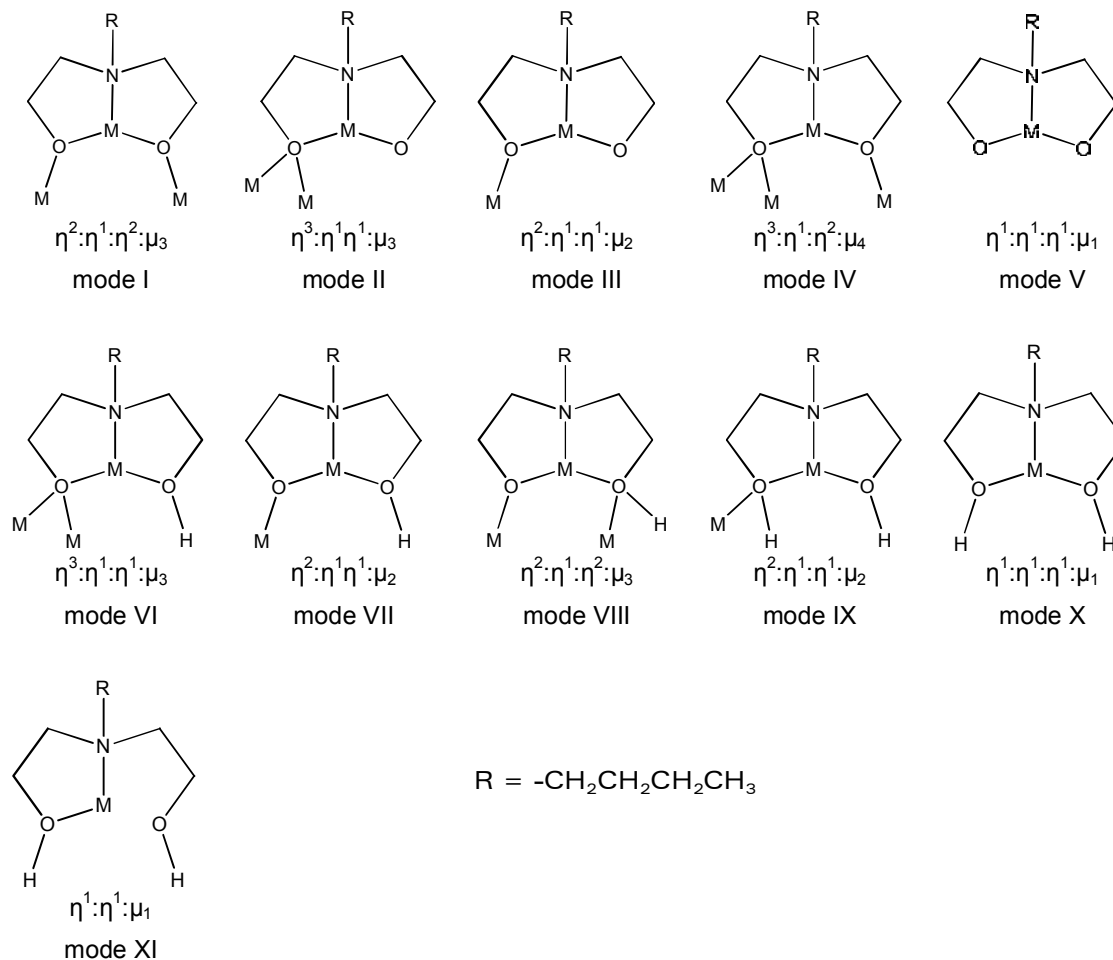


Figure 18: Some reported coordination modes of ligand *n*-bdeaH₂ (mode I (Foguet-Albiol, 2005: 4282ff), mode II (Biswas, 2007: 1059ff), mode III (Le Bris, 2007: 80ff), mode IV (Saalfrank, 2005: 1149ff), mode V (Lermontova, 2006: 5710), mode VI (Foguet-Albiol, 2005: 897ff), mode VII (Mishra, 2007: 602), mode VIII (Mishra, 2007: 602), mode IX (Zhang, 2005: 1185ff), mode X (Le Bris, 2007: 80ff))

2-Hydroxymethylpyridine (hmpH) was the second ligand used in this thesis. hmpH can be regarded as a derivative of *n*bdaH₂, but with only one alcohol arm and also a more rigid system as a result of the presence of the pyridine ring. In this case, the flexibility of *n*-bdeaH₂ is restricted and the number of reported heterometallic structures with hmpH as ligand is limited (Taguchi, 2010: 199ff; Stamatatos, 2008: 5006ff). In particular in the field of heterometallic 3*d*-4*f* metal complexes, the number of publications with hmpH as ligand is small and the subsequent work reported here shows, that the potential of this ligand seems not to have been fully exploited.

As a consequence of the more restricted flexibility of hmpH, the number of coordination modes known so far is much lower than in the case of diethanolamine derivatives (Figure 19).

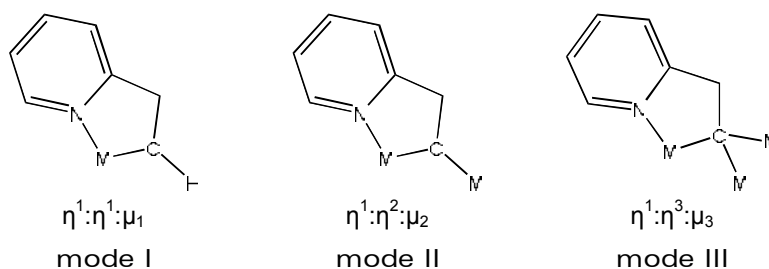


Figure 19: Coordination modes of ligand hmpH (Efthymiou, 2009: 3373ff; Stamatatos, 2009: 3308ff)

Moreover, the use of a derivative of hmpH with a longer alcohol arm, 2-Hydroxyethylpyridine, was explored but it was not possible to obtain any new and not already published results with this. However, with this ligand, the possibility of synthesising many unknown complexes containing 3d-4f metals seems to be reasonable and could be fruitful for further study since, the more flexible arm should lead to more variety in the form and properties of the resulting metal complexes.

1.11 Co-ligand selection

After the discovery of the SMM phenomenon, various synthetic techniques were applied in order to synthesise compounds that would exhibit this behaviour. One of these techniques demands careful selection of a metal / ligand / co-ligand system, in which the co-ligand is a useful tool to construct high-nuclearity complexes. Carboxylate moieties are one of the most studied multibridging groups in inorganic chemistry. They can undergo self-assembly complexation reactions with metal ions to produce polynuclear metal compounds in which they can assume various coordination modes and can bridge many metal centres. Therefore pivalates of different transition metals have been used to provide this carboxylic acid as co-ligand to obtain novel 3d-4f metal aggregates. Polynuclear metal carboxylates are good candidates for the investigation of magnetic exchange coupling interactions between neighbouring metal ions.

Common coordination modes for carboxylate groups are illustrated below (Figure 20).

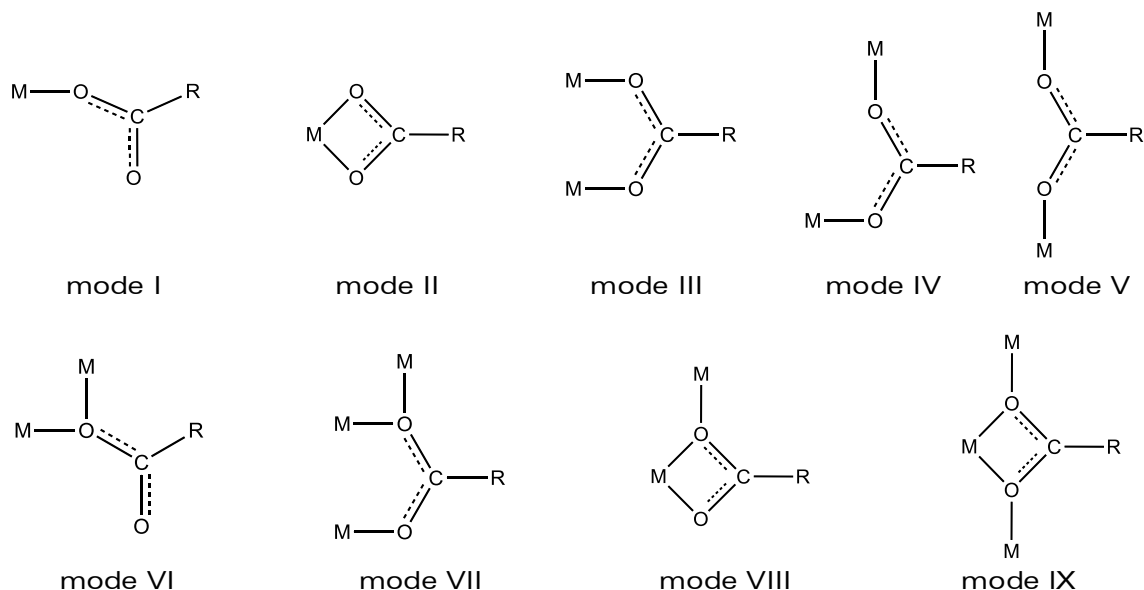


Figure 20: Common coordination modes of the carboxylate group.

1.12 Precursors as starting materials

In the following section the used polynuclear precursor compounds should be introduced. As described, there are different ways to obtain polynuclear compounds. One synthetic route to such compounds is alcoholysis of a preformed small nuclearity cluster, such as those described below. This type of reaction has several precedents in the literature (Mereacre, 2007: 9248f; Parsons, 1996: 1825ff; Ammala, 2000: 1688ff) and it has often led to the aggregation of small units into larger clusters.

1.12.1 $[\text{Mn}^{\text{II}}_4\text{Mn}^{\text{III}}_2\text{O}_2(\text{O}_2\text{CCMe}_3)_{10}(\text{py})_{2.5}] \cdot (\text{HO}_2\text{CCMe}_3)_{1.5}$ (1)

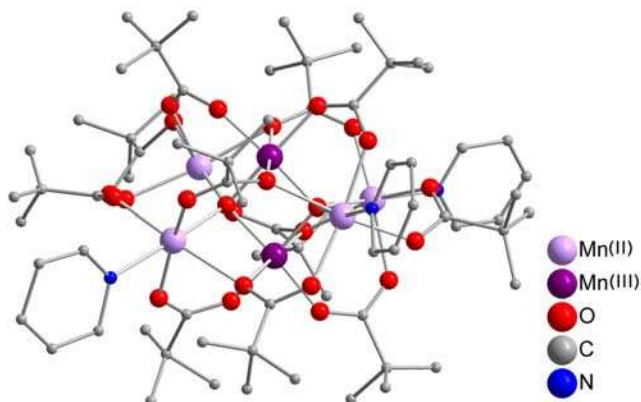


Figure 21: Molecular structure of $[\text{Mn}_6\text{O}_2(\text{piv})_{10}(\text{py})_{2.5}]$

Among the various Mn^{III} sources which have been explored in the past are $\{\text{Mn}_3\text{O}\}^{6+/7+}$ and $\{\text{Mn}^{\text{III}}_4\text{O}_2\}^{8+}$.

They have proved useful in developing routes to a variety of higher nuclearity complexes (Mishra, 2005: 54ff; Mishra, 2008: 1940ff). However, there are only very few examples where $[\text{Mn}_6\text{O}_2(\text{piv})_{10}(\text{py})_{2.5}]$ (Figure 21) was used as a source for manganese (Mereacre, 2010: 4918ff; Mereacre, 2008: 3577ff; Mereacre, 2010: 5293ff) and it thus seemed to be worthwhile to explore the use of this as a promising precursor for accessing new and interesting metal complexes.

The cluster consists of a $\{\text{Mn}^{\text{II}}_4\text{Mn}^{\text{III}}_2\text{O}_2\}^{10+}$ core and peripheral ligation is provided by ten pivalates and two pyridines. The metal ions form two tetranuclear units, which share a common edge, corresponding to the pair of Mn^{III} ions situated between the two sets of Mn^{II} ions.

1.12.2 $[\text{Mn}^{\text{III}}_8\text{Mn}^{\text{IV}}_4\text{O}_{12}(\text{CH}_3\text{COO})_{12}(\text{CHCl}_2\text{COO})_4]\cdot 4\text{H}_2\text{O}$ (3)

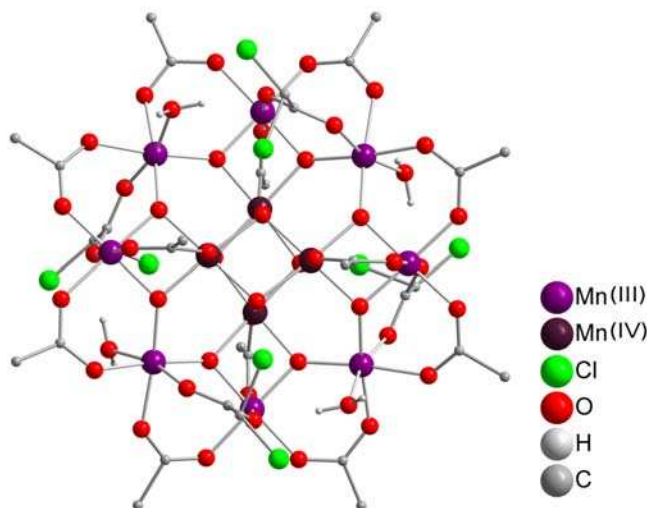


Figure 22: Molecular structure of Mn_{12} -DCA

The use of Mn_{12} as starting material has not been reported in the literature. Up to now, only the attachment of Mn_{12} aggregates on to gold surfaces has been studied (Otero, 2009: 10107ff; Gómez-Segura, 2007: 3699ff; Gatteschi, 2008: 1701ff). In addition, several papers report on changing the ligation of this well-known complex. Since the solubility of Mn_{12}DCA is higher in organic solvents like acetone or methanol, this makes Mn_{12}DCA accessible for other reactants. Moreover, it was shown, that Mn_{12} with 16 DCA ligands exhibits SMM-behaviour (Soler, 2003: 1777ff) and recent studies on **3** also show SMM behaviour for this compound. Further investigations are currently done to fully examine the properties of this compound.

Given that these properties remain in new compositions starting from this compound, the idea to build up larger aggregates was explored. From previous work, it seemed useful to explore incorporating lanthanide ions into the fragments of the $\{\text{Mn}_{12}\}$ precursor to improve the SMM-behaviour by increasing the anisotropy and the nuclearity of the system.

Here, the presence of four dichloroacetates gave also a means of finding out more about the synthetic pathways and how the final product is formed during the reaction by using the dichloroacetates as markers in the resulting product showing the origin of the fragments used in forming the final product.

The structure is composed of a discrete dodecanuclear $[\text{Mn}_{12}\text{O}_{12}(\text{CH}_3\text{COO})_{12}(\text{CHCl}_2\text{COO})_4]$ molecule and waters of hydration. The overall structure of the Mn_{12} complex consists of a $\text{Mn}^{\text{IV}}_4\text{O}_4$ core surrounded by a $\text{Mn}^{\text{III}}_8\text{O}_8$ ring (Figure 22).

The ligation is provided by eight acetates sitting in equatorial positions and connecting the Mn^{III} ions of the outer ring. Above and below the disk-like molecule there are eight other axial carboxylate groups (Figure 23). These remaining eight acetates are separated into two groups, each comprising two acetates and two dichloroacetates. Each group of four carboxylates shields the disc-like metal core in the axial direction. It is noteworthy that here the ligation alternates between acetate and dichloroacetate and also that the dichloroacetate ligands are always above and below the plane of the core (Figure 23).

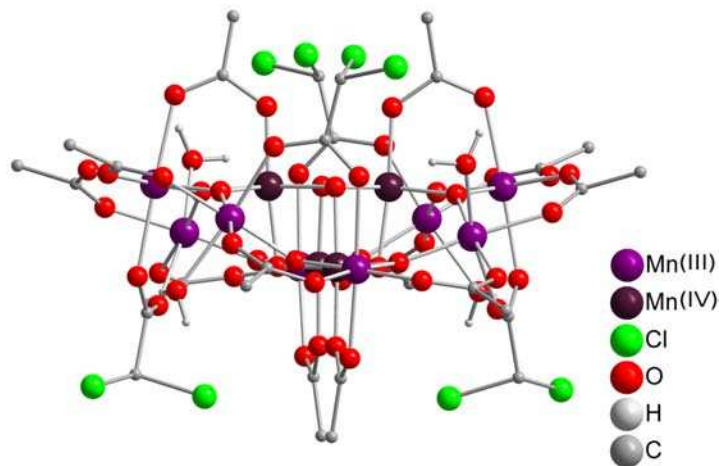


Figure 23: Side view of the Mn_{12} -DCA cluster with the axial carboxylate groups in sight.

This appears to be a general trend. The thermodynamically most stable Mn_{12} compounds are those where the unsubstituted carboxylates are in equatorial positions around the core, forming the strongest bonds (short Mn–O distances) while the weaker substituted carboxylates occupy the axial positions. This is where the weakest bonds are formed as a result of the Jahn–Teller distortions imposed by the Mn^{III} ions. This consistent location of the dichloroacetate ligands in the axial positions also makes this derivative especially suitable for the controlled adsorption on substrates such as gold or silicon giving a preferential orientation of the molecules (Fleury, 2009: 2192ff).

1.12.3 $[\text{Co}^{\text{II}}_2(\mu\text{-OH}_2)(\text{O}_2\text{CCMe}_3)_4(\text{HO}_2\text{CCMe}_3)_4]$ (4)

The reaction of cobalt carbonate with pivalic acid, followed by crystallisation from MeCN led to a violet crystalline product of **4** (Figure 24). The two cobalt(II) sites are bridged by two carboxylates in a *syn,syn*-mode and by μ -bridging water molecule. In **4** the coordination spheres of each six-coordinate Co site is completed by two protonated pivalate ligands and by one deprotonated pivalate. The deprotonated pivalates form strong hydrogen bonds of 2.55 Å to the $\mu\text{-OH}_2$. This raises a question of whether the more accurate description is as a $\mu\text{-OH}_2$ and two deprotonated pivalates or as a $\mu\text{-O}$ and two HO_2CCMe_3 ligands. Valence-bond sum analysis supports the presence of Co^{II} . The Co-O bonds then lie between those expected for $\text{Co}^{\text{II}}\text{-(OH)}$ (average 1.91 Å) and $\text{Co}^{\text{II}}\text{-(H}_2\text{O)}$ (average 2.14 Å) (Brown, 1985: 244ff; Allen, 1993: 31ff) this is consistent with the strong hydrogen bonding found.

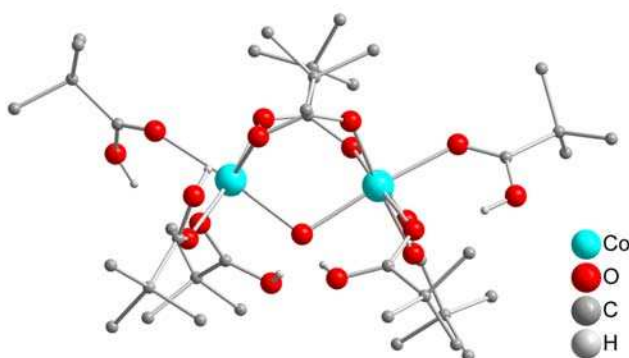


Figure 24: Molecular structure of Co_2 -pivalate

Synthetically this precursor was used to various Co compounds like Co_7 pivalate (Aromí, 2003: 5142ff) or the Co_{36} Cluster made by Alborés and Rentschler (Alborés, 2009: 9366ff).

1.12.4 $[\text{Co}^{\text{III}}_3(\mu_3\text{-O})(\text{O}_2\text{CCMe}_3)_6(\text{py})_3] \cdot \text{O}_2\text{CCMe}_3 \cdot \text{H}_2\text{O} \cdot 3.5\text{HO}_2\text{CCMe}_3$ (5)

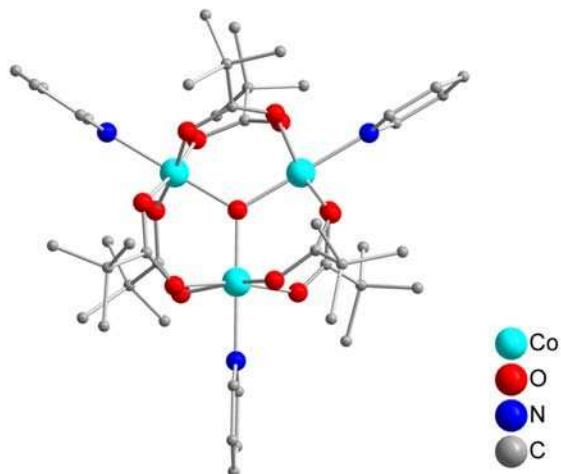


Figure 25: Molecular structure of Co_3 -pivalate

Compound 5 is a typical oxo-centred carboxylate triangle of side 3.21 Å, featuring exclusively Co^{III} sites around a central μ₃-oxide (Figure 25) possessing three diamagnetic Co^{III} ions. Each edge of the triangle is further bridged by two *syn,syn*-bridging pivalates, with a terminal pyridine ligand completing the coordination environment around each octahedral cobalt site. A similar oxo-centred cobalt(III) triangle has been reported for acetate (Beattie, 1996: 2141ff).

Within this thesis this precursor was used for several reactions to see the influence of the slight change from {Co₂} to {Co₃}. Unfortunately with this precursor it was not possible to crystallise any product, except a Co^{III}₃Dy^{III}₃(μ₃-OH)₄(bdea)₃(piv)₆(OH₂)₃(NO₃)₂, which was already made by Klöwer et al. (Klöwer, 2009: 57ff). However, this starting material seems to be a promising candidate for the synthesis of further complexes due to two facts: There are no examples in literature, where {Co₃} was used as starting material and secondly the use of diamagnetic Co^{III} is interesting in cases, where a non-paramagnetic ion is needed to avoid magnetic contribution to a system.

1.12.5 [Fe^{III}₃O(O₂CCMe₃)₆(H₂O)₃]·O₂CCMe₃·2HO₂CCMe₃ (6)

The reaction of Fe(NO₃)₃·9H₂O with 2,2-dimethylpropanoic acid gives after recrystallisation precursor **6**. The iron atoms form a triangle of side 3.31 Å, with an almost coplanar central oxygen atom sitting in the middle and on the three-fold axis, displaced negligibly (0.009 Å) out of the plane formed by the three iron ions. Peripheral ligation is provided by six μ-pivalates, where each side of the triangle is formed by two pivalates. One water molecule is coordinated to each iron.

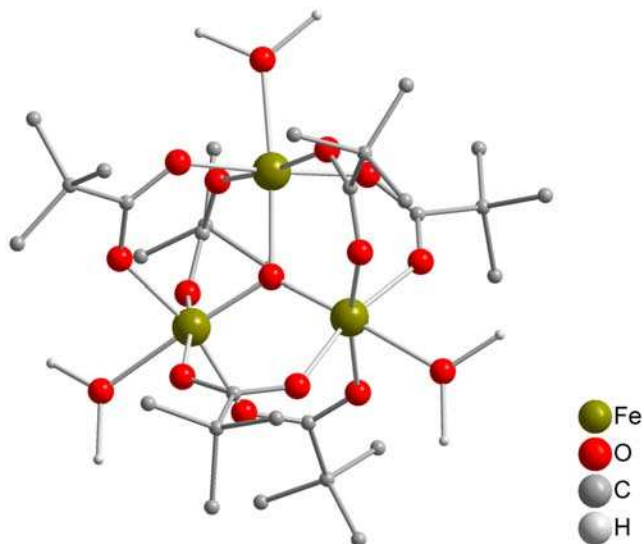


Figure 26: Molecular structure of precursor compound **6**

The trinuclear carboxylate complexes of the type {M₃O(O₂CR)₆L₃} (where M is a di- or tri-positive transition metal ion and L is a terminal ligand) were among the first polynuclear complexes studied with respect to their magnetic properties (Kambe, 1950: 48ff). Such complexes contain a triangular arrangement of metal

ions bridged by a central oxo-group and the carboxylate groups each span two metal atoms about the periphery of the $[M_3(\mu_3-O)]^{n+}$ core.

A great number of these complexes has been synthesised to date (Bond, 1998: 1845ff; Wu, 1998: 1913ff; Taguchi, 2010: 9131ff; Kiskin, 2004: 734ff).

The structure of the Fe_3O -triangle (Figure 26) was first published by Blake and Fraser in 1975 (Blake, 1975: 193ff). The derivate used in this thesis with water as coordinating solvent, was prepared by a slight modification of the literature method (Batsanov, 1988: 266ff).

Previously the precursor $[Fe_3O(piv)_6(H_2O)_3]$ used here was shown to result in polynuclear compounds (Mereacre, 2009: 3551ff) or respectively the $3d-4f$ network $[Fe_3(\mu_3-O)(\mu-O_2C^tBu)_6(im)_3]_2[La_2(\mu-O_2C^tBu)_4(\eta-O_2C^tBu)_4] \cdot 2C_2H_5OH$ (im=imidazole) (Isilak, 2009: 1102ff).

1.12.6 $[(Fe^{III}_3O)_2(O)_2(O_2CCMe_3)_{12}(HO_2CCMe_3)_2]$ (7)

The use of the Fe_3O -precursor **6** described above, has already led to numerous new compounds in work from other groups. In contrast, **7** has so far exclusively been a target molecule (Micklitz, 1989: 372ff, Çelenligil-Çetin, 2000: 5838ff) and never used as starting material. Compound **7** was simply made by adding hydrogen peroxide to compound **6**. The distinctive feature in this structure is a central η^2, μ_4 -peroxo unit which, in conjunction with two pivalate moieties, bridge two $[Fe_3O(O_2CCMe_3)_5(HO_2CCMe_3)]^{2+}$ units.

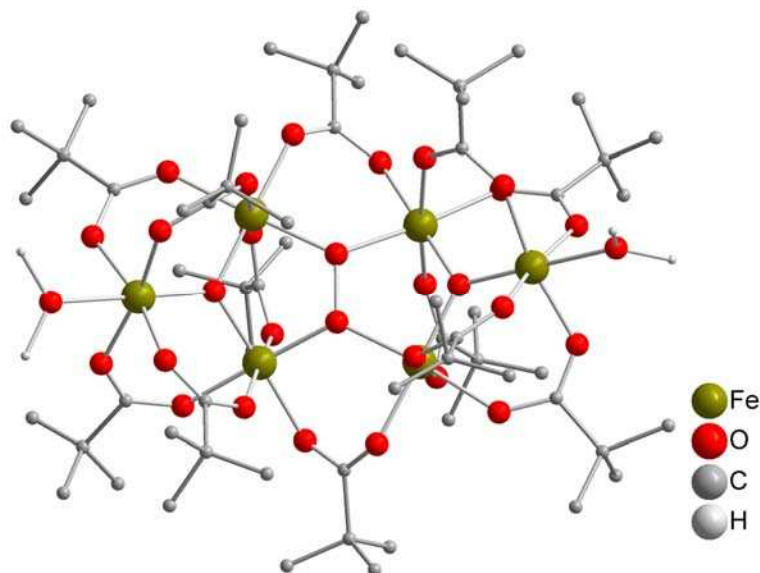


Figure 27: Molecular structure of Fe_6 -pivalate

1.12.7 $[Dy_2(O_2CCMe_3)_6(HO_2CCMe_3)_6] \cdot HO_2CCMe_3$ (8)

In all of the reactions presented here, a precursor complex of a transition metal and a lanthanide salt (usually nitrate or chloride) were used as the source of the metal cations. In order to understand the influence of the starting material on the final product, the metal-containing starting materials could easily be altered. For

example, it would be possible to investigate whether changing the counterions would give the same product. Also, if the product obtained is independent of the metal complexes or salts used, then this would support the fact that the precursor compounds decompose in the reaction solution to single cations, which then reassemble to give the final product. In other words, the final product should be the same, even if the 3d metal is added as a salt and the lanthanide comes from a pivalate complex. This was found not to be the case, for example, when the reaction which resulted in the $\text{Mn}_4\text{Dy}_6\text{Li}_2$ complex (Compound **27**) was carried out under the same conditions, but with the metal sources changed from $[\text{Mn}_6\text{O}_2(\text{piv})_{10}(\text{py})_{2.5}]$ and $\text{Dy}(\text{NO}_3)_3 \cdot 6\text{H}_2\text{O}$ to $\text{Mn}(\text{NO}_3)_3 \cdot 4\text{H}_2\text{O}$ and $\text{Dy}_2(\text{piv})_{12}$ (Compound **8**). In this case instead of the $\text{Mn}_4\text{Dy}_6\text{Li}_2$ complex (Compound **27**) described in this thesis, yellow-orange crystals appeared after several hours, which did not contain lanthanide ions (qualitative test with oxalic acid was negative) and which were too small to be studied by X-ray diffraction.

Although it was thus not possible to find out the structure of this alternative product, FT-IR and elemental analysis showed, that a completely different product was obtained, which shows that the formation of the products in solution is more complicated than imagined.

The basic structural element of this compound is a centrosymmetrical dimer formed by two $\text{Dy}(\text{O}_2\text{CCH}_3)_3$ fragments and six non-protonated pivalates. The two Dy^{III} ions, which lie at a long, nonbonding distance are eight-coordinate and are linked through bridging pivalato groups. In addition, each metal atom coordinates four oxygen atoms from the mono-dentate pivalato anion and three terminal oxygen atoms from pivalic acid (Fomina, 2004: 1349ff).

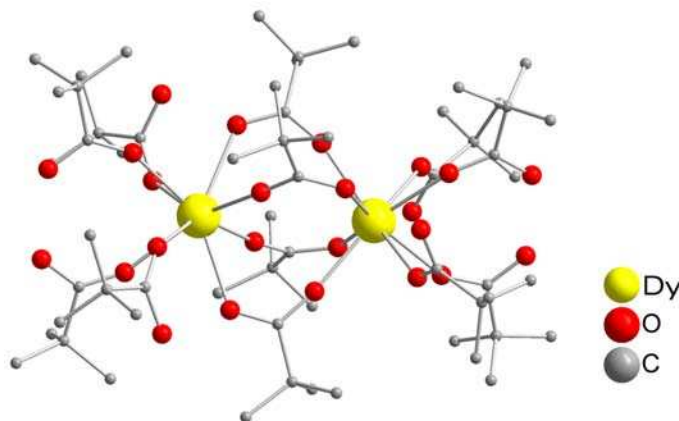


Figure 28: Molecular structure of Dy_2 -pivalate. H atoms and pivalates situated in the crystal lattice are omitted for clarity.

1.13 Crystallisation methods

In order to substantiate the structure of a compound, single crystal X-ray diffraction is the most useful method of choice. This makes it necessary to have a crystalline compound, which is furthermore able to diffract X-rays sufficiently to allow for a single crystal structure analysis.

There are various methods to achieve the first requirement, which are discussed in detail below.

The crystallisation methods for air-sensitive and non-air-sensitive compounds differ in some details. Since within the scope of this dissertation experiments were carried out exclusively under aerobic conditions, only the crystallisation methods of non-air-sensitive compounds are discussed.

When the solubility of a compound in a solvent is exceeded, its solution becomes supersaturated and the compound may precipitate or crystallize. The rate of precipitation, the resulting particle size (whether colloidal or coarse), and the particle size distribution depend upon two successive and largely independent processes. These are nucleation and crystallisation (i.e., growth of nuclei). When a solution of a salt is super cooled or when a chemical reaction produces a salt in a concentration exceeding its solubility product, the separation of excess solid from the supersaturated solution is far from instantaneous. Clusters of ions or molecules called nuclei must exceed a critical size before they become stable and capable of growing into colloidal size crystals. These embryonic particles have much more surface for a given weight of material than larger and more stable crystals. Therefore, they have a higher surface free energy and greater solubility.

The occurrence of nucleation depends upon the relative supersaturation. If C is the actual concentration of the solute before crystallisation and C_s is its solubility limit, then $C - C_s$ is the supersaturation and $(C - C_s)/C_s$ is the relative supersaturation. Von Weimarn recognised that the rate or velocity of nucleation (number of nuclei formed per liter per second) is proportional to the relative supersaturation. This statement refers to homogeneous nucleation, where the nuclei have the same chemical composition as the crystallising phase. If the solution contains solid impurities, such as dust particles in suspension, these may act as nuclei or centers of crystallization (heterogeneous nucleation).

Once nuclei have formed, crystallisation begins. Nuclei grow by the aggregation of ions or molecules from solution. Crystallisation continues until the supersaturation is relieved (i.e. until $C = C_s$) and may result in the formation of either colloidal or coarse particles. The rate of crystallisation or growth of nuclei is proportional to the supersaturation:

$$\frac{dm}{dt} = \frac{A_{sp}D}{\delta}(C-C_s)$$

This equation is similar to the Noyes-Whitney equation that governs particle dissolution except that $C < C_s$ for the latter process, making dm/dt negative. In both equations, m is the mass of material crystallising out in time t , D is the diffusion coefficient of the solute molecules or ions δ is the length of the diffusion path or the thickness of the liquid layer adhering to the growing particles, and A_{sp} is their specific surface area. The presence of dissolved impurities may affect the rate of crystallisation and even change the crystal habit, provided that these impurities are surface-active and become adsorbed onto the nuclei or growing crystals.

Von Weimarn found that the particle size of the crystals depends strongly upon the concentration of the precipitating substance. At very low concentrations and slight relative supersaturation, diffusion is quite slow because the concentration gradient that drives the process is very small. Sufficient nuclei will usually form to relieve the slight supersaturation. However, crystal growth is limited by the small amount of excess dissolved material available to each particle and, therefore, the particles cannot grow beyond colloidal dimensions.

At intermediate concentrations, the extent of nucleation is somewhat greater and much more material is available for crystal growth. Therefore, coarse crystals form rather than colloidal particles. At high concentrations, nuclei appear so quickly and in such large numbers that supersaturation is relieved before any appreciable diffusion can occur.

Low solubility is a necessary condition for producing colloidal dispersions. Another phenomenon is that aging increases particle size. The gradual increase in the particle size of crystals in their mother liquor is a recrystallisation process called Ostwald ripening. Very small particles have a higher solubility than large particles of the same substance due to their greater specific surface area and higher surface free energy. In a saturated solution containing precipitated particles with a wide range of particle sizes, the very smallest particles dissolve spontaneously and deposit onto the larger particles. The growth of the larger crystals at the expense of the very small ones occurs because this process lowers the free energy of the dispersion. Adding small amounts of surface-active compounds that adsorb at the particle surface slows down the process.

Increasing the solubility of the precipitate accelerates the spontaneous coarsening of colloidal dispersions upon aging. The colloidal particles gradually grow in size by Ostwald ripening, forming large crystals that can be removed quantitatively by filtration. The supersaturation never again reaches sufficiently high values for forming new nuclei because it is relieved by the continuous growth of the existing nuclei (Hulliger, 1994: 151ff; Shinoda, 1983).

There are three ways to exceed the lower limit of the solubility:

- concentrating the solution
- changing of the temperature
- changing the composition of the solvent

For successful crystal growth two points are very important:

- the solution should be left without much air/mechanical disturbance and
- the parameters mentioned above should change as slow as possible.

1.13.1 Evaporation

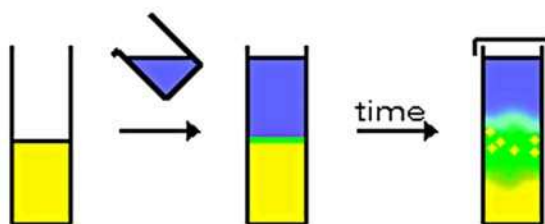
The method of slow evaporation fulfils all of these conditions very well and was used in most of cases in the work described here. For his method, a vial containing the crystallisation solution is closed with a cap, into which a varying number of holes are punched with a needle, depending on the solvent used. While with solvents like acetone with a low boiling point and a high vapour pressure only a few holes are necessary, the evaporation of water or toluene can be slow enough for any closure to be unnecessary. The interested reader is referred to literature such as (Dunskii, 1978: 131ff) or (Pillai, 2009: 1643ff).

1.13.2 Vapour and Liquid Diffusion

Liquid and vapour diffusion methods are often used when evaporation methods do not succeed. For both methods it is necessary to find two solvents or solvent mixtures in which the compound is soluble in one system but insoluble in the other.

For liquid diffusion (Scheme 2) the two solvent systems should be immiscible or nearly immiscible, while for vapour diffusion (Scheme 3) the solvent systems should be miscible. Crystal growth may be slowed and thus enhanced by cooling the sample slightly.

Liquid diffusion normally requires that the less dense solvent system is carefully layered on top of the more dense solvent system. The sample can be dissolved in either one of the two solvents. Hence, crystals will grow at the interface between the two layers. If spontaneous precipitation forms, the two layers should be separated by a third solvent layer, which is not miscible with either of the layers or with the compound, to slow down the reaction and thus grow larger crystals.

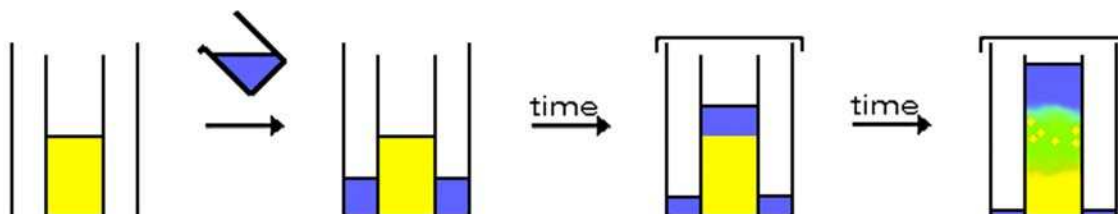


Scheme 2: Schematic of the liquid diffusion method

With the vapour diffusion method, also called vial-in-vial diffusion, the dissolved sample is put in vial A (yellow), which is in turn placed in a slightly bigger vial B (Scheme 3), which contains a small quantity of a solvent system in which the sample is not soluble (blue). The outer vial is closed and vapour from the solvent in vial B will then diffuse into the solution of vial A, causing a solvent system, which becomes more and more disadvantageous for the compound to remain in solution, leading to crystallisation in favourable conditions.

The diffusion of the solvent (e.g. diethylether) is explainable with the vapour pressure, bringing the solvent in the gas phase and the partial pressure of the gaseous phase, which is causing the azeous phase diffusing into the other solvent. The ratio between the concentration of the gas in the solution c_{sol} and its partial pressure p_{gas} is a constant, the so-called Henry constant k_{H} . The Henry constant is temperature dependent and defined as:

$$k_{\text{H}} = \frac{c_{\text{sol}}}{p_{\text{gas}}}$$



Scheme 3: Schematic of the vapour diffusion method

1.13.3 Thermal Gradient

The third and last method, which should be discussed here, is the thermal gradient method, which often produces usually crystals of very high quality. In this method, the saturated solution is placed in a sealed vial and is cooled down slowly. As the solubility of the substance decreases with the decreasing temperature of the solvent the product may crystallise.

Within this work, all three methods were applied.

2 Structure and magnetic properties of manganese-lanthanide aggregates

2.1 Structure of tetranuclear complexes

The reaction of the preformed precursor compound $\{\text{Mn}_6\}$ (**1**), $\text{La}(\text{NO}_3)_3$ and hmpH in acetone led to a brown solution from which well-formed dark brown crystals of compound **9** could be isolated after four days. The structure will be discussed in the following section.

2.1.1 Structure of $[\text{Mn}^{\text{III}}_2\text{La}^{\text{III}}_2(\text{hmp})_6(\text{piv})_2(\text{NO}_3)_4]$ (**9**)

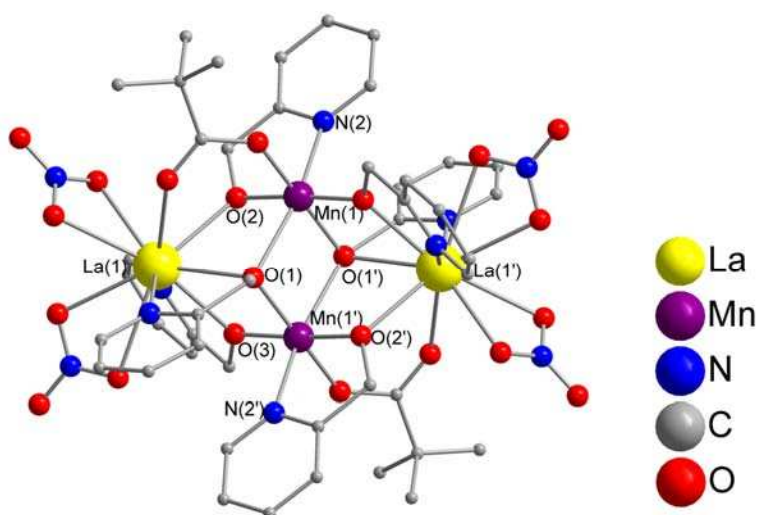


Figure 29: Molecular structure of $[\text{Mn}^{\text{III}}_2\text{La}^{\text{III}}_2(\text{hmp})_6(\text{piv})_2(\text{NO}_3)_4]$

X-ray crystallographic studies reveal that complex **9** crystallises in the monoclinic space group $P2_1/c$ with $Z=2$ possessing a $\{\text{Mn}^{\text{III}}_2\text{La}^{\text{III}}_2\}$ butterfly core with centrosymmetric site symmetry. The crystal structure and its polyhedral representation (along the a -axis) are shown in the figure above (Figure 30).

The butterfly core comprises two outer "wingtip" nona-coordinate La^{III} ions and two inner hexa-coordinate Mn^{III} ions, representing the body. All four metals are strictly coplanar. The oxidation states of $\text{Mn}(1)$ and $\text{La}(1)$ were determined by consideration of the coordination geometry (bond lengths, coordination numbers and the presence of Jahn-Teller elongation axes for $\text{Mn}(1)$) and by bond valence sum calculations (Liu, 1993: 4102ff).

The Mn centres $\text{Mn}(1)$ and the inversion-related $\text{Mn}(1')$ are each chelated by one, while the lanthanum ions are each chelated by two deprotonated hmpH ligands. The two independent pivalate ligands exhibit a *syn-syn* bidentate coordination mode, connecting $\text{Mn}(1)$ with $\text{La}(1)$ and $\text{Mn}(1')$ with $\text{La}(1')$, respectively. Two chelating nitrates complete the coordination sphere of the rare earth metal ions.

The four metal ions are held together by six alkoxo oxygens. Two of them ($\text{O}(1)$ and $\text{O}(1')$) are μ_3 -bridging and come from one La^{III} -chelating hmp⁻-ligand, respectively.

Both are displaced 1.057(5) Å above and below the plane formed by the metal ions, respectively. The remaining four alkoxide oxygens ((O2), (O3) and their inversion-relations) are all μ_2 -bridging. Two come from the Mn^{III}-chelating, and two from the La^{III}-chelating hmp⁻ligands, respectively, resulting in the described {Mn^{III}₂La^{III}₂O₆}⁶⁺ unit.

Overall, Mn(1) shows the expected Jahn-Teller elongated octahedral geometry, with the Jahn-Teller axis defined by O(1) and N(2), while the coordination geometry of the deca-coordinate Ln^{III} ions approximates to a bicapped square antiprism. This stands in contrast to the Mn^{III}₂La^{III}₂ butterfly compound found by Akhtar et al. using n-bdeaH₂ as ligand (Akhtar, 2009: 1698ff), where the lanthanum forms a tricapped trigonal prism environment.

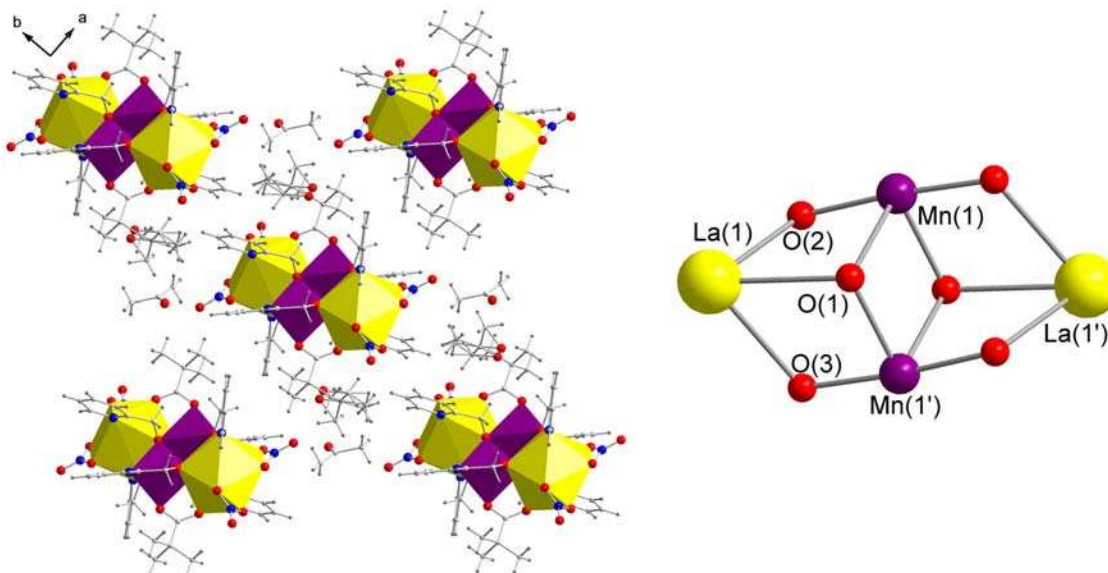


Figure 30: Polyhedral representation along the c-axis of compound **9** with La polyhedra being violet and the Mn octahedra pink (left) and the metal core of **9**.

Related butterfly complexes [Mn₂Ln₂O₂(piv)₈(pivH)₂(MeOH)₂] (Ln = Dy and Gd) have been published by Winpenny (Benelli, 1999: 4125ff), while Brechin and co-workers have also reported a {Mn^{III}₂Dy^{III}₂} complex (Mishra, 2005: 2086ff). Another butterfly complex [Mn₂Ln₂O₂(O₂CPh)₆(OMe)₄(MeOH)₄] (Ln = Y and Yb) was reported in 2006 as well (Murugesu, 2006: 613).

Nevertheless complex **9** is the first example of this type of Mn₂Ln₂ complex with a lighter rare earth metal in combination with hmpH as ligand.

The investigation of the magnetic behaviour of compound **9** was not measured due to limited time on the SQUID magnetometer and other compounds having higher priority. However, the Jahn-Teller axes are oriented parallel and magnetic measurements are planned to find out if compound **9** exhibits SMM behaviour.

In order to find out the oxidation states of the transition metals one method which was used was bond valence sum calculation. The summary of the calculation is shown at the end of any structure description.

The interested reader is referred to literature on the subject such as (Brown, 1985: 244ff) to find further explanation about the exact calculations done to obtain the oxidation state of the coordinated metal ion.

Bond Valence Sum Calculations (Brown, 1985: 244ff):

respective atom	Mn(1)
estimated oxidation state	
Mn ^{II}	3.03
Mn ^{III}	2.79
Mn ^{IV}	2.90
calculated oxidation state	Mn ^{III}

2.2 Structure and magnetic properties of hexanuclear complexes

Performing the same reaction, which led to compound **9**, described above, but replacing **1** {Mn₆} by **3** {Mn₁₂} as the preformed precursor compound used as starting source for manganese, resulted in a hexanuclear compound of formula [Mn^{III}₄La^{III}₂(μ₄-O)(μ₃-O)(hmp)₇(OAc)₂(NO₃)₅]-acetone (Figure 31). In the following section the structure will be described and the magnetic measurements show that **10** displays frequency dependent out-of-phase signals indicative of slow relaxation of magnetisation and thus single molecule magnet behaviour.

2.2.1 Structure of Mn^{III}₄La^{III}₂(μ₄-O)(μ₃-O)(hmp)₇(O₂CMe)(O₂CCHCl₂)(NO₃)₅(OH₂)_{0.5}·3acetone (**10**)

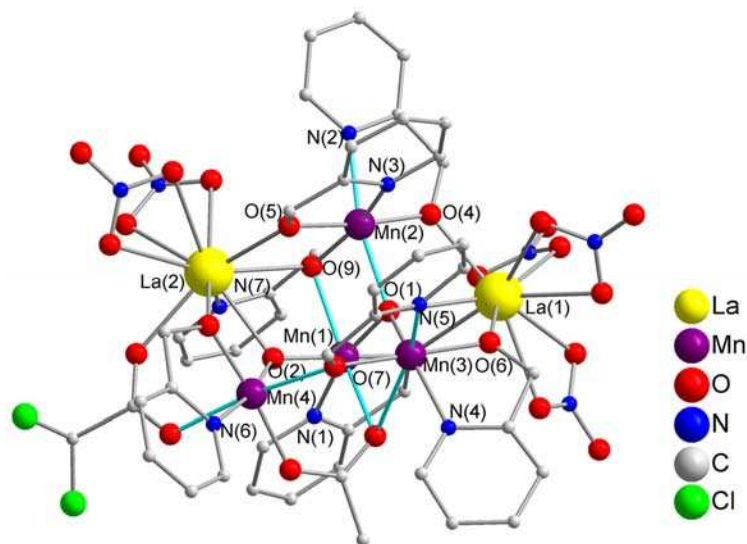


Figure 31: Molecular structure of [Mn^{III}₄La^{III}₂(μ₄-O)(μ₃-O)(hmp)₇(O₂CMe)(O₂CCHCl₂)(NO₃)₅(OH₂)_{0.5}]-3acetone with Jahn-Teller axes (turquoise). Organic hydrogen atoms and solvent molecules are omitted for clarity.

The metal oxidation states of Mn^{III} and La^{III} and the deprotonation levels of O²⁻, OAc⁻, DCAc⁻ and the hmp⁻ ions were established by charge considerations, bond

valence sum calculations (Liu, 1993: 4102ff), inspection of metric parameters (Table 2 and Table 3) and the observation of Jahn–Teller elongation axes of Mn^{III}.

Single-crystal X-ray diffraction studies of the black crystals show a rather unsymmetrical molecular structure of **10** (Figure 31), which crystallises in the monoclinic space group P2₁/c with Z=4 (Figure 32).

The molecular structure can be seen as a {Mn^{III}₄La^{III}₂}¹⁸⁺ core, which consists of the aforementioned {Mn^{III}₂La^{III}₂} butterfly core of compound **9** (vide supra), with an additional two Mn^{III} centres coordinated. Thus compound **10** represent an extended version of compound **9**. Here Mn(1) and Mn(2) form the body and La(1) and La(2) represent the wings of the butterfly core, held together by one μ₄-bridging oxygen and the oxygen atom of a deprotonated η¹:η³:μ₃-hydroxymethanol (hmp) ligand. Three further deprotonated hmp-ligands and a η¹:η²:μ₃-bridging acetate connects the two additional Mn^{III} ions to the core.

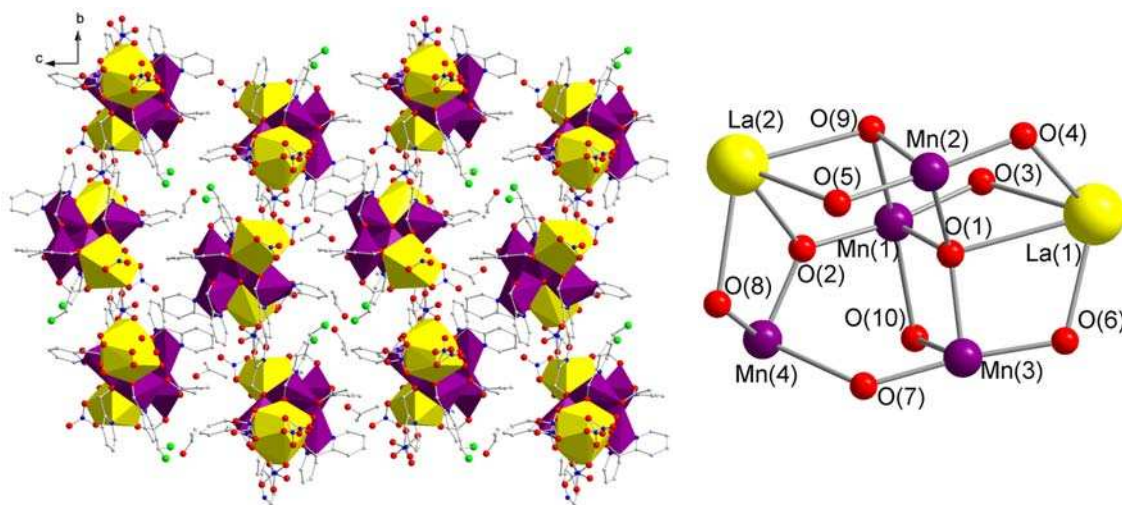


Figure 32: Crystal packing of **10** in the polyhedral representation, projected along the *a* axis. La polyhedra are yellow and the Mn octahedra are violet (left) and the metal core of **10**.

All of the Mn^{III} centers are six-coordinate with near-octahedral geometry and both La^{III} ions are ten-coordinate with coordination polyhedra that may best be described as bicapped square antiprismatic (Figure 33). However, this is just an approximation, as, in particular, the coordination sphere of La(1) is fairly distorted.

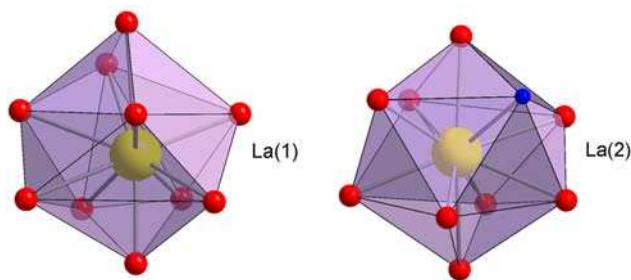


Figure 33: The bicapped square antiprismatic coordination polyhedra around La(1) and La(2).

Mn(1) and Mn(4) are chelated by one, while Mn(2) and Mn(3) are chelated by two deprotonated hmp⁻-ligands. Mn(1) is part of the aforementioned Mn₂La₂-butterfly body and is connected to Mn(3) via a η²-bridging alkoxy coming from a η¹:η²:μ₃-acetate, which connects the latter Mn(3) with Mn(4). The latter is additionally linked to La(2) by an μ-dichloroacetate ligand coming from the [Mn₁₂O₁₂(Ac)₁₂(DCAc)₄] derivate used in the synthesis.

La(1) is surrounded only by the alkoxy groups of Mn-chelating hmp⁻-ligands, while La(2) is chelated itself by a hmp⁻-ligand. The deca-coordinate environment is completed by three or, respectively, two nitrates.

The structure described here is not part of a isostructural series with a range of lanthanides but rather an unrelated composition. Performing the same reaction, in the attempt to introduce any other lanthanide, resulted in all cases with the formation of [Mn^{III}₂Mn^{II}₂(hmp)₆(NO₃)₄].2acetone (Figure 34). The reason may be the large ionic radius of La^{III}, which is the largest of all rare earth metals and which leads to the relatively high coordination number of ten in this compound. However, even using cerium, where the coordination number of ten is not unusual, exclusively the [Mn₄(hmp)₆(NO₃)₄] complex was obtained.

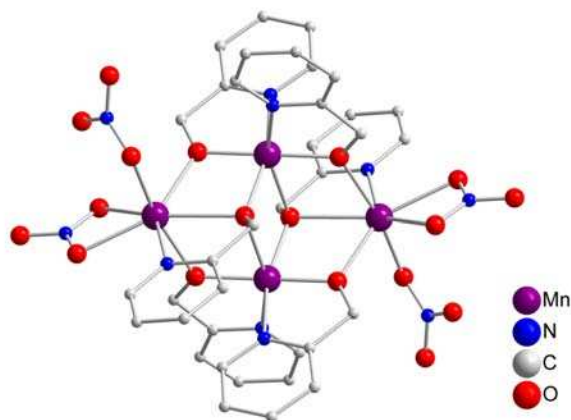


Figure 34: Structure of [Mn^{III}₂Mn^{II}₂(hmp)₆(NO₃)₄].2acetone. Organic hydrogen atoms and solvent molecules are omitted for clarity.

This example represents very well the influence of changing the precursor. Here, the replacement of [Mn₆O₂(piv)₁₀(py)_{2.5}] by [Mn₁₂O₁₂(Ac)₁₂(DCAc)₄] as Mn source results in a cluster which contains more manganese ions, although the stoichiometric amount of manganese was not changed.

Even though this particular derivative and the method using [Mn₁₂O₁₂(Ac)₁₂(DCAc)₄] as starting material have not been reported previously, the Mn₄-core has been studied sufficiently (Lecren, 2005: 11311ff; Wittick, 2006: 1534ff; Yang, 2003: 1857ff) and further investigation was not deemed necessary for this thesis.

Bond Valence Sum Calculations (Brown, 1985: 244ff):

resp. atom	Mn(1)	Mn(2)	Mn(3)	Mn(4)
est. ox. state				
Mn ^{II}	3.28	3.23	3.16	3.31
Mn ^{III}	3.03	3.00	2.95	3.06
Mn ^{IV}	3.13	3.07	3.01	3.16
calc. ox. state	Mn ^{III}	Mn ^{III}	Mn ^{III}	Mn ^{III}

La1-O6	2.395(13)	Mn2-O9	2.030(11)
La1-O4	2.442(12)	Mn2-N3	2.096(14)
La2-O3	2.207(16)	Mn2-O1	2.123(10)
La2-O4	2.583(13)	Mn2-N2	2.210(13)
La2-O6	2.617(13)	Mn3-O6	1.892(11)
La2-O5	2.456(8)	Mn3-O7	1.904(9)
La2-O2	2.469(9)	Mn3-O1	1.911(9)
La2-O8	2.580(9)	Mn3-N4	2.072(13)
La2-O9	2.602(11)	Mn3-N5	2.166(14)
La2-N7	2.708(15)	Mn4-O2	1.820(9)
Mn1-O2	1.820(10)	Mn4-O8	1.893(10)
Mn1-O3	1.908(12)	Mn4-N6	2.033(12)
Mn1-O1	1.923(11)	Mn4-O7	2.292(10)
Mn1-N1	2.051(19)	Mn2-O5	1.875(9)
Mn1-O9	2.262(10)	Mn2-O4	1.883(11)

Table 2: Selected bond lengths for 10.

O6-La1-O4	110.6(4)	O5-Mn2-O4	174.2(5)
O3-La2-O4	91.7(4)	O5-Mn2-O9	83.8(4)
O3-La2-O6	108.0(4)	O4-Mn2-O9	99.5(5)
O4-La2-O6	99.8(4)	O5-Mn2-N3	80.4(4)
O5-La2-O2	81.3(3)	O4-Mn2-N3	96.4(6)
O5-La2-O8	75.8(3)	O9-Mn2-N3	164.1(5)
O2-La2-O8	61.8(3)	O5-Mn2-O1	99.6(4)
O5-La2-O9	62.1(3)	O4-Mn2-O1	85.7(4)
O2-La2-O9	63.6(3)	O9-Mn2-O1	81.0(4)
O13-La2-O9	126.3(4)	N3-Mn2-O1	99.9(4)
O8-La2-O9	114.1(3)	O5-Mn2-N2	95.7(5)
O5-La2-N7	123.3(6)	O4-Mn2-N2	79.1(5)
O2-La2-N7	79.3(4)	O9-Mn2-N2	98.0(5)
O13-La2-N7	75.7(6)	N3-Mn2-N2	85.4(5)
O8-La2-N7	134.3(4)	O1-Mn2-N2	164.4(5)
O9-La2-N7	61.5(6)	Mn3-O1-Mn2	134.6(5)
O2-Mn1-O3	170.6(6)	Mn1-O1-Mn2	103.6(4)
O2-Mn1-O1	100.2(4)	Mn3-O1-La2	103.3(4)
O3-Mn1-O1	87.8(6)	Mn1-O1-La2	94.7(4)
O2-Mn1-N1	91.5(7)	Mn2-O1-La2	100.4(4)
O3-Mn1-N1	81.3(7)	Mn3-O1-La1	98.7(4)
O1-Mn1-N1	166.1(6)	Mn1-O1-La1	107.3(4)
O2-Mn1-O9	81.1(4)	Mn2-O1-La1	96.0(4)
O3-Mn1-O9	95.6(5)	La2-O1-La1	12.66(9)
O1-Mn1-O9	79.8(4)	Mn4-O2-Mn1	130.3(5)
N1-Mn1-O9	109.8(5)	Mn4-O2-La2	106.7(4)

O6-Mn3-O7	172.2(5)	Mn1-O2-La2	117.2(4)
O6-Mn3-O1	87.1(5)	O2-Mn4-O8	88.7(4)
O7-Mn3-O1	99.2(4)	O2-Mn4-N6	168.8(5)
O6-Mn3-N4	80.8(5)	O8-Mn4-N6	81.6(5)
O7-Mn3-N4	95.4(5)	O11-Mn4-N6	92.0(5)
O1-Mn3-N4	151.5(5)	O2-Mn4-O7	94.8(4)
O6-Mn3-N5	93.5(6)	O8-Mn4-O7	95.0(4)
O7-Mn3-N5	79.7(5)	N6-Mn4-O7	91.7(4)
O1-Mn3-N5	115.7(5)	Mn3-O1-Mn1	112.3(5)
N4-Mn3-N5	90.8(5)		

Table 3: Selected bond angles for **10**.

2.2.2 Magnetic properties of $[\text{Mn}^{\text{III}}_4\text{La}^{\text{III}}_2(\mu_4\text{-O})(\mu_3\text{-O})(\text{hmp})_7(\text{OAc})_2(\text{NO}_3)_5]$

There are few studies of the magnetic properties of highly asymmetric complexes such as the present case. The magnetic data of a powdered sample of compound **10** were collected in the temperature range 1.8-300 K. A plot of the χT product versus temperature, measured in a field of 1000 Oe, is shown in Figure 35. The experimental χT product at room temperature is slightly lower than the expected value (Benelli, 2002: 2369ff) as can be seen in the Table 4, staying nevertheless in good agreement with the presence of four $S = 2$ Mn^{III} ions. However, this deviance is due to the antiferromagnetic interactions within the molecule. The χT product decreases continuously from a value of $9.93 \text{ cm}^3 \text{ Kmol}^{-1}$ over the range of 300-20 K to reach an approximate plateau at about $3.5 \text{ cm}^3 \text{ Kmol}^{-1}$, representing the probable spin ground state of the molecule. This quasi-plateau is followed by a sharp drop at 5 K to reach $2.86 \text{ cm}^3 \text{ Kmol}^{-1}$ at 1.8 K. Decreases in χT of the latter type, at low temperatures, are often ascribed to zero-field splitting of the cluster ground state and/or weak intermolecular antiferromagnetic coupling. A more detailed conclusion requires a fitting of the χT curve.

The observed magnetisation isotherms (2-5 K) for **10** reveal rather unusual intersecting dependence of M on H , with the largest value of M at 1.8 K and 7 T being only $1.81 \mu_B$. Such a crossing point for the M versus H plots (here at around 40000 Oe) is indicating of level crossing. Therefore, the observed magnetisation for compound **10** is certainly influenced by excited states with higher magnetic moment than the ground state.

The field dependence of the magnetisation at low temperatures also does not show saturation even at 7 T, which indicates the presence of magnetic anisotropy and/or the lack of a well-defined ground state suggesting the presence of low-lying excited states that are likely populated when a field is applied. Furthermore, the plot of the M versus H/T at low temperatures for compounds **10** show that the curves are not superposed, as expected for an anisotropic system, giving a further indication of the presence of magnetic anisotropy and also the low lying excited states already suggested.

For compound **10** the ac susceptibility behaviour was also measured. In zero dc field, a frequency dependence of the ac susceptibility is observed (Figure 37). It is clear that there is slow relaxation of the magnetisation below 4 K (Figure 37). This feature alone (shape and frequency dependence) is not sufficient to categorise this compound a SMM but strongly suggests this as slow relaxation of magnetisation is a first indication for SMM behaviour. To substantiate this hypothesis, a dc field was applied to see if the relaxation would slow down. Indeed in SMMs with a relaxation partially influenced by quantum effects, the application of a small dc field removes the state degeneracy of the two potential diagram describing the magnetism of such a system and thus the possibility of quantum tunnelling inducing the slowing down of the relaxation of the magnetisation.

In the case of compound **10** it was not possible to analyse the relaxation behaviour in this way since the the relaxation mode could not be moved at high frequency (i.e. the slow relaxation could not be slowed down) under a small dc field. This observation shows that if this compound is a SMM, it does not have a relaxation influenced by quantum effects at 1.8 K and above. Lower temperature measurements should help to establish the nature of the behaviour in more detail.

Compound	χT expected for each Ln at RT (cm ³ Kmol ⁻¹)	Ground state of Ln ion	χT expected for each complex ^a (cm ³ Kmol ⁻¹)
Mn ₄ La ₂ (10)	0	¹ S ₀	12

Compound	χT measured at 300K per complex (cm ³ Kmol ⁻¹)	χT measured at 1.8 K per complex (cm ³ Kmol ⁻¹)	Magnetisation at 2 K and 7 T (μ_B)
Mn ₄ La ₂ (10)	9.93	2.86	1.81

Table 4: Magnetic data summarised from the dc measurements. ^a taking into account a g factor of Mn metal ions of 2.

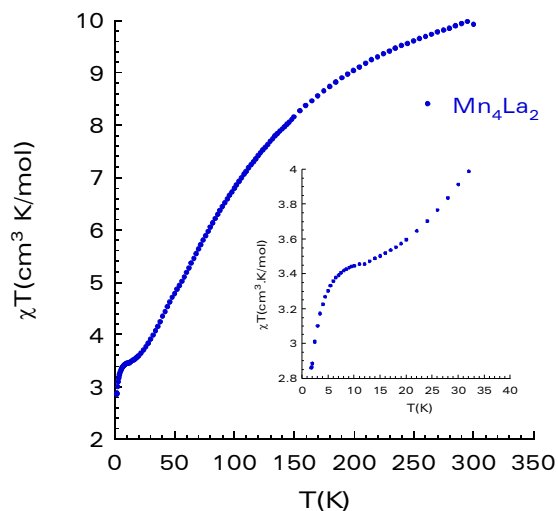


Figure 35: Temperature-dependence of the χT product under 0.1 T for compound **10**.

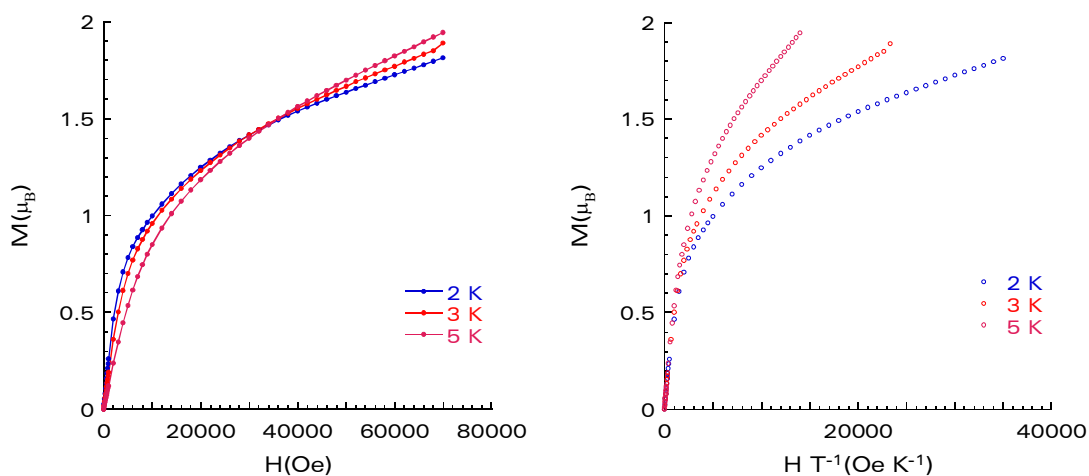


Figure 36: Plot of magnetisation M vs. H (left) and M vs. H/T (right) between 2 K and 5 K for **10**. The solid lines are to guide the eye.

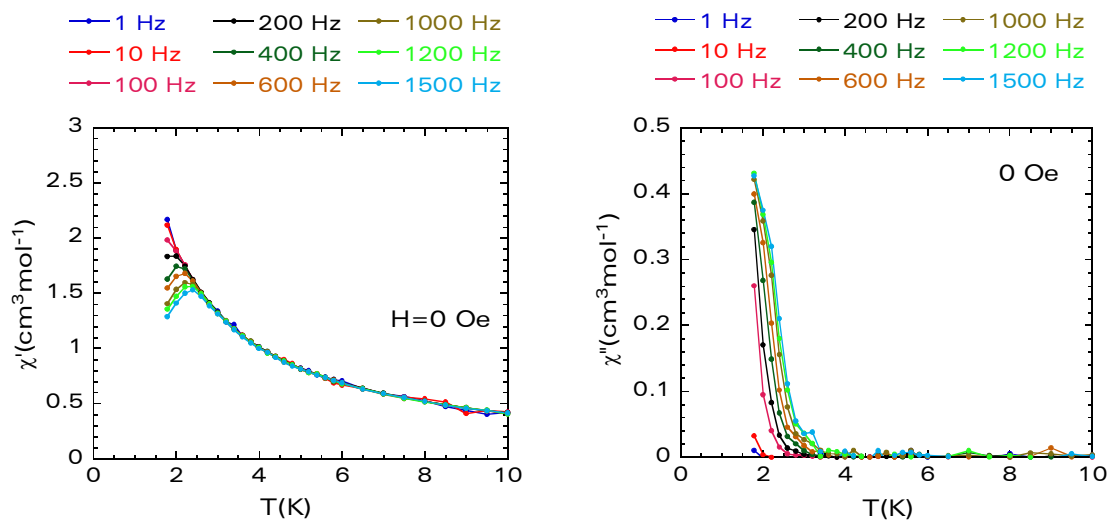


Figure 37: Temperature-dependent ac susceptibilities of **10** from 1.8 K to 10 K under zero dc field at indicated frequencies.

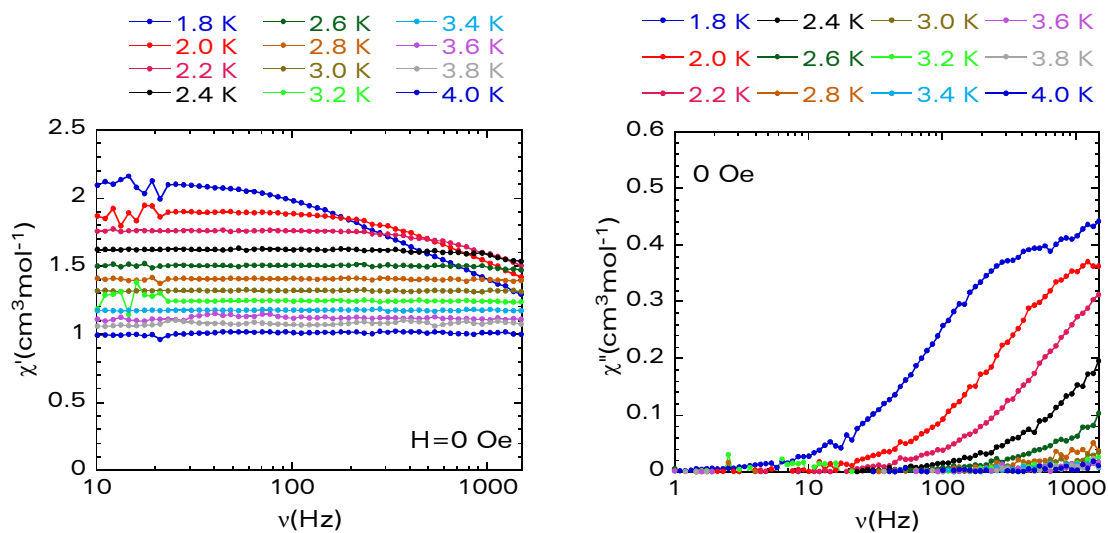


Figure 38: Frequency-dependent ac susceptibilities of **10** from 1.8 K to 4 K under zero dc field at indicated frequencies.

2.2.3 Structure of $[\text{Mn}^{\text{III}}_2\text{Dy}^{\text{III}}_4(\mu_4\text{-O})_2(\text{hmp})_4(\text{pic})_2(\text{piv})_6(\mu\text{-N}_3)_2]\cdot 4\text{CH}_3\text{CN}$ (14)

An isostructural family of hexanuclear aggregates $[\text{Mn}^{\text{III}}_2\text{Ln}^{\text{III}}_4(\text{O})(\text{hmp})_4(\text{Pic})_2(\text{Piv})_6(\text{N}_3)_2]\cdot 4\text{MeCN}$ (where $\text{Ln} = \text{Eu}^{\text{III}}$ (11), Gd^{III} (12), Tb^{III} (13), Dy^{III} (14), Ho^{III} (15) and Er^{III} (16)) is reported. They were obtained from the reactions of 2-(2-hydroxymethyl)pyridine (hmpH) with the preformed hexanuclear manganese complex **1** $\{\text{Mn}_6\}$, and the respective lanthanide salt. The complexes **11-12** and **13-16** are respectively isomorphous and represent a new heterometallic $3d\text{-}4f$ complex type for this class of ligand. The structural core of **11-16** consists of a defect Ln_4 dicubane flanked by two Mn^{III} ions. The magnetic properties of **11-15** were investigated by variable temperature magnetic susceptibility and magnetisation measurements. The magnetic data of these compounds suggest that antiferromagnetic interactions are present between adjacent paramagnetic centers.

Compound **14** (Dy) crystallises in the triclinic space group $P\bar{1}$ with $Z=4$. The two independent molecules each contain four dysprosium atoms and two manganese atoms. Single-crystal X-ray diffraction studies reveal that the core structure of **14** has a tetranuclear arrangement of Dy^{III} ions with non-crystallographic inversion symmetry centre. The Dy^{III} ions form a structure which is often encountered in polynuclear metal complexes, which has been described as a butterfly structure (Vincent, 1989: 2086). As in most tetranuclear compounds (Aromí, 2006: 1ff), the four Dy^{III} ions are not precisely coplanar. However, $\text{Dy}(1)$, $\text{Dy}(2)$, $\text{Dy}(3)$ and $\text{Dy}(4)$ are coplanar to within $0.0043(2)$ Å. The two μ_4 -bridging oxygen atoms $\text{O}(1)$ and $\text{O}(2)$ are located on opposite sides of the Dy_4 core and are displaced out of that plane by $0.953(5)$ Å and $0.957(5)$ Å, respectively.

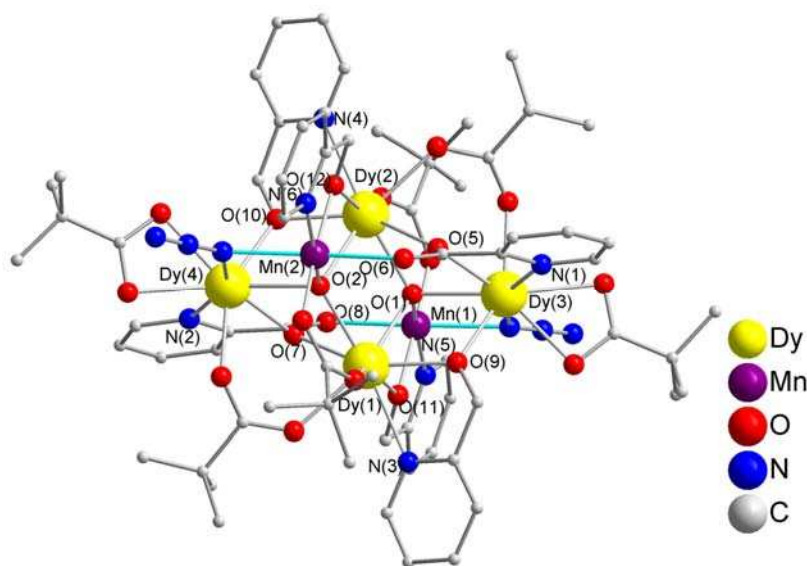


Figure 39: Molecular structure of $[\text{Mn}^{\text{III}}_2\text{Dy}^{\text{III}}_4(\mu_4\text{-O})_2(\text{hmp})_4(\text{pic})_2(\text{piv})_6(\mu\text{-N}_3)_2]\cdot 4\text{CH}_3\text{CN}$ with Jahn-Teller axes (turquoise). Organic hydrogen atoms and solvent molecules are omitted for clarity.

The oxidation states of the manganese and the lanthanide ions were determined by consideration of the coordination geometry (bond lengths, coordination numbers and the presence of Jahn–Teller elongation axes for Mn(1) and Mn(2)) and by bond valence sum analysis (Liu, 1993: 4102ff). Selected metrical parameters are summarised in Table 6 and Table 7. All Dy^{III} atoms are eightfold coordinated, with Dy(1) and Dy(2) forming the butterfly body and Dy(3) and Dy(4) the wings, respectively. Dy(1) and Dy(2) are coordinated by seven oxygens and one nitrogen coming from the deprotonated hydroxymethylpyridine (hmpH) ligand and the other two (Dy(3) and Dy(4)) are surrounded by six oxygens and two nitrogens, one coming from the to the picolinic acid oxidised hmpH ligand and one from an end-on μ_2 -coordinating azide coligand. Here all Dy^{III} ions feature a distorted dodecahedron environment (Figure 41).

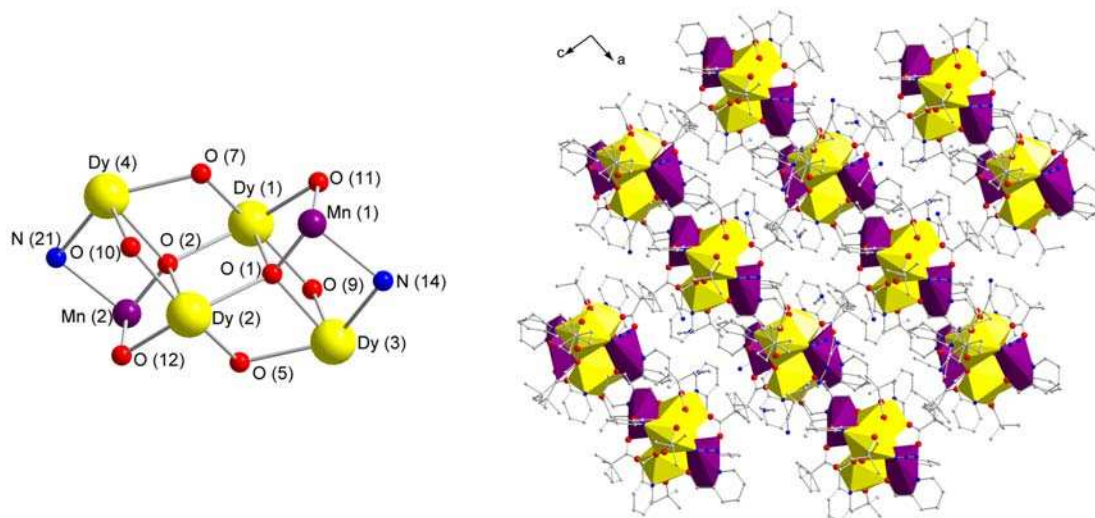


Figure 40: The {Mn^{III}₂Dy^{III}₄(μ_4 -O)₂} core of 14 (left) and part of the structure of 14 in the polyhedral representation, projected along the b axis. All Dy polyhedra are yellow and the Mn octahedra are violet.

The six independent pivalate ligands in the asymmetric unit exhibit two different coordination modes. Two form a *syn-syn* bidentate bridge between Dy(1) and Dy(4), and Dy(2) and Dy(3), respectively, while two others also bridge in a *syn,syn* mode Dy(1) and Mn(2), or Dy(2) and Mn(1), respectively. The remaining two pivalates chelate Dy(3) and Dy(4).

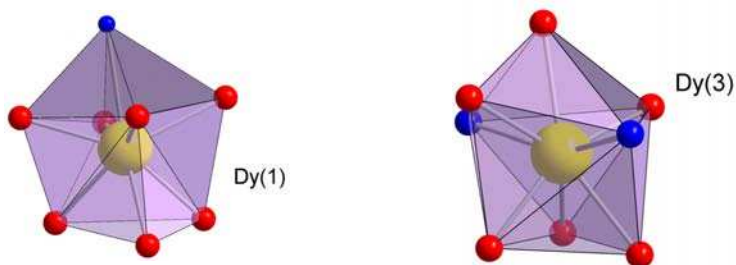


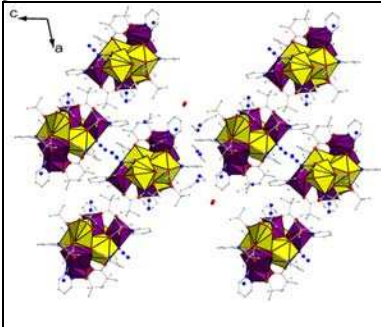
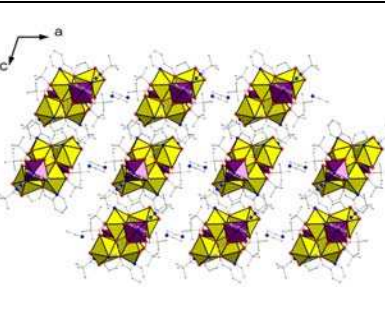
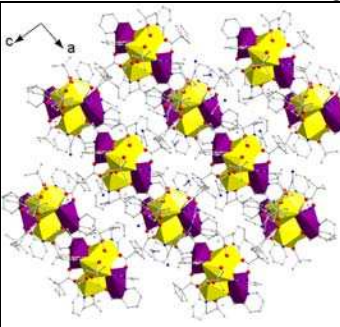
Figure 41: Distorted dodecahedron environment of Dy(1) and Dy(3), representing the coordination polyhedra of all four Dy^{III} ions in 14.

The Dy₄ butterfly core is held together by two μ_4 -bridging oxygens (O(1) and O(2)), which are also connected to the two manganese ions.

Another four μ_2 -bridging alkoxide oxygens, which are coming both from the hmp⁻-ligands chelating Dy(1) and Dy(2) and from the picolate ligands, which chelate Dy(3) or Dy(4), respectively, complete the $\{\text{Mn}^{\text{III}}_2\text{Dy}^{\text{III}}_4\text{O}_6\}^{6+}$ unit.

Performing the reaction with Tb (**13**), Ho (**15**) and Er (**16**) gave the isomorphous product with four molecules of acetonitrile per molecule. For Eu (**11**) and Gd (**12**) x-ray diffraction studies revealed that the structures are isostructural but with two MeCN solvent molecules leading to a monoclinic unit cell.

The corresponding synthetic reaction was also carried out with samarium. However, this gave a very different structure, with an unsymmetrical Mn_4Sm_4 core. Unfortunately the crystals were of poor quality, and the crystal structure could not be fully refined.

	Sm	Eu	Gd	Tb	Dy	Ho	Er
							
space group	$P\bar{1}$		$C2/c$				$P\bar{1}$
a=15.34 Å	$\alpha=101.89^\circ$	a=29.67 Å	$\alpha=90^\circ$	a=19.56 Å	$\alpha=106.86^\circ$	b=20.77 Å	$\beta=91.12^\circ$
b=16.62 Å	$\beta=100.92^\circ$	b=14.22 Å	$\beta=108.16^\circ$	b=24.07 Å	$\beta=102.11^\circ$	c=24.07 Å	$\gamma=102.11^\circ$
c=25.52 Å	$\gamma=97.80^\circ$	c=21.66 Å	$\gamma=90^\circ$				
	$\{\text{Mn}_4\text{Sm}_4\}$		$\{\text{Mn}_2\text{Ln}_4\} \cdot 2\text{CH}_3\text{CN}$				$\{\text{Mn}_2\text{Ln}_4\} \cdot 4\text{CH}_3\text{CN}$

Bond Valence Sum Calculations (Brown, 1985: 244ff):

respective atom	Mn(1)	Mn(2)
estimated oxidation state		
Mn^{II}	3.27	3.27
Mn^{III}	3.04	3.04
Mn^{IV}	3.12	3.11
calc. oxidation state	Mn^{III}	Mn^{III}

Compound	a	b	c	V
Mn_2Eu_4 (11)	29.671(3)	14.2200(9)	21.663(2)	8684.8(13)
Mn_2Gd_4 (12)	29.7074(11)	14.2061(5)	21.6628(6)	8687(7)
Mn_2Tb_4 (13)	19.7985(4)	21.0543(5)	24.4422(5)	9494(3)
Mn_2Dy_4 (14)	19.5580(8)	20.7692(10)	24.0713(10)	9115.3(7)
Mn_2Ho_4 (15)	19.7379(6)	21.0014(6)	24.3715(6)	9420(4)
Mn_2Er_4 (16)	19.7596(1)	20.9834(1)	24.3329(2)	9421(1)

Compound	α	β	γ
Mn ₂ Eu ₄ (11)	90	108.158(12)	90
Mn ₂ Gd ₄ (12)	90	108.147(3)	90
Mn ₂ Tb ₄ (13)	107.013(2)	91.141(2)	102.002(2)
Mn ₂ Dy ₄ (14)	106.861(3)	91.128(3)	102.110(4)
Mn ₂ Ho ₄ (15)	106.954(3)	91.068(3)	101.946(3)
Mn ₂ Er ₄ (16)	106.651(1)	90.906(1)	102.057(1)

Table 5: Summary of selected cell parameters.

Eu1-O5	2.352(8)	Eu2-O2	2.425(9)
Eu1-O7	2.383(9)	Eu2-O1	2.442(8)
Eu1-O1	2.399(8)	Eu2-O11	2.459(10)
Eu1-O9	2.417(9)	Eu2-O10	2.523(9)
Eu1-O4	2.425(9)	Eu2-N1	2.619(11)
Eu1-O1	2.449(8)	Mn1-O1	1.842(9)
Eu1-O2	2.640(9)	Mn1-O4	1.956(9)
Eu1-N3	2.713(12)	Mn1-O6	1.998(9)
Eu1-O8	3.046(11)	Mn1-N2	2.076(12)
Eu2-O5	2.340(9)	Mn1-O3	2.245(9)
Eu2-O8	2.375(9)	O1-Eu1	2.449(8)

Table 6: Selected bond lengths for **11**.

O5-Eu1-O7	81.4(3)	O4-Eu1-O2	74.8(3)
O5-Eu1-O1	71.9(3)	O1-Eu1-O2	66.1(3)
O7-Eu1-O1	130.9(3)	O5-Eu1-N3	63.8(3)
O5-Eu1-O9	133.8(3)	O7-Eu1-N3	70.2(3)
O7-Eu1-O9	91.7(4)	O1-Eu1-N3	126.8(3)
O1-Eu1-O9	136.2(3)	O9-Eu1-N3	70.9(4)
O5-Eu1-O4	86.4(3)	O4-Eu1-N3	82.3(3)
O7-Eu1-O4	152.5(3)	O1-Eu1-N3	146.2(3)
O1-Eu1-O4	66.5(3)	O2-Eu1-N3	138.4(3)
O9-Eu1-O4	79.2(3)	O5-Eu1-O8	155.5(3)
O5-Eu1-O1	110.4(3)	O7-Eu1-O8	74.3(3)
O7-Eu1-O1	76.0(3)	O1-Eu1-O8	127.1(3)
O1-Eu1-O1	75.9(3)	O9-Eu1-O8	46.1(3)
O9-Eu1-O1	112.0(3)	O4-Eu1-O8	114.4(3)
O4-Eu1-O1	131.5(3)	O1-Eu1-O8	66.4(3)
O5-Eu1-O2	145.7(3)	O2-Eu1-O8	57.3(3)
O7-Eu1-O2	126.9(3)	N3-Eu1-O8	104.5(3)
O1-Eu1-O2	74.3(3)	O5-Eu2-O8	140.9(3)
O9-Eu1-O2	71.0(3)	O5-Eu2-O2	76.5(3)
O8-Eu2-O2	69.9(3)	O10-Eu2-N1	74.5(3)
O5-Eu2-O1	71.4(3)	O1-Mn1-O4	88.1(4)
O8-Eu2-O1	78.6(3)	O1-Mn1-O6	100.8(4)
O2-Eu2-O1	69.7(3)	O4-Mn1-O6	169.7(4)
O5-Eu2-O11	140.2(3)	O1-Mn1-N2	168.8(4)
O8-Eu2-O11	77.9(4)	O4-Mn1-N2	80.8(4)
O2-Eu2-O11	127.0(4)	O6-Mn1-N2	90.3(4)
O1-Eu2-O11	142.4(3)	O1-Mn1-O3	102.8(4)
O5-Eu2-O10	87.9(3)	O4-Mn1-O3	88.6(4)
O8-Eu2-O10	130.7(3)	O6-Mn1-O3	84.5(4)
O2-Eu2-O10	138.4(3)	N2-Mn1-O3	79.3(4)
O1-Eu2-O10	140.8(3)	Mn1-O1-Eu1	103.8(4)
O11-Eu2-O10	52.8(3)	Mn1-O1-Eu2	106.2(3)
O5-Eu2-N1	76.9(3)	Eu1-O1-Eu2	105.5(3)
O8-Eu2-N1	104.8(4)	Mn1-O1-Eu1	129.6(4)
O2-Eu2-N1	64.5(3)	Eu1-O1-Eu1	104.1(3)
O1-Eu2-N1	128.9(3)	Eu2-O1-Eu1	105.6(3)

O11-Eu2-N1	85.6(4)		
------------	---------	--	--

Table 7: Selected bond angles for **11**.

Dy1-O9	2.287(5)	Dy3-O5	2.416(5)
Dy1-O2	2.333(5)	Dy3-N1	2.596(7)
Dy1-O11	2.355(5)	Dy4-O10	2.266(4)
Dy1-O1	2.386(4)	Dy4-O2	2.376(5)
Dy1-O7	2.494(5)	Dy4-O7	2.429(5)
Dy1-N3	2.564(6)	Dy4-N2	2.572(7)
Dy2-O10	2.286(5)	Mn1-O1	1.850(5)
Dy2-O1	2.332(5)	Mn1-O11	1.908(5)
Dy2-O12	2.343(5)	Mn1-N5	2.026(7)
Dy2-O2	2.390(4)	Mn1-O8	2.276(5)
Dy2-O5	2.510(5)	Mn2-O2	1.847(5)
Dy2-N4	2.572(6)	Mn2-O12	1.908(5)
Dy3-O9	2.256(5)	Mn2-N6	2.057(7)
Dy3-O1	2.378(5)	Mn2-O6	2.272(5)
Dy3-O21	2.392(6)		

Table 8: Selected bond lengths for **14**.

O9-Dy1-O2	109.61(17)	O5-Dy3-N1	64.19(19)
O9-Dy1-O11	89.27(18)	O10-Dy4-O2	73.52(17)
O2-Dy1-O11	132.42(17)	O10-Dy4-O7	74.03(17)
O9-Dy1-O1	72.73(17)	O2-Dy4-O7	67.92(16)
O2-Dy1-O1	77.78(16)	O10-Dy4-N2	88.70(19)
O11-Dy1-O1	66.55(16)	O2-Dy4-N2	132.10(18)
O9-Dy1-O7	148.99(16)	O7-Dy4-N2	64.45(18)
O2-Dy1-O7	67.50(17)	O1-Mn1-O11	87.6(2)
O11-Dy1-O7	74.21(17)	O1-Mn1-N5	167.2(2)
O1-Dy1-O7	76.61(16)	O11-Mn1-N5	81.5(2)
O9-Dy1-N3	65.83(18)	O1-Mn1-O8	104.9(2)
O2-Dy1-N3	149.06(18)	O11-Mn1-O8	88.1(2)
O11-Dy1-N3	78.48(18)	O9-Dy3-N1	87.5(2)
O1-Dy1-N3	125.24(17)	O1-Dy3-N1	131.37(19)
O7-Dy1-N3	132.81(19)	O17-Mn1-O8	86.7(2)
O10-Dy2-O1	107.46(18)	N5-Mn1-O8	81.5(2)
O10-Dy2-O12	90.99(18)	O2-Mn2-O12	87.6(2)
O1-Dy2-O12	132.80(17)	O2-Mn2-N6	167.4(2)
O10-Dy2-O2	72.93(16)	O12-Mn2-N6	81.1(2)
O1-Dy2-O2	77.72(16)	O2-Mn2-O6	104.1(2)
O12-Dy2-O2	66.61(16)	O12-Mn2-O6	88.1(2)
O10-Dy2-O5	148.37(16)	N6-Mn2-O6	81.2(2)
O1-Dy2-O5	66.73(17)	Mn1-O1-Dy2	129.5(3)
O12-Dy2-O5	74.91(18)	Mn1-O1-Dy3	107.8(2)
O15-Dy2-O5	70.39(18)	Dy2-O1-Dy3	108.92(19)
O2-Dy2-O5	75.49(16)	Mn1-O1-Dy1	101.7(2)
O10-Dy2-N4	66.17(18)	Dy2-O1-Dy1	102.33(17)
O1-Dy2-N4	148.07(18)	Dy3-O1-Dy1	103.21(19)
O12-Dy2-N4	79.13(19)	Mn2-O2-Dy1	130.0(2)
O2-Dy2-N4	125.29(17)	Mn2-O2-Dy4	107.2(2)
O5-Dy2-N4	135.23(18)	Dy1-O2-Dy4	109.26(18)
O9-Dy3-O1	73.42(17)	Mn2-O2-Dy2	101.53(19)
O9-Dy3-O5	74.02(18)	Dy1-O2-Dy2	102.17(18)
O1-Dy3-O5	67.61(17)	Dy4-O2-Dy2	103.22(18)
O5-Dy3-O22	134.67(18)		

Table 9: Selected bond angles for **14**.

2.2.4 Magnetic properties of $[\text{Mn}^{\text{III}}_2\text{Ln}^{\text{III}}_4(\mu_4\text{-O})_2(\text{hmp})_4(\text{pic})_2(\text{piv})_6(\mu\text{-N}_3)_2]\cdot 4\text{CH}_3\text{CN}$

Variable-temperature dc magnetic susceptibility data for compounds **11-15** were collected in the temperature range 1.8-300 K under an applied field of 1000 Oe (Figure 42). The samples were checked for the presence of ferromagnetic impurities by measuring the magnetisation as a function of the field at 100 K. Perfect straight lines were observed indicating the absence of such impurities. The dc magnetic data of **11-15** are summarised in Table 10. The observed χT products at RT are in relatively good agreement with the expected values for four non-interacting Ln^{III} and two Mn^{III} ions. The temperature dependence of the magnetic susceptibilities for **13** (Tb), **14** (Dy) and **15** (Ho) show similar thermal evolution in the full temperature range. From 300 K, the χT product decreases continuously, initially slowly down to 50 K, then increasingly rapidly, reaching a minimum value for χT at 2.24, 15.61 and 6.50 $\text{cm}^3 \text{Kmol}^{-1}$ for **13** (Tb), **14** (Dy) and **15** (Ho), respectively. For **12** (Gd) the χT product at 1000 Oe is almost independent of the temperature down to 30 K before it undergoes a sharp drop to 19.63 $\text{cm}^3 \text{Kmol}^{-1}$ at 1.8 K. For compound **11** (Eu) the χT product first undergoes a very slow decrease at higher temperatures resulting in a pseudo-plateau in the range 50-10 K followed by a rapid decrease on lowering the temperature from 30 to 1.8 K. The first slow decrease is due to the depopulation of the low lying excited states of the Eu by decreasing temperature. The final decrease of χT suggests the presence of weak antiferromagnetic intermolecular interactions and/or a significant magnetic anisotropy.

The field dependence of the magnetisation at low temperatures shows that the magnetisation increases smoothly with increasing applied dc field without saturation even at 7 T for all compounds. The magnitudes of magnetisation are also given in Table 10 for all compounds. This behaviour indicates the presence of magnetic anisotropy. Furthermore, the plots of the M versus H/T at low temperatures for compounds **11-15** show that the curves are not superposed, as would be expected for an isotropic system, giving a further indication of the presence of magnetic anisotropy even for **12** (Gd) (which comes from anisotropic Mn^{III} ions).

The magnetisation versus field data of **13** (Tb) shows a slope which is less steep at low field and increases around $H = 1.4$ T (Figure 45). Moreover, it should be noted that for **13-15** an inflection point on the M versus H is seen around 2000 Oe. This is typical of level crossing and the observed magnetisation for compounds **13-15** are likely influenced by field induced stabilisation of excited states with higher magnetic moment than the ground state. Since the spin ground state is difficult to define in a Dy(III) containing complex, it is also difficult to determine both the magnitude of the magnetic exchange interactions and the identity of the magnetic spins involved in the feature observed at 1.7 T. Above this field the magnetisation increases slowly reaching at 7 T the value of 26.08 μ_B but without showing true saturation. This value is roughly consistent with that expected for four uncorrelated Tb^{III} and two Mn^{III} magnetic moments. The application of a field stronger than 2 T apparently overcomes all antiferromagnetic interactions.

The presence of magnetic anisotropy was probed further by examining the magnetisation relaxation under zero dc field for all of the compounds **11-15**. It was found that only compound **13** (Tb) exhibits slow relaxation of its magnetisation under these conditions. However, **13** (Tb) shows only very weak frequency dependence of both in-phase and out-of-phase components. For **13** (Tb) the ground state is a singlet as proved by the maximum of χ (Figure 48) but the weak antiferromagnetic interactions are overcome at 1.4T by the applied dc field. Furthermore there is a strong contradiction between a singlet ground state for **13** (Tb) and slow relaxation of the magnetisation. The slow relaxation is likely due to an excited state which is still postulated.

The ratio of the intensity of the out-of-phase and in-phase signal is about 1:20, which indicates that the slow relaxation probably comes from an excited state. Dc fields up to 1500 Oe were applied to slow down the relaxation of magnetisation. In SMMs with a relaxation partially influenced by quantum effects, the application of a small dc field removes the ground state degeneracy and thus the possibility of quantum tunnelling, inducing a slowing down of the relaxation of the magnetisation. This application revealed no influence on the relaxation by resonant quantum tunnelling of magnetisation.

Compound	χT expected for each Ln at RT (cm ³ Kmol ⁻¹)	Ground state of Ln ion	χT expected for each complex ^a (cm ³ Kmol ⁻¹)
Mn ₂ Eu ₄ (11)	0	⁷ F ₀	6
Mn ₂ Gd ₄ (12)	7.88	⁸ S _{7/2}	37.52
Mn ₂ Tb ₄ (13)	11.82	⁷ F ₆	53.24
Mn ₂ Dy ₄ (14)	14.17	⁶ H _{15/2}	62.71
Mn ₂ Ho ₄ (15)	14.075	⁵ I ₈	62.18

Compound	χT measured at 300K per complex (cm ³ Kmol ⁻¹)	χT measured at 1.8 K per complex (cm ³ Kmol ⁻¹)	Magnetisation at 1.8 K and 7 T (μ_B)
Mn ₂ Eu ₄ (11)	13.43	5.34	6.59
Mn ₂ Gd ₄ (12)	37.50	19.63	33.58
Mn ₂ Tb ₄ (13)	57.57	2.24	31.82
Mn ₂ Dy ₄ (14)	67.71	15.61	32.50
Mn ₂ Ho ₄ (15)	66.62	6.50	35.49

Table 10: Magnetic data summarised from the dc measurements. ^a taking into account a g factor of Mn metal ions of 2.

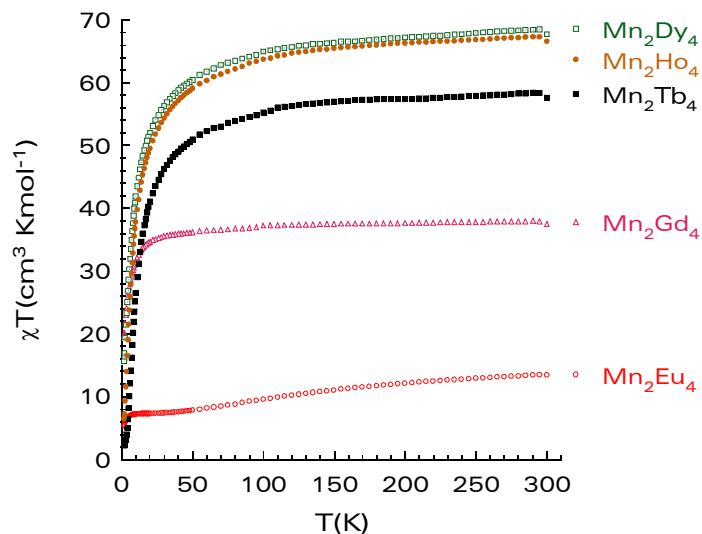


Figure 42: Temperature-dependence of the χT product under 0.1 T for compound 11-15.

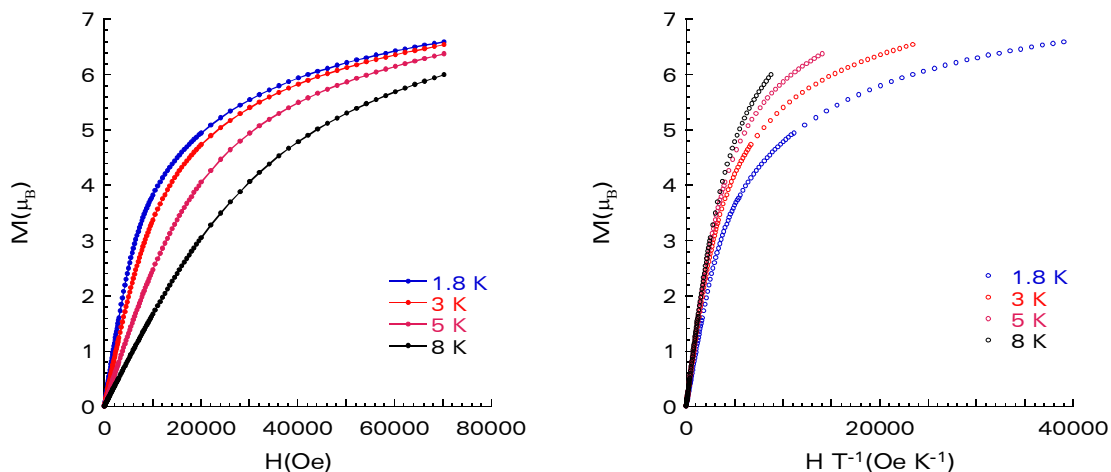


Figure 43: Plot of magnetisation M vs. H (left) and M vs. H/T (right) between 1.8 K and 8 K for 11. The solid lines are to guide the eye.

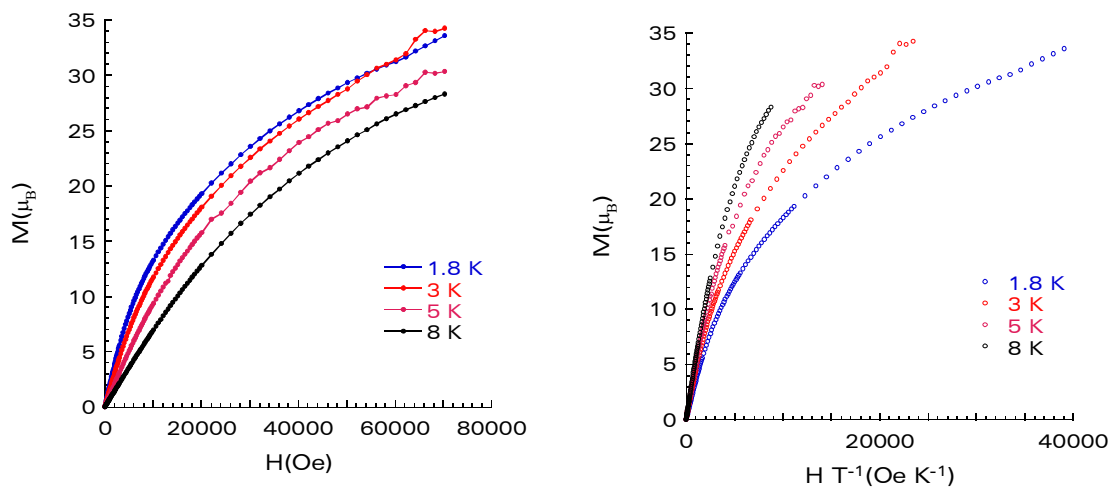


Figure 44: Plot of magnetisation M vs. H (left) and M vs. H/T (right) between 1.8 K and 8 K for 12. The solid lines are to guide the eye.

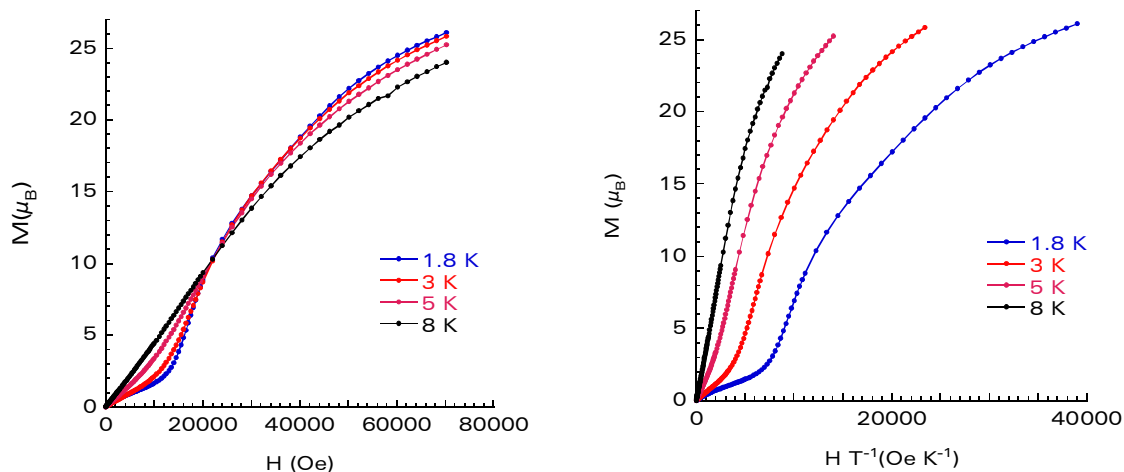


Figure 45: Plot of magnetisation M vs. H (left) and M vs. H/T (right) between 1.8 K and 8 K for **13**. The solid lines are to guide the eye.

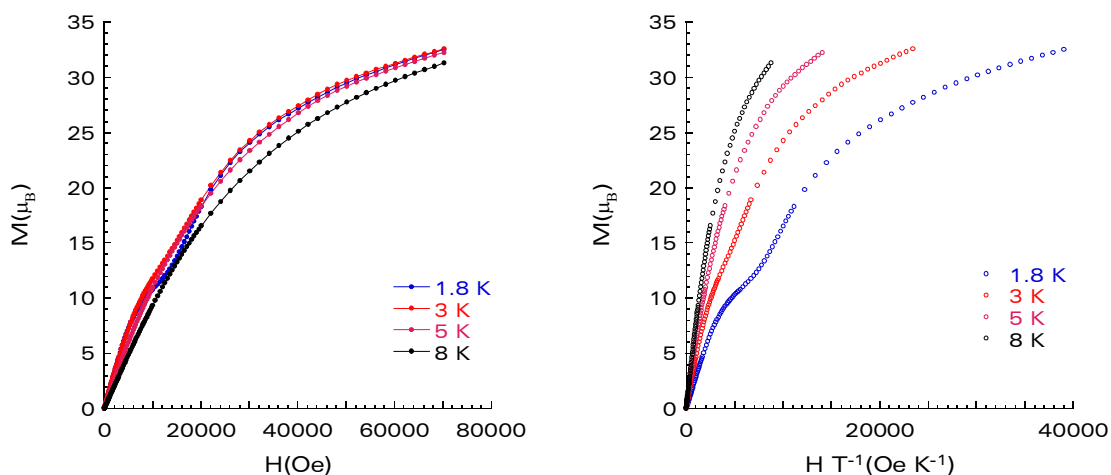


Figure 46: Plot of magnetisation M vs. H (left) and M vs. H/T (right) between 1.8 K and 8 K for **14**. The solid lines are to guide the eye.

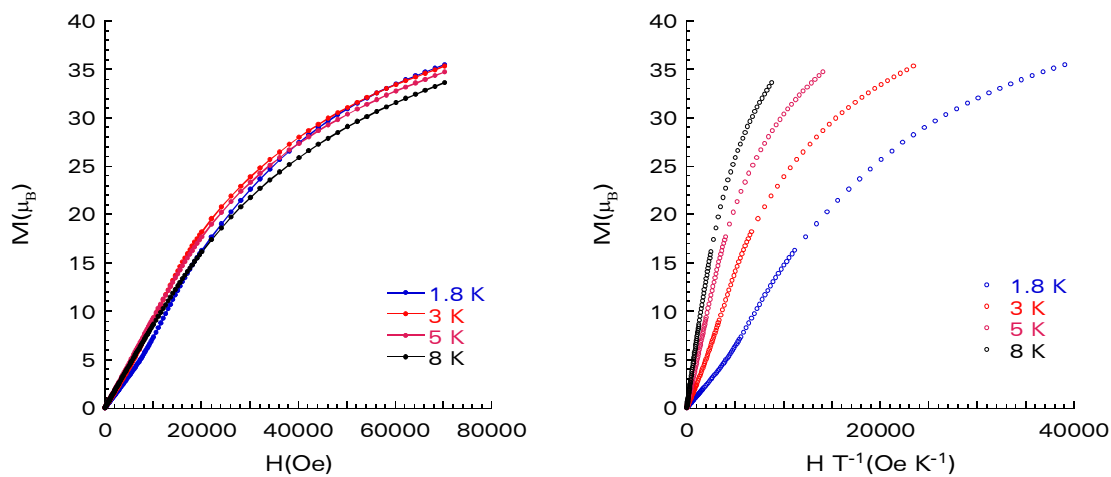


Figure 47: Plot of magnetisation M vs. H (left) and M vs. H/T (right) between 1.8 K and 8 K for **15**. The solid lines are to guide the eye.

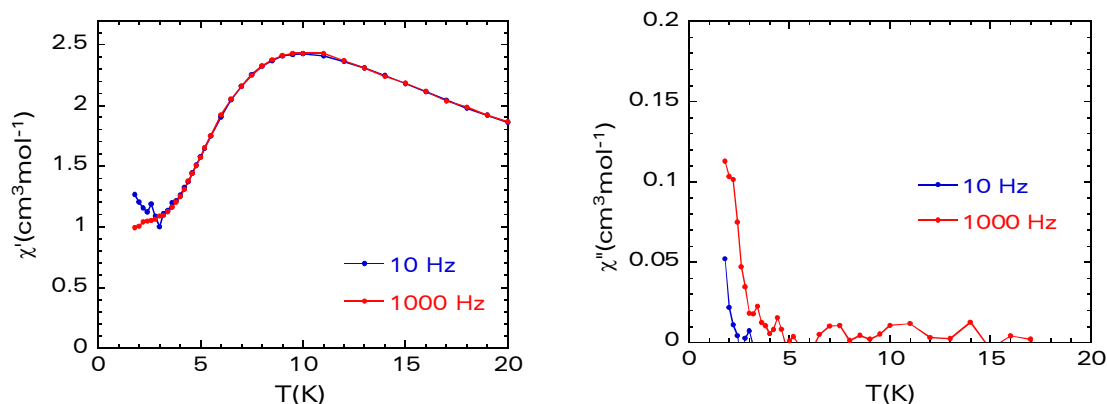


Figure 48: Plots of the in-phase and out-of-phase ac susceptibility for **13**.

2.3 Structure and magnetic properties of heptanuclear complexes

The reaction of $\{Mn_6\}$ (**1**) with *n*-butyldiethanolamine (*n*-bdeaH₂) and Ln(NO₃)₃·6H₂O in MeCN gave a brown solution from which dark-brown crystals of [Mn₄Ln₃(O)₃(*n*-bdea)(*n*-bdeaH)₂(N₃)(piv)₉(NO₃)] where Ln = Gd (**17**), Dy (**18**), Ho (**19**) and Er (**20**) could be isolated after one week. Magnetic measurements reveal that compound **18** (Dy) and **19** (Ho) show slow relaxation of magnetisation as expected for single molecule magnets.

2.3.1 Structure of [Mn^{II}Mn^{III}₂Mn^{IV}Ho^{III}(μ₄-O)(μ₃-OH)₂(*n*-bdea)₃(piv)₉(N₃)(NO₃)]·MeCN (**19**)

The complexes **17-20** contain different 4*f*-metals but are isomorphous and crystallise at room temperature in the orthorhombic space group Pbc_a (Table 5). The structure of **19** (Ho) is described here as representative for the whole series, for which selected metrical parameters are summarised in Table 12. The molecular structure (Figure 49) consists of an asymmetric {Mn₄Ho₃}²¹⁺ core, held together by two (μ₃-O)²⁻ and one (μ₄-O)²⁻ ligands and one oxygen atom of a monodeprotonated η³:η¹:η²:μ₄-diethanolamine ligand. Peripheral ligation is provided by another monodeprotonated η²:η¹:η²:μ₃- and a doubly deprotonated η²:η¹:η²:μ₃- diethanolamine ligand, nine pivalate anions, one nitrate anion and one azide anion. The pivalates occur in four different bridging modes: chelating, μ₂-bridging, η²:η¹:μ₂- and η²:η¹:μ₃-bridging. The metal oxidation states (Mn^{II}, Mn^{III}, Mn^{IV}, Ho^{III}) and the deprotonation levels of O²⁻, *n*-bdea²⁻ and *n*-bdeaH⁻ ions were established by charge considerations, bond valence sum calculations (Liu, 1993: 4102ff), inspection of metric parameters and the observation of Jahn–Teller elongation axes of Mn^{III}.

All four Mn atoms are six-coordinate. Ho(1) and Ho(2) are eight-coordinate with a coordination polyhedron that could be described as a distorted square antiprism, while Ho(3) is nine-coordinate with a coordination polyhedron that may best be described as a tricapped trigonal prism (Figure 52).

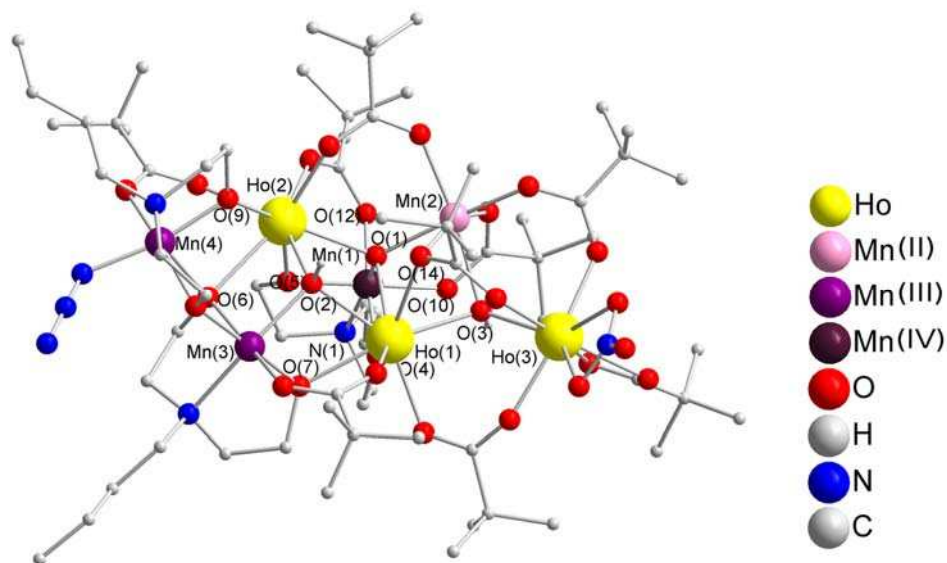


Figure 49: Molecular structure of $\text{Mn}^{\text{II}}\text{Mn}^{\text{III}}_2\text{Mn}^{\text{IV}}\text{Ho}^{\text{III}}(\mu_4\text{-O})(\mu_3\text{-O})_2(\text{n-bdea})_3(\text{N}_3)(\text{piv})_9(\text{NO}_3)$. Organic hydrogen atoms and solvent molecules are omitted for clarity.

Inspection of the central core reveals a sort of basket formed by Ho(1), Ho(2), Mn(1) and Mn(3) (Figure 50).

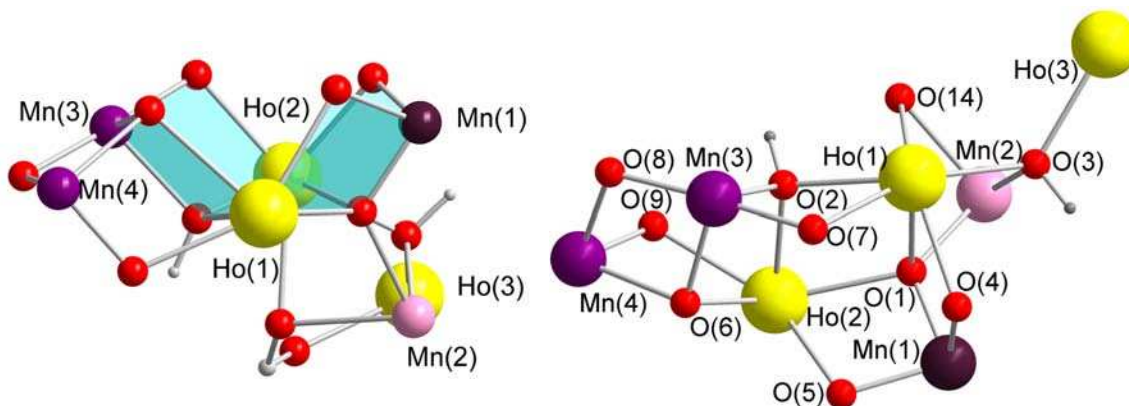


Figure 50: View of the "basket"-like geometry (left) within the metal core (right).

Alternatively one could describe the metal core as two distorted butterflies sharing one wing-edge (Figure 51). Here, the wing atom (Ho(1) of the butterfly given in pink in Figure 51 and spanned by Ho(1)-Ho(3) and Mn(2), also corresponds to the body atom of the second turquoise-coloured butterfly formed by Mn(3), Mn(4), Ho(1) and Ho(2). Mn(1) is connected to the first mentioned butterfly by O(1), the μ_4 -bridging oxygen and two μ -pivalates bridging in a *syn,syn*-mode to Mn(2) and Ho(1), respectively. One chelating *n-bdea*²⁻-ligand is completing the coordination sphere of Mn(1).

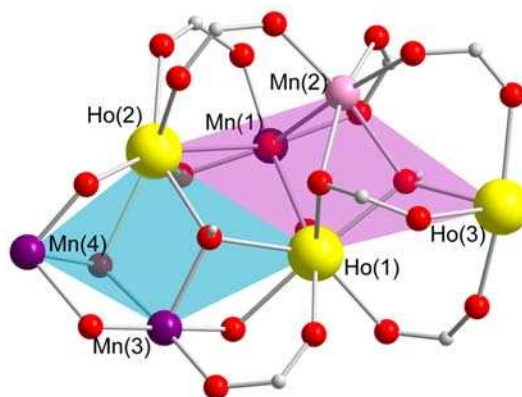


Figure 51: View of the metal core with colour-marked butterfly cores.

In addition to the μ_3 -O(3) and μ_4 -O(1) ligands bridged to the Ho^{III} ions, Mn(2) is coordinated to pivalates to complete the octahedral coordination environment with the fourth pivalate connecting Mn(2) to Mn(1).

Mn(3) is connected to Ho(2) by a μ -pivalate, chelated by a *n*-bdea²⁻-ligand and connected to Mn(4) by an alkoxy arm of the Mn(4) chelating *n*-bdea²⁻-ligand, whose coordination sphere is completed by an end-on-coordinating azide and a μ -pivalate, which connects Mn(4) to Ho(1).

Each monodeprotonated *n*-bdeaH⁻ and doubly-deprotonated *n*-bdea²⁻ group act as tridentate chelates to Mn(1), (Mn(3) and Mn(4), while Mn(2) and each Ho^{III} are not chelated by these, but rather bound to the core by pivalates. The Mn^{III} ions Mn(3) and Mn(4) have the expected octahedral geometries with Jahn–Teller elongations along one axis, while the geometries of Mn^{II} (Mn(2)) and Mn^{IV} (Mn(1)) are rather symmetric octahedra.

Compound **17-20** represent the first examples reported so far of compounds containing Mn^{II}, Mn^{III} and Mn^{IV} in combination with a 4*f*-metal ion. Up to now, only some pure Mn containing-clusters with mixed-oxidation states exist so far, e.g. the Mn₇ published by the group of Christou et al. in 2006 (Mishra, 2006: 10197ff).

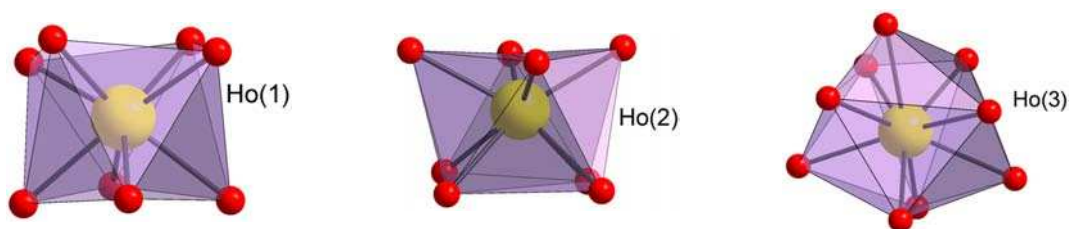


Figure 52: The square antiprismatic coordination polyhedra around Ho(1) and Ho(2) and the triaugmented triangular prism of Ho(3).

The Mn₄Ln₃ molecules are very closely isostructural. The only significant differences lie in the respective Ln–O bond distances, which decrease across the series in line with the expected contraction of the lanthanide ionic radii. Moreover, for all structures the packing is such that there are no inter-cluster interactions or pathways (Figure 53) which could lead to long-range magnetic ordering effects and one can be confident that the behaviour seen in the magnetic studies is of molecular origin.

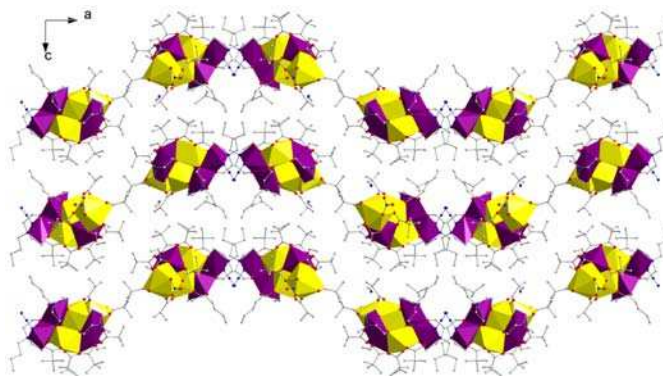


Figure 53: Part of the structure of **19** in the polyhedral representation, projected along the *b* axis. Ho(1)-(3) polyhedra are yellow and the Mn octahedra are violet.

It appears that this series of compounds show phase transition and/or pseudo-symmetry behaviour. In other words, these compounds crystallise in different space groups depending on the temperature. Although this may be interesting from a crystallographic point of view, it makes obtaining good quality crystal structures rather difficult. Compound **20** (Er) has a well-defined monoclinic cell at 100 K, with systematic absences for the space group $P2_1/c$. However, when the structure is solved and refined in this space group, three of the metal sites seem to be disordered, each over two adjacent positions. The systematic absences for the *c*-glide are clean, those for the 2_1 screw axis rather less so, and so refinement in the lower-symmetry space group Pc was attempted with two independent molecules in the asymmetric unit. However, the pseudo-symmetry relating these two molecules is such that correlation between corresponding parameters of pseudo-symmetrically related atoms becomes very high, and full refinement was not possible. For compounds **17** (Gd), **18** (Dy) and **19** (Ho) the unit cells appear orthorhombic, and are derived from that of compound **20** (Er) by a change in beta from 95.392 to ca. 90 degrees, together with a doubling of the *a*-axis. This change in space group may reflect the smaller ionic radius of the Er^{3+} cation. That the unit cell for these compounds is derived from a monoclinic one in this way may explain the problems encountered. For these three compounds, at 100 K the orthorhombic space group $Pbca$ was indicated, although some of the systematic absences were not particularly clean. Indeed, refinement in this space group proved problematic, and it appears that at this temperature the crystal symmetry is in fact monoclinic (but with β very close to 90 degrees). But the resulting pseudo-symmetry again resulted in high correlation and poor refinement. However, during a measurement of compound **19** (Ho), the cooling system accidentally failed and the crystal warmed to room temperature. Examining the data, it appeared that at this point in the measurement the crystal underwent a rather sharp phase transition from monoclinic (but quasi-orthorhombic) back to clean orthorhombic symmetry. The data measured after the cooling failure could be integrated separately, and the structure was solved and refined in space group $Pbca$, with no particular problems other than the higher degree of rotational disorder of the *n*-butyl groups of the ligands at this higher temperature. The unit cell of compound **20** (Er) was checked at room temperature and found also to be orthorhombic, and very similar to the others.

Bond Valence Sum Calculations (Brown, 1985: 244ff):

resp. atom	Mn(1)	Mn(2)	Mn(3)	Mn(4)
est. ox. state				
Mn ^{II}	4.02	1.96	3.21	3.24
Mn ^{III}	3.70	1.80	2.95	3.01
Mn ^{IV}	3.85	1.88	3.07	3.08
calc. ox. state	Mn ^{IV}	Mn ^{II}	Mn ^{III}	Mn ^{III}

compound	a	b	c	V
Mn ₄ Gd ₃ (17)	13.4221(12)	26.739(2)	54.022(5)	19388(3)
Mn ₄ Dy ₃ (18)	13.4288(10)	26.7203(19)	53.932(4)	19352(4)
Mn ₄ Ho ₃ (19)	13.5875(3)	27.0030(6)	54.4932(17)	19993.7(9)
Mn ₄ Er ₃ (20)	13.8035(5)	27.247(16)	54.8616(2)	20633(31)

Table 11: Summary of selected cell parameters of **17**, **18**, **19** and **20** selected at RT.

Ho1-O3	2.308(4)	Mn1-O12	1.926(5)
Ho1-O4	2.315(4)	Mn1-O10	1.932(5)
Ho1-O7	2.365(4)	Mn1-N1	2.127(6)
Ho1-O2	2.372(4)	Mn2-O1	2.139(4)
Ho1-O1	2.426(4)	Mn2-O11	2.145(5)
Ho1-O14	2.450(5)	Mn2-O3	2.270(4)
Ho2-O2	2.327(5)	Mn2-O14	2.372(5)
Ho2-O5	2.374(5)	Mn3-O7	1.872(5)
Ho2-O1	2.376(4)	Mn3-O8	1.926(5)
Ho2-O13	2.376(5)	Mn3-O6	2.044(5)
Ho2-O9	2.396(4)	Mn3-O2	2.073(5)
Ho2-O6	2.544(5)	Mn3-N2	2.272(6)
Ho3-O3	2.340(5)	Mn4-O9	1.870(5)
Ho3-N4	2.867(10)	Mn4-N11	1.955(9)
Mn1-O1	1.790(4)	Mn4-O8	2.032(6)
Mn1-O4	1.870(5)	Mn4-O6	2.210(5)
Mn1-O5	1.886(5)	Mn4-N3	2.292(7)

Table 12: Selected Bond lengths for **19**.

O3-Ho1-O4	83.86(16)	O1-Mn1-N1	166.4(2)
O22-Ho1-O4	77.63(18)	O4-Mn1-N1	84.4(2)
O3-Ho1-O7	159.29(16)	O5-Mn1-N1	83.1(2)
O22-Ho1-O7	82.57(18)	O12-Mn1-N1	91.4(2)
O4-Ho1-O7	77.00(16)	O10-Mn1-N1	87.7(2)
O3-Ho1-O2	129.62(15)	O1-Mn2-O11	92.51(19)
O4-Ho1-O2	108.94(16)	O24-Mn2-O3	95.5(2)
O7-Ho1-O2	65.52(16)	O1-Mn2-O3	80.93(16)
O3-Ho1-O1	74.40(15)	O11-Mn2-O3	90.16(19)
O4-Ho1-O1	63.53(15)	O1-Mn2-O14	80.00(17)
O7-Ho1-O1	103.37(15)	O11-Mn2-O14	161.11(19)
O2-Ho1-O1	69.53(14)	O3-Mn2-O14	71.62(16)
O3-Ho1-O14	69.59(15)	O7-Mn3-O8	177.0(2)
O4-Ho1-O14	133.90(16)	O7-Mn3-O6	98.6(2)
O7-Ho1-O14	130.15(15)	O8-Mn3-O6	79.2(2)
O2-Ho1-O14	67.09(16)	O7-Mn3-O2	80.88(18)
O1-Ho1-O14	73.15(16)	O8-Mn3-O2	100.6(2)
O2-Ho2-O5	101.07(16)	O6-Mn3-O2	80.75(19)
O2-Ho2-O1	71.13(15)	O7-Mn3-N2	79.7(2)
O5-Ho2-O1	65.17(15)	O8-Mn3-N2	98.0(2)
O2-Ho2-O13	147.40(16)	O6-Mn3-N2	81.0(2)
O5-Ho2-O13	74.58(16)	O2-Mn3-N2	151.0(2)
O1-Ho2-O13	78.06(15)	O9-Mn4-N11	169.0(3)
O2-Ho2-O9	72.43(17)	O9-Mn4-O8	93.7(2)

O5-Ho2-O9	144.27(16)	N11-Mn4-O8	94.5(3)
O1-Ho2-O9	137.43(17)	O9-Mn4-O6	83.52(19)
O13-Ho2-O9	129.35(17)	N11-Mn4-O6	105.9(3)
O2-Ho2-O6	66.22(16)	O8-Mn4-O6	73.16(19)
O5-Ho2-O6	78.16(15)	O9-Mn4-N3	80.6(2)
O1-Ho2-O6	115.50(15)	N11-Mn4-N3	93.7(3)
O13-Ho2-O6	140.18(17)	O8-Mn4-N3	79.1(3)
O9-Ho2-O6	66.98(16)	O6-Mn4-N3	146.9(2)
O15-Ho3-N4	70.5(2)	Mn1-O1-Mn2	122.3(2)
O3-Ho3-N4	148.2(2)	Mn1-O1-Ho2	103.10(19)
O1-Mn1-O4	86.03(19)	Mn2-O1-Ho2	124.89(19)
O1-Mn1-O5	88.16(19)	Mn1-O1-Ho1	104.39(18)
O4-Mn1-O5	95.1(2)	Mn2-O1-Ho1	92.46(16)
O1-Mn1-O12	99.2(2)	Ho2-O1-Ho1	105.64(15)
O4-Mn1-O12	172.1(2)	Mn3-O2-Ho2	109.8(2)
O5-Mn1-O12	91.0(2)	Mn3-O2-Ho1	100.57(18)
O1-Mn1-O10	101.6(2)	Ho2-O2-Ho1	109.00(17)
O4-Mn1-O10	88.0(2)	Mn2-O3-Ho1	92.32(16)
O5-Mn1-O10	170.0(2)	Mn2-O3-Ho3	118.67(19)
O12-Mn1-O10	85.1(2)	Ho1-O3-Ho3	118.88(19)

Table 13: Selected bond angles for **19**.

2.3.2 Magnetic properties of $[\text{Mn}^{\text{II}}\text{Mn}^{\text{III}}_2\text{Mn}^{\text{IV}}\text{Ln}^{\text{III}}_3(\mu_4\text{-O})(\mu_3\text{-OH})_2(\text{n-bdea})_3(\text{piv})_9(\text{N}_3)(\text{NO}_3)]\cdot\text{MeCN}$

Direct current (dc) magnetic susceptibility data for compounds **18** (Dy) and **19** (Ho) were collected in the 1.8-300 K temperature range under a field of 0.1 T (Figure 54). For compound **18** (Dy) the χT product at 300 K corresponds well to the expected value for one Mn^{II} , two Mn^{III} and one Mn^{IV} ions and the three Dy^{III} ions. For **19** (Ho) the experimentally found value for χT is slightly less than the expected value for the three Mn ions of different oxidation states and three Ho^{III} ions (51.08 instead of 54.39 $\text{cm}^3 \text{Kmol}^{-1}$). In both cases the χT products decrease slowly and constantly above 50 K from 54.36 and 51.08 $\text{cm}^3 \text{Kmol}^{-1}$ at 300 K to 51.5 and 46.4 $\text{cm}^3 \text{Kmol}^{-1}$ at 50 K for compound **18** (Dy) and **19** (Ho), respectively. This decrease is due to a depopulation of stark sublevels of the Ln^{III} ions and/or intramolecular antiferromagnetic interactions. While the χT product of **19** (Ho) drops below 50 K abruptly to a χT value of 33.8 $\text{cm}^3 \text{Kmol}^{-1}$, the slope for χT of **18** (Dy) drops down only until 8 K to a value of 47.2 $\text{cm}^3 \text{Kmol}^{-1}$, remains shortly on a plateau until ca. 3 K before it achieves a final drop to 45.7 at 1.8 K. The plateau is possibly the result of the stabilisation of the spin ground state of compound **18** (Dy). The exiguous break in the χT plot for **19** (Ho) at about 100 K is due to a rotation of the sample at this point.

Field-dependence measurements of the magnetisation up to 7 T were performed at 2 K for both compounds **18** (Dy) and **19** (Ho) and are shown in Figure 55 and Figure 56. The plots show a relative increase of the magnetisation at low fields, followed by an almost linear increase without clear saturation up to 7 T, where values of 27.15 and 25.87 μ_{B} are reached for **18** (Dy) and **19** (Ho), respectively. Indeed these values do not represent the expected magnitudes for three isolated Dy^{III} ($S=5/2$) or Ho^{III} ($S=2$) ions, respectively and one Mn^{II} ($S=5/2$), two Mn^{III} ($S=2$) and one Mn^{IV} ($S=3/2$) ion, 31 or 28 μ_{B} , respectively, likely due to the spin-orbit coupling of the Ln^{III} ions.

This behaviour is likely related to the population of excited states and to the intrinsic magnetic anisotropy of the Ln^{III} ions, especially in the case of Dy^{III} in **18** (Dy). The crossing point in the M versus H curves for compound **18** (Dy) is seen at about 60000 Oe. This is typical of level crossing and the observed magnetisation for compound **18** (Dy) is likely influenced by field induced stabilisation of excited states with higher magnetic moment than the ground state.

As a result of the magnetic anisotropy present in both compounds, the alternating current (ac) susceptibility measurements were checked under zero dc fields. For both tested compounds **18** (Dy) and **19** (Ho) an in-phase and out-of-phase (χ' and χ'') signal was detected. However, the ratio between in-phase and out-of-phase signal is in the case of Dy (**18**) 1:100 and in the case for Ho (**19**) even lower (1:200) indicating that the signals are very weak and the compounds exhibit no virtual slow relaxation of the magnetisation above 1.8 K.

The magnetic properties of compound **17** (Gd) and **20** (Er) were not measured due to limited time on the SQUID magnetometer and the decision to focus the measurements on compounds, which contain the most promising lanthanides like Dy^{III}.

Although the example of Mn₁₉ (Ako, 2006: 4926ff; Waldmann, 2008: 3486ff) has shown, that too high symmetry can lead to highly isotropic systems resulting in a very low or even non-existent energy barrier, essential for slow relaxation of magnetisation, as a result of the orientations of the individual ions easy axes of magnetisation cancelling each other, it was shown here, that in these particular examples, where the alignment of the orientations of the individual ions easy axes of magnetisation are strongly asymmetric, it does not have any positive effect on the anisotropy of the system and thus on the behaviour as SMMs.

Compound	χT expected for each Ln at RT (cm ³ Kmol ⁻¹)	Ground state of Ln ion	χT expected for each complex ^a (cm ³ Kmol ⁻¹)
Mn ₄ Dy ₃ (18)	14.17	⁶ H _{15/2}	54.78
Mn ₄ Ho ₃ (19)	14.075	⁵ I ₈	54.39

Compound	χT measured at 300K per complex (cm ³ Kmol ⁻¹)	χT measured at 1.8 K per complex (cm ³ Kmol ⁻¹)	Magnetisation at 1.8 K and 7 T (μ_B)
Mn ₄ Dy ₃ (18)	54.36	45.76	27.15
Mn ₄ Ho ₃ (19)	51.08	33.82	25.87

Table 14: Magnetic data summarised from the dc measurements. ^a taking into account a g factor of Mn metal ions of 2.

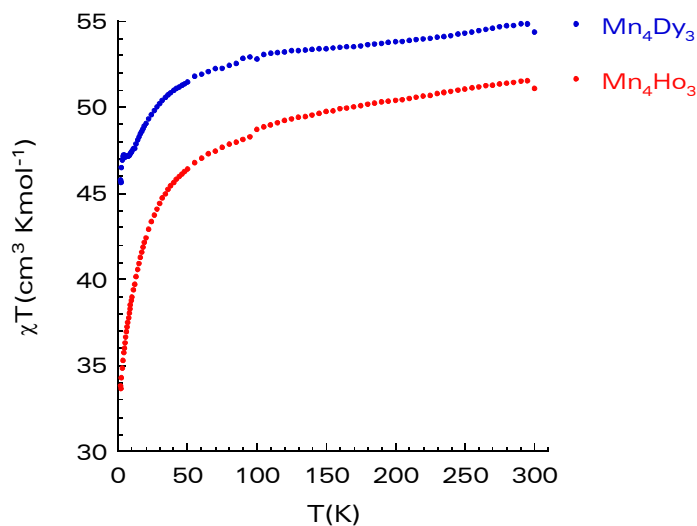


Figure 54: Temperature-dependence of the χT product under 1000 Oe for compound **18** and **19**.

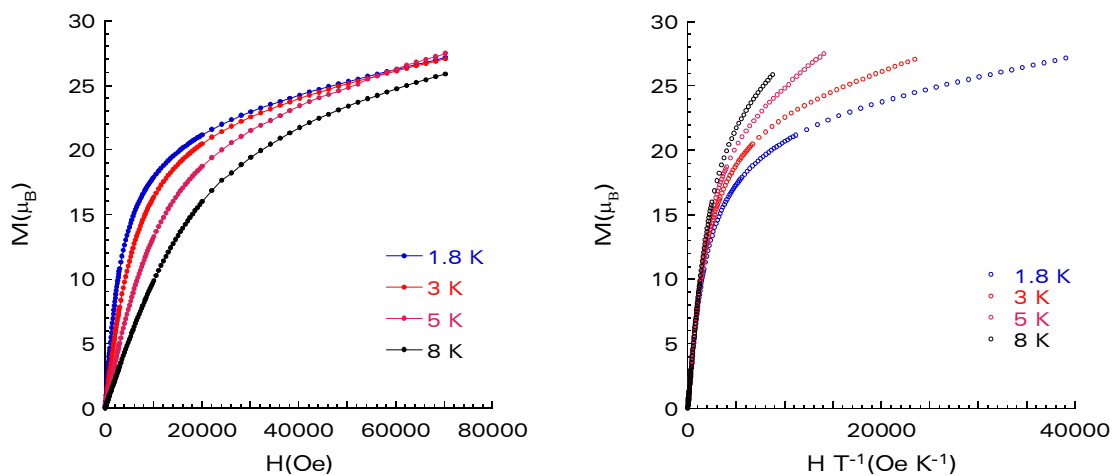


Figure 55: Plot of magnetisation M vs. H (left) and M vs. H/T (right) between 1.8 K and 8 K for **18**. The solid lines are to guide the eye.

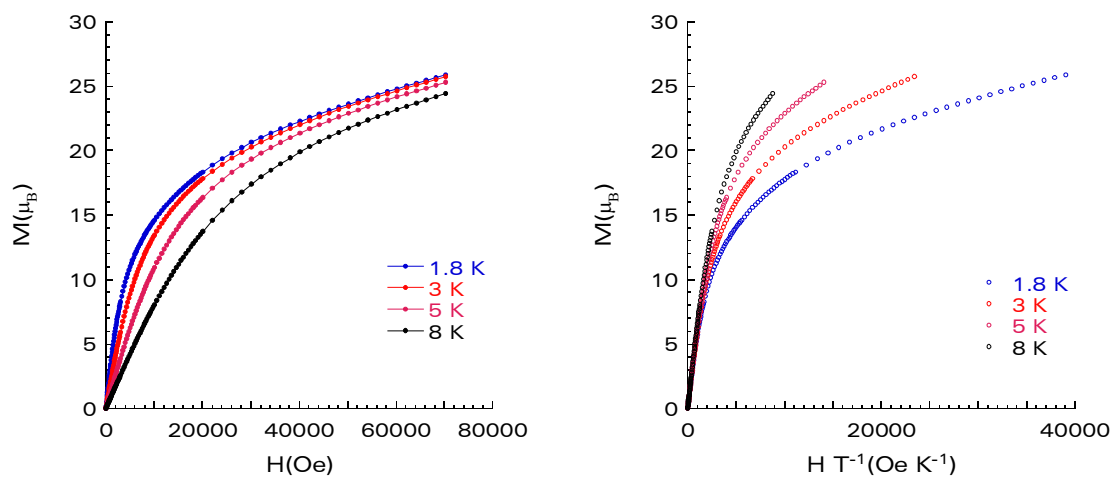


Figure 56: Plot of magnetisation M vs. H (left) and M vs. H/T (right) between 1.8 K and 8 K for **19**. The solid lines are to guide the eye.

2.4 Structure and magnetic properties of dodecanuclear complexes

The use of $\{\text{Mn}_6\}$ (1), *n*-butyldiethanolamine (*n*-bdeaH₂), LiOH and the respective lanthanide salt in 3*d*-4*f* chemistry produces a family of clusters of general formula $[\text{Mn}^{3.5}_4\text{Ln}^{\text{III}}_6\text{Li}_2(\mu_3\text{-O})_2(\mu_5\text{-CO}_3)_2(\text{n-bdea})_6(\text{piv})_{12}(\text{NO}_3)_2]\cdot 3\text{CH}_3\text{CN}$, where Ln = Pr (21), Nd (22), Sm (23), Eu (24), Gd (25), Tb (26), Dy (27) and Ho (28).

The molecular structure describes a planar disc-like Ln₆ ring separated by two pairs of Mn^{3.5} ions. Magnetic studies reveal that 27 (Dy) display slow relaxation of magnetisation as expected for single molecule magnets and calcinated 27 (Dy) shows a catalytic effect on the oxidation of CO to CO₂.

2.4.1 Structure of $[\text{Mn}^{3.5}_4\text{Gd}^{\text{III}}_6\text{Li}_2(\mu_3\text{-O})_2(\mu_5\text{-CO}_3)_2(\text{n-bdea})_6(\text{piv})_{12}(\text{NO}_3)_2]\cdot 3\text{CH}_3\text{CN}$ (25)

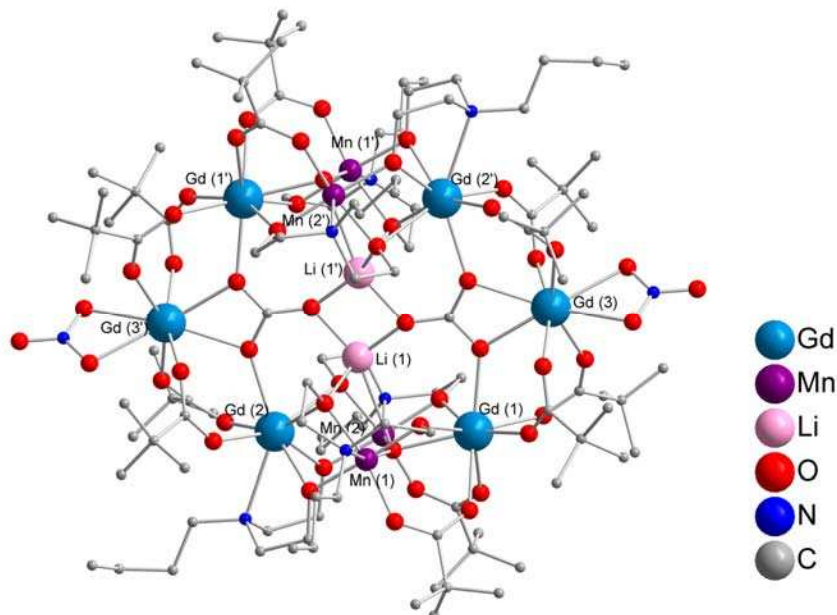


Figure 57: Molecular structure of $[\text{Mn}^{\text{IV}}_2\text{Mn}^{\text{III}}_2\text{Gd}^{\text{III}}_6\text{Li}_2(\mu_3\text{-O})_2(\mu_5\text{-CO}_3)_2(\text{n-bdea})_6(\text{piv})_{12}(\text{NO}_3)_2]\cdot 3\text{CH}_3\text{CN}$, 25. Organic hydrogen atoms and solvent molecules are omitted for clarity.

Compound 25 (Gd) forms long, black needle-shaped crystals. The complexes 21-29 are isostructural and the compounds crystallise isomorphously in the monoclinic space group $P2_1/n$ with $Z=2$. The structure of 25 (Gd) is described here as representative for the whole series from 21-27, for which selected metrical parameters are summarised in Table 16-Table 23. The polyhedral representation (along the *b*-axis) is illustrated below (Figure 58).

The molecular structure consists of a centrosymmetric $\{\text{Mn}_4\text{Gd}_6\text{Li}_2\}^{34+}$ core, held together by two carbonates, two $(\mu_3\text{-O})^{2-}$ ligands and the oxygen atoms of two doubly-deprotonated $\eta^2:\eta^2:\eta^1:\mu_3\text{-}$ and four doubly-deprotonated $\eta^2:\eta^2:\eta^1:\mu_4\text{-}$ diethanolamine ligands (Figure 57).

Peripheral ligation is provided by twelve μ -pivalate anions and two nitrate anions, which chelate Gd(3) and Gd(3'). Two lithium ions in the interior of the core complete the structure.

The metal oxidation states ($\text{Mn}^{3.5}$ and Gd^{III}) and the deprotonation levels of O^{2-} , $n\text{-bdea}^{2-}$ and $n\text{-bdeaH}^-$ ions were established by charge considerations, bond valence sum calculations (Liu, 1993: 4102ff).

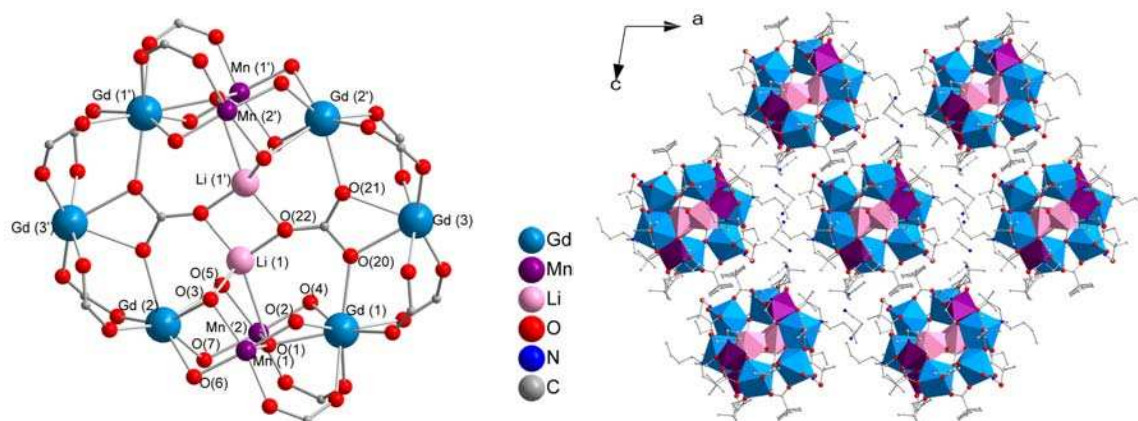


Figure 58: Left: Metal core of **25**. Right: Part of the structure of **25** in the polyhedral representation, projected along the b axis. Gd(1)-(3) polyhedra are yellow, Mn octahedra are violet and Li tetrahedra are rose.

All four Mn atoms are six-coordinate and all Gd atoms are eightfold coordinate. Two of them, Gd(1) and Gd(1'), feature a slightly distorted square antiprism environment of eight oxygen with O-O distances within 2.5253 and 3.1156 Å. O(1), O(2), O(4) and O(20) are coplanar to within 0.0592 Å. O(9), O(11), O(12) and O(14) are coplanar to within 0.0170 Å. The two planes above are nearly parallel - they make a dihedral angle of only 1.6 degrees.

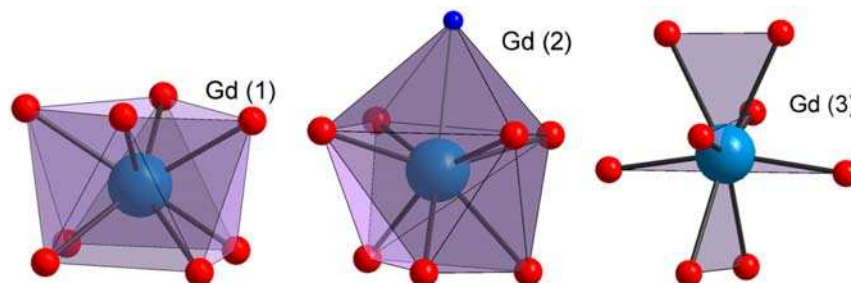


Figure 59: The coordination polyhedra around Gd(1), Gd(2) and Gd(3): square antiprism, dodecahedron and distorted bisdisphenoid.

The mutual O-O distances of O-atoms belonging to the top plane and the bottom plane are within the range of 2.900 - 3.090 Å, thus constructing the rather regular but slightly distorted square antiprism coordination environment of the Gd ions.

In contrast Gd(2) and Gd(2') are coordinated by seven oxygen and one nitrogen atom. The three oxygen atoms O(3), O(5) and O(21) form a plane which is almost coplanar to the plane formed by O(6), O(7) and O(17) at an angle of 2.644°. O(19) is slightly above the latter plane at 0.2013 Å.

The N(3)-Gd(2) bond is nearly perpendicular to the plane formed by the oxygen atoms O(3), O(5) and O(21) with a tilt angle of 7.821° . Viewing along the N(3)-Gd(2) bond, the three oxygens O(3), O(5) and O(21) form a slightly distorted triangle within the angle range of 57.028° and 64.165° whereas the oxygens O(6), O(7), O(17) and O(19) form a distorted square within a range 85.715 to 94.483° . This leads to a distorted dodecahedral environment for Gd(2) and Gd(2').

The environment of the third Gd site Gd(3) and Gd(3') can be described as a distorted bisdisphenoid type (Wells, 1984) comprising eight oxygen atoms.

Inspection of the arrangement of the metals in the core reveals, that all six Gd coordination sites form a coplanar ring to within $0.0240(2)$ Å consisting of two halves separated by 5.6549 Å whereas the Gd-Gd distances within each half are found to be $4.3266(6)$ and $4.3602(5)$ Å, respectively.

The Gd-Gd angle within each half is distorted to $104.00(1)$ being smaller than a regular hexagon angle. The elongated Gd(1)-Gd(2) distance representing the opening of the hexagon of $5.6549(5)$ Å is due to the fact that a plane formed by four manganese atoms intersects the Gd-ring with the nearly perpendicular angle of $89.48(2)^\circ$. This manganese plane consists of two pairs of manganese atoms with a Mn-Mn distance of $3.6400(15)$ Å. Each manganese pair is situated somewhat outside the Gd hexagon. The distance between these pairs is found to be $7.760(2)$ Å thus forming a slightly distorted rectangle with a Mn-Mn-Mn angle of 93.515° .

Each manganese pair consists of two corner connected distorted octahedra formed by five oxygen and one nitrogen atoms, respectively. Both nitrogen atoms are trans to the corner connecting oxygen. The tilt angle between the two corner connected octahedra is observed as 147.997° .

Two lithium ions serve as charge compensation to the anionic heteropolynuclear complex and are trapped by carbonate- and diethanolate-oxygens. The alkali metals are situated in the middle of the rectangular formed by the four manganese coordination sites, where each lithium ion is about 0.2 Å above and below this plane, respectively.

The coordination spheres of the heteronuclear complex is formed by six completely deprotonated *N*-*n*-butyldiethanolamine ligands (*n*-bdea), where two point up and down almost perpendicular to the Gd hexagon plane, respectively and the other two *n*-*N*-butyldiethanolamine ligands are situated close to the plane.

Twelve pivalates (*piv*) are connecting via *syn,syn*-bridging pairwise the Gd atoms within the two halves of the Gd hexagon. Both halves are connected via Gd-(*piv*)-Mn bridges and Mn-(*n*-bdea)-Gd bridges.

On the elongated side of the Gd hexagon two nitrate anions complete the coordination sphere of the Gd(3) and Gd(3'), respectively.

The void of the Gd hexagon is filled with two carbonates and the two lithium ions mentioned above.

The coordination environments of Mn(1) and Mn(2) are very similar, and are roughly intermediate between what would be expected for Mn^{III} and Mn^{IV}. Indeed, charge balance requires two Mn^{III} and two Mn^{IV} ions in the structure.

Bond valence sum calculations indicate intermediate valences, i.e. ca. 3.5. It is of interest to determine if the oxidation states are genuinely delocalised, which might result in ferromagnetic coupling as a result of double-exchange in the dinuclear units, or are localised but disordered, in which case superexchange will result.

The yttrium analogue **29** is as mentioned isostructural to the afore described compound **25** and isomorphous to the Ho derivative **28**. However, **29** (Y) include eight rather than three acetonitrile molecules per complex and it is to be assumed that this is the same for **28** (Ho) due to the same unit cell parameters (Table 15). Two crystals are said to be isostructural if they have the same structure, but not necessarily the same cell dimensions. However, two crystals are said to be isomorphous if both have the same space group and unit-cell dimensions and the types and the positions of atoms in both are the same (Iucr, 2006).

The question of whether the coordinating anions in the middle of the metal core are carbonates or nitrates is justified. The CHN values will give no sufficient answer, as the values differ too little. However, several points confirm the fact, that it is a carbonate that connects the lithium ions with the lanthanides rather than a nitrate.

First of all from the crystallographical point of view: the XO_3 ($X = N$ or C) is held rigidly within the molecule, so none of its atoms should vibrate with a higher amplitude than the others. Regarding the temperature factors of the X, where X is supposed to be carbon, show that they are similar to the oxygens. Considering nitrogen instead of carbon will result in the temperature factor for the nitrogen going quite a bit higher than that of the oxygens.

Additionally, the Bond Valence Sum Calculations show that the oxidation states of the manganese ions are around 3.5. Thus, charge considerations necessitate two anions with two negative charges each. Changing CO_3 by NO_3 would indeed not lead to a strong change of the bond lengths of the manganese and thus to a change of the oxidation states of the manganese ions including the formation of Jahn-Teller axes as expected for Mn^{III} ions.

With cerium it was not possible to obtain a similar structure, but an already published Ce^{IV}_6 complex (Mereacre, 2009: 2524ff), which seems to be thermodynamically favoured.

Detailed information about the bond lengths and angles are found in Table 16-Table 23.

Bond Valence Sum Calculations (Brown, 1985: 244ff):

respective atom	Mn(1)	Mn(2)
estimated oxidation state		
Mn^{II}	3.59	3.65
Mn^{III}	3.21	3.36
Mn^{IV}	3.44	3.5
calc. oxidation state	$Mn^{3.5}$	$Mn^{3.5}$

Compound	a	b	c	V
Mn ₄ Pr ₆ (21)	19.1528(19)	15.2274(15)	26.697(3)	7658.1(13)
Mn ₄ Nd ₆ (22)	19.1127(1)	15.5506(7)	26.5793(1)	7756(10)
Mn ₄ Sm ₆ (23)	19.4126(7)	15.4350(4)	26.9611(1)	7954(7)
Mn ₄ Eu ₆ (24)	19.3683(8)	15.4191(4)	26.9509(1)	7922(8)
Mn ₄ Gd ₆ (25)	19.0162(12)	15.2263(7)	26.6159(18)	7592.9(8)
Mn ₄ Tb ₆ (26)	19.2759(6)	15.3828(3)	26.7685(9)	7819.3(6)
Mn ₄ Dy ₆ (27)	18.8860(16)	15.1696(13)	26.450(2)	7474.3(11)
Mn ₄ Ho ₆ (28)	28.7327(5)	18.1269(4)	34.4563(7)	16957(8)
Mn ₄ Y ₆ (29)	28.4767(12)	17.9812(7)	34.0806(17)	16478.2(13)

Compound	α	β	γ
Mn ₄ Pr ₆ (21)	90	100.398(2)	90
Mn ₄ Nd ₆ (22)	90	100.927(6)	90
Mn ₄ Sm ₆ (23)	90	100.049(5)	90
Mn ₄ Eu ₆ (24)	90	100.177(5)	90
Mn ₄ Gd ₆ (25)	90	99.851(5)	90
Mn ₄ Tb ₆ (26)	90	99.892(4)	90
Mn ₄ Dy ₆ (27)	90	99.472(1)	90
Mn ₄ Ho ₆ (28)	90	109.104(2)	90
Mn ₄ Y ₆ (29)	90	109.219(4)	90

Table 15: Selected cell parameters for compounds 21-29.

Pr1-O14	2.417(5)	Pr3-O16A	2.367(6)
Pr1-O1	2.422(4)	Pr3-O16B	2.44(2)
Pr1-O12	2.429(5)	Pr3-O20	2.499(4)
Pr1-O20	2.456(4)	Mn1-O1	1.858(5)
Pr1-O4	2.463(5)	Mn1-O2	1.894(4)
Pr1-O9	2.468(4)	Mn1-O6	1.914(4)
Pr1-O2	2.488(4)	Mn1-O8	1.933(4)
Pr1-O11	2.491(4)	Mn1-O3	1.966(4)
Pr2-O17	2.407(4)	Mn1-N1	2.197(5)
Pr2-O19	2.444(4)	Mn2-O4	1.892(4)
Pr2-O7	2.446(4)	Mn2-O7	1.909(4)
Pr2-O6	2.453(4)	Mn2-O10	1.943(4)
Pr2-O3	2.484(4)	Mn2-O1	1.949(5)
Pr2-O5	2.560(4)	Mn2-O5	1.963(4)
Pr2-N3	2.702(5)	Mn2-N2	2.231(5)
Pr3-O13B	2.282(17)	Li1-O5	1.933(11)
Pr3-O15A	2.321(6)	Li1-O3	1.980(11)
Pr3-O15B	2.32(2)	Pr3-O13A	2.397(6)
Pr3-O18B	2.33(2)	Pr3-O18A	2.403(6)

Table 16: Selected bond lengths for 21.

O14-Pr1-O1	140.15(17)	O15A-Pr3-O13A	91.3(2)
O14-Pr1-O12	80.10(18)	O15B-Pr3-O13A	110.9(6)
O1-Pr1-O12	138.62(18)	O18B-Pr3-O13A	152.5(5)
O14-Pr1-O20	84.24(16)	O16A-Pr3-O13A	92.3(2)
O1-Pr1-O20	107.78(13)	O13B-Pr3-O18A	156.4(6)
O12-Pr1-O20	79.81(16)	O15A-Pr3-O18A	88.9(2)
O14-Pr1-O4	82.00(16)	O15B-Pr3-O18A	65.6(6)
O1-Pr1-O4	63.54(15)	O18B-Pr3-O18A	38.5(5)
O12-Pr1-O4	154.77(17)	O16A-Pr3-O18A	95.0(2)
O20-Pr1-O4	80.84(15)	O13A-Pr3-O18A	162.06(19)
O14-Pr1-O9	113.64(16)	O13B-Pr3-O16B	84.8(8)
O1-Pr1-O9	78.61(15)	O15A-Pr3-O16B	153.3(5)

O12-Pr1-O9	74.01(17)	O15B-Pr3-O16B	167.7(7)
O20-Pr1-O9	144.56(16)	O18B-Pr3-O16B	91.9(7)
O4-Pr1-O9	129.98(14)	O16A-Pr3-O16B	35.7(5)
O14-Pr1-O2	156.09(16)	O13A-Pr3-O16B	62.3(5)
O1-Pr1-O2	62.66(15)	O18A-Pr3-O16B	117.4(5)
O12-Pr1-O2	79.67(16)	O13B-Pr3-O20	84.4(5)
O20-Pr1-O2	79.75(14)	O15A-Pr3-O20	79.77(18)
O4-Pr1-O2	112.51(14)	O15B-Pr3-O20	70.8(6)
O9-Pr1-O2	72.47(14)	O18B-Pr3-O20	117.4(5)
O14-Pr1-O11	73.49(16)	O16A-Pr3-O20	124.81(17)
O1-Pr1-O11	77.05(14)	O13A-Pr3-O20	77.64(17)
O12-Pr1-O11	119.01(15)	O18A-Pr3-O20	84.76(17)
O20-Pr1-O11	146.69(15)	O16B-Pr3-O20	97.2(5)
O4-Pr1-O11	71.92(14)	O1-Mn1-O2	85.78(19)
O9-Pr1-O11	68.52(15)	O1-Mn1-O6	96.12(18)
O2-Pr1-O11	128.13(14)	O2-Mn1-O6	176.69(18)
O17-Pr2-O19	98.41(15)	O1-Mn1-O8	97.74(18)
O17-Pr2-O7	80.80(14)	O2-Mn1-O8	93.08(17)
O19-Pr2-O7	147.92(14)	O6-Mn1-O8	89.36(17)
O17-Pr2-O6	143.51(14)	O1-Mn1-O3	90.98(18)
O19-Pr2-O6	79.06(14)	O2-Mn1-O3	95.49(17)
O7-Pr2-O6	82.91(13)	O6-Mn1-O3	81.78(16)
O17-Pr2-O3	154.49(14)	O8-Mn1-O3	168.20(18)
O19-Pr2-O3	87.62(14)	O1-Mn1-N1	165.4(2)
O7-Pr2-O3	106.93(13)	O2-Mn1-N1	81.6(2)
O6-Pr2-O3	61.93(13)	O6-Mn1-N1	96.18(19)
O17-Pr2-O5	93.43(14)	O8-Mn1-N1	90.33(19)
O19-Pr2-O5	150.81(14)	O3-Mn1-N1	82.92(18)
O7-Pr2-O5	60.36(13)	O4-Mn2-O7	176.38(18)
O6-Pr2-O5	106.40(13)	O4-Mn2-O10	93.10(18)
O3-Pr2-O5	71.06(13)	O7-Mn2-O10	90.41(17)
O17-Pr2-N3	75.97(15)	O4-Mn2-O1	84.05(19)
O19-Pr2-N3	81.80(15)	O7-Mn2-O1	96.33(18)
O7-Pr2-N3	66.79(14)	O10-Mn2-O1	98.22(17)
O6-Pr2-N3	67.61(14)	O4-Mn2-O5	95.26(18)
O3-Pr2-N3	129.53(14)	O7-Mn2-O5	81.14(16)
O5-Pr2-N3	127.11(14)	O10-Mn2-O5	168.59(17)
O13B-Pr3-O15A	68.5(6)	O1-Mn2-O5	90.37(17)
O13B-Pr3-O15B	91.0(8)	O4-Mn2-N2	80.2(2)
O15A-Pr3-O15B	24.7(6)	O7-Mn2-N2	98.8(2)
O13B-Pr3-O18B	158.2(7)	O10-Mn2-N2	91.6(2)
O15A-Pr3-O18B	113.2(5)	O1-Mn2-N2	161.9(2)
O15B-Pr3-O18B	96.2(8)	O5-Mn2-N2	82.2(2)
O13B-Pr3-O16A	108.5(6)	O5-Li1-O3	97.1(4)
O15A-Pr3-O16A	155.3(2)	Mn1-O1-Mn2	148.3(2)
O15B-Pr3-O16A	155.3(6)	Mn1-O1-Pr1	105.3(2)
O18B-Pr3-O16A	60.2(5)	Mn2-O1-Pr1	103.9(2)
O13B-Pr3-O13A	25.1(5)		

Table 17: Selected bond angles for 21.

Gd1-O14	2.337(5)	Gd3-O13	2.333(5)
Gd1-O12	2.359(5)	Gd3-O20	2.438(5)
Gd1-O1	2.371(5)	Gd3-N4	2.930(7)
Gd1-O20	2.405(5)	Mn1-O2	1.889(5)
Gd1-O9	2.419(5)	Mn1-O1	1.902(6)
Gd1-O4	2.420(5)	Mn1-O6	1.917(5)
Gd1-O2	2.423(5)	Mn1-O8	1.950(5)
Gd1-O11	2.431(5)	Mn1-O3	1.985(5)
Gd2-O17	2.338(5)	Mn1-N1	2.222(6)
Gd2-O19	2.364(5)	Mn2-O1	1.884(6)
Gd2-O6	2.386(5)	Mn2-O4	1.897(5)
Gd2-O7	2.399(4)	Mn2-O7	1.917(5)
Gd2-O3	2.410(5)	Mn2-O10	1.937(5)
Gd2-O21	2.438(5)	Mn2-O5	1.953(5)

Gd2-O5	2.512(5)	Mn2-N2	2.194(7)
Gd2-N3	2.661(7)	Li1-O22	1.861(13)
Gd3-O15	2.274(5)	Li1-O5	1.919(13)
Gd3-O16	2.316(5)	Li1-O3	1.960(14)
Gd3-O18	2.323(5)		

Table 18: Selected bond lengths for **25**.

O14-Gd1-O12	79.6(2)	O15-Gd3-O13	90.7(2)
O14-Gd1-O1	139.38(19)	O16-Gd3-O13	91.4(2)
O12-Gd1-O1	140.0(2)	O18-Gd3-O13	161.85(19)
O14-Gd1-O20	81.30(18)	O15-Gd3-O20	80.51(18)
O12-Gd1-O20	79.60(18)	O16-Gd3-O20	127.21(17)
O1-Gd1-O20	109.23(16)	O18-Gd3-O20	83.64(18)
O14-Gd1-O9	114.61(19)	O13-Gd3-O20	78.28(18)
O12-Gd1-O9	73.17(19)	O15-Gd3-N4	73.7(2)
O1-Gd1-O9	79.84(18)	O16-Gd3-N4	78.34(19)
O20-Gd1-O9	144.66(18)	O18-Gd3-N4	98.0(2)
O14-Gd1-O4	80.92(18)	O13-Gd3-N4	98.9(2)
O12-Gd1-O4	153.94(19)	O20-Gd3-N4	154.08(18)
O1-Gd1-O4	63.34(18)	O2-Mn1-O1	84.3(2)
O20-Gd1-O4	80.45(17)	O2-Mn1-O6	176.6(2)
O9-Gd1-O4	131.33(19)	O1-Mn1-O6	95.7(2)
O14-Gd1-O2	154.50(18)	O2-Mn1-O8	93.4(2)
O12-Gd1-O2	80.10(18)	O1-Mn1-O8	98.0(2)
O1-Gd1-O2	64.13(18)	O6-Mn1-O8	90.0(2)
O20-Gd1-O2	79.96(17)	O2-Mn1-O3	96.3(2)
O9-Gd1-O2	73.59(17)	O1-Mn1-O3	90.6(2)
O4-Gd1-O2	112.61(16)	O6-Mn1-O3	80.3(2)
O14-Gd1-O11	73.31(19)	O8-Mn1-O3	167.7(2)
O12-Gd1-O11	116.90(18)	O2-Mn1-N1	81.3(2)
O1-Gd1-O11	78.15(18)	O1-Mn1-N1	163.2(2)
O20-Gd1-O11	145.73(19)	O6-Mn1-N1	98.1(2)
O9-Gd1-O11	68.7(2)	O8-Mn1-N1	91.5(2)
O4-Gd1-O11	73.23(18)	O3-Mn1-N1	82.5(2)
O2-Gd1-O11	130.33(18)	O1-Mn2-O4	83.4(2)
O17-Gd2-O19	96.39(18)	O1-Mn2-O7	95.6(2)
O17-Gd2-O6	142.65(18)	O4-Mn2-O7	175.7(2)
O19-Gd2-O6	80.14(18)	O1-Mn2-O10	97.9(2)
O17-Gd2-O7	80.71(17)	O4-Mn2-O10	93.7(2)
O19-Gd2-O7	147.58(18)	O7-Mn2-O10	90.6(2)
O6-Gd2-O7	83.00(16)	O1-Mn2-O5	91.4(2)
O17-Gd2-O3	154.06(18)	O4-Mn2-O5	95.7(2)
O19-Gd2-O3	88.32(17)	O7-Mn2-O5	80.1(2)
O6-Gd2-O3	63.28(17)	O10-Mn2-O5	167.5(2)
O7-Gd2-O3	108.40(16)	O1-Mn2-N2	162.3(3)
O17-Gd2-O5	92.59(17)	O4-Mn2-N2	80.3(2)
O19-Gd2-O5	151.28(17)	O7-Mn2-N2	100.1(2)
O6-Gd2-O5	108.28(16)	O10-Mn2-N2	90.2(2)
O7-Gd2-O5	60.88(16)	O5-Mn2-N2	83.2(2)
O3-Gd2-O5	72.44(16)	O22-Li1-O5	142.4(7)
O17-Gd2-N3	74.59(19)	O22-Li1-O22	93.2(6)
O19-Gd2-N3	79.97(19)	O5-Li1-O22	101.4(6)
O6-Gd2-N3	68.16(18)	O22-Li1-O3	115.7(6)
O7-Gd2-N3	68.07(18)	O5-Li1-O3	97.2(6)
O3-Gd2-N3	131.30(18)	O22-Li1-O3	96.3(5)
O5-Gd2-N3	128.75(17)	Mn2-O1-Mn1	148.1(3)
O15-Gd3-O16	152.0(2)	Mn2-O1-Gd1	105.5(2)
O15-Gd3-O18	87.9(2)	Mn1-O1-Gd1	104.0(2)
O16-Gd3-O18	98.3(2)		

Table 19: Selected bond angles for **25**.

Dy1-O14	2.310(6)	Dy3-O18	2.313(6)
Dy1-O12	2.318(5)	Dy3-O20	2.414(5)

Dy1-O1	2.324(5)	Dy3-N4	2.920(7)
Dy1-O20	2.380(5)	Mn1-O2	1.885(5)
Dy1-O11	2.399(5)	Mn1-O1	1.908(6)
Dy1-O4	2.404(5)	Mn1-O6	1.918(5)
Dy1-O9	2.410(5)	Mn1-O8	1.944(5)
Dy1-O2	2.416(6)	Mn1-O3	1.988(5)
Dy2-O17	2.305(5)	Mn1-N1	2.233(7)
Dy2-O19	2.333(6)	Mn2-O1	1.876(6)
Dy2-O6	2.364(5)	Mn2-O4	1.906(5)
Dy2-O7	2.378(6)	Mn2-O7	1.925(5)
Dy2-O3	2.392(5)	Mn2-O10	1.931(5)
Dy2-O5	2.505(5)	Mn2-O5	1.949(5)
Dy2-N3	2.646(6)	Mn2-N2	2.185(7)
Dy3-O15	2.244(6)	Li1-O5	1.904(14)
Dy3-O16	2.286(6)	Li1-O3	1.929(14)
Dy3-O13	2.298(6)		

Table 20: Selected bond lengths for 27.

O14-Dy1-O12	79.6(2)	O6-Dy2-N3	68.45(18)
O14-Dy1-O1	139.3(2)	O7-Dy2-N3	68.1(2)
O12-Dy1-O1	140.1(2)	O3-Dy2-N3	131.92(18)
O14-Dy1-O20	80.5(2)	O5-Dy2-N3	128.83(19)
O12-Dy1-O20	79.41(18)	O15-Dy3-O16	151.6(2)
O1-Dy1-O20	109.91(18)	O15-Dy3-O13	90.2(2)
O14-Dy1-O11	73.5(2)	O16-Dy3-O13	91.1(2)
O12-Dy1-O11	116.43(19)	O15-Dy3-O18	88.1(2)
O1-Dy1-O11	78.15(19)	O16-Dy3-O18	98.9(2)
O20-Dy1-O11	145.75(19)	O13-Dy3-O18	162.0(2)
O14-Dy1-O4	80.3(2)	O15-Dy3-O20	80.5(2)
O12-Dy1-O4	153.6(2)	O16-Dy3-O20	127.45(19)
O1-Dy1-O4	63.8(2)	O13-Dy3-O20	78.45(18)
O20-Dy1-O4	80.56(18)	O18-Dy3-O20	83.62(19)
O11-Dy1-O4	73.42(19)	O15-Dy3-N4	73.4(2)
O14-Dy1-O9	115.0(2)	O16-Dy3-N4	78.4(2)
O12-Dy1-O9	73.1(2)	O13-Dy3-N4	98.6(2)
O1-Dy1-O9	79.68(19)	O18-Dy3-N4	98.1(2)
O20-Dy1-O9	144.67(19)	O20-Dy3-N4	153.8(2)
O11-Dy1-O9	68.5(2)	O2-Mn1-O1	83.5(2)
O4-Dy1-O9	131.52(19)	O2-Mn1-O6	176.1(2)
O14-Dy1-O2	154.18(19)	O1-Mn1-O6	96.8(2)
O12-Dy1-O2	80.19(19)	O2-Mn1-O8	93.4(2)
O1-Dy1-O2	64.34(19)	O1-Mn1-O8	97.8(2)
O20-Dy1-O2	80.13(18)	O6-Mn1-O8	90.3(2)
O11-Dy1-O2	130.48(19)	O2-Mn1-O3	96.3(2)
O4-Dy1-O2	113.01(18)	O1-Mn1-O3	91.2(2)
O9-Dy1-O2	73.73(19)	O6-Mn1-O3	79.8(2)
O17-Dy2-O19	96.16(19)	O8-Mn1-O3	167.4(2)
O17-Dy2-O6	142.58(18)	O2-Mn1-N1	80.8(2)
O19-Dy2-O6	80.76(19)	O1-Mn2-O4	82.7(2)
O17-Dy2-O7	80.43(18)	O1-Mn2-O7	96.1(2)
O19-Dy2-O7	147.58(19)	O4-Mn2-O7	175.4(2)
O6-Dy2-O7	82.82(18)	O1-Mn2-O10	97.8(2)
O17-Dy2-O3	153.77(18)	O4-Mn2-O10	93.7(2)
O19-Dy2-O3	88.70(19)	O7-Mn2-O10	90.9(2)
O6-Dy2-O3	63.64(17)	O1-Mn2-O5	92.3(2)
O7-Dy2-O3	108.60(17)	O4-Mn2-O5	96.0(2)
O17-Dy2-O5	91.89(17)	O7-Mn2-O5	79.7(2)
O19-Dy2-O5	151.27(19)	O10-Mn2-O5	166.9(2)
O6-Dy2-O5	108.68(17)	O1-Mn2-N2	161.9(3)
O7-Dy2-O5	61.02(17)	O4-Mn2-N2	80.4(3)
O3-Dy2-O5	72.72(17)	O7-Mn2-N2	100.2(2)
O21-Dy2-O5	73.54(17)	O10-Mn2-N2	89.7(2)
O17-Dy2-N3	74.27(19)	O5-Mn2-N2	83.2(2)
O19-Dy2-N3	79.9(2)	O5-Li1-O3	98.6(6)

O1-Mn1-N1	162.1(2)	O3-Li1-O22	95.9(6)
O6-Mn1-N1	98.3(2)	Mn2-O1-Mn1	146.1(3)
O8-Mn1-N1	91.5(2)	Mn2-O1-Dy1	106.5(3)
O3-Mn1-N1	82.3(2)	Mn1-O1-Dy1	105.0(2)

Table 21: Selected bond angles for **27**.

Y1-O14	2.295(4)	Y3-O16	2.289(5)
Y1-O12	2.307(4)	Y3-O20	2.408(3)
Y1-O1	2.327(4)	Y3-N4	2.902(6)
Y1-O9	2.373(4)	Mn1-O2	1.892(4)
Y1-O11	2.392(4)	Mn1-O6	1.901(4)
Y1-O4	2.404(4)	Mn1-O1	1.925(4)
Y1-O2	2.406(4)	Mn1-O8	1.956(4)
Y2-O19	2.303(4)	Mn1-O3	1.978(4)
Y2-O17	2.325(4)	Mn1-N1	2.247(5)
Y2-O7	2.362(4)	Mn2-O1	1.861(4)
Y2-O6	2.385(4)	Mn2-O4	1.890(4)
Y2-O3	2.388(4)	Mn2-O7	1.914(4)
Y2-O20	2.405(4)	Mn2-O10	1.924(4)
Y2-O5	2.406(4)	Mn2-O5	1.945(4)
Y2-N3	2.624(5)	Mn2-N2	2.197(5)
Y3-O13	2.243(4)	Li1-O3	1.930(11)
Y3-O18	2.263(5)	Li1-O5	1.938(11)
Y3-O15	2.271(5)		

Table 22: Selected bond lengths for **29**.

O14-Y1-O12	79.39(15)	O13-Y3-O18	152.88(16)
O14-Y1-O1	139.57(15)	O13-Y3-O15	90.26(18)
O12-Y1-O1	140.21(15)	O18-Y3-O15	90.57(18)
O14-Y1-O9	114.94(15)	O13-Y3-O16	87.13(17)
O12-Y1-O9	72.85(15)	O18-Y3-O16	98.64(18)
O1-Y1-O9	80.27(14)	O15-Y3-O16	164.61(15)
O14-Y1-O11	74.00(15)	O13-Y3-O20	131.67(15)
O12-Y1-O11	116.76(15)	O18-Y3-O20	75.19(14)
O1-Y1-O11	78.15(14)	O15-Y3-O20	95.42(15)
O9-Y1-O11	68.78(15)	O16-Y3-O20	75.27(14)
O14-Y1-O4	80.33(14)	O13-Y3-N4	78.60(19)
O12-Y1-O4	153.37(14)	O18-Y3-N4	74.45(19)
O1-Y1-O4	63.81(14)	O15-Y3-N4	98.2(2)
O9-Y1-O4	132.03(14)	O16-Y3-N4	96.2(2)
O11-Y1-O4	73.36(14)	O20-Y3-N4	146.72(18)
O14-Y1-O2	153.68(15)	O2-Mn1-O6	174.03(17)
O12-Y1-O2	80.45(14)	O2-Mn1-O1	82.43(17)
O1-Y1-O2	64.18(14)	O6-Mn1-O1	95.43(17)
O9-Y1-O2	74.47(15)	O2-Mn1-O8	93.94(17)
O11-Y1-O2	130.83(14)	O6-Mn1-O8	91.90(17)
O4-Y1-O2	112.49(13)	O1-Mn1-O8	99.05(18)
O19-Y2-O17	97.84(15)	O2-Mn1-O3	94.69(17)
O19-Y2-O7	145.30(15)	O6-Mn1-O3	79.73(16)
O17-Y2-O7	79.44(15)	O1-Mn1-O3	90.71(17)
O19-Y2-O6	80.13(14)	O8-Mn1-O3	167.74(17)
O17-Y2-O6	144.58(14)	O2-Mn1-N1	81.80(18)
O7-Y2-O6	82.69(14)	O6-Mn1-N1	99.38(18)
O19-Y2-O3	88.29(14)	O1-Mn1-N1	161.98(18)
O17-Y2-O3	152.52(14)	O8-Mn1-N1	90.69(18)
O7-Y2-O3	110.11(13)	O3-Mn1-N1	81.95(17)
O6-Y2-O3	62.82(13)	O1-Mn2-O4	83.65(16)
O19-Y2-O20	76.91(14)	O1-Mn2-O7	96.43(17)
O17-Y2-O20	80.45(14)	O4-Mn2-O7	175.81(18)
O7-Y2-O20	135.27(14)	O1-Mn2-O10	97.86(18)
O6-Y2-O20	132.02(14)	O4-Mn2-O10	93.75(17)
O3-Y2-O20	74.88(12)	O7-Mn2-O10	90.39(17)
O19-Y2-O5	152.29(15)	O1-Mn2-O5	90.82(17)

O17-Y2-O5	89.52(14)	O4-Mn2-O5	96.38(17)
O7-Y2-O5	62.28(14)	O7-Mn2-O5	79.44(17)
O6-Y2-O5	108.72(13)	O10-Mn2-O5	167.33(16)
O3-Y2-O5	73.82(13)	O1-Mn2-N2	163.38(18)
O20-Y2-O5	78.06(13)	O4-Mn2-N2	81.75(17)
O19-Y2-N3	76.77(16)	O7-Mn2-N2	97.56(18)
O17-Y2-N3	76.99(15)	O10-Mn2-N2	90.98(19)
O7-Y2-N3	68.87(15)	O5-Mn2-N2	82.99(18)
O6-Y2-N3	68.08(14)	O3-Li1-O5	96.2(4)
O3-Y2-N3	130.41(14)	Mn2-O1-Mn1	147.1(2)
O20-Y2-N3	142.34(13)	Mn2-O1-Y1	105.99(18)
O5-Y2-N3	130.93(15)	Mn1-O1-Y1	104.70(17)

Table 23: Selected bond angles for **29**.

2.4.2 Magnetic properties of $[\text{Mn}^{3.5}_4\text{Ln}^{\text{III}}_6\text{Li}_2(\mu_3\text{-O})_2(\mu_5\text{-CO}_3)_2(\text{n-bdea})_6(\text{piv})_{12}(\text{NO}_3)_2]\cdot 3\text{CH}_3\text{CN}$

The dc magnetic susceptibility (χ) data for compounds **21-29** were collected in the 1.8–300 K temperature range at 1000 Oe as shown in Figure 60. For all compounds except **24** (Eu) and **29** (Y), the measured room temperature χT values (18.39, 18.53, 9.93, 59.06, 81.80 and 96.39 $\text{cm}^3\text{K}\cdot\text{mol}^{-1}$ for **21** (Pr), **22** (Nd), **23** (Sm), **25** (Gd), **26** (Tb), **27** (Dy), respectively) stand in good agreement with the values expected (19.36, 19.58, 10.29, 57.03, 80.61, and 94.82 $\text{cm}^3\text{K}\cdot\text{mol}^{-1}$) for isolated spin centres: two $S=2$ Mn^{III} , two $S=3/2$ Mn^{IV} and six Pr^{III} ($S=1$, $g=0.8$, $L=5$, $^3\text{H}_4$) in **21** or Nd^{III} ($S=3/2$, $g=0.73$, $L=6$, $^4\text{I}_{9/2}$) in **22** or Sm^{III} ($S=5/2$, $g=0.29$, $L=5$, $^6\text{H}_{5/2}$) in **23** or Gd^{III} ($S=7/2$, $g=2$, $L=0$, $^8\text{S}_{7/2}$) in **25** or Tb^{III} ($S=3$, $g=1.5$, $L=3$, $^7\text{F}_6$) in **26** or Dy^{III} ($S=5/2$, $g=1.33$, $L=5$, $^6\text{H}_{15/2}$) in **27** (Dy) metal ions (Table 24). In the case of compound **24** (Eu) the deviation of the χT value is due to the population of low lying excited states of the Eu ions. On lowering the temperature, the χT product of **27** (Dy) first gradually decreases to 88.92 $\text{cm}^3\text{K}\cdot\text{mol}^{-1}$ at around 12 K and then increases up to a value of 90.61 $\text{cm}^3\text{K}\cdot\text{mol}^{-1}$ at 4.5 K, before it experiences a sharp drop to 72.39 $\text{cm}^3\text{K}\cdot\text{mol}^{-1}$ at 1.8 K. Above 4.5 K, this behaviour is typically seen when antiferromagnetic (AF) interactions are dominant in a complex that possesses two types of spin that arrange in a ferrimagnetic manner. It should be noted that the thermal depopulation of the Dy^{III} Stark sublevels of the $^6\text{H}_{13/2}$ state might also be partially responsible for the decrease of χT above 17 K and the spin orbit interaction might be also responsible for the decrease of χT above 17 K. The behaviour of **25** (Gd) is similar to that of the formerly described compound except for the drop at the end. The χT product of **25** (Gd) gradually decreases continuously to a value of 51.62 $\text{cm}^3\text{K}\cdot\text{mol}^{-1}$ at 19 K before it increases abruptly to 61 $\text{cm}^3\text{K}\cdot\text{mol}^{-1}$ at 1.8 K. For **21** (Pr) the χT value constantly decreases on lowering the temperature to a value of 8.84 $\text{cm}^3\text{K}\cdot\text{mol}^{-1}$ at 1.8 K. This behaviour is the result of strongly antiferromagnetic interactions between the spin carriers. The temperature dependence of the dc susceptibility is similar for compounds **22** (Nd), **23** (Sm), **24** (Eu) and **29** (Y) (Figure 60) and thus the analysis of their experimental data is the same as for **21** (Pr). The non-compensation of the spin carriers in compound **21** (Pr), **22** (Nd), **25** (Gd), **26** (Tb) and **27** (Dy) suggests a large-spin ground state for these complexes. Moreover, the decrease of χT below 5 K for **27** (Dy) is likely

to be associated with intercomplex antiferromagnetic interactions and/or magnetic anisotropy.

For compound **29** (Y) the χT data were fit by considering two $S = 3/2$, $S = 2$. This model of a dimer of Mn^{IV} ($S=3/2$) and Mn^{III} ($S=2$) fits the data very well with 19% of Curie $S = 2$ spins impurities and 81% of the complex with $J/k_B = -19$ K and $g = 2$ (Figure 69). The Hamiltonian which was used is $H=-2J(S_1 \cdot S_2)$ with $S_1=3/2$; $S_2=2$.

This antiferromagnetic behaviour confirms that the Mn oxidation states are localised but disordered, and that superexchange, not double-exchange, is operating.

Field dependence of magnetisation (Figure 61 - Figure 68) performed at 1.8 K for **21-29** reveals a lack of saturation even at 7 T for **21-24** and **26-29** indicating that 1) excited states are probably populated in particular for the case with Eu, but also 2) that magnetic anisotropy might be present, as expected for $Mn^{III/IV}$ - and Ln^{III} -based (with $Ln^{III} = Pr^{III}$ and Tb^{III} Dy^{III}) compounds. This estimation is supported by the almost saturated magnetisation curve for **25** (Gd), where six isotropic Gd^{III} are present. However, the reduced magnetisation curves are not completely superimposed in the case of **25** (Gd), representing the anisotropy of the $Mn^{III/IV}$ ions. Caused by the large scale, the reduced magnetisation curves of **25** (Gd) seems to be superimposed and the question could appear, why in the case of Gd one see no anisotropy and in the case of Y one see anisotropy of the Mn ions. This is only due to the large scale differences

To probe the presence of slow relaxation in these molecular systems and thus the presence of SMM behaviour, ac susceptibility measurements were performed on these compounds. The measurements were made in the 1–1500 Hz frequency range and at temperatures between 1.8 and 10 K. Only **27** (Dy) displays frequency-dependent out-of-phase signals (Figure 70) suggesting that they behave as SMMs. Unfortunately, the ac data show an absence of any χ'' maximum above 1.8 K even at 1500 Hz. In SMMs with a relaxation partially influenced by quantum effects, the application of small dc field removes the state degeneracy and thus the possibility of quantum tunnelling in SMMs inducing a slowing down of the magnetization relaxation. In this case even the application of small dc fields does not slow down the relaxation of the magnetisation, suggesting a weak influence of quantum effects in the temperature range studied. Thus, it is not possible to estimate a barrier height. Compound **26** (Tb) also shows a frequency dependence of the ac signals, but with a ratio of 100:1 between χ' and χ'' signal it is indicative for a very fast relaxation.

Compound	χT expected for each Ln at RT (cm ³ Kmol ⁻¹)	Ground state of Ln ion	χT expected for each complex ^a (cm ³ Kmol ⁻¹)
Mn ₄ Pr ₆ (21)	1.60	³ H ₄	19.36
Mn ₄ Nd ₆ (22)	1.64	⁴ I _{9/2}	19.58
Mn ₄ Sm ₆ (23)	0.09	⁶ H _{5/2}	10.29
Mn ₄ Eu ₆ (24)	0	⁷ F ₀	9.75
Mn ₄ Gd ₆ (25)	7.88	⁸ S _{7/2}	57.03
Mn ₄ Tb ₆ (26)	11.82	⁷ F ₆	80.61
Mn ₄ Dy ₆ (27)	14.17	⁶ H _{15/2}	94.82
Mn ₄ Y ₆ (29)	0	-	9.75

Compound	χT measured at 300K per complex (cm ³ Kmol ⁻¹)	χT measured at 1.8 K per complex (cm ³ Kmol ⁻¹)	Magnetisation at 1.8 K and 7 T (μ_B)
Mn ₄ Pr ₆ (21)	18.39	8.84	11.60
Mn ₄ Nd ₆ (22)	18.53	7.71	13.91
Mn ₄ Sm ₆ (23)	9.93	2.45	4.72
Mn ₄ Eu ₆ (24)	16.66	1.94	4.00
Mn ₄ Gd ₆ (25)	59.06	61.00	44.23
Mn ₄ Tb ₆ (26)	81.80	61.04	32.39
Mn ₄ Dy ₆ (27)	96.39	72.39	38.57
Mn ₄ Y ₆ (29)	6.87	1.10	2.57

Table 24: Magnetic data summarised from the dc measurements. ^a taking into account a *g* factor of Mn metal ions of 2.

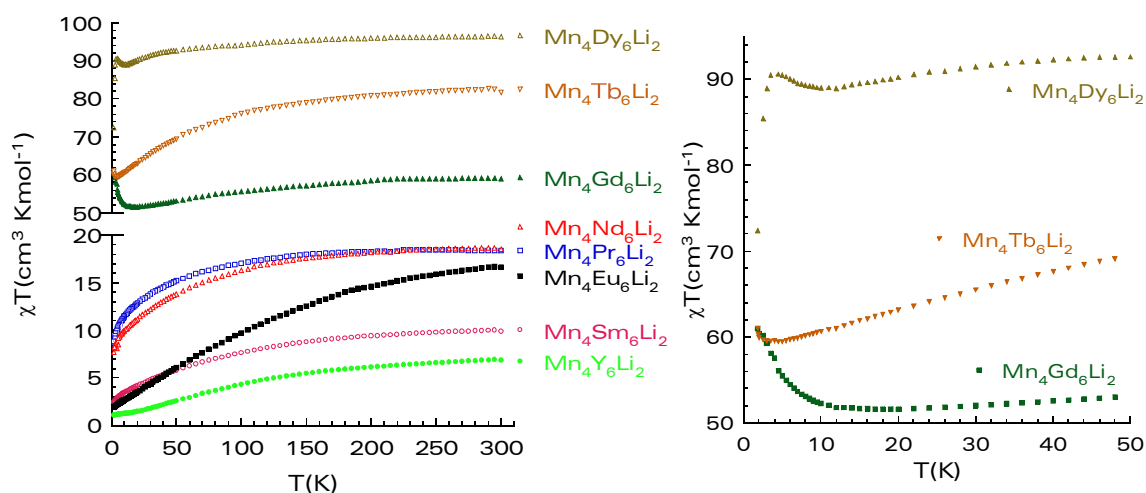


Figure 60: Temperature-dependence of the χT product under 0.1 T for compound **21- 29**.

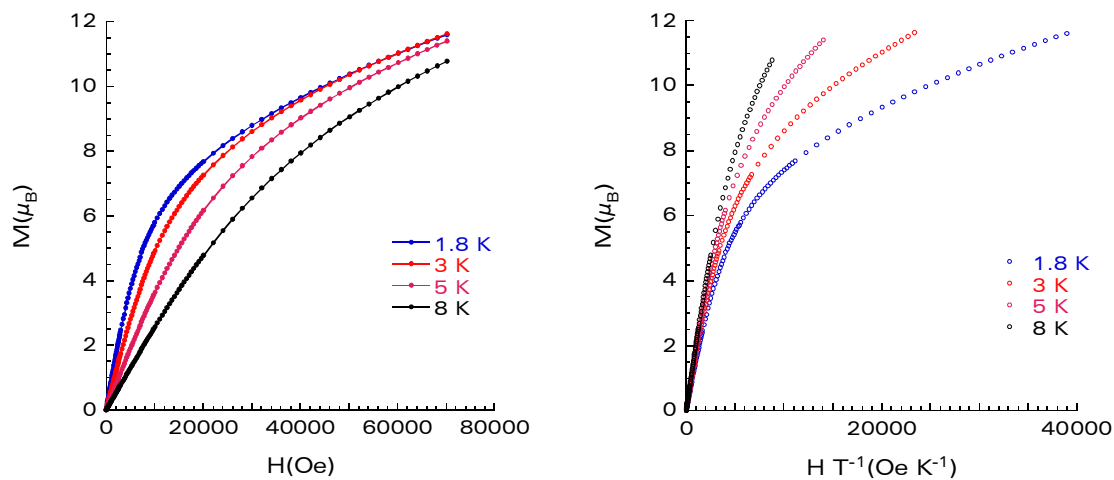


Figure 61: Plot of magnetisation M vs. H (left) and M vs. H/T (right) between 1.8 K and 8 K for **21**. The solid lines are to guide the eye.

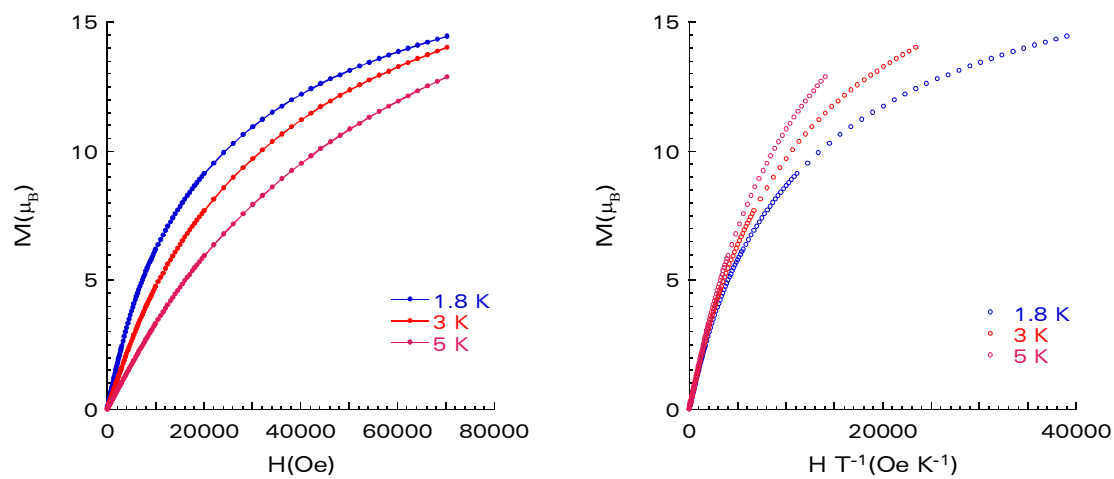


Figure 62: Plot of magnetisation M vs. H (left) and M vs. H/T (right) between 1.8 K and 5 K for **22**. Plots for 2 K were omitted, as the temperature problems occurred during the measurement. The solid lines are to guide the eye.

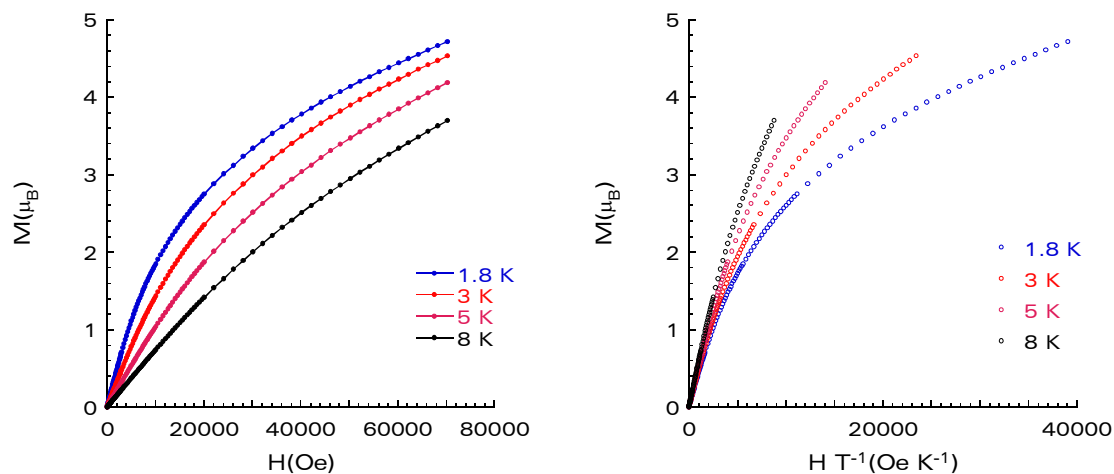


Figure 63: Plot of magnetisation M vs. H (left) and M vs. H/T (right) between 1.8 K and 8 K for **23**. The solid lines are to guide the eye.

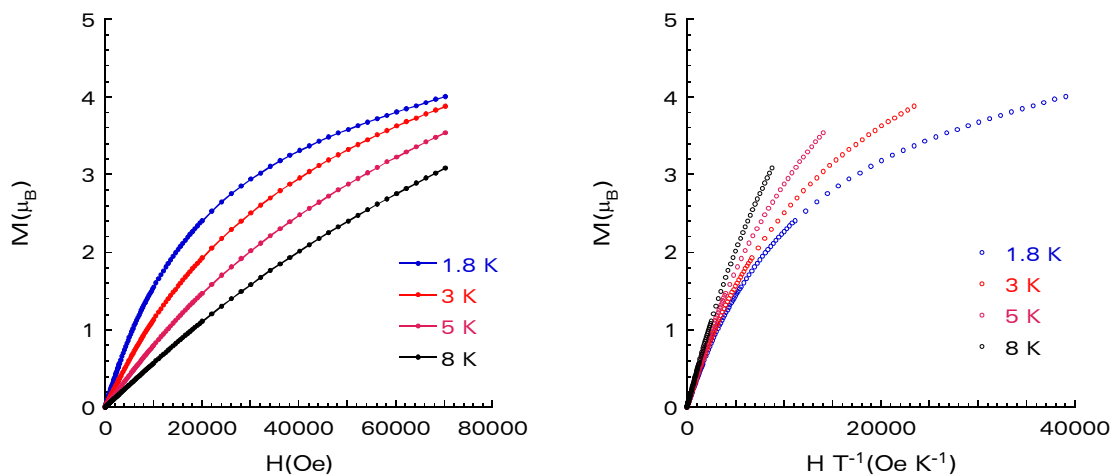


Figure 64: Plot of magnetisation M vs. H (left) and M vs. H/T (right) between 1.8 K and 8 K for **24**. The solid lines are to guide the eye.

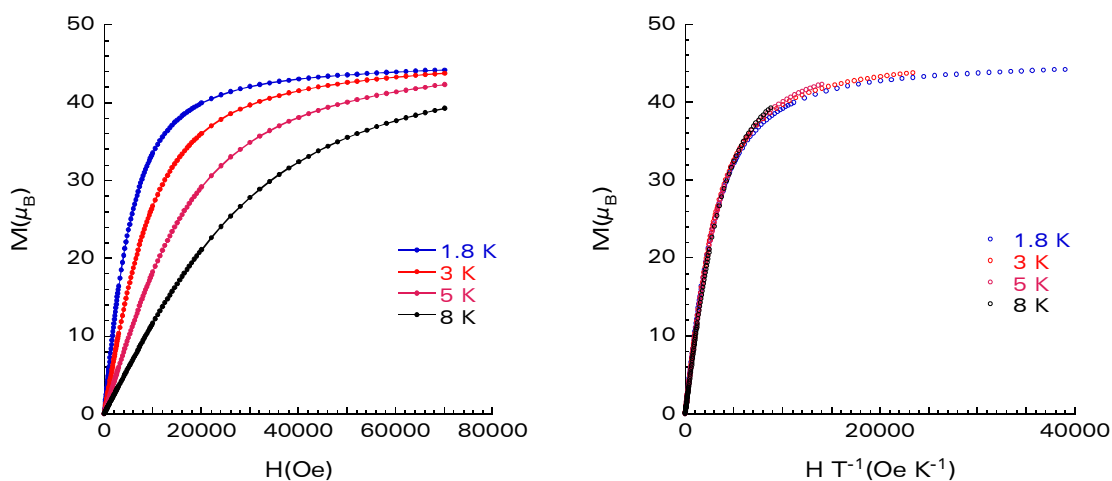


Figure 65: Plot of magnetisation M vs. H (left) and M vs. H/T (right) between 1.8 K and 8 K for **25**. The solid lines are to guide the eye.

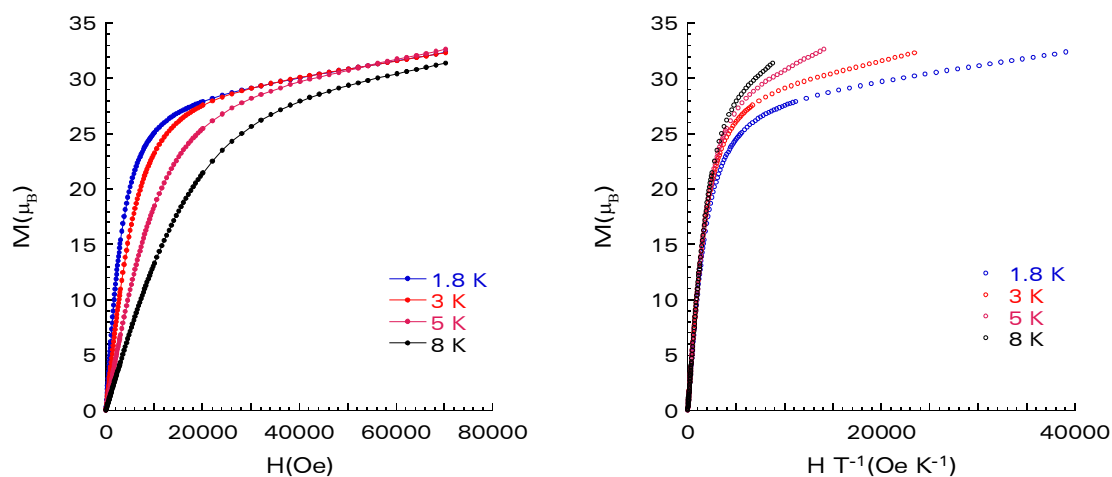


Figure 66: Plot of magnetisation M vs. H (left) and M vs. H/T (right) between 1.8 K and 8 K for **26**. The solid lines are to guide the eye.

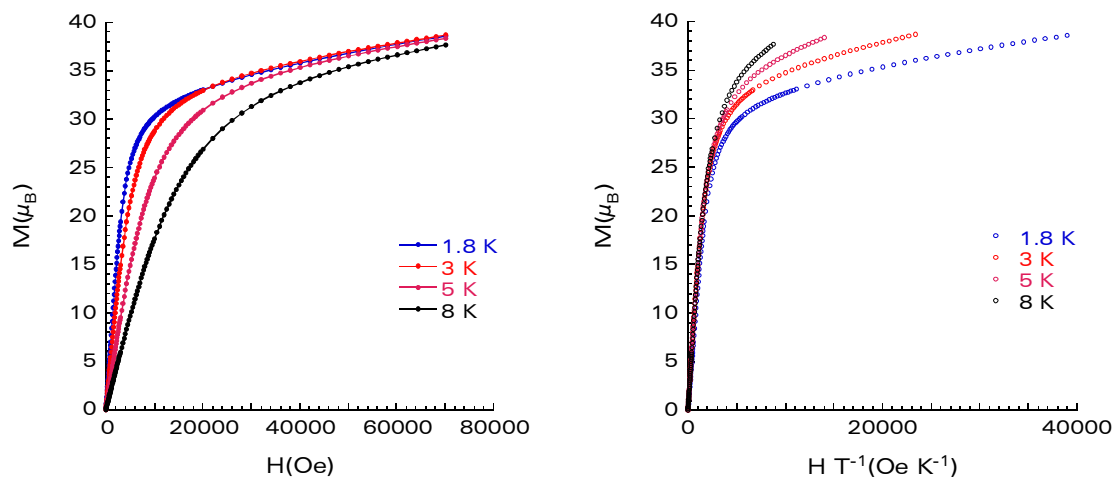


Figure 67: Plot of magnetisation M vs. H (left) and M vs. H/T (right) between 1.8 K and 8 K for **27**. The solid lines are to guide the eye.

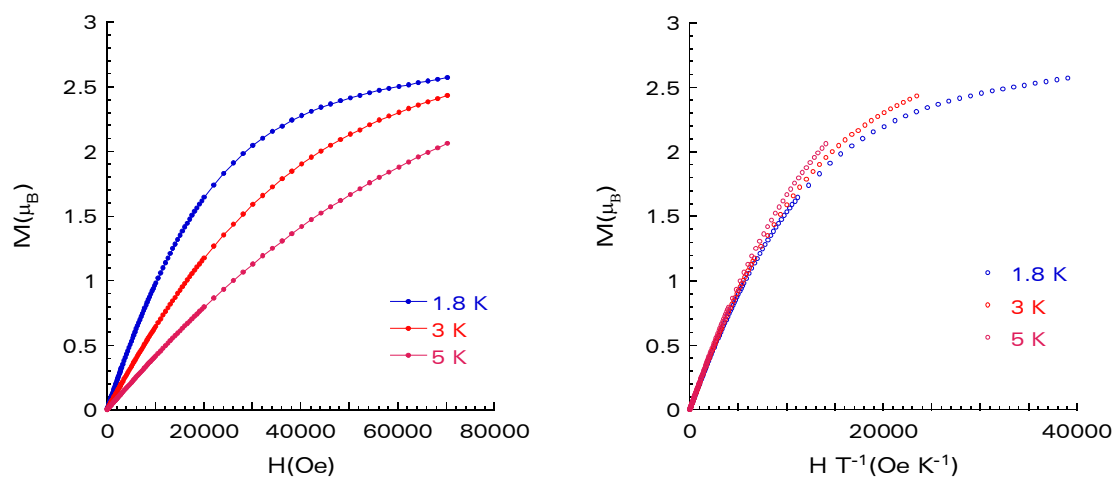


Figure 68: Plot of magnetisation M vs. H (left) and M vs. H/T (right) between 1.8 K and 5 K for **29**. The solid lines are to guide the eye.

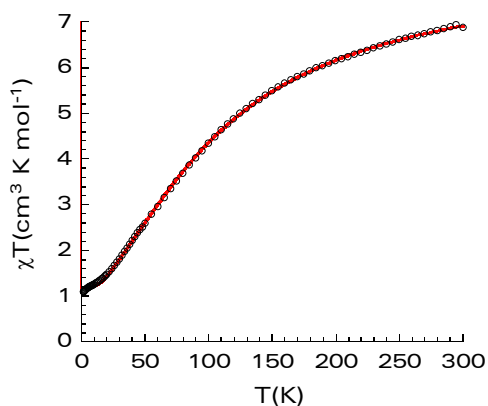


Figure 69: χT plot for compound **29**. The line represents the best-fit calculated values.

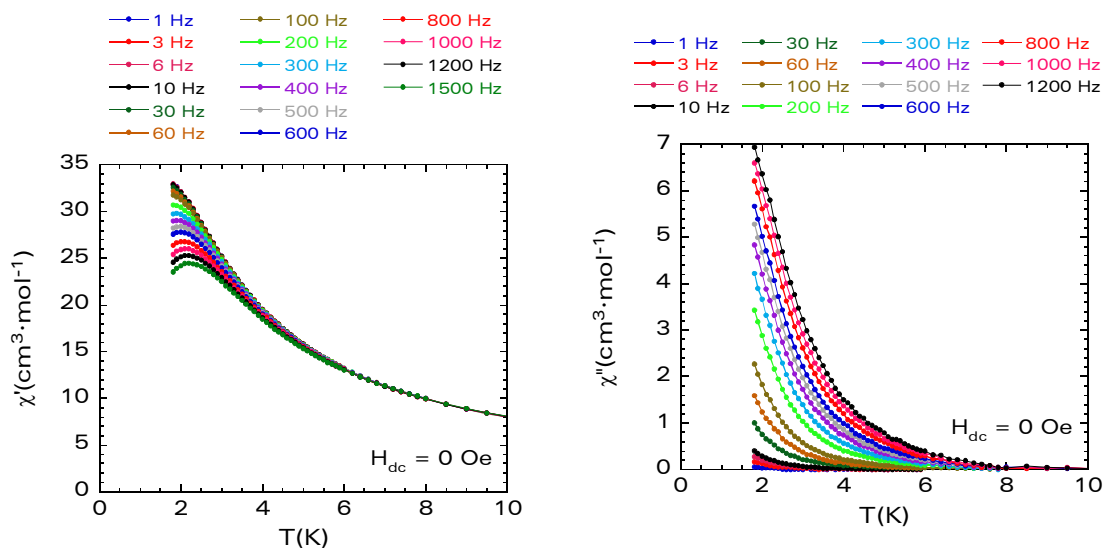


Figure 70: Temperature-dependent ac susceptibilities of **27** below 10 K under zero dc field at indicated frequencies.

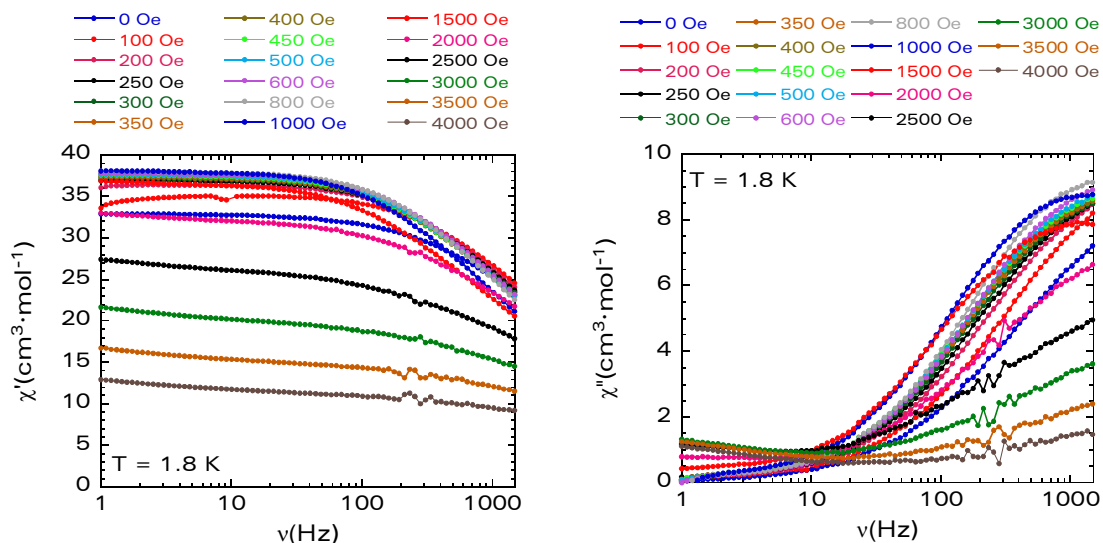


Figure 71: Frequency dependence of the in-phase (left) and out-of-phase (right) ac susceptibility as a function of the dc applied field and measured at 1.8 K for **27**.

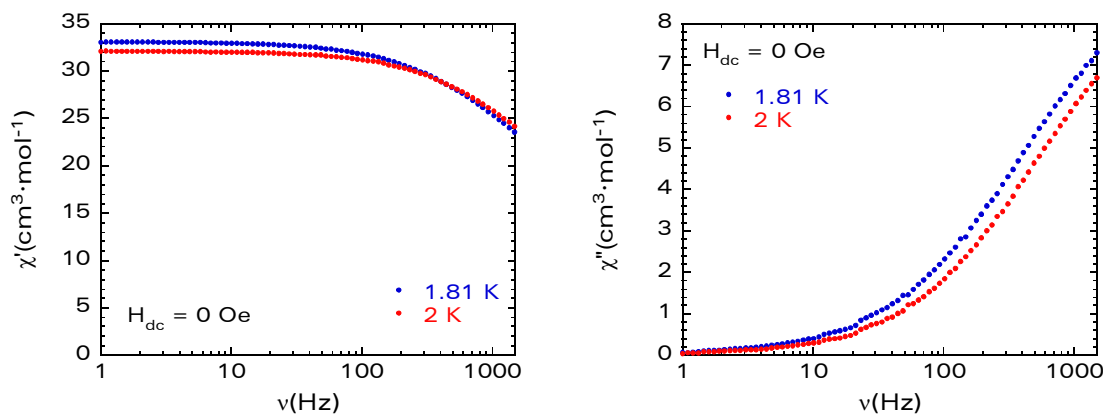


Figure 72: Frequency dependence in zero dc field of the in-phase (χ') and the out-of-phase (χ'') ac susceptibility component at 1.81 K and 2K for **27**.

2.4.3 Catalytic Oxidation properties of calcinated $[\text{Mn}^{\text{IV}}_2\text{Mn}^{\text{III}}_2\text{Dy}^{\text{III}}_6\text{Li}_2(\mu_3\text{-O})_2(\mu_5\text{-CO}_3)_2(\text{n-bdea})_6(\text{piv})_{12}(\text{NO}_3)_2] \cdot 3\text{CH}_3\text{CN}$

Diesel engines exhibit the highest efficiency for automobiles as well as for ships and work machines. As a consequence, the low fuel consumption leads to reduced emissions of the greenhouse gas CO_2 . However, a serious constraint of diesel engines is the emission of air pollutants, including hydrocarbons (HC), carbon monoxide (CO), nitrogen oxides (NO_x), and soot. Several after-treatment techniques for removing these pollutants from the oxygen-rich diesel exhaust have been developed (Zelenka, 1996: 3ff; Twigg, 2007: 2ff). In order to remove these components from diesel exhaust the simultaneous catalytic conversion of NO_x and soot into N_2 and CO_2 might be a suitable procedure (Teraoka 1995: L181ff; Kureti, 2003: 281ff).

Within this thesis a qualitative experiment has shown that the polynuclear compound **27** is a precursor for a mixed-metal oxide system that acts as a catalyst for the oxidation of CO to CO_2 .

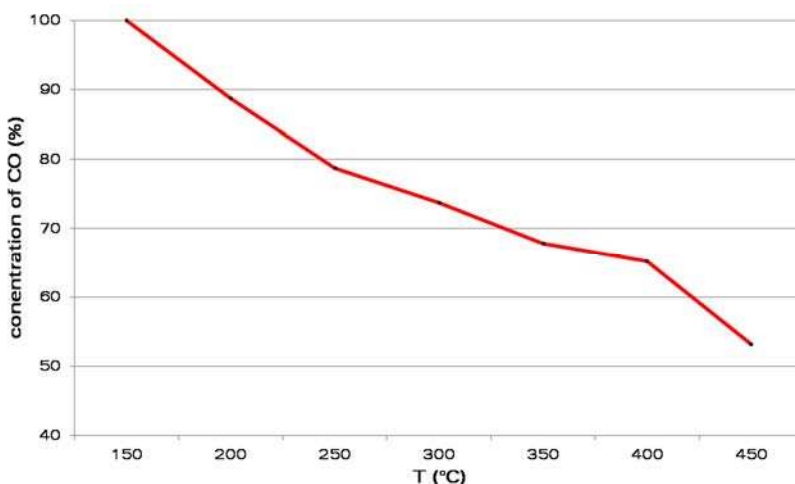


Figure 73: Temperature dependent catalytic oxidation of CO to CO_2 by calcinated **27**.

About one gramme of compound **27** was calcinated in air at 600°C for 2 hours to remove all organic components. The resulting oxide of the compound weighed 320mg and was charged into the quartz glass tube reactor of 6 mm diameter and 50 cm length fixed with quartz wool. The device was then heated to 450°C and the reaction mixture (5 vol% O_2 , 500 ppm CO, remainder N_2) was added at a flow rate of 500 ml/min. The temperature was then decreased in steps of 50 K and the concentration of CO was measured continuously with a MultiGas™ 2030 FT-IR Continuous Gas Analyser from MKS Instruments.

The graph shows, that at 450°C about 47% of the CO gas is converted to CO_2 .

From the present study it was concluded that in presence of the oxide catalyst derived from **27** the CO conversion is substantially enhanced, leading to the production of CO_2 . The mechanism of the CO reaction includes the adsorption and desorption of CO and CO_2 .

It should be noted, that the catalytic capability is to some extent dependent on the particle size (Rivoirard, 2003: 622ff; Cherkezova-Zheleva, 2010) and moreover from the quantity of the used catalyst. Therefore the adsorption of dissolved **27** on a substrate such as zeolite, followed by pyrolysis, could lead to an improved catalytic behaviour.

For the elucidation of the catalytic capability of this oxide material and for comparison, further experiments with simulated mixtures of Mn_2O_3 , Dy_2O_3 and Li_2O are currently in progress.

3 Structure and magnetic properties of iron-lanthanide aggregates

3.1 Structure and magnetic properties of hexanuclear complexes

The one pot reaction of $\{\text{Fe}_3\}$ (**4**), $\text{Pr}(\text{NO}_3)_3$ and *n*-butyldiethanolamine (*n*-bdea H_2) in acetonitrile yielded, after slow diffusion of acetone into the reaction mixture, well-formed brown crystals of **30** with the general formula $\text{Fe}^{\text{III}}_4\text{Ln}^{\text{III}}_2(\mu_4\text{-O})_2(\text{n-bdea})_4(\text{piv})_4(\text{NO}_3)_2(\text{H}_2\text{O})_2\cdot\text{MeCN}$ where Ln = Pr (**30**), Nd (**31**), Sm (**32**), Eu (**33**), Gd (**34**) and Y (**35**). The aggregates **30-35** were all obtained in the same manner, are isomorphous and differ only in the nature of the lanthanides. The structure of the Fe_4Pr_2 complex **30** will therefore be described in detail as a representative. Magnetic studies show that the three compounds show a similar temperature dependence of their magnetic susceptibilities over the range 1.8–300 K. The observed decrease of χT with decreasing temperature for all three compounds is most probably the result of antiferromagnetic interactions between Fe–Ln centres. Mössbauer investigations show that there is no residual paramagnetism in the system coming from the Fe_6 .

3.1.1 Structure of $[\text{Fe}^{\text{III}}_4\text{Pr}^{\text{III}}_2(\mu_4\text{-O})_2(\text{n-bdea})_4(\text{piv})_4(\text{NO}_3)_2(\text{H}_2\text{O})_2]\cdot\text{MeCN}$ (**30**)

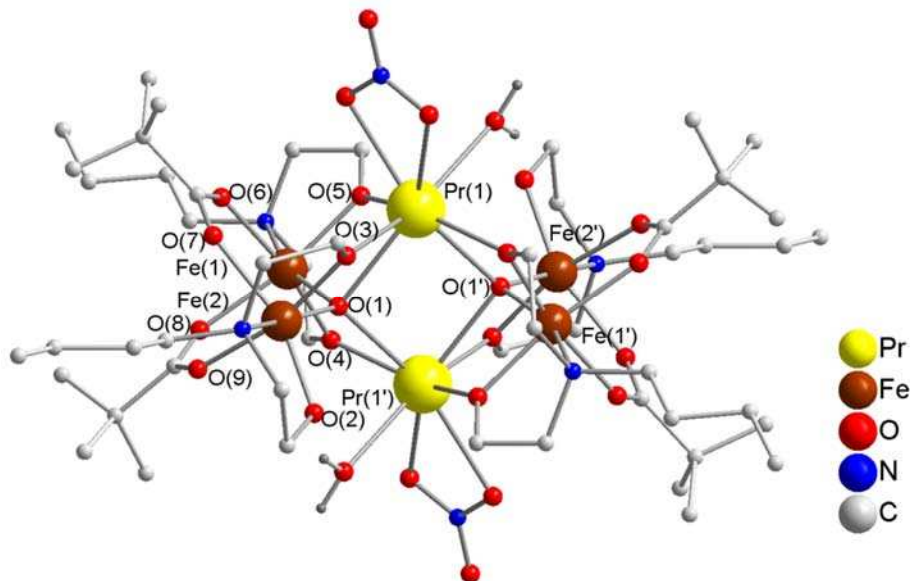


Figure 74: Molecular structure of the $[\text{Fe}^{\text{III}}_4\text{Pr}^{\text{III}}_2(\mu_4\text{-O})_2(\text{n-bdea})_4(\text{piv})_4(\text{NO}_3)_2(\text{H}_2\text{O})_2]\cdot\text{MeCN}$ aggregate in **30**. Organic hydrogen atoms are omitted for clarity.

Single-crystal X-ray diffraction studies show that compound **30** (Figure 105) crystallises in the triclinic space group $P\bar{1}$ with $Z=1$. Selected metric parameters and bond distances and angles for compounds **30-35** are summarised in Table 26-Table 35. The metal oxidation states (Fe^{III} , Ln^{III}) and the deprotonation levels of O^{2-} and *n*-bdea $^{2-}$ ions were established by charge considerations and bond valence sum calculations (Liu, 1993: 4102ff).

It should be noted that although all the compounds in this series crystallise isostructural, the other members of the series have one molecule of acetone in the lattice, instead of the MeCN in **30**.

The molecule contains four Fe^{III} and two Pr^{III} ions forming a distorted bicapped parallelogram, which can also be thought of as a distorted octahedron. In this, the four Fe^{III} ions define the parallelogram with side lengths of 3.2145 Å and 5.2656 Å and angles of 81° (Fe(1)-Fe(2)-Fe(1')) and 99° and the two Pr^{III} are at the points of the shortened and distorted octahedron (Figure 75 left) displaced 1.9173 Å above and below the Fe₄ plane.

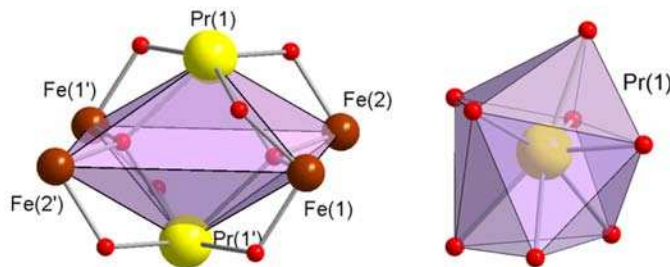


Figure 75: The distorted octahedral coordination polyhedron of the core (left) and dodecahedral environment around Pr^{III}.

All the metal ions are held together by two μ_4 -bridging oxygen atoms O(1) and O(1'). The octa-coordinate environment of Pr^{III} is completed by three μ_2 -alkoxy bridges coming from the doubly deprotonated n-butyldiethanolamine (n-bdea) ligands, each connecting the lanthanide with another iron ion and with Pr-O distances in the range 2.370(3) - 2.573(4) Å, one water molecule and a chelating nitrate to give the distorted dodecahedral geometry of Pr^{III} (Figure 75 right). Each Fe^{III} is chelated by a doubly deprotonated n-bdea²⁻ ligand with the nitrogen *trans* to the (μ_4 -O) ligand in the interior of the metal core and Fe-O bond lengths between 1.928(3) and 2.005(4) Å. The n-bdea²⁻ ligands bridge in two different modes. While the Fe(1) chelating ligand possess two μ_2 -bridging oxygen ions, Fe(2) is coordinated in a $\eta^2:\eta^1:\eta^1:\mu_2$ mode and thus only one alkoxy arm is μ_2 -bridging. The Fe^{III} ions are six-coordinate with typical octahedral geometries. The coordination shell of the aggregate is completed by four pivalate ligands that each form a *syn,syn*-bridge between the adjacent Fe centres (Fe(1) and (Fe(2))). The pivalate ligands are alternately above and below the Fe₄-rectangle with an angle to this plane of circa 45°.

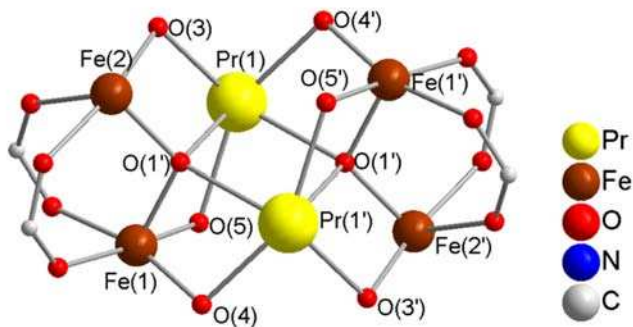


Figure 76: Core structure of compound **30**.

Compounds **30-35** crystallise isomorphous and differ only slightly in the respective Ln-O bond distances, which decrease across the series in line with the expected contraction of the lanthanide ionic radii. Furthermore, for all structures the packing (Figure 77) is such that there are no inter-cluster interactions or pathways which could lead to long-range magnetic ordering effects and it is thus reasonable to assign the behaviour observed in the magnetic studies as being of molecular origin.

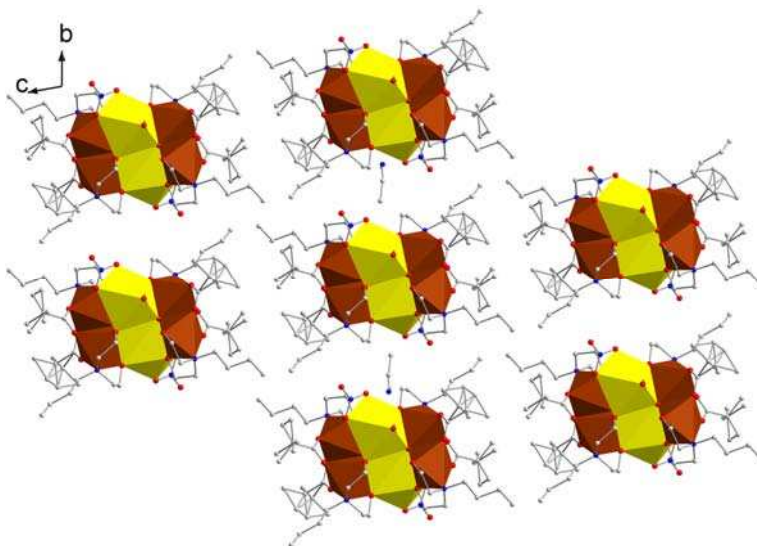


Figure 77: View along the a-axis with the cluster aggregates shown as polyhedral representations. H atoms are omitted for clarity.

Performing the reaction in acetonitrile and subsequent slow evaporation gives mainly a yellow crystalline product, which was not suitable for single crystal X-ray diffraction and only a small amount of brown crystals of **30**. With slow diffusion of acetone, it was possible to obtain solely the brown crystals of **30** suitable for single crystal X-ray diffraction. Moreover it was also possible to obtain pure crystals using methanol as the slow diffusion solvent, although the appearance of the crystals differed from that of the acetone product (Figure 78).

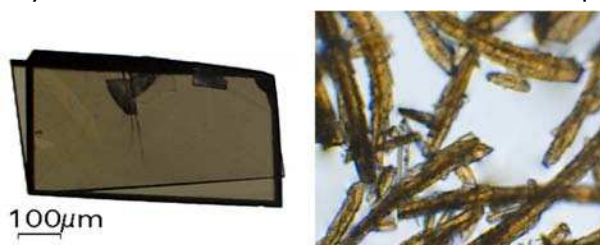


Figure 78: Enlarged view of the crystals obtained from slow diffusion with acetone (left) and methanol (right).

These were not suitable for single-crystal analysis. X-ray powder diffraction (Figure 79) confirmed that the crystals from acetone and methanol have different crystal structures. Refinement of the powder diffraction data affirmed that both compounds exhibit different unit cell parameters:

	Compound 30 (acetone)	unknown compound (MeOH)
a [Å]	10.3828(10)	11.2446(25)
b [Å]	11.5447(11)	9.9441(21)
c [Å]	17.3466(17)	17.3436(50)
α [°]	97.505(11)	101.610(19)
β [°]	106.252(11)	102.772(18)
γ [°]	97.510(11)	95.840(53)
V [Å ³]	1948.3(3)	1830.79(84)

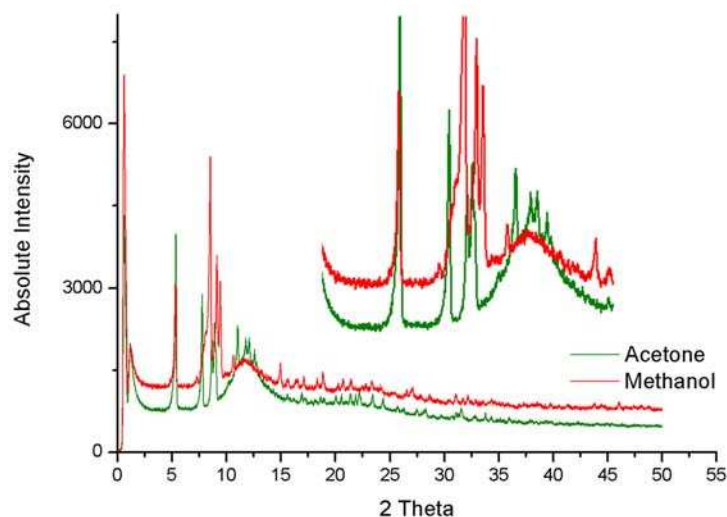


Figure 79: X-ray powder diffraction pattern of Fe_4Pr_2 obtained by slow diffusion of acetone (green) and methanol (red).

The reaction that led to complex **30** was also performed using **7** in place of **6** as starting material. FT-IR spectra (Figure 80) of the products were highly similar, suggesting that the same complex had formed. Probably the starting material **7** decomposes during the reaction to reform **6**, leading to the formation of the previously described compound **30**.

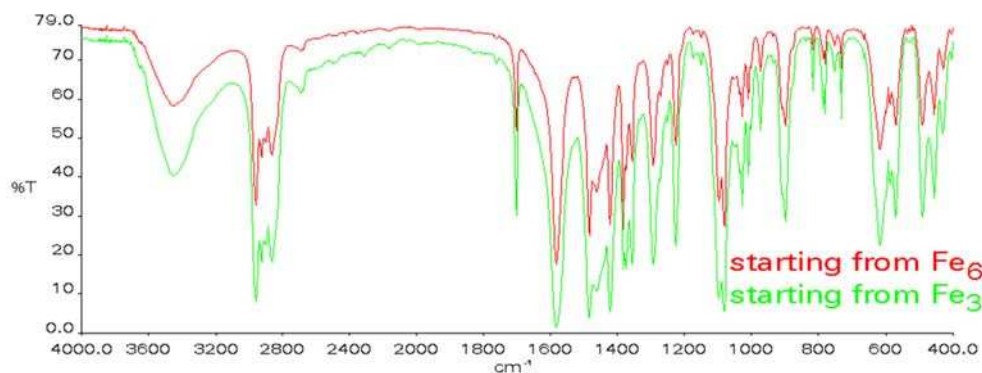


Figure 80: Comparison of the IR of **30** (green) made with **6** as starting material and the product obtained from **7** as precursor compound (red).

Bond Valence Sum Calculations (Brown, 1985: 244ff):

respective atom	Fe(1)	Fe(2)
est. oxidation state		
Fe ^{II}	2.47	2.44
Fe ^{III}	2.93	2.89
calc. oxidation state	Fe ^{III}	Fe ^{III}

Compound	a	b	c	V
Fe ₄ Pr ₂ (30)	10.3828(10)	11.5447(11)	17.3466(17)	1948.3(3)
Fe ₄ Nd ₂ (31)	10.3419(8)	11.6491(9)	17.3102(1)	1969(2)
Fe ₄ Sm ₂ (32)	10.2621(10)	11.6226(11)	17.2553(17)	1943.1(3)
Fe ₄ Eu ₂ (33)	10.2636(10)	11.6162(12)	17.2433(19)	1942.8(3)
Fe ₄ Gd ₂ (34)	10.2927(9)	11.5720(9)	17.2195(14)	1937.9(3)
Fe ₄ Y ₂ (35)	10.2665(10)	11.5663(11)	17.1509(15)	1924.2(3)

Compound	α	β	γ
Fe ₄ Pr ₂ (30)	97.505(11)	106.252(11)	97.510(11)
Fe ₄ Nd ₂ (31)	98.724(9)	105.332(9)	95.201(9)
Fe ₄ Sm ₂ (32)	98.746(11)	105.378(11)	95.125(11)
Fe ₄ Eu ₂ (33)	98.697(12)	105.296(12)	94.982(12)
Fe ₄ Gd ₂ (34)	98.481(10)	105.349(10)	95.225(10)
Fe ₄ Y ₂ (35)	98.376(11)	105.369(11)	95.339(11)

Table 25: Summary of selected cell parameters.

Pr1-O4	2.370(3)	Fe1-O8	2.066(4)
Pr1-O5	2.402(4)	Fe1-N2	2.233(4)
Pr1-O3	2.427(4)	Fe2-O1	1.928(3)
Pr1-O1	2.505(4)	Fe2-O2	1.937(4)
Pr1-O1	2.573(4)	Fe2-O3	2.000(4)
Fe1-O1	1.933(3)	Fe2-O7	2.127(4)
Fe1-O4	1.988(4)	Fe2-N1	2.269(4)
Fe1-O5	2.005(4)	O1-Pr1	2.573(4)
Fe1-O6	2.055(4)		

Table 26: Selected bond lengths for **30**.

O4-Pr1-O5	150.06(14)	O4-Fe1-N2	81.29(16)
O4-Pr1-O3	82.09(14)	O5-Fe1-N2	81.37(15)
O5-Pr1-O3	117.11(13)	O6-Fe1-N2	88.52(17)
O4-Pr1-O1	108.81(13)	O8-Fe1-N2	95.42(17)
O5-Pr1-O1	65.04(11)	O1-Fe2-O2	97.48(16)
O3-Pr1-O1	65.29(13)	O1-Fe2-O3	85.27(16)
O4-Pr1-O1	66.54(12)	O2-Fe2-O3	106.1(2)
O5-Pr1-O1	83.60(12)	O1-Fe2-O7	101.07(15)
O3-Pr1-O1	120.67(13)	O2-Fe2-O7	158.92(18)
O1-Pr1-O1	78.63(12)	O3-Fe2-O7	85.4(2)
O13-Pr1-O1	78.10(12)	O9-Fe2-O7	80.7(2)
O1-Fe1-O4	87.73(15)	O1-Fe2-N1	163.85(16)
O1-Fe1-O5	84.15(14)	O2-Fe2-N1	80.56(17)
O4-Fe1-O5	100.87(17)	O3-Fe2-N1	79.96(16)
O1-Fe1-O6	104.98(16)	O7-Fe2-N1	84.30(16)
O4-Fe1-O6	165.35(18)	Fe2-O1-Fe1	112.74(17)
O5-Fe1-O6	87.87(19)	Fe2-O1-Pr1	103.77(15)
O1-Fe1-O8	101.00(15)	Fe1-O1-Pr1	102.88(14)
O4-Fe1-O8	87.5(2)	Fe2-O1-Pr1	133.29(16)
O5-Fe1-O8	170.45(19)	Fe1-O1-Pr1	98.92(14)

4 STRUCTURE AND MAGNETIC PROPERTIES OF COBALT-LANTHANIDE AGGREGATES

O6-Fe1-O8	83.0(2)	Pr1-O1-Pr1	101.38(12)
O1-Fe1-N2	159.81(15)		

Table 27: Selected bond angles for **30**.

Sm1-O4	2.340(4)	Fe1-O6	2.062(5)
Sm1-O3	2.387(4)	Fe1-O8	2.078(5)
Sm1-O5	2.397(4)	Fe1-N2	2.228(5)
Sm1-O1	2.452(4)	Fe2-O1	1.937(4)
Sm1-O1	2.523(4)	Fe2-O2	1.946(5)
Sm1-N3	2.980(6)	Fe2-O3	2.006(5)
Fe1-O1	1.933(4)	Fe2-O7	2.140(5)
Fe1-O4	1.994(5)	Fe2-N1	2.257(5)
Fe1-O5	2.000(5)	O1-Sm1	2.523(4)

Table 28: Selected bond lengths for **32**.

O4-Sm1-O3	81.70(18)	O5-Fe1-O8	171.2(2)
O4-Sm1-O5	150.61(16)	O6-Fe1-O8	83.6(2)
O3-Sm1-O5	118.81(16)	O1-Fe1-N2	158.90(18)
O4-Sm1-O1	110.52(16)	O4-Fe1-N2	81.37(19)
O3-Sm1-O1	66.86(15)	O5-Fe1-N2	81.36(18)
O5-Sm1-O1	65.26(15)	O6-Fe1-N2	88.2(2)
O4-Sm1-O1	67.71(14)	O8-Fe1-N2	95.5(2)
O3-Sm1-O1	121.35(17)	O1-Fe2-O2	96.8(2)
O5-Sm1-O1	83.17(14)	O1-Fe2-O3	85.07(17)
O1-Sm1-O1	78.54(14)	O2-Fe2-O3	106.4(2)
O4-Sm1-N3	102.33(17)	O1-Fe2-O7	101.13(19)
O3-Sm1-N3	78.97(18)	O2-Fe2-O7	159.7(2)
O5-Sm1-N3	102.24(17)	O3-Fe2-O7	84.8(2)
O1-Sm1-N3	127.33(16)	O1-Fe2-N1	164.07(18)
O1-Sm1-N3	153.65(16)	O2-Fe2-N1	81.0(2)
O1-Fe1-O4	87.39(17)	O3-Fe2-N1	80.46(19)
O1-Fe1-O5	83.31(17)	O7-Fe2-N1	84.2(2)
O4-Fe1-O5	100.8(2)	Fe1-O1-Fe2	111.59(19)
O1-Fe1-O6	105.70(18)	Fe1-O1-Sm1	103.81(18)
O4-Fe1-O6	165.06(19)	Fe2-O1-Sm1	103.08(16)
O5-Fe1-O6	88.1(2)	Fe1-O1-Sm1	98.82(16)
O1-Fe1-O8	101.66(19)	Fe2-O1-Sm1	134.5(2)
O4-Fe1-O8	86.8(2)	Sm1-O1-Sm1	101.46(14)

Table 29: Selected bond angles for **32**.

Eu1-O4	2.330(7)	Fe1-O8	2.073(8)
Eu1-O3	2.386(8)	Fe1-N2	2.228(10)
Eu1-O5	2.390(6)	Fe2-O1	1.939(7)
Eu1-O1	2.435(7)	Fe2-O2	1.960(9)
Eu1-O1	2.521(7)	Fe2-O3	1.999(8)
Eu1-N3	2.959(10)	Fe2-O9	2.079(8)
Fe1-O1	1.932(7)	Fe2-O7	2.138(9)
Fe1-O4	1.990(8)	Fe2-N1	2.267(9)
Fe1-O5	2.012(8)	O1-Eu1	2.521(7)
Fe1-O6	2.060(8)		

Table 30: Selected bond lengths for **33**.

O4-Eu1-O3	81.6(3)	O4-Fe1-O8	87.1(3)
O4-Eu1-O5	150.9(3)	O5-Fe1-O8	171.1(3)
O3-Eu1-O5	118.8(3)	O6-Fe1-O8	83.5(4)
O4-Eu1-O1	110.3(3)	O1-Fe1-N2	158.9(3)
O3-Eu1-O1	66.9(2)	O4-Fe1-N2	81.1(3)
O5-Eu1-O1	65.5(3)	O5-Fe1-N2	81.9(3)
O13-Eu1-O1	140.0(3)	O6-Fe1-N2	88.4(4)
O4-Eu1-O1	67.8(2)	O8-Fe1-N2	95.0(3)
O3-Eu1-O1	121.4(3)	O1-Fe2-O2	97.2(3)
O5-Eu1-O1	83.3(2)	O1-Fe2-O3	84.9(3)
O13-Eu1-O1	78.9(3)	O2-Fe2-O3	106.7(4)

4 STRUCTURE AND MAGNETIC PROPERTIES OF COBALT-LANTHANIDE AGGREGATES

O1-Eu1-O1	78.3(2)	O1-Fe2-O7	101.4(3)
O4-Eu1-N3	102.5(3)	O2-Fe2-O7	158.9(4)
O3-Eu1-N3	78.3(3)	O3-Fe2-O7	84.9(4)
O5-Eu1-N3	102.0(3)	O9-Fe2-O7	81.0(4)
O1-Eu1-N3	126.8(3)	O1-Fe2-N1	164.0(3)
O11-Eu1-N3	25.8(3)	O2-Fe2-N1	80.8(4)
O1-Eu1-N3	154.5(3)	O3-Fe2-N1	80.5(3)
O10-Eu1-N3	25.6(3)	O9-Fe2-N1	96.0(3)
O1-Fe1-O4	87.5(3)	O7-Fe2-N1	84.0(3)
O1-Fe1-O5	82.8(3)	Fe1-O1-Fe2	111.3(3)
O4-Fe1-O5	100.5(3)	Fe1-O1-Eu1	104.4(3)
O1-Fe1-O6	105.6(3)	Fe2-O1-Eu1	103.3(3)
O4-Fe1-O6	165.3(3)	Fe1-O1-Eu1	98.7(3)
O5-Fe1-O6	88.1(3)	Fe2-O1-Eu1	134.0(4)
O1-Fe1-O8	102.2(3)	Eu1-O1-Eu1	101.7(2)

Table 31: Selected bond angles for 33.

Gd1-O4	2.326(4)	Fe1-O8	2.075(5)
Gd1-O3	2.365(5)	Fe1-N2	2.218(5)
Gd1-O5	2.366(4)	Fe2-O1	1.933(4)
Gd1-O1	2.423(4)	Fe2-O2	1.946(5)
Gd1-O1	2.495(4)	Fe2-O3	1.993(5)
Fe1-O1	1.939(4)	Fe2-O7	2.137(5)
Fe1-O4	1.982(5)	Fe2-N1	2.254(6)
Fe1-O5	1.996(4)	O1-Gd1	2.495(4)
Fe1-O6	2.050(5)		

Table 32: Selected bond lengths for 34.

O4-Gd1-O3	81.79(18)	O4-Fe1-N2	81.3(2)
O4-Gd1-O5	151.27(17)	O5-Fe1-N2	81.46(19)
O3-Gd1-O5	118.56(16)	O6-Fe1-N2	88.3(2)
O4-Gd1-O1	109.93(15)	O8-Fe1-N2	95.7(2)
O3-Gd1-O1	66.83(15)	O1-Fe2-O2	97.06(19)
O5-Gd1-O1	66.03(14)	O1-Fe2-O3	84.39(18)
O4-Gd1-O1	68.01(15)	O2-Fe2-O3	107.1(2)
O3-Gd1-O1	121.70(16)	O1-Fe2-O7	101.59(18)
O5-Gd1-O1	83.56(14)	O2-Fe2-O7	158.9(2)
O1-Gd1-O1	78.10(14)	O3-Fe2-O7	84.7(2)
O1-Fe1-O4	86.99(17)	O9-Fe2-O7	80.3(2)
O1-Fe1-O5	83.06(16)	O1-Fe2-N1	163.36(18)
O4-Fe1-O5	101.3(2)	O2-Fe2-N1	80.7(2)
O1-Fe1-O6	106.21(19)	O3-Fe2-N1	80.6(2)
O4-Fe1-O6	164.9(2)	O7-Fe2-N1	84.1(2)
O5-Fe1-O6	87.8(2)	Fe2-O1-Fe1	110.90(19)
O1-Fe1-O8	101.83(18)	Fe2-O1-Gd1	103.47(17)
O4-Fe1-O8	86.9(2)	Fe1-O1-Gd1	103.47(16)
O5-Fe1-O8	170.8(2)	Fe2-O1-Gd1	134.51(18)
O6-Fe1-O8	83.4(2)	Fe1-O1-Gd1	98.92(17)
O1-Fe1-N2	158.33(19)	Gd1-O1-Gd1	101.90(14)

Table 33: Selected bond angles for 34.

Y1-O4	2.285(5)	Fe1-O6	2.059(5)
Y1-O5	2.328(4)	Fe1-O8	2.065(5)
Y1-O3	2.345(5)	Fe1-N2	2.223(6)
Y1-O1	2.387(4)	Fe2-O2	1.939(5)
Y1-O1	2.472(4)	Fe2-O1	1.945(4)
Y1-N3	2.920(6)	Fe2-O3	2.001(5)
Fe1-O1	1.943(4)	Fe2-O7	2.148(5)
Fe1-O4	1.987(5)	Fe2-N1	2.268(6)
Fe1-O5	1.994(5)	O1-Y1	2.472(4)

Table 34: Selected bond lengths for 35.

O4-Y1-O5	152.01(17)	O5-Fe1-O8	170.9(2)
----------	------------	-----------	----------

O4-Y1-O3	81.23(19)	O6-Fe1-O8	83.4(2)
O5-Y1-O3	118.91(18)	O1-Fe1-N2	157.7(2)
O4-Y1-O1	109.00(17)	O4-Fe1-N2	81.2(2)
O5-Y1-O1	66.68(16)	O5-Fe1-N2	82.0(2)
O3-Y1-O1	67.92(16)	O6-Fe1-N2	88.2(2)
O13-Y1-O1	140.50(16)	O8-Fe1-N2	95.9(2)
O4-Y1-O1	68.67(16)	O2-Fe2-O1	96.9(2)
O5-Y1-O1	83.62(16)	O2-Fe2-O3	106.9(2)
O3-Y1-O1	122.63(17)	O1-Fe2-O3	84.11(19)
O13-Y1-O1	79.03(16)	O2-Fe2-O7	158.8(2)
O1-Y1-O1	77.23(17)	O1-Fe2-O7	102.13(19)
O4-Y1-N3	102.37(18)	O3-Fe2-O7	84.4(2)
O5-Y1-N3	100.97(18)	O9-Fe2-O7	80.8(3)
O3-Y1-N3	77.80(18)	O2-Fe2-N1	80.7(2)
O13-Y1-N3	76.66(18)	O1-Fe2-N1	162.8(2)
O1-Y1-N3	128.28(18)	O3-Fe2-N1	80.3(2)
O1-Y1-N3	153.96(18)	O9-Fe2-N1	97.0(2)
O1-Fe1-O4	86.26(18)	O7-Fe2-N1	83.8(2)
O1-Fe1-O5	82.34(18)	Fe1-O1-Fe2	110.1(2)
O4-Fe1-O5	100.9(2)	Fe1-O1-Y1	103.43(18)
O1-Fe1-O6	107.0(2)	Fe2-O1-Y1	103.38(18)
O4-Fe1-O6	165.2(2)	Fe1-O1-Y1	98.88(17)
O5-Fe1-O6	87.7(2)	Fe2-O1-Y1	134.7(2)
O1-Fe1-O8	101.9(2)	Y1-O1-Y1	102.77(17)
O4-Fe1-O8	87.4(2)		

Table 35: Selected bond angles for **35**.

3.1.2 Magnetic properties of $[\text{Fe}^{\text{III}}_4\text{Ln}^{\text{III}}_2(\mu_4\text{-O})_2(\text{n-bdea})_4(\text{piv})_4(\text{NO}_3)_2(\text{H}_2\text{O})_2]$

Compound	χT expected for each Ln at RT ($\text{cm}^3\text{Kmol}^{-1}$)	Ground state of Ln ion	χT expected for non-interacting ions per complex ^a ($\text{cm}^3\text{Kmol}^{-1}$)
Fe_4Pr_2 (30)	1.60	$^3\text{H}_4$	20.70
Fe_4Sm_2 (32)	0.09	$^6\text{H}_{5/2}$	17.68
Fe_4Gd_2 (34)	7.88	$^8\text{S}_{7/2}$	33.26

Compound	χT measured at 300K per complex ($\text{cm}^3\text{Kmol}^{-1}$)	χT measured at 2 K per complex ($\text{cm}^3\text{Kmol}^{-1}$)	Magnetisation at 2 K and 7 T (μ_B)
Fe_4Pr_2 (30)	8.53	0.27	1.27
Fe_4Sm_2 (32)	7.02	0.28	0.59
Fe_4Gd_2 (34)	23.01	8.21	14.95

Table 36: Magnetic data summarised from the dc measurements. ^a taking into account a g factor of Fe^{III} metal ions of 2.

The magnetic properties of **30** (Pr), **32** (Sm) and **34** (Gd) were investigated by solid state magnetic susceptibility (χ_M) measurements in the 2 K–300 K range in a 1000 Oe dc field. The resulting data for complexes **30** (Pr), **32** (Sm) and **34** (Gd) are shown as $\chi_M T$ versus T plot below (Figure 81).

For complex **30** (Pr), **32** (Sm) and **34** (Gd) the $\chi_M T$ values of 8.53, 7.02 and 23.01 $\text{cm}^3 \text{Kmol}^{-1}$ at 300 K are significantly less than the values expected for 4 Fe^{III} ($S = 5/2$, $g = 2$) and 2 Pr^{III} ($S=1$, $g=0.8$, $L=5$, $^3\text{H}_4$) in **30** or 2 Sm^{III} ($S=5/2$, $g=0.29$, $L=5$, $^6\text{H}_{5/2}$) in **32** or 2 Gd^{III} ($S=7/2$, $g=2$, $L=0$, $^8\text{S}_{7/2}$) in **34** non-interacting ions of 20.70, 17.68 and 33.26 $\text{cm}^3 \text{Kmol}^{-1}$, respectively (assuming $g = 2$ for Fe^{III}). This is consistent with considerable antiferromagnetic exchange interactions between the Fe^{III} ions mainly through the $\mu_4\text{-O}$ and, to a lesser degree, through the carboxylate ligands. The $\chi_M T$ value of **34** (Gd) decreases steadily to 15.3 $\text{cm}^3 \text{Kmol}^{-1}$ at 13 K followed by a sharp drop to 8.2 $\text{cm}^3 \text{Kmol}^{-1}$ at 1.8 K. Complexes **30** (Pr) and **32** (Sm) behave in a similar fashion to each other. The $\chi_M T$ value for both complexes decreases with decreasing temperature to almost the same values (0.27 and 0.28 for **30** and **32**) at 1.8 K, whereupon for Sm (**32**) a plateau is reached at about 14 K and $\sim 0.3 \text{ cm}^3 \text{Kmol}^{-1}$.

Magnetisation curves for **34** (Gd) show no significant anisotropy contribution for this compound since there is a true saturation of the magnetisation and the superimposed reduced magnetisation curves, whereas **30** (Pr) and **32** (Sm) are strongly anisotropic.

The data suggest predominantly antiferromagnetic exchange interactions within all three complexes. The presence of spin-orbit coupling effects in **30** and **32** (Pr and Sm) makes the fitting of the data to obtain $\text{Fe}^{\text{III}} \text{Fe}^{\text{III}}$ and $\text{Fe}^{\text{III}} \text{Ln}^{\text{III}}$ exchange parameters far from straightforward. A more complete magnetic analysis of complexes **30–35** is thus the objective of future work including the Dy and in particular the Y analogue, which has so far been obtained only in a very low yield and therefore not measured magnetically, yet.

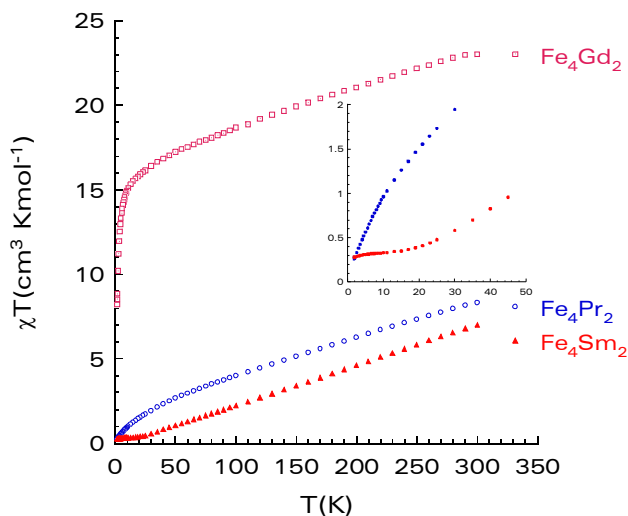


Figure 81: Temperature dependence of the χT product for polycrystalline samples of compounds **30**, **32** and **34** at 1000 Oe.

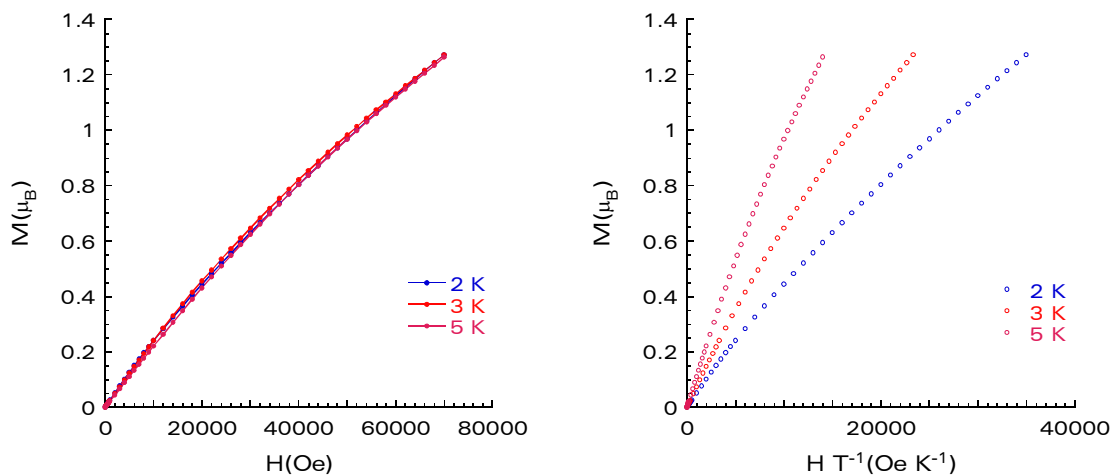


Figure 82: Plot of magnetisation (M) vs. H and H/T , respectively, between 2 K and 5 K for **30**. The solid lines are to guide the eye.

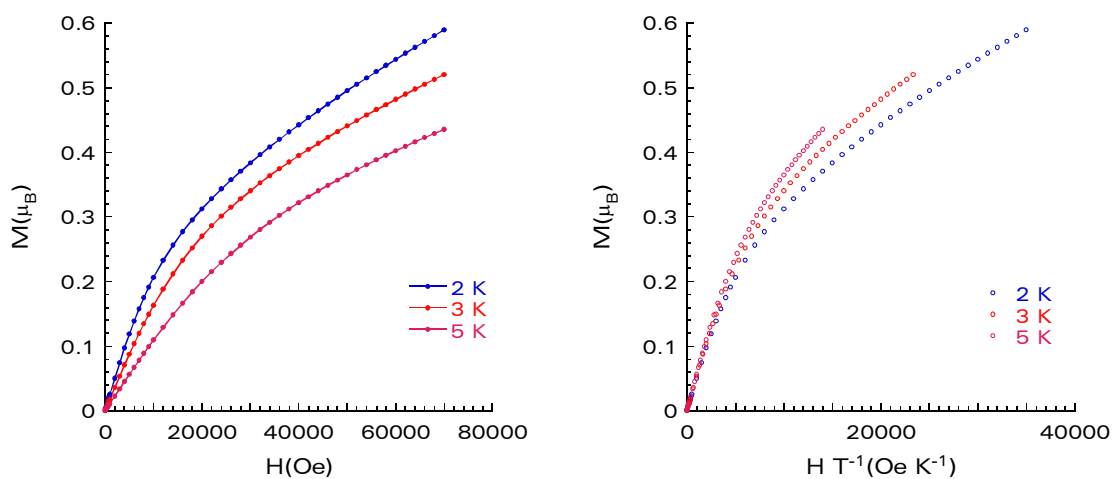


Figure 83: Plot of magnetisation (M) vs. H and H/T , respectively, between 2 K and 5 K for **32**. The solid lines are to guide the eye.

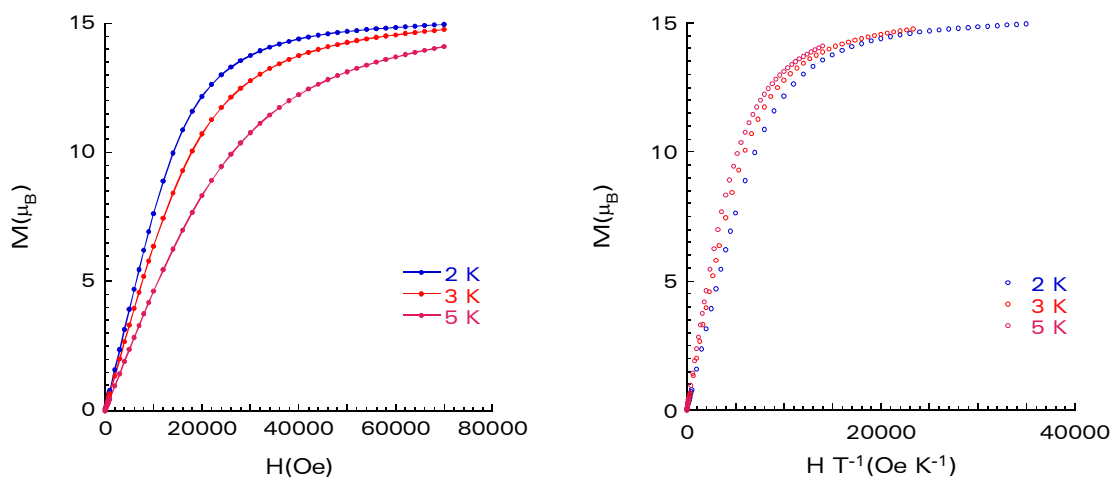


Figure 84: Plot of magnetisation (M) vs. H and H/T , respectively, between 2 K and 5 K for **34**. The solid lines are to guide the eye.

A lack of anisotropy for **34** (Gd) results in no out-of-phase ac magnetic susceptibility signal down to 1.8 K, indicating the absence of a significant barrier to magnetisation relaxation. However, despite the presence of anisotropy in compounds **30** (Pr) and **32** (Sm) the ac susceptibility of compounds **30**, **32** and **34** in zero dc field shows a complete absence of out-of-phase components above 1.8 K, and no slow relaxation is observed in this series of compounds at this temperature.

3.1.3 Mössbauer measurement on $[\text{Fe}^{\text{III}}_4\text{Pr}^{\text{III}}_2(\mu_4\text{-O})_2(\text{n-bdea})_4(\text{piv})_4(\text{NO}_3)_2(\text{H}_2\text{O})_2]$

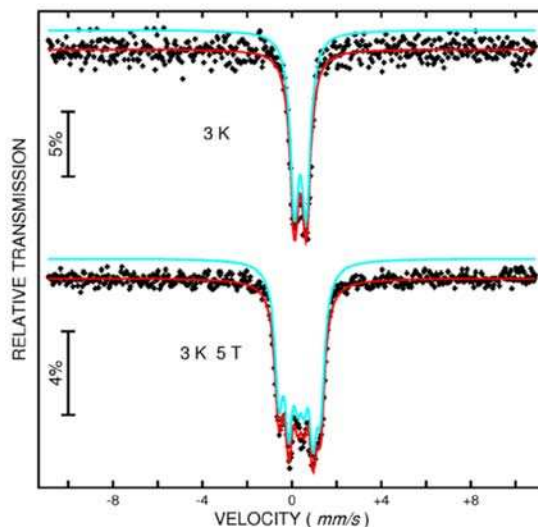


Figure 85: The ^{57}Fe Mössbauer spectra for **30** at 3 K in zero applied field and at 3 K in field of 5 T.

The Mössbauer spectrum of **30** was examined in zero field at 3 K. The spectrum consists of a single broad quadrupole doublet with isomer shift $\delta = 0.48$ mm/s and quadrupole splitting $\Delta E_Q = 0.52$ mm/s or with two doublets with essentially the same isomer shift, slightly narrower lines and different quadrupole splitting. In essence these parameters are comparable to those found in oxo-bridged high-spin ferric complexes (Greenwood, 1971: 148ff; Blume, 1967: 305ff). No magnetic hyperfine structure was observed at 3 K, the lowest temperature studied. Such evolution of the Mössbauer spectra is expected for molecular complexes containing an even number of antiferromagnetically exchanged-coupled high-spin ferric ions which produce simple Mössbauer spectra typical of diamagnetic complexes (Armstrong, 1984: 3653ff).

The spectrum of cluster **30** in an external magnetic field of 5 T at 3 K oriented perpendicular to the gamma radiation direction and parallel to sample holder, is depicted above (Figure 85). This spectrum is characteristic of a diamagnetic ground state spin complex as the field observed at the iron sites equals that of the applied field H_0 . In other words, there is no detectable contribution from magnetic hyperfine interaction other than the applied field and therefore no residual paramagnetism at 3 K.

As within this thesis Mössbauer spectroscopy was only used for one single experiment, a profound introduction about this technique need to be dispensed with. For a detailed introduction about Mössbauer spectroscopy different literature is recommended like (Gütlich, 1970: 133ff) or (Mössbauer, 1958: 124ff).

3.2 Structure and magnetic properties of hexanuclear Fe(III) complexes

The reaction of {Fe₃} (**6**) with 2-(2-hydroxymethyl)pyridine (hmpH) and the respective lanthanide salt yielded hexanuclear [Fe^{III}₆(μ₃-O)₂(hmp)₆(piv)₆]²⁺ [Ln(NO₃)₅]²⁻ with Ln = Eu (**36**), Gd (**37**), Dy (**38**), Ho (**39**) and Er (**40**). The structure can be described as the salt of a cationic Fe₆ octahedron and an anionic Ln(NO₃)₅ counterion.

Variable-temperature solid-state magnetic susceptibility measurements in the temperature range 1.8–300 K were carried out for all complexes and for all complexes a predominantly antiferromagnetic exchange interaction between the iron metal centres was observed.

3.2.1 Structure of [Fe^{III}₆(μ₃-O)₂(hmp)₆(piv)₆]²⁺[Gd(NO₃)₅]²⁻ (**37**)

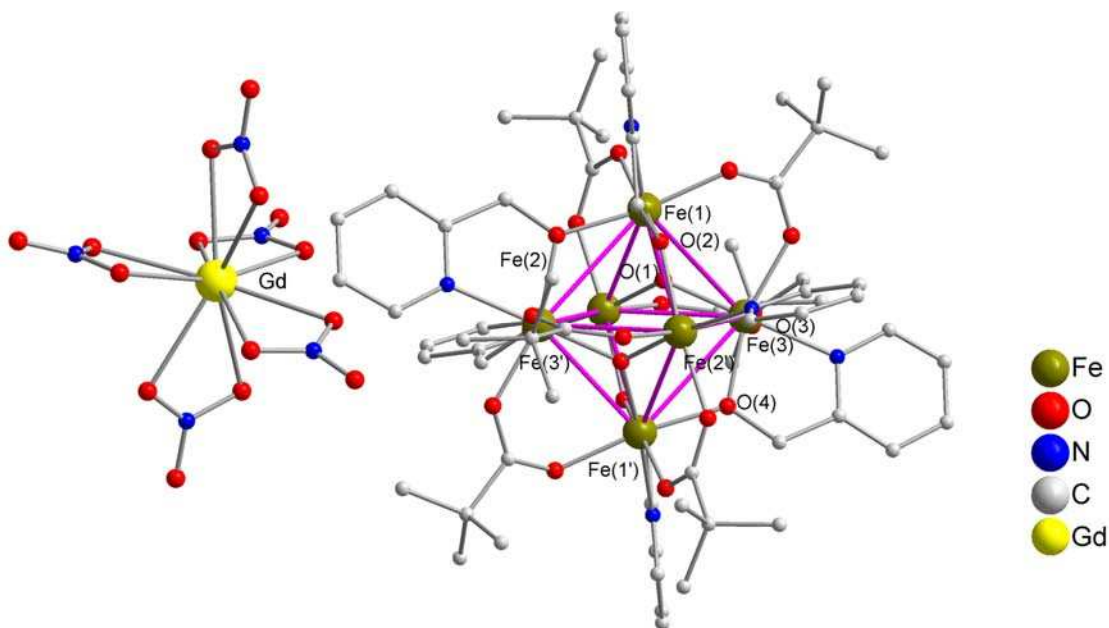


Figure 86: Molecular structure of the [Fe^{III}₆(μ₃-O)₂(hmp)₆(piv)₆]²⁺[Gd(NO₃)₅]²⁻ aggregate in **37**. Organic hydrogen atoms are omitted for clarity.

Compound **37** crystallises in the monoclinic space group C 2/c with Z=4. The compound is built up of a cation containing six Fe^{III} ions, two μ₃-oxo ligands, six deprotonated hydroxymethylpyridine (hmp) ligands and six pivalate coligands. The counterion is a Gd^{III} ion surrounded by five nitrate ions, resulting in a decanuclear environment for the lanthanide ion forming a bicapped square antiprism. This environment is known also for other lanthanide nitrates like the anion [Ce(NO₃)₅]²⁻. The Fe₆ unit has crystallographic inversion symmetry, while the [Gd(NO₃)₅]²⁻ ion is disordered about a twofold rotation axis.

The cation of compound **37** consists of two $\{\text{Fe}_3(\mu_3\text{-O})\}^{7+}$ triangular units held together in a face-to-face fashion by six bridging hmp⁻ groups. All the iron atoms have the same coordination environment, as the corresponding metal-ligand bond lengths do not differ significantly. Each $\eta^1:\eta^2:\mu$ - hmp⁻ group chelates an iron atom and bridges with its oxygen atom to an iron atom in the neighbouring $\{\text{Fe}_3\text{O}\}$ unit.

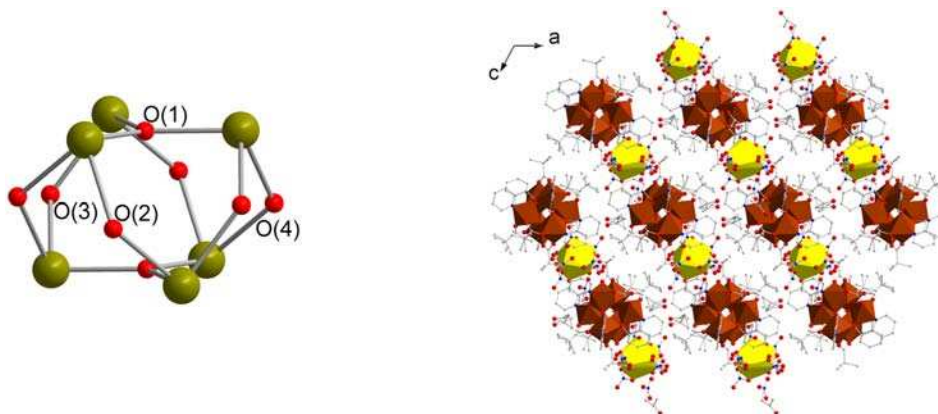


Figure 87: Left: View of the core of the Fe_6 cation. Right: View along the a-axis with the cluster aggregates shown as polyhedral representations. H atoms are omitted for clarity with Fe^{III} shown in brown colour and Gd^{III} in yellow colour.

Each $\text{Fe}\cdots\text{Fe}$ pair within a $\{\text{Fe}_3\text{O}\}$ unit is additionally bridged by a 'BuCO₂⁻ group, completing six-coordinate, near octahedral geometry at each metal. The cation has crystallographic C_i symmetry, but virtual S_6 symmetry with the S_6 axis passing through the $\mu_3\text{-O}^{2-}$ atom O(1) and its symmetry-related partner O(1'). The trigonal antiprismatic disposition of the two $\{\text{Fe}_3\text{O}\}$ units gives an octahedral Fe_6 topology, emphasised in Figure 86 by joining the $\text{Fe}\cdots\text{Fe}$ neighbours with pink lines. From this alternative viewpoint, the cation may be described as an Fe_6 octahedron with two opposite faces bridged by $\mu_3\text{-O}^{2-}$ ions and six edges bridged by $\mu\text{-O}(\text{hmp})$ atoms. Despite this variety of bridges, however, the Fe_6 octahedron is only slightly distorted: $\text{Fe}\cdots\text{Fe}$ separations within the $\{\text{Fe}_3\text{O}\}$ units (average 3.3445 Å) are only slightly shorter than the rest (average 3.4741 Å). The non-adjacent $\text{Fe}\cdots\text{Fe}$ separations are much longer (average 4.8224 Å). Complex **37** joins only a small number of other hexanuclear Fe^{III} complexes that contain an Fe_6 octahedron. These comprise the $[\text{Fe}_6\text{O}(\text{OMe})_{18}]^{2-}$ (Hegetschweiler, 1992: 1299ff), $[\text{Fe}_6\text{O}_2(\text{O}_2\text{C}^t\text{Bu})_6(\text{hmp})_6]^{2-}$ (Brechtin, 2000: 389ff), $[\text{Fe}_6\text{O}(\text{L}_3)_6]^{2-}$ and $[\text{Fe}_6\text{O}(\text{L}_3)_3(\text{OMe})_3\text{Cl}_6]^{2-}$ (Hegetschweiler, 1990: 3625ff; Cornia, 1996: 4414ff) clusters, where L_3 is a polyolato ligand. In these previously reported species, the core is more symmetric than that in **1**, consisting of an Fe_6 octahedron at the centre of which is a $\mu_6\text{-O}^{2-}$ ion and which has a alkoxide-like oxygen atom bridging each of the twelve Fe edges, i.e. effectively a $\{\text{Fe}_6(\mu_6\text{-O})(\mu\text{-OR})_{12}\}$ core with virtual O_h core symmetry. Another compound of this family is the $[\text{Fe}_6\text{O}_2(\text{piv})_6(\text{PdoIH})_6]$ motif, where PdoIH₂ is Propane-1,2-diol (Nayak, 2008: 51ff).

Bond Valence Sum Calculations (Brown, 1985: 244ff):

respective atom	Fe(1)	Fe(2)	Fe(3)
est. ox. state			
Fe ^{II}	2.55	2.53	2.55
Fe ^{III}	3.01	2.99	3.02
calc. ox. state	Fe ^{II}	Fe ^{II}	Fe ^{III}

Compound	a	b	c	V
Fe ₆ Eu (36)	27.248(13)	15.821(7)	26.412(11)	10060(11)
Fe ₆ Gd (37)	26.920(4)	15.589(2)	26.079(4)	9660(2)
Fe ₆ Dy (38)	27.4001(2)	15.7843(8)	26.4138(2)	10178(1)
Fe ₆ Ho (39)	27.3588(2)	15.6478(9)	26.6457(2)	10136(17)
Fe ₆ Er (40)	26.5943(16)	15.6322(5)	27.3747(16)	10110(9)

Compound	α	β	γ
Fe ₆ Eu (36)	90	117.93(5)	90
Fe ₆ Gd (37)	90	118.037(2)	90
Fe ₆ Dy (38)	90	117.005(9)	90
Fe ₆ Ho (39)	90	117.303(11)	90
Fe ₆ Er (40)	90	117.326(6)	90

Table 37: Summary of selected cell parameters.

Fe1-O1	1.932(3)	Gd1-O22	2.328(14)
Fe1-O4	2.008(3)	Gd1-O61	2.378(12)
Fe1-O2	2.019(4)	Gd1-O32	2.408(11)
Fe1-N1	2.176(5)	Gd1-O21	2.419(18)
Fe2-O1	1.933(3)	Gd1-O41	2.443(10)
Fe2-O2	2.012(3)	Gd1-O31	2.461(12)
Fe2-O3	2.016(3)	Gd1-O42	2.465(14)
Fe2-N2	2.177(4)	Gd1-O62	2.491(12)
Fe3-O1	1.931(3)	Gd1-O51	2.57(2)
Fe3-O3	2.007(3)	Gd1-O52	2.676(15)
Fe3-O4	2.020(3)	Gd1-N21	2.741(11)
Fe3-N3	2.172(4)	Gd1-N61	2.846(11)

Table 38: Selected bond lengths for **37**.

O1-Fe1-O4	95.13(13)	O1-Fe2-N2	173.42(16)
O1-Fe1-O2	102.79(14)	O2-Fe2-N2	90.85(16)
O4-Fe1-O2	83.43(14)	O3-Fe2-N2	77.50(15)
O10-Fe1-O2	94.85(16)	O1-Fe3-O3	95.69(14)
O1-Fe1-N1	175.01(16)	O1-Fe3-O4	103.31(13)
O4-Fe1-N1	89.86(16)	O3-Fe3-O4	82.90(14)
O10-Fe1-N1	80.55(17)	O1-Fe3-N3	175.38(15)
O2-Fe1-N1	77.69(17)	O3-Fe3-N3	88.88(15)
O5-Fe1-N1	84.68(18)	O4-Fe3-N3	77.84(15)
O1-Fe2-O2	95.48(14)	Fe1-O1-Fe3	119.74(16)
O1-Fe2-O3	101.39(13)	Fe1-O1-Fe2	120.79(16)
O2-Fe2-O3	83.72(13)	Fe3-O1-Fe2	119.21(16)

Table 39: Selected bond lengths for **37**.

3.2.2 Magnetic properties of $[\text{Fe}^{\text{III}}_6(\mu_3\text{-O})_2(\text{hmp})_6(\text{piv})_6]^{2+}[\text{Ln}(\text{NO}_3)_6]^{2-}$

The thermal dependences of $\chi_M T$ are shown in the Figure 88 for compounds **36-40**. The $\chi_M T$ product for all compounds decreases more and more rapidly with decreasing temperature starting at 9.07, 14.45, 22.29, 19.67 and 17.10 $\text{cm}^3 \text{Kmol}^{-1}$ at 300 K, respectively, and finally reach a low-temperature limit of 0.07, 8.23, 9.94, 3.33, 6.30 $\text{cm}^3 \text{Kmol}^{-1}$ for **36** (Eu), **37** (Gd), **38** (Dy), **39** (Ho) and **40** (Er), respectively. The χT values observed at 300 K (9.07, 14.45, 22.29, 19.67 and 17.10 $\text{cm}^3 \text{Kmol}^{-1}$) deviate significantly from the expected values of $\chi_M T$ 26.25, 34.13, 40.43, 40.30 and 37.72 $\text{cm}^3 \text{Kmol}^{-1}$ for **36** (Eu), **37** (Gd), **38** (Dy), **39** (Ho) and **40** (Er), respectively. This is due to the strong antiferromagnetic interactions between the iron centers as expected for Fe^{III} ions. It is likely that the magnetic properties of **36-40** result, to a first approximation from the separate contributions of the Fe_6 and Ln^{III} units.

The observed decrease in the χT product is typical for dominant antiferromagnetic interactions. However, the spin orbit interaction may also participate to this behaviour except for the Gd compound **37** (Gd). For the trivalent rare earth ions presented here, the $^{2S+1}L_J$ free-ion ground state is well separated in energy from the first excited state, such that only this ground state is thermally populated at room temperature and below (Andruh, 1993: 1616ff). The slow depopulation of the excited states of the lanthanide ion on decreasing the temperature can thus be excluded as a reason for the decreasing $\chi_M T$ product.

Although the Fe_6 cation is antiferromagnetically coupled and thus the contribution of these Fe^{III} ions is supposed to be zero, it seems that this Fe_6 unit provides a magnetic contribution under field. This would explain also the severe deviation of the experimental χT values from the expected values for seven non-interacting ions at 300 K.

However, on lowering the temperature, this contribution of the Fe_6 unit becomes increasingly smaller down to 1.8 K. The case of **37** (Gd) shows very well that the contribution of the Fe_6 cation is becoming nearly zero due to the nearly perfect antiferromagnetic alignment of the spins in the Fe_6 octahedron at this low temperature. Here the values for χT at 1.8K (8.23 $\text{cm}^3 \text{Kmol}^{-1}$) are nearly the same like for a single Gd^{III} ion (7.88 $\text{cm}^3 \text{Kmol}^{-1}$). In the cases of the other compounds these values are not in such a good agreement which is probably due to antiferromagnetic interaction between the resulting spin of the Fe_6 octahedron and the Ln^{III} ion. Because of the more isotropic character of the Gd^{III} ion this effect is not that big in this case.

The field dependence of the magnetisation of compounds **37-40** at low temperatures shows that the magnetisation increases rapidly with increasing applied dc field but without saturation even at 7 T. Only in the case of **37** can a well-defined saturation be observed at about $7.81\mu_B$, which is slightly higher than the expected value for a free Gd^{III} ion of $7\mu_B$. This is probably due to the contribution of the Fe_6 unit, although the spin carriers of the cation are antiferromagnetically coupled. The magnitude of magnetisation is also given in Table 40.

The non-saturation of the magnetisation of the other derivatives indicates the presence of magnetic anisotropy and/or the lack of a well-defined ground state suggesting the presence of low-lying excited states that might be populated when a field is applied. Furthermore, the plots of the M versus H/T at low temperatures for compounds **38-40** show that the curves are not superposed, as expected for an anisotropic system, giving a further indication of the presence of magnetic anisotropy and also the low-lying excited states already suggested.

Compound	χT expected for each Ln at RT ($\text{cm}^3\text{Kmol}^{-1}$)	Ground state of Ln ion	χT expected for each complex ^a ($\text{cm}^3\text{Kmol}^{-1}$)
Fe ₆ Eu (36)	0	⁷ F ₀	26.25
Fe ₆ Gd (37)	7.88	⁸ S _{7/2}	34.13
Fe ₆ Dy (38)	14.17	⁶ H _{15/2}	40.43
Fe ₆ Ho (39)	14.07	⁵ I ₈	40.30
Fe ₆ Er (40)	11.48	⁴ I _{15/2}	37.72

Compound	χT measured at 300K per complex ($\text{cm}^3\text{Kmol}^{-1}$)	χT measured at 1.8 K per complex ($\text{cm}^3\text{Kmol}^{-1}$)	Magnetisation at 1.8 K and 7 T (μ_B)
Fe ₆ Eu (36)	9.07	0.07	0.36
Fe ₆ Gd (37)	14.45	8.23	7.81
Fe ₆ Dy (38)	22.29	9.94	6.63
Fe ₆ Ho (39)	19.67	3.33	5.35
Fe ₆ Er (40)	17.10	6.30	4.37

Table 40: Magnetic data summarised from the dc measurements. ^a taking into account a g factor of Fe^{III} metal ions of 2.

The presence of slow relaxation in these molecular systems was systematically probed through ac susceptibility measurements, carried out in the frequency range 100-1500 Hz and at temperatures between 1.8 and 10 K. At zero dc applied field, no out-of-phase component of the susceptibility was detected down to 1.8 K for all four compounds. SMM properties of lanthanide-containing polynuclear complexes are known to be modulated by the metal ions used, the largest energy barriers being mostly observed for Dy^{III} compounds (Sessoli, 2009: 2328ff; Mereacre, 2008: 3577ff). Nonetheless, it is now well-established that mononuclear lanthanide complexes may behave as SMM, when their coordination environment results in highly anisotropic situations. In particular, the highest anisotropy barriers have been found in mononuclear bisphthalocyanine-based lanthanide sandwich complexes of Tb^{III}. In this family of compounds, the Dy^{III} complex also exhibits slow relaxation of magnetisation, but at much lower temperatures. In these compounds, the square antiprismatic coordination environment of the lanthanide ion is thought to be a key factor for optimising the anisotropy of the system (Ishikawa, 2003: 8694f). In the case of the Dy compound **38** the distribution of the nitrate ligands seems not to induce any significant anisotropy and slow relaxation is thus not observed.

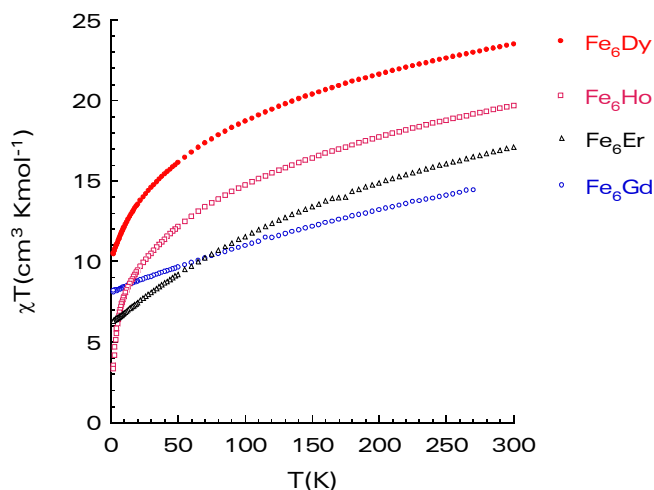


Figure 88: Temperature dependence of the χT product for polycrystalline samples of compounds **37**, **38**, **39** and **40** at 1000 Oe (left) and 10000 Oe (right).

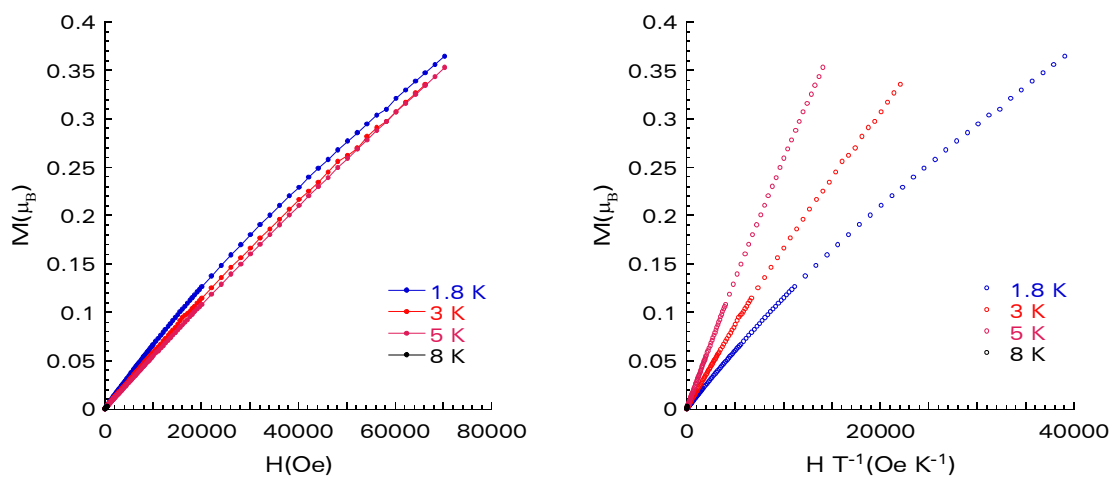


Figure 89: Plot of magnetisation (M) vs. H and H/T , respectively, between 2 K and 8 K for **36**. The solid lines are to guide the eye.

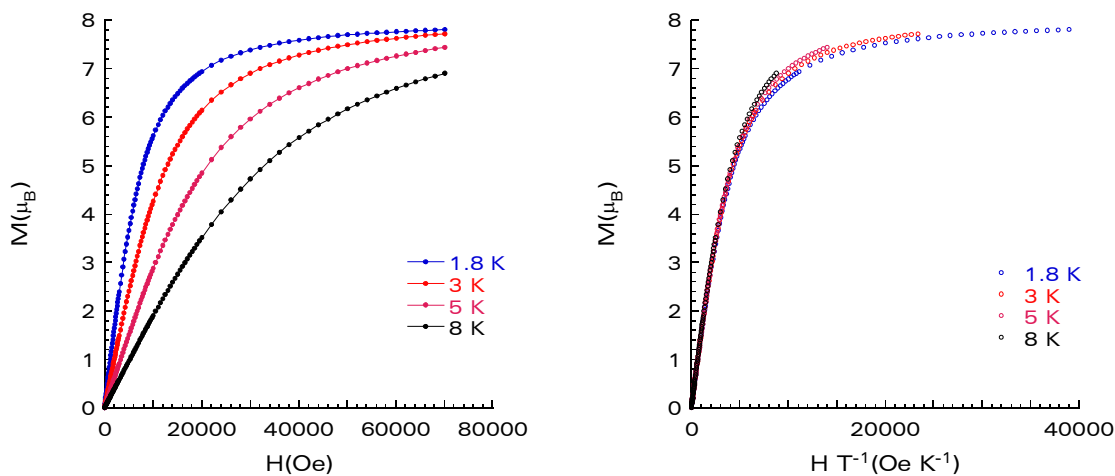


Figure 90: Plot of magnetisation (M) vs. H and H/T , respectively, between 2 K and 8 K for **37**. The solid lines are to guide the eye.

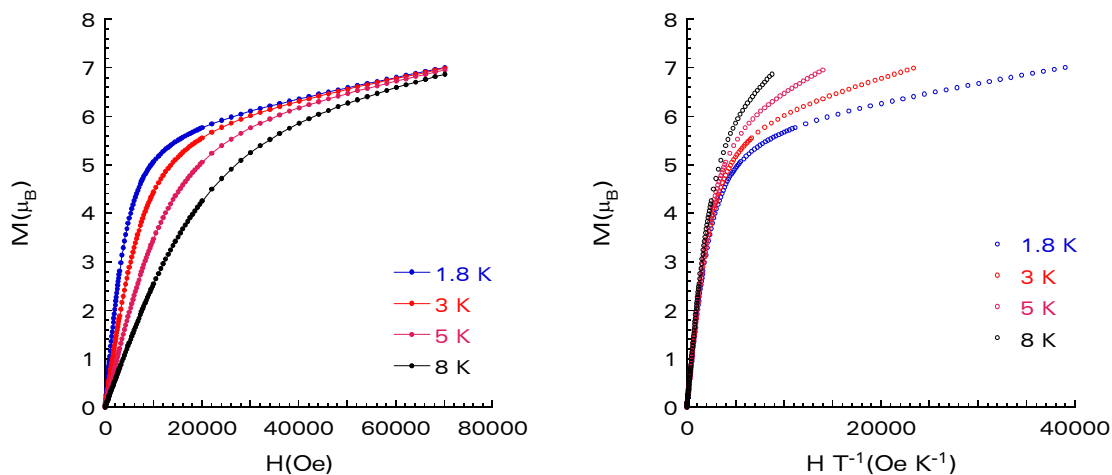


Figure 91: Plot of magnetisation (M) vs. H and H/T , respectively, between 2 K and 8 K for **38**. The solid lines are to guide the eye.

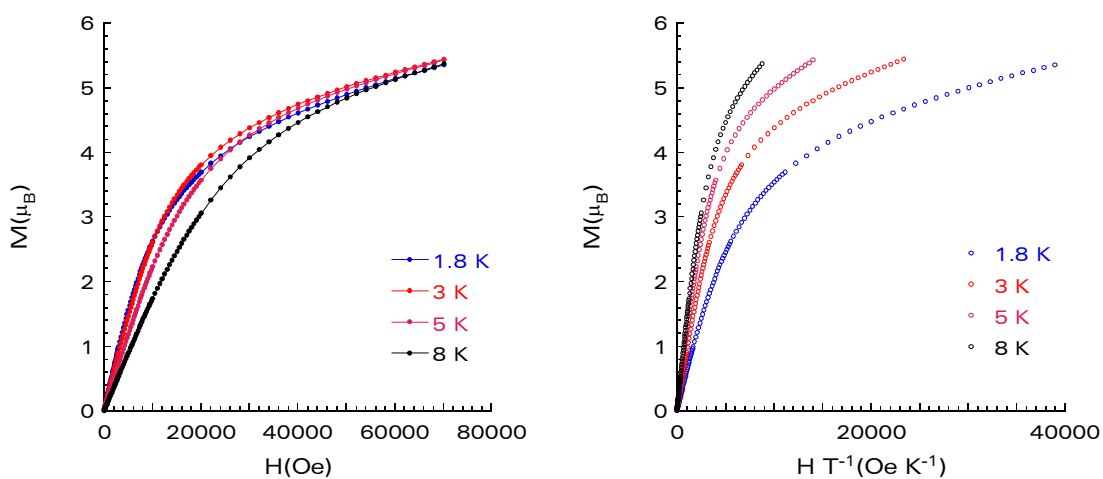


Figure 92: Plot of magnetisation (M) vs. H and H/T , respectively, between 2 K and 8 K for **39**. The solid lines are to guide the eye.

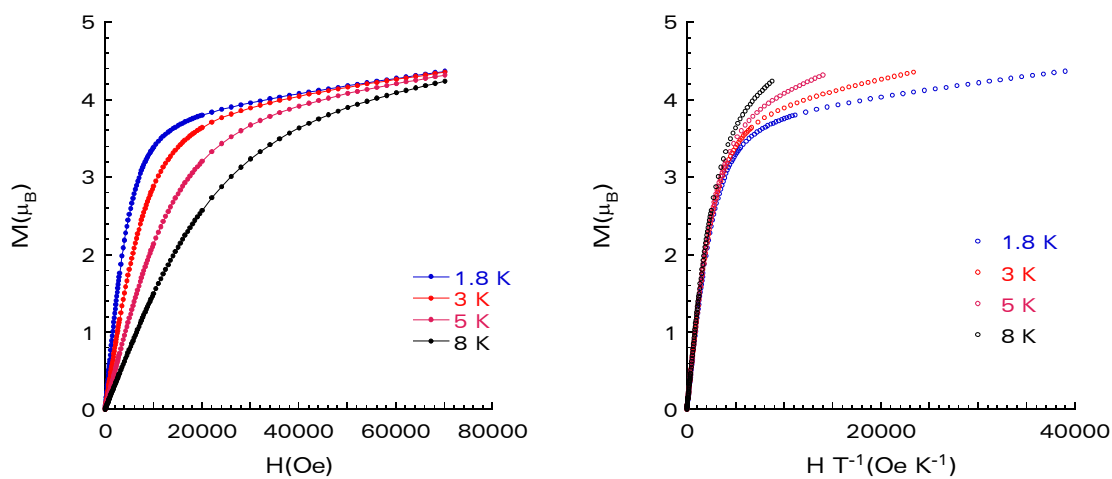


Figure 93: Plot of magnetisation (M) vs. H and H/T , respectively, between 2 K and 8 K for **40**. The solid lines are to guide the eye.

4 Structure and magnetic properties of cobalt-lanthanide aggregates

4.1 Structure and magnetic properties of hexanuclear complexes

The structures and magnetic properties of a family of new hexanuclear heterometallic $3d-4f$ complexes $[\text{Co}^{\text{III}}_2\text{Dy}^{\text{III}}_4(\mu_3\text{-OH})_2(\text{hmp})_4(\text{piv})_8(\text{N}_3)_2(\text{NO}_3)_2]\cdot 2\text{CH}_3\text{CN}$, where Ln = Pr(**41**), Sm (**42**), Eu (**43**), Gd (**44**), Tb (**45**), Dy (**46**), Ho (**47**) and Er (**48**) are reported. The metal topology in the aggregates can be described as consisting of a defect Ln_4 -dicubane. Complexes **41-48** are prepared by the reactions of 2-(2-hydroxymethyl)pyridine (hmpH) with the preformed dinuclear cobalt pivalate complex $\{\text{Co}_2\}$, the respective lanthanide salt, KOH and NaN_3 . The magnetic properties of the complexes **42-48** were investigated using variable temperature magnetic susceptibility and magnetisation measurements. The Dy^{III} analogue **46** show frequency-dependent ac susceptibilities indicative of a slow relaxation of magnetisation and is therefore considered as Single-Molecule Magnet.

4.1.1 Structure of $[\text{Co}^{\text{III}}_2\text{Dy}^{\text{III}}_4(\mu_3\text{-OH})_2(\text{hmp})_4(\text{piv})_8(\text{N}_3)_2(\text{NO}_3)_2]\cdot 2\text{CH}_3\text{CN}$ (**46**)

Single-crystal X-ray diffraction studies reveal that compound **46** crystallise in the monoclinic space group C2/c with $Z=4$ and thus compounds **41-46** are isomorphous. Therefore the structure of compound **46** (Dy) should be discussed as a representative for the whole family. The core structure of **46** has a tetranuclear arrangement of four Dy^{III} ions with a crystallographic inversion symmetry flanked by two diamagnetic Co^{III} ions. The oxidation states of the cobalt and the lanthanide ions were estimated by consideration of its coordination geometry, its bond lengths, the coordination numbers, the charge balance and by bond valence sum analysis (Wood, 1998: 4149ff; Brese, 1991: 192ff).

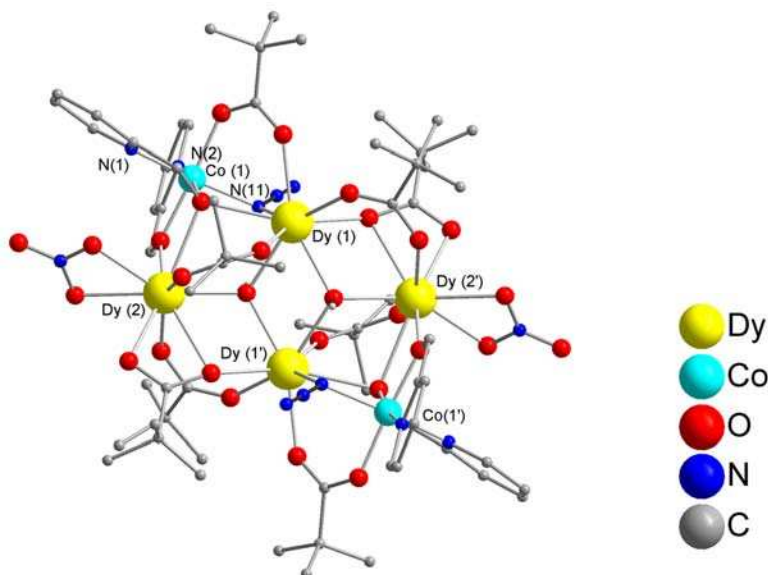


Figure 94: Molecular structure of $[\text{Co}^{\text{II}}_2\text{Dy}^{\text{III}}_4(\text{hmp})_4(\text{piv})_8(\text{N}_3)_2(\text{NO}_3)] \cdot 2\text{CH}_3\text{CN}$. Atoms marked with primes are inversion-center-generated. Organic hydrogen atoms and solvent molecules are omitted for clarity.

In contrast to the previously presented $\text{Mn}^{\text{II}}_2\text{Dy}^{\text{III}}_4$ aggregate and most other tetranuclear compounds (Christou, 2000: 66ff) the four Dy^{III} ions are precisely coplanar, as shown in Figure 95. The two oxygen atoms (O1) of the $\mu_3\text{-OH}$ ligands are located on opposite sides of the Dy_4 plane and are displaced out of that plane by 0.6220 Å. This is significantly less than in the comparable pure Dy_4 analogues of Lin or Zheng (Lin, 2009: 9489ff; Zheng, 2008: 10813ff), where the distance is 0.9051 Å and 0.9218 Å, respectively.

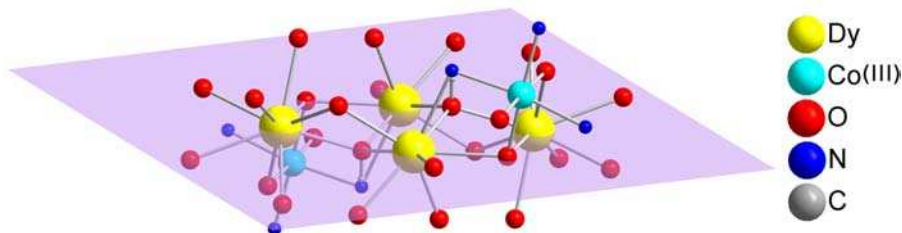


Figure 95: Side view (core only) of the tetranuclear core with the flanking Co^{III} showing the coplanarity in the Dy_4 core of **46**.

The hydroxo forms an almost symmetrical triple bridge, with the Dy-O1 distances 2.275(3), 2.389(3) and 2.351(3) Å and the Dy-O1-Dy angles 113.44(11), 112.69(11) and 113.43(12)°, which is about six degrees more than in the case of Lin. $\text{Dy}(1)$ is octa-coordinate and its coordination polyhedron may be best described as a distorted square antiprism (Figure 96 left) consisting of seven oxygen and one nitrogen.

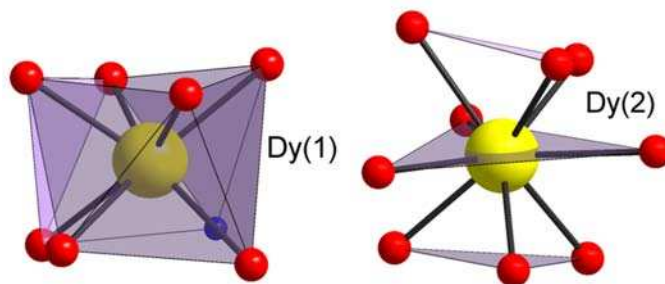


Figure 96: Views of the inner coordination polyhedra of **46** showing the square antiprism coordination of Dy(1) and the three-face centred trigonal prism stereochemistry about Dy(2).

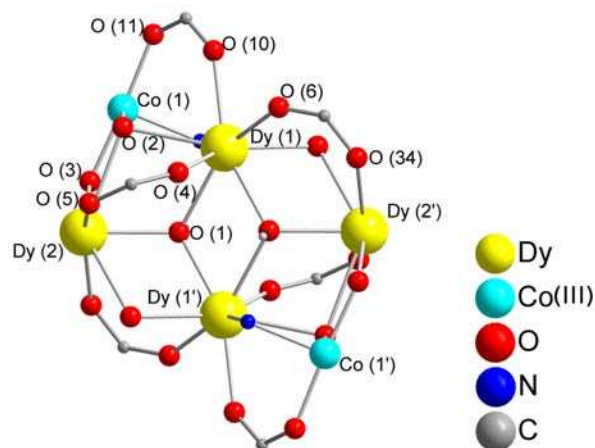


Figure 97: Core view of compound **46**.

It is connected to Dy(2') by two pivalates, which form simple bridges, and the former mentioned μ_3 -OH. The second μ_3 -OH, another bridging pivalate and a bridging alkoxide oxygen coming from a deprotonated hmp ligand form the connection to Dy(2). The third bridge of the latter μ_3 bridging hmp ligand links to Co(1), which is in total chelated by two independent organic ligands via the nitrogen and the methoxy oxygen atoms. One coordinating end-on 1,1-azide bridge and a further bridging pivalate to Dy(1) complete the slightly distorted octahedral coordination sphere of Co(1) which thus consists of three nitrogen and three oxygen atoms. The bond lengths of cobalt and oxygen are between 1.880(3) and 1.921(3) Å and Co-N bond lengths are between 1.918(3) and 1.974(4) Å.

The nine-coordinate environment of Dy(2) is exclusively provided by oxygen donors, resulting in a slightly distorted tricapped trigonal prism coordination sphere (Figure 96 right), which is a common geometry for nine-coordinate hydrated salts of the lanthanide elements such as $[\text{Eu}(\text{H}_2\text{O})_9]^{3+}$.

The derivatives **47** (Ho) and **48** (Er) are isostructural to the above-mentioned complex **46** but both crystallise in the triclinic space group $P\bar{1}$ rather than the monoclinic space group $C2/c$ discussed before.

While the hmpH ligand is known very well in 3d, 4d and 5d transition-metal complexes (e.g. Cao, 2008: 1ff; Taher, 2010: 1ff), only a few examples in the field of 3d-4f coordination chemistry are known (He, 2005: 8285ff). In particular compound **46** (Dy) is the first example of a cobalt/lanthanide compound with 2-hydroxymethylpyridine as ligand.

It is tempting to imagine that the 4-fold axes of the square antiprisms might correspond to the magnetic easy axes of the Dy^{III} ions. However, the atoms surrounding the eight-coordinate Dy^{III} ions Dy(1) and Dy(1') are not equivalent, with some "harder" ligand atoms (hydroxo and alkoxo) than others (neutral oxygens and azide). Furthermore, the distributions of hard and soft atoms are unsymmetrical relative to the principal axes of the antiprisms, so that it would be unwise to try to estimate the directions of the easy axes. The same applies to the other Dy^{III}, where the easy axis of magnetisation might be the C₃ axis. Such tetranuclear structures are often viewed in terms of two edge-sharing triangles, which in this case are close to equilateral, because the distances for Dy(1)···Dy(2), Dy(1)···Dy(2') and Dy(1)···Dy(1') in **46** (Dy) are 3.9001(3), 3.8677(3), and 3.9455(3) Å, respectively.

It should be noted, that the same reaction with an equimolar quantity of Y(NO₃)₃·6H₂O gave crystals of a not yet fully refined structure, which exhibit a linear Co-Y-Y-Co chain, which will be subject to future further investigation.

Bond Valence Sum Calculations (Brown, 1985: 244ff):

respective atom	Co(1)
estimated oxidation state	
Co ^{II}	2.967
Co ^{III}	3.262

Compound	a	b	c	V
Co ₂ Pr ₄ (41)	24.109(3)	18.9152(15)	19.909(2)	9050.2(16)
Co ₂ Sm ₄ (42)	24.7100(2)	18.9670(9)	20.2500(1)	9444(20)
Co ₂ Eu ₄ (43)	24.3688(7)	18.8564(7)	20.0951(5)	9199(8)
Co ₂ Gd ₄ (44)	23.8887(19)	18.5208(15)	19.8980(16)	8775.2(12)
Co ₂ Tb ₄ (45)	24.3414(6)	18.7135(4)	20.1179(5)	9132(6)
Co ₂ Dy ₄ (46)	23.9666(12)	18.4531(11)	19.8875(9)	8766.8(8)
Co ₂ Ho ₄ (47)	13.5562(10)	13.8969(10)	13.9677(10)	2215.2(3)
Co ₂ Er ₄ (48)	13.5725(14)	13.9107(15)	13.9731(14)	2220.4(4)

Compound	α	β	γ
Co ₂ Pr ₄ (41)	90	94.553(9)	90
Co ₂ Sm ₄ (42)	90	95.667(11)	90
Co ₂ Eu ₄ (43)	90	94.916(3)	90
Co ₂ Gd ₄ (44)	90	94.608(1)	90
Co ₂ Tb ₄ (45)	90	94.744(3)	90
Co ₂ Dy ₄ (46)	90	94.621(4)	90
Co ₂ Ho ₄ (47)	84.951(1)	69.693(1)	64.180(1)
Co ₂ Er ₄ (48)	85.082(2)	69.662(2)	64.198(2)

Table 41: Summary of selected cell parameters.

Pr1-O6	2.380(3)	Pr2-O5	2.527(3)
Pr1-O4	2.385(3)	Pr2-O13	2.618(3)
Pr1-O10	2.433(3)	Pr2-O8	2.687(3)
Pr1-O1	2.437(2)	Pr2-O2	2.688(3)
Pr1-O1	2.473(3)	Pr2-N3	2.982(3)
Pr1-O8	2.497(3)	Co1-O3	1.883(3)

4 STRUCTURE AND MAGNETIC PROPERTIES OF COBALT-LANTHANIDE AGGREGATES

Pr1-O2	2.565(2)	Co1-O2	1.914(2)
Pr1-N11	2.583(3)	Co1-N2	1.921(3)
Pr2-O1	2.379(2)	Co1-O11	1.925(3)
Pr2-O3	2.444(2)	Co1-N1	1.933(3)
Pr2-O7	2.455(3)	Co1-N11	1.982(3)
Pr2-O9	2.479(3)	O1-Pr1	2.437(2)
Pr2-O12	2.518(3)		

Table 42: Selected bond lengths for **41**.

O6-Pr1-O4	84.04(16)	O1-Pr2-O8	72.09(8)
O6-Pr1-O10	80.15(10)	O3-Pr2-O8	143.19(8)
O4-Pr1-O10	113.52(12)	O7-Pr2-O8	75.66(9)
O6-Pr1-O1	79.21(10)	O9-Pr2-O8	50.70(9)
O4-Pr1-O1	71.39(10)	O3-Pr2-O5	133.14(9)
O10-Pr1-O1	158.11(9)	O7-Pr2-O5	148.71(10)
O6-Pr1-O1	144.44(10)	O9-Pr2-O5	74.30(11)
O4-Pr1-O1	73.85(14)	O5-Pr2-O8	74.76(9)
O10-Pr1-O1	134.11(9)	O1-Pr2-O2	71.33(8)
O1-Pr1-O1	67.59(10)	O3-Pr2-O2	59.86(8)
O6-Pr1-O8	77.52(11)	O7-Pr2-O2	131.38(9)
O4-Pr1-O8	143.75(10)	O9-Pr2-O2	149.29(9)
O10-Pr1-O8	93.87(9)	O5-Pr2-O2	75.65(9)
O1-Pr1-O8	74.62(9)	O8-Pr2-O2	125.48(8)
O1-Pr1-O8	104.41(9)	O1-Pr2-N3	151.22(9)
O6-Pr1-O2	125.71(9)	O3-Pr2-N3	73.75(9)
O4-Pr1-O2	69.59(10)	O7-Pr2-N3	96.71(10)
O10-Pr1-O2	69.41(9)	O9-Pr2-N3	83.65(10)
O1-Pr1-O2	129.77(8)	O5-Pr2-N3	96.63(11)
O1-Pr1-O2	72.08(8)	O8-Pr2-N3	134.33(9)
O8-Pr1-O2	145.61(8)	O2-Pr2-N3	93.66(9)
O6-Pr1-N11	145.78(12)	O3-Co1-O2	85.14(11)
O4-Pr1-N11	127.10(14)	O3-Co1-N2	85.45(12)
O10-Pr1-N11	74.52(10)	O2-Co1-N2	170.57(13)
O1-Pr1-N11	120.74(9)	O3-Co1-N1	92.61(12)
O1-Pr1-N11	67.27(9)	O2-Co1-N1	84.09(12)
O8-Pr1-N11	81.59(9)	N2-Co1-N1	96.85(13)
O2-Pr1-N11	65.29(9)	O3-Co1-N11	91.93(13)
O1-Pr2-O3	77.46(9)	O2-Co1-N11	90.91(12)
O1-Pr2-O7	77.29(9)	N2-Co1-N11	88.90(13)
O3-Pr2-O7	77.90(9)	N1-Co1-N11	172.94(14)
O1-Pr2-O9	121.82(9)	Pr2-O1-Pr1	111.49(10)
O3-Pr2-O9	145.45(10)	Pr2-O1-Pr1	109.73(9)
O7-Pr2-O9	79.21(11)	Pr1-O1-Pr1	112.41(10)
O1-Pr2-O5	102.86(11)		

Table 43: Selected bond angles for **41**.

Gd1-O4	2.301(3)	Gd2-O5	2.414(3)
Gd1-O6	2.327(3)	Gd2-O12	2.446(3)
Gd1-O10	2.368(3)	Gd2-O13	2.544(3)
Gd1-O1	2.381(3)	Gd2-O8	2.647(3)
Gd1-O1	2.409(3)	Gd2-O2	2.650(3)
Gd1-O8	2.432(3)	Co1-O3	1.877(3)
Gd1-O2	2.503(3)	Co1-O2	1.903(3)
Gd1-N11	2.511(3)	Co1-N2	1.921(3)
Gd2-O1	2.301(3)	Co1-N1	1.922(3)
Gd2-O7	2.363(3)	Co1-O11	1.925(3)
Gd2-O3	2.379(3)	Co1-N11	1.970(3)
Gd2-O9	2.397(3)	O1-Gd1	2.381(3)

Table 44: Selected bond lengths for **44**.

O4-Gd1-O6	77.93(12)	O1-Gd2-O5	96.57(10)
O4-Gd1-O10	109.50(10)	O7-Gd2-O5	148.38(10)
O6-Gd1-O10	76.95(10)	O3-Gd2-O5	132.05(9)

4 STRUCTURE AND MAGNETIC PROPERTIES OF COBALT-LANTHANIDE AGGREGATES

O4-Gd1-O1	73.46(10)	O9-Gd2-O5	75.34(10)
O6-Gd1-O1	81.17(10)	O1-Gd2-O8	71.29(9)
O10-Gd1-O1	156.58(10)	O7-Gd2-O8	76.56(9)
O4-Gd1-O1	80.27(11)	O3-Gd2-O8	143.34(8)
O6-Gd1-O1	146.15(10)	O9-Gd2-O8	52.00(9)
O10-Gd1-O1	135.28(9)	O5-Gd2-O8	72.60(9)
O1-Gd1-O1	67.91(11)	O1-Gd2-O2	69.87(9)
O4-Gd1-O8	141.08(10)	O7-Gd2-O2	132.50(9)
O6-Gd1-O8	76.48(10)	O3-Gd2-O2	60.58(8)
O10-Gd1-O8	92.65(9)	O9-Gd2-O2	146.98(9)
O1-Gd1-O8	74.03(9)	O5-Gd2-O2	72.78(9)
O1-Gd1-O8	106.42(9)	O8-Gd2-O2	123.42(8)
O4-Gd1-O2	73.03(9)	O3-Co1-O2	84.74(11)
O6-Gd1-O2	125.41(9)	O3-Co1-N2	85.54(13)
O10-Gd1-O2	70.91(9)	O2-Co1-N2	170.24(13)
O1-Gd1-O2	130.14(9)	O3-Co1-N1	91.99(12)
O1-Gd1-O2	70.89(8)	O2-Co1-N1	84.12(12)
O8-Gd1-O2	145.81(9)	N2-Co1-N1	97.03(13)
O4-Gd1-N11	134.65(11)	O3-Co1-O11	176.90(12)
O6-Gd1-N11	143.48(11)	O2-Co1-O11	95.86(11)
O10-Gd1-N11	76.04(10)	N2-Co1-O11	93.90(13)
O1-Gd1-N11	119.24(10)	N1-Co1-O11	85.05(12)
O1-Gd1-N11	68.02(10)	O3-Co1-N11	92.29(13)
O8-Gd1-N11	80.69(10)	O2-Co1-N11	90.46(12)
O2-Gd1-N11	66.53(9)	N2-Co1-N11	89.12(13)
O1-Gd2-O7	79.81(9)	N1-Co1-N11	172.76(14)
O1-Gd2-O3	78.29(9)	O11-Co1-N11	90.75(13)
O7-Gd2-O3	78.38(9)	Gd2-O1-Gd1	112.49(11)
O1-Gd2-O9	122.78(10)	Gd2-O1-Gd1	112.82(10)
O7-Gd2-O9	80.37(10)	Gd1-O1-Gd1	112.09(11)
O3-Gd2-O9	146.50(10)		

Table 45: Selected bond angles for 44.

Dy1-O4	2.275(3)		
Dy1-O6	2.295(3)	Dy2-O5	2.377(3)
Dy1-O10	2.333(3)	Dy2-O2	2.637(3)
Dy1-O1	2.351(3)	Dy2-O8	2.685(4)
Dy1-O1	2.389(3)	Co1-O3	1.880(3)
Dy1-O8	2.396(3)	Co1-O2	1.906(3)
Dy1-N11	2.479(4)	Co1-N2	1.918(3)
Dy1-O2	2.480(3)	Co1-O11	1.921(3)
Dy2-O1	2.275(3)	Co1-N1	1.930(4)
Dy2-O7	2.335(3)	Co1-N11	1.974(4)
Dy2-O3	2.346(3)	O1-Dy1	2.351(3)
Dy2-O9	2.357(3)		

Table 46: Selected bond lengths for 46.

O4-Dy1-O6	76.97(14)	O1-Dy2-O5	94.57(11)
O4-Dy1-O10	109.06(13)	O7-Dy2-O5	147.86(11)
O6-Dy1-O10	76.29(11)	O3-Dy2-O5	132.37(11)
O4-Dy1-O1	74.20(11)	O9-Dy2-O5	75.50(12)
O6-Dy1-O1	81.93(11)	O1-Dy2-O2	69.94(9)
O10-Dy1-O1	156.38(10)	O7-Dy2-O2	132.64(10)
O4-Dy1-O1	80.83(13)	O3-Dy2-O2	61.21(9)
O6-Dy1-O1	145.98(11)	O9-Dy2-O2	146.64(11)
O10-Dy1-O1	136.01(10)	O5-Dy2-O2	72.28(10)
O1-Dy1-O1	67.31(11)	O1-Dy2-O8	70.39(10)
O4-Dy1-O8	141.39(12)	O7-Dy2-O8	76.78(11)
O6-Dy1-O8	76.58(12)	O3-Dy2-O8	143.47(10)
O10-Dy1-O8	91.30(12)	O9-Dy2-O8	51.68(11)
O1-Dy1-O8	74.66(11)	O5-Dy2-O8	71.63(10)
O1-Dy1-O8	107.27(10)	O2-Dy2-O8	122.78(9)
O4-Dy1-N11	135.87(13)	O3-Co1-O2	84.65(12)

4 STRUCTURE AND MAGNETIC PROPERTIES OF COBALT-LANTHANIDE AGGREGATES

O6-Dy1-N11	143.07(13)	O3-Co1-N2	85.74(14)
O10-Dy1-N11	76.26(11)	O2-Co1-N2	170.36(15)
O1-Dy1-N11	118.47(11)	O3-Co1-O11	177.18(14)
O1-Dy1-N11	68.68(11)	O2-Co1-O11	95.54(13)
O8-Dy1-N11	79.83(12)	N2-Co1-O11	94.09(15)
O4-Dy1-O2	73.51(11)	O3-Co1-N1	92.05(15)
O6-Dy1-O2	125.05(11)	O2-Co1-N1	84.32(14)
O10-Dy1-O2	71.26(10)	N2-Co1-N1	96.74(15)
O1-Dy1-O2	130.32(10)	O11-Co1-N1	85.17(14)
O1-Dy1-O2	71.07(9)	O3-Co1-N11	91.97(15)
O8-Dy1-O2	145.10(11)	O2-Co1-N11	89.63(14)
N11-Dy1-O2	66.94(10)	N2-Co1-N11	89.99(15)
O1-Dy2-O7	80.11(11)	O11-Co1-N11	90.85(15)
O1-Dy2-O3	79.45(10)	N1-Co1-N11	172.40(15)
O7-Dy2-O3	78.18(11)	Dy2-O1-Dy1	113.43(12)
O1-Dy2-O9	121.62(11)	Dy2-O1-Dy1	113.44(11)
O7-Dy2-O9	80.47(12)	Dy1-O1-Dy1	112.69(11)
O3-Dy2-O9	146.59(12)		

Table 47: Selected bond angles for 46.

Ho1-O8	2.287(3)	Ho2-O5	2.354(2)
Ho1-O6	2.296(2)	Ho2-O12	2.414(2)
Ho1-O4	2.296(2)	Ho2-O13	2.479(2)
Ho1-O1	2.330(2)	Ho2-O2	2.527(2)
Ho1-O10	2.334(2)	Ho2-N3	2.866(3)
Ho1-O1	2.407(2)	Co1-O3	1.873(2)
Ho1-O2	2.494(2)	Co1-O2	1.902(2)
Ho1-N11	2.517(3)	Co1-O11	1.910(2)
Ho2-O9	2.273(3)	Co1-N2	1.914(3)
Ho2-O1	2.282(2)	Co1-N1	1.938(3)
Ho2-O7	2.311(2)	Co1-N11	1.953(3)
Ho2-O3	2.322(2)		

Table 48: Selected bond lengths for 47.

O8-Ho1-O6	78.99(9)	O7-Ho2-O5	143.76(8)
O8-Ho1-O4	149.65(9)	O3-Ho2-O5	134.47(8)
O6-Ho1-O4	76.75(9)	O9-Ho2-O2	146.43(8)
O8-Ho1-O1	108.85(9)	O1-Ho2-O2	71.96(8)
O6-Ho1-O1	142.44(8)	O7-Ho2-O2	128.37(8)
O4-Ho1-O1	80.83(9)	O3-Ho2-O2	64.14(8)
O8-Ho1-O10	85.54(9)	O5-Ho2-O2	71.98(8)
O6-Ho1-O10	76.28(8)	O12-Ho2-O2	82.92(8)
O4-Ho1-O10	105.92(9)	O13-Ho2-O2	121.42(8)
O1-Ho1-O10	139.53(8)	O9-Ho2-N3	88.64(9)
O8-Ho1-O1	83.68(9)	O1-Ho2-N3	168.37(8)
O6-Ho1-O1	76.47(8)	O7-Ho2-N3	102.03(9)
O4-Ho1-O1	73.15(8)	O3-Ho2-N3	77.49(8)
O1-Ho1-O1	68.33(9)	O5-Ho2-N3	101.35(9)
O10-Ho1-O1	152.13(8)	O12-Ho2-N3	26.40(8)
O8-Ho1-O2	136.80(8)	O13-Ho2-N3	26.08(9)
O6-Ho1-O2	127.84(8)	O2-Ho2-N3	102.27(8)
O4-Ho1-O2	73.36(8)	O3-Co1-O2	86.23(10)
O1-Ho1-O2	71.81(8)	O3-Co1-O11	175.74(10)
O10-Ho1-O2	72.27(8)	O2-Co1-O11	96.41(10)
O1-Ho1-O2	130.95(8)	O3-Co1-N2	85.13(11)
O8-Ho1-N11	75.12(9)	O2-Co1-N2	171.35(12)
O6-Ho1-N11	143.49(9)	O11-Co1-N2	92.24(12)
O4-Ho1-N11	134.44(9)	O3-Co1-N1	91.30(11)
O1-Ho1-N11	71.54(9)	O2-Co1-N1	84.27(11)
O10-Ho1-N11	76.44(9)	O11-Co1-N1	85.65(11)
O1-Ho1-N11	124.82(8)	N2-Co1-N1	96.32(12)
O2-Ho1-N11	64.03(8)	O3-Co1-N11	91.54(11)
O9-Ho2-O1	101.71(9)	O2-Co1-N11	87.08(10)

4 STRUCTURE AND MAGNETIC PROPERTIES OF COBALT-LANTHANIDE AGGREGATES

O9-Ho2-O7	78.50(9)	O11-Co1-N11	91.93(11)
O1-Ho2-O7	75.24(8)	N2-Co1-N11	92.75(12)
O9-Ho2-O3	149.29(9)	N1-Co1-N11	170.70(12)
O1-Ho2-O3	90.88(8)	Ho2-O1-Ho1	113.56(9)
O7-Ho2-O3	77.84(8)	Ho2-O1-Ho1	119.17(10)
O9-Ho2-O5	74.78(9)	Ho1-O1-Ho1	111.67(9)
O1-Ho2-O5	86.64(8)		

Table 49: Selected bond angles for **47**.

Er1-O8	2.269(5)	Er2-O5	2.340(4)
Er1-O4	2.283(5)	Er2-O12	2.402(5)
Er1-O6	2.289(4)	Er2-O13	2.484(5)
Er1-O10	2.327(4)	Er2-O2	2.519(4)
Er1-O1	2.331(4)	Er2-N3	2.860(6)
Er1-O1	2.395(4)	Co1-O3	1.878(4)
Er1-O2	2.484(5)	Co1-O11	1.907(4)
Er1-N11	2.513(5)	Co1-O2	1.909(4)
Er2-O9	2.256(5)	Co1-N2	1.910(5)
Er2-O1	2.275(5)	Co1-N1	1.939(6)
Er2-O7	2.303(4)	Co1-N11	1.955(6)
Er2-O3	2.305(4)	O1-Er1	2.395(4)

Table 50: Selected bond lengths for **48**.

O8-Er1-O4	149.71(17)	O7-Er2-O3	77.74(16)
O8-Er1-O6	78.97(17)	O9-Er2-O5	74.65(17)
O4-Er1-O6	76.65(17)	O1-Er2-O5	86.35(16)
O8-Er1-O10	85.21(17)	O7-Er2-O5	143.70(16)
O4-Er1-O10	105.95(17)	O3-Er2-O5	134.67(15)
O6-Er1-O10	76.28(16)	O9-Er2-O2	146.13(16)
O8-Er1-O1	108.99(17)	O7-Er2-O2	128.45(16)
O4-Er1-O1	80.83(16)	O3-Er2-O2	64.52(14)
O6-Er1-O1	142.17(15)	O5-Er2-O2	71.84(15)
O10-Er1-O1	139.82(15)	O9-Er2-N3	88.54(17)
O8-Er1-O1	83.74(16)	O1-Er2-N3	168.98(16)
O4-Er1-O1	73.30(16)	O7-Er2-N3	102.03(17)
O6-Er1-O1	76.41(15)	O3-Er2-N3	77.52(16)
O10-Er1-O1	152.02(15)	O5-Er2-N3	101.32(17)
O1-Er1-O1	68.15(18)	O2-Er2-N3	102.54(16)
O8-Er1-O2	136.73(16)	O3-Co1-O11	176.3(2)
O4-Er1-O2	73.35(15)	O3-Co1-O2	85.91(19)
O6-Er1-O2	127.92(16)	O11-Co1-O2	96.30(19)
O10-Er1-O2	72.47(15)	O3-Co1-N2	85.6(2)
O1-Er1-O2	71.88(15)	O11-Co1-N2	92.2(2)
O1-Er1-O2	130.96(15)	O2-Co1-N2	171.5(2)
O8-Er1-N11	74.77(18)	O3-Co1-N1	91.6(2)
O4-Er1-N11	134.80(18)	O11-Co1-N1	85.7(2)
O6-Er1-N11	143.25(17)	O2-Co1-N1	84.6(2)
O10-Er1-N11	76.33(17)	N2-Co1-N1	96.3(2)
O1-Er1-N11	71.96(16)	O3-Co1-N11	91.7(2)
O1-Er1-N11	124.77(16)	O11-Co1-N11	91.4(2)
O2-Er1-N11	64.29(16)	O2-Co1-N11	86.9(2)
O9-Er2-O1	101.20(17)	N2-Co1-N11	92.7(2)
O9-Er2-O7	78.56(17)	N1-Co1-N11	170.6(2)
O1-Er2-O7	75.25(16)	Er2-O1-Er1	113.36(19)
O9-Er2-O3	149.21(16)	Er2-O1-Er1	119.66(19)
O1-Er2-O3	91.47(16)	Er1-O1-Er1	111.85(18)

Table 51: Selected bond angles for **48**.

4.1.2 Magnetic properties of $[\text{Co}^{\text{III}}_2\text{Ln}^{\text{III}}_4(\mu_3\text{-OH})_2(\text{hmp})_4(\text{piv})_8(\text{N}_3)_2(\text{NO}_3)_2]\cdot 2\text{CH}_3\text{CN}$

The short metal-metal distances (3.86–3.94 Å) within the $[\text{Co}^{\text{III}}_2\text{Ln}^{\text{III}}_4(\text{hmp})_4(\text{piv})_8(\text{N}_3)_2(\text{NO}_3)_2]$ complexes make these compounds interesting for a study of the magnetic exchange interactions between the paramagnetic centres. Here, temperature-dependent studies of the magnetic susceptibility (χ_m) are presented for the complexes **42-48**.

Compound	χT expected for each Ln at RT ($\text{cm}^3\text{Kmol}^{-1}$)	Ground state of Ln ion	χT expected for each complex ($\text{cm}^3\text{Kmol}^{-1}$)
Co_2Sm_4 (42)	0.09	$^6\text{H}_{5/2}$	0.36
Co_2Eu_4 (43)	0	$^7\text{F}_0$	0
Co_2Gd_4 (44)	7.88	$^8\text{S}_{7/2}$	31.52
Co_2Tb_4 (45)	11.82	$^7\text{F}_6$	47.24
Co_2Dy_4 (46)	14.17	$^6\text{H}_{15/2}$	56.71
Co_2Ho_4 (47)	14.07	$^5\text{I}_8$	56.18
Co_2Er_4 (48)	11.48	$^4\text{I}_{15/2}$	45.89

Compound	χT measured at 300K per complex ($\text{cm}^3\text{Kmol}^{-1}$)	χT measured at 1.8 K per complex ($\text{cm}^3\text{Kmol}^{-1}$)	Magnetisation at 1.8 K and 7 T (μ_B)
Co_2Sm_4 (42)	0.39	0.04	0.50
Co_2Eu_4 (43)	5.20 (270 K)	0.03	0.34
Co_2Gd_4 (44)	33.45	12.97	29.81
Co_2Tb_4 (45)	50.09 (270 K)	18.41	23.43
Co_2Dy_4 (46)	57.41	32.30	26.55
Co_2Ho_4 (47)	57.91	13.15	25.95
Co_2Er_4 (48)	45.84	12.42	22.01

Table 52: Magnetic data summarised from the dc measurements.

The dc magnetic susceptibility (χ) data for compounds **42-48** were collected in the 1.8–300 K temperature range at 1000 Oe (Figure 98). For **43** (Eu), the measured χT value at 270 K of $5.20 \text{ cm}^3 \text{ Kmol}^{-1}$ (Figure 98) is more than that expected ($0 \text{ cm}^3 \text{ Kmol}^{-1}$) for two Co^{III} ($S=0$) and four Eu^{III} ($S=0$, $L=3$, $^7\text{F}_0$) non-interacting ions. For most of the Ln^{III} ions, the energy separation between the $^{2s+1}\text{L}_J$ ground state and the first excited state is so large that only the ground state is thermally populated at room and low temperatures, except for the Sm^{III} and Eu^{III} ions, in which the excited states may be thermally populated because of the weak energy separation (Li, 2006: 6308ff). The ground state itself, $^7\text{F}_0$, of Eu^{III} is nonmagnetic. However, since there is a certain amount of magnetic moment from the excited state ($^7\text{F}_1$, $^7\text{F}_2$, $^7\text{F}_3$, $^7\text{F}_4$, $^7\text{F}_5$, $^7\text{F}_6$) the value for χT is slightly higher than the expected one. The decrease in χT values for **43** (Eu) on lowering the temperature attributes to the thermal depopulation of these excited levels.

On the other hand, the static measurements for all the other compounds lead to a room temperature χT value which is always in relatively good agreement with the values expected for isolated spin centres (Table 52). For **46** (Dy) and **44** (Gd) the χT product at 1000 Oe is essentially temperature independent over the range of 300-50 K and respectively for **45** (Tb), **47** (Ho) and **48** (Er) from 300 K to 100 K indicating paramagnetic behaviour for these compounds. For **46** (Dy) the χT product rapidly increases on lowering the temperature from 10 K to 1.8 K showing that weak ferromagnetic behaviour is present. For **44** (Gd) the evolution of the χT product shows a contrary behaviour. On lowering the temperature from 10 K to 1.8 K the χT product decreases rapidly, indicating weak antiferromagnetic coupling in this system.

The temperature dependence of the dc susceptibility is similar for compounds **45** (Tb), **47** (Ho) and **48** (Er) (Figure 98) and thus the analysis of their experimental data is the same. The χT product shows a very slow decrease at higher temperatures with the rate of decrease becoming steadily larger below 100K. This is likely due to spin orbit interaction. It is thus likely that this thermal behaviour is associated with the thermal depopulation of the Ln^{III} excited states and that Ln...Ln interactions are insignificant by comparison.

The χT product of compounds **42** (Sm) and **43** (Eu) show markedly different behaviour from this. For **42** (Sm) the χT product is almost zero over the complete temperature range of the measurement, indicating nearly diamagnetic behaviour of the Sm^{III} ion. **43** (Eu) in turn shows a strong and constant decrease of the χT product on lowering the temperature as a result of the depopulation of the excited states of the Eu^{III} ion.

The field dependence of the magnetisation of compounds **42-48** at low temperatures shows that the magnetisation increases smoothly with increasing applied dc field without saturation even at 7 T or in the case of **46** (Dy) even at 9T (Figure 103). Only in the case of **44** (Gd) can a well-defined saturation be observed. The magnitude of magnetisation is also given in Table 52. This behaviour indicates the presence of magnetic anisotropy. Furthermore, the plots of the M versus H/T at low temperatures for compounds **42-48** show that the curves are not superposed, as would be expected for an anisotropic system, giving a further indication of the presence of magnetic anisotropy and also the low-lying excited states already suggested.

The presence of magnetic anisotropy was probed further by examining the magnetisation relaxation under zero dc field for all compounds **42-48** with an oscillating ac field of 3 Oe. It was found that only compound **46** (Dy) exhibits slow relaxation of its magnetisation under these conditions. Figure 106 shows that the frequency dependence of both in-phase and out-of-phase components can be observed in zero dc field below 3.3 K indicating potential slow relaxation of the magnetisation. The ratio of the intensity of the in-phase and out-of-phase signal is about 4.5:1, which indicates that this behaviour is intrinsically molecular (Benelli, 2002: 2369ff).

In addition, frequency sweeping ac susceptibilities (Figure 107) were measured at different temperatures, and frequency dependence indicates that this compound is a SMM. To study the relaxation behaviour further and check for quantum tunnelling effects above 1.8 K, the frequency dependence of the ac susceptibility at 1.8 K was also measured with application of small dc fields up

to 600 Oe. In SMMs with a relaxation partially influenced by quantum effects, the application of a small dc field removes the ground state degeneracy and thus the possibility of quantum tunnelling, inducing a slowing down of the magnetisation relaxation (Koizumi, 2007: 8445ff; Lecren, 2005: 11311ff). Apart from compound **46** (Dy), which shows single molecule magnet behaviour, all other compounds show no significant frequency dependence of the ac measurements and thus no indication for SMM behaviour.

An Arrhenius plot was constructed from the ac χ_M'' vs. ν data for compound **46** (Dy) and gave $U_{\text{eff}} = 3.6$ K and $\tau_0 = 5.2 \cdot 10^{-6}$ s, where τ_0 is the pre-exponential factor (Figure 109). The ac data are one source of kinetic data, since at the temperature of the peak maximum of the χ_M'' signal, the relaxation rate $1/\tau$, where τ is the relaxation lifetime, is equal to the angular frequency ω ($\omega = 2\pi\nu$, where ν is the ac field oscillation frequency) (Brechtin, 2005: 502ff). The U_{eff} of 3.8 K is hence even lower than the energy barriers in pure planar Dy_4 -compounds, where the values for U_{eff} are between 6.2 K and 170 K and the pre-exponential factors range between $2.4 \cdot 10^{-5}$ and $4 \cdot 10^{-7}$ s (Abbas, 2010: 8067ff; Zheng, 2008: 10813ff; Lin, 2009: 9489ff).

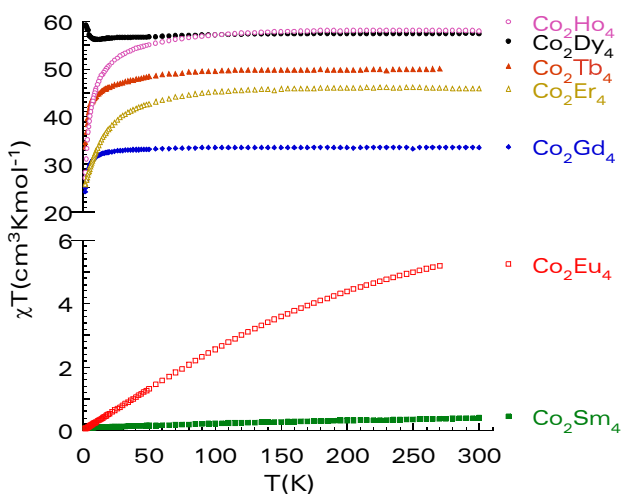


Figure 98: Temperature dependence of the χT product for polycrystalline samples of compounds **42-48** at 1000 Oe.

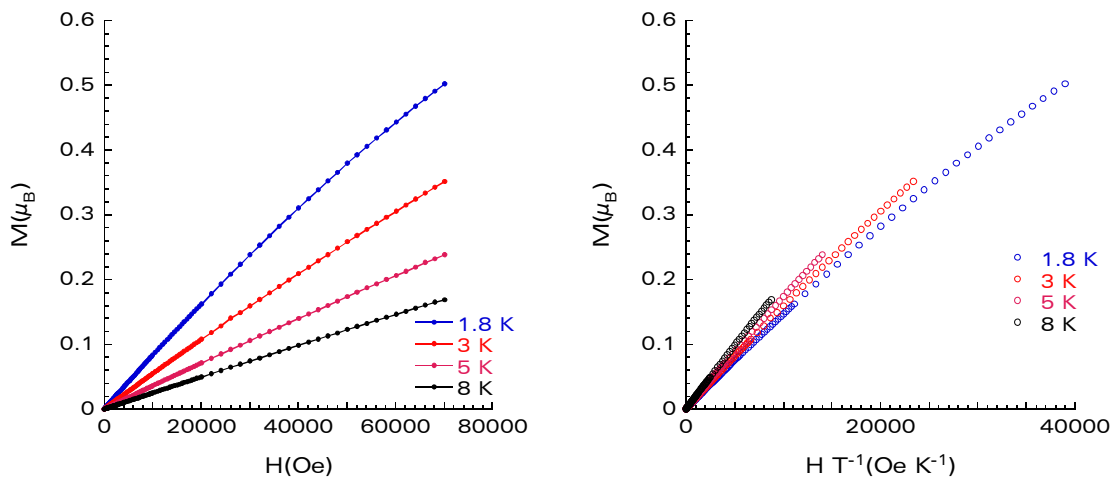


Figure 99: Plot of magnetisation (M) vs. H and H/T , respectively, between 1.8 K and 8 K for **42**. The solid lines are to guide the eye.

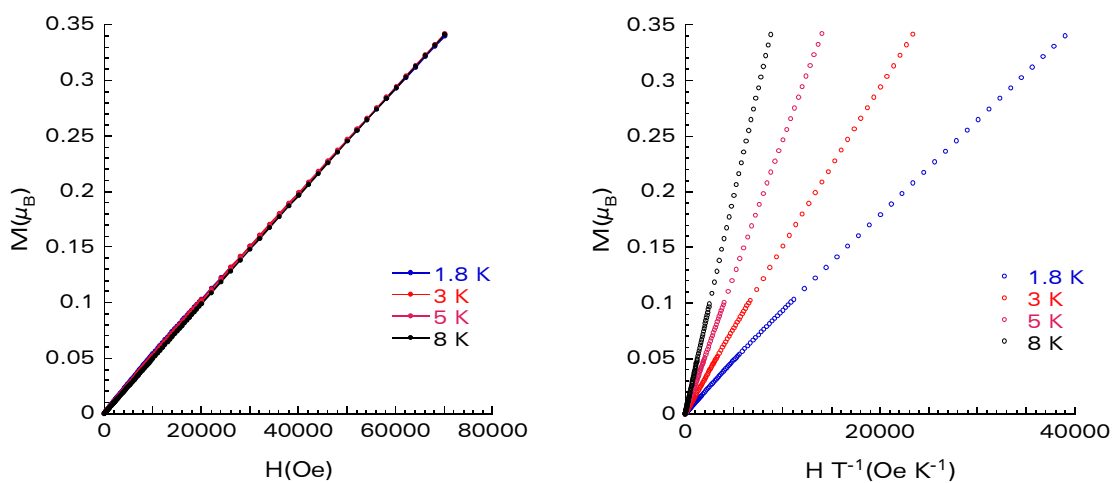


Figure 100: Plot of magnetisation (M) vs. H and H/T , respectively, between 1.8 K and 8 K for **43**. The solid lines are to guide the eye.

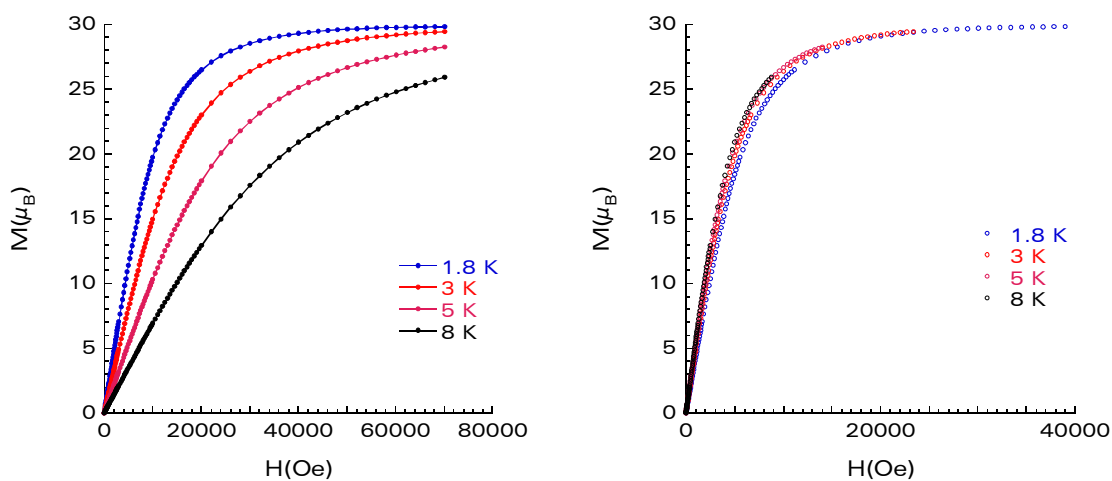


Figure 101: Plot of magnetisation (M) vs. H and H/T , respectively, between 1.8 K and 8 K for **44**. The solid lines are to guide the eye.

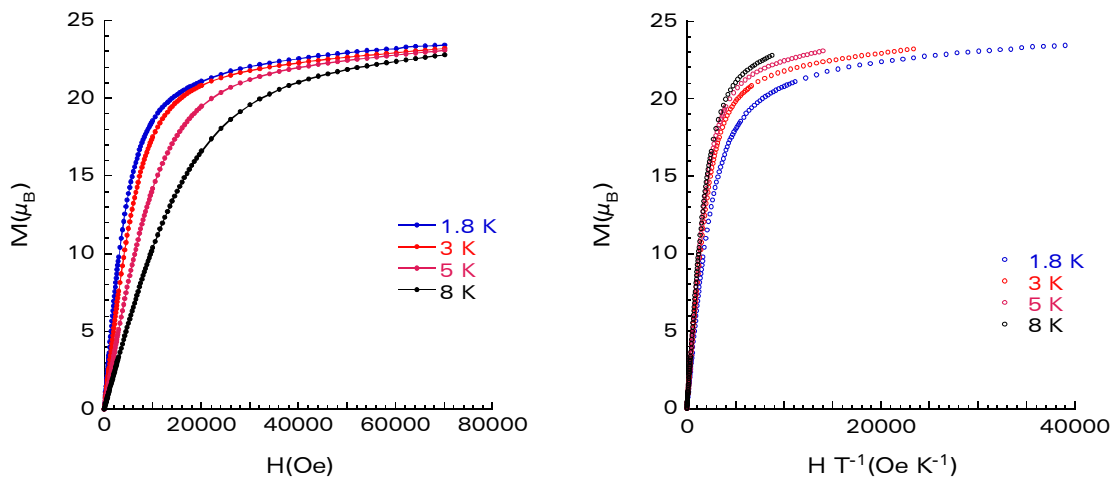


Figure 102: Plot of magnetisation (M) vs. H and H/T , respectively, between 1.8 K and 8 K for **45**. The solid lines are to guide the eye.

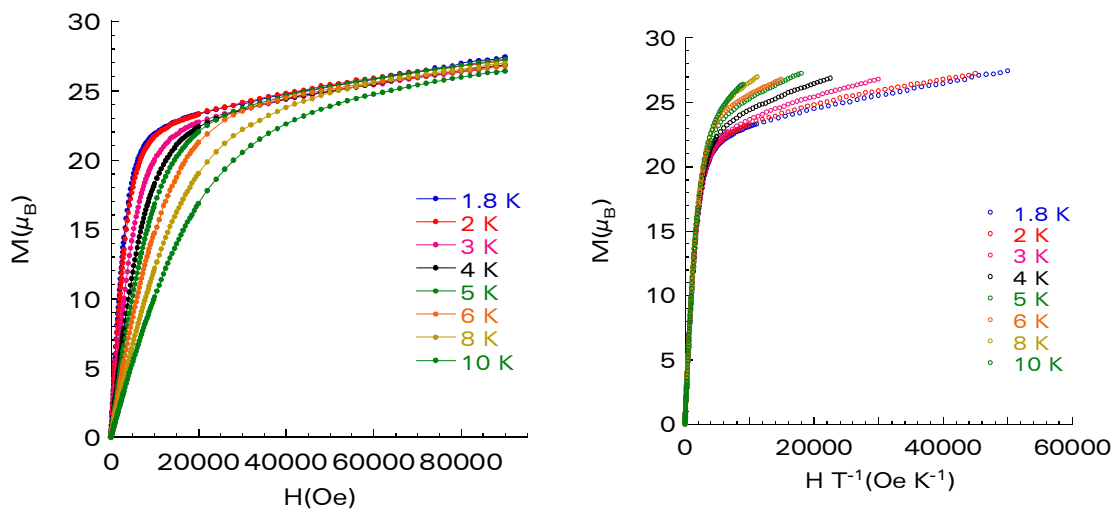


Figure 103: Plot of magnetisation (M) vs. H and H/T , respectively, between 1.8 K and 10 K for **46** up to 9T. The solid lines are to guide the eye.

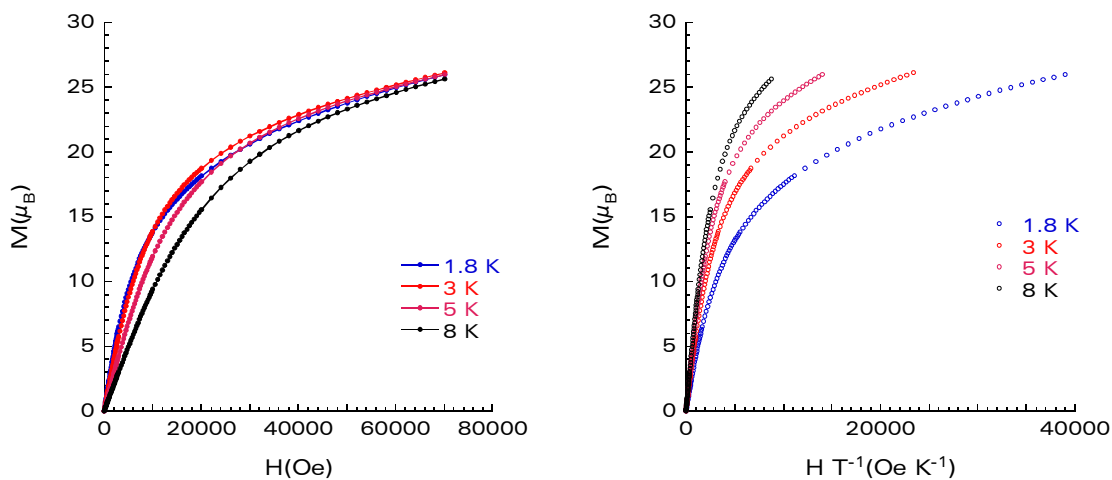


Figure 104: Plot of magnetisation (M) vs. H and H/T , respectively, between 1.8 K and 8 K for **47**. The solid lines are to guide the eye.

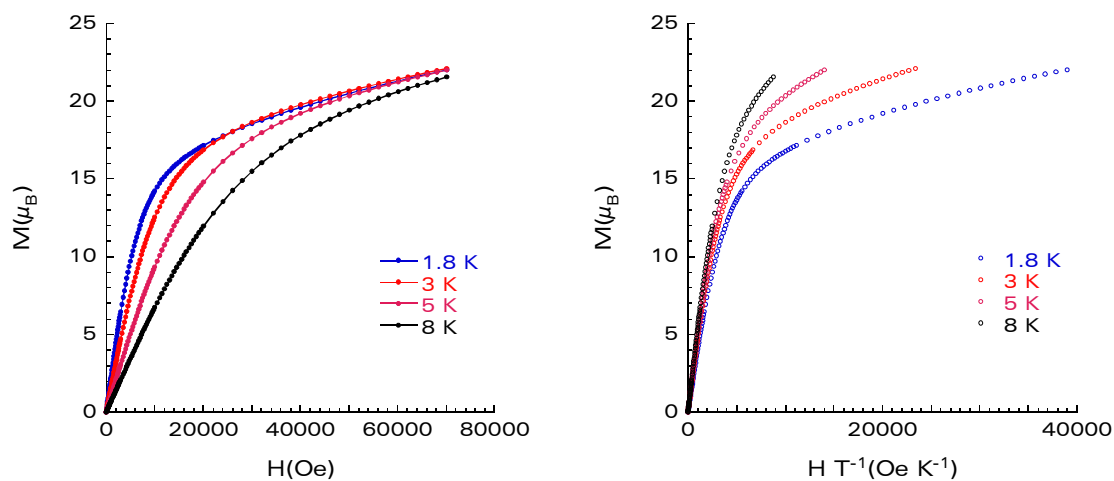


Figure 105: Plot of magnetisation (M) vs. H and H/T , respectively, between 1.8 K and 8 K for **48**. The solid lines are to guide the eye.

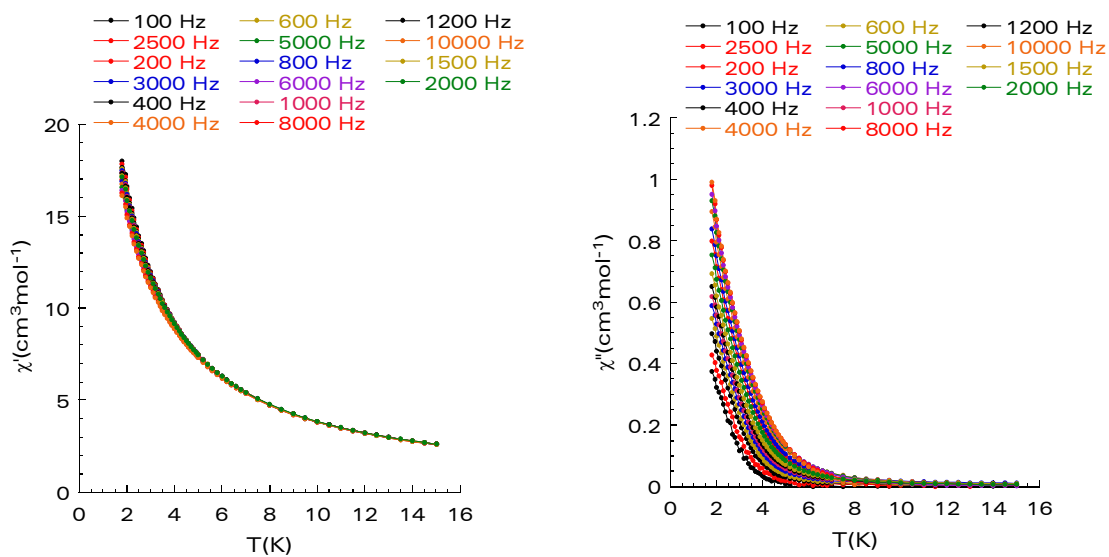


Figure 106: Temperature dependence of the in-phase (χ') and the out-of-phase (χ'') ac susceptibility components at different frequencies for **46**.

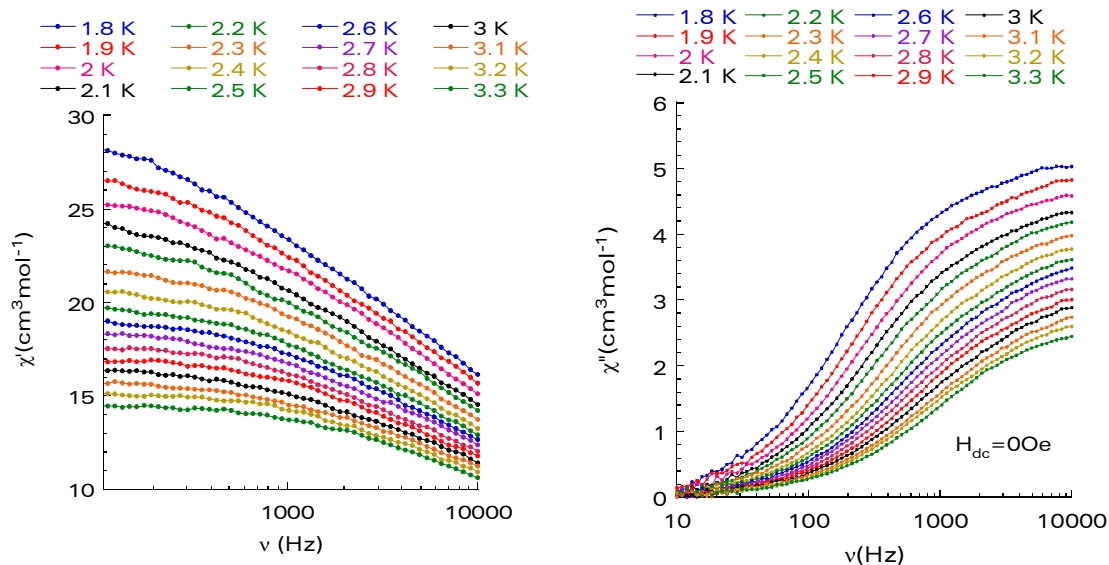


Figure 107: Zero dc field ac susceptibility measurements for **46** as a function of the frequency at different temperatures in-phase (left) and out-of-phase signals (right).

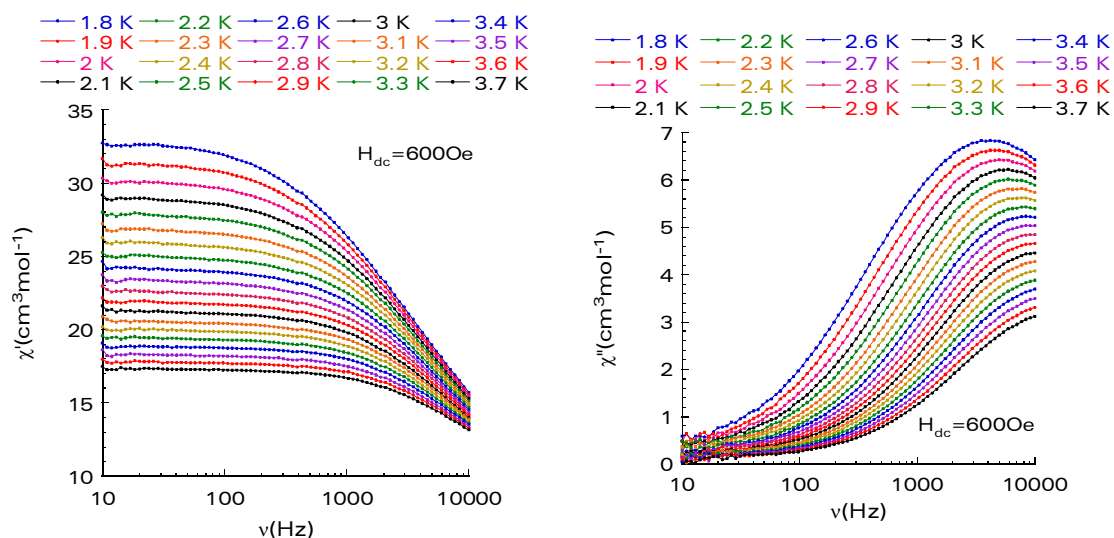


Figure 108: Ac susceptibility measurements for **46** as a function of the frequency at different temperatures in-phase (left) and out-of-phase signals (right) with an applied dc field of 600 Oe.

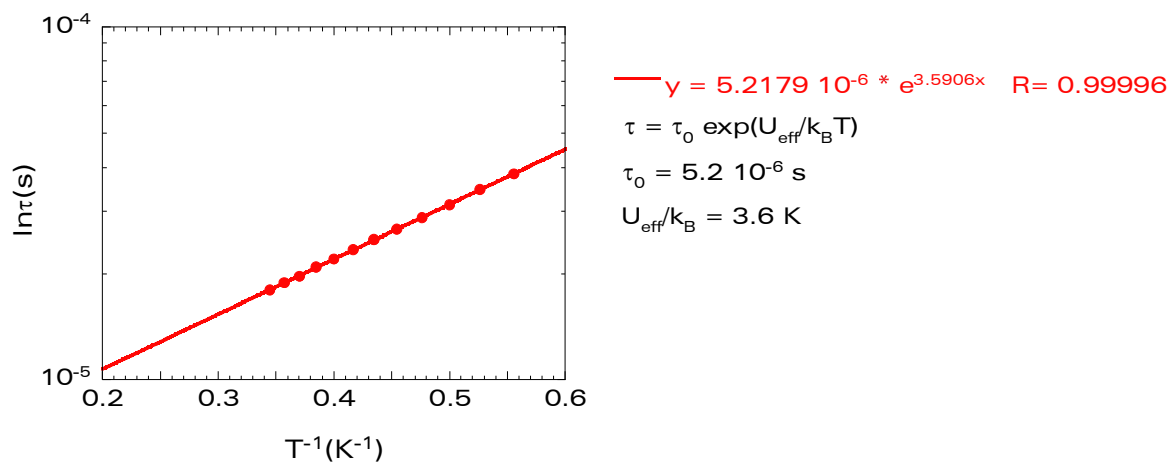


Figure 109: Plot of relaxation time (τ) vs. $1/T$ using ac χ''_M data for complex **46**. The solid line is the fit of the data to the Arrhenius equation.

5 Summary

The compounds obtained within this thesis exhibit a wide range of structural motifs and interesting magnetic properties. The results were divided into three parts: *3d-4f* complexes containing manganese, iron and cobalt as transition metal, respectively. Numerous compounds were successfully synthesised, crystallographically characterised and many of them were studied magnetically.

Within this thesis a synthetic method has been developed in order to have access to a wide range of different structural motifs exhibiting different magnetic properties. In this development polynuclear precursor compounds were used to obtain with the help of various crystallisation types suitable crystals for X-ray measurements. In order to study these compounds, a systematic survey with a variation of *3d* metals with different d^n configurations was successfully done.

In Chapter 2 Mn-Ln complexes were presented containing Mn in d^3 , d^4 and d^5 configuration. One highlight was a ring structure containing two dinuclear Mn^{III}-Mn^{IV} units, six Ln^{III} and two Li⁺ ions. The structural motif thus represents a combination of *2s*, *3d* and *4f* elements, exhibiting SMM behaviour in the case of the Dy derivative. Calcination yielded a mixed-metal oxide which was shown to be an effective catalyst for the oxidation of CO to CO₂. Another highlight in this chapter was the combination of three different oxidation states of manganese within one compound in combination with a *4f* metal, which represents the first example of such an aggregate.

In chapter 3 a number of d^5 configuration iron compounds containing Ln^{III} ions are described. The highlight here was the synthetic strategy, with which a series of six hexanuclear [Fe^{III}₄Ln^{III}₂(μ₄-O)₂(nBu-dea)₄(piv)₄(NO₃)₂(H₂O)₂] **30-35** complexes could be obtained. The strongly antiferromagnetically coupled Fe^{III} ions are unlikely to contribute to any slow relaxation of the system, in cases where the system contains any anisotropic lanthanide ions. Since the Fe^{III}₄-Ln^{III}₂ complexes reported here do not contain sufficiently anisotropic lanthanides, no SMM-behaviour in the temperature range used for the experiments was observed. Nevertheless it should be part of future work to prepare the Dy analogue in higher yield in order to determine if this analogue exhibits slow relaxation of magnetisation.

Chapter 4 describes eight complexes comprising two diamagnetic Co^{III} ions flanking a Dy₄ butterfly core. The magnetic study of the Dy derivative showed interesting behaviour. Although it might be assumed that the diamagnetic Co^{III} ions will not affect the magnetic behaviour of the Dy^{III}₄ core, already known for its SMM behaviour, it was found that the height of the energy barrier was essentially halved as a result of the presence of the Co^{III}. It was also interesting to compare this motif with the Mn₂Dy₄-aggregate described in chapter 2. It is well known, that the *3d* and *4f* anisotropies can have an additive or subtractive effect, according to the geometries of the resulting complexes.

In the case described here the additional d^4 anisotropy from the Mn^{III} ions in Mn_2Dy_4 does not seem necessary or even helpful to improve the SMM behaviour of the Dy_4 SMM. This might be explained by the fact, that in the Co^{III} aggregate the μ_3 -bridging oxygens are in fact hydroxy ligands, while in the Mn aggregate $3d$ metals are connected directly to the oxygens within the butterfly.

The use of lanthanides to obtain new structural motifs with improved magnetic properties seems to be a promising strategy. The reasons are the often high anisotropy and large spin contributed by Ln^{III} ions. The ground terms indicate large spin orbital contribution for lanthanides (except for Gd^{III}) and the anisotropy can vary from easy to hard axis in nature, depending on the geometry of the ligand field. It seems that subtle changes to the environment of the Ln^{III} ion can exert large effects on the electronic properties, as seen in the case of Mn_2Dy_4 and Co_2Dy_4 .

6 Conclusion

New synthetic strategies were developed for the synthesis of *3d-4f* heterometallic complexes, and a variety of such *3d-4f* compounds with diverse structures and, in some cases, novel topologies have been synthesised. The magnetic properties of the compounds were investigated, and some show magnetic slow relaxation consistent with Single Molecule Magnet behaviour. It was noted that the complexes showing the clearest SMM behaviour were those involving isotropic or even diamagnetic transition metal ions. A possible explanation might be that if the uniaxial anisotropy contribution from cations such as Mn^{III} is to some extent orthogonal to that from the lanthanide ions, then the overall molecular uniaxial anisotropy would be reduced, not enhanced.

The orbital contribution to the electronic properties of most lanthanide ions, which can result in large anisotropies, also means that understanding the magnetic properties of complexes involving lanthanide ions is still far from straightforward. However, the availability of more sophisticated physical measurements and recent advances in *ab initio* calculation methods is dramatically improving this area of magnetochemistry, and in the not too distant future a much clearer view of magnetic interactions involving lanthanide ions can be expected. For this to be possible, though, a range of *3d-4f* systems needs to be available, and the compounds described in this thesis might be then considered as useful model systems for the study of magnetic interactions involving lanthanide and transition metal ions.

This work has opened the next phase of exploration of *3d-4f* metal complexes through the use of novel precursors. However, given the large number of combination of *3d* and *4f* metal ions there is still much work to be done before systematic trends can be identified.

7 Experimental section

7.1 Elemental analysis

Elemental analyses for C, H and N were performed using an Elementar Vario EL analyser and were carried out at the Institute of Inorganic Chemistry, Karlsruhe Institute of Technology. The analyses were done in duplicate and the value given as "found" is the average of results. Since calculated values for the solvent-free and solvated compounds can differ enormously, the calculated values for both are given.

Samples lose solvent easily, which is reflected in the results of the elemental analyses. This, coupled with the fact that volatile lattice solvents are easily replaced by water molecules, explains the different overall formulations for the compounds when comparing X-ray crystal structure analyses with the results of the microanalysis experiments.

7.2 Fourier-Transform-Infrared-Spectroscopy (FT-IR)

FT-IR spectroscopy was used to characterise the synthesised coordination compounds by observing the characteristic bands for the organic ligands, principally in the fingerprint region. The spectra were measured using KBr disks which were prepared by mixing a few milligrams of sample with ca. 100 mg of KBr and grinding them together. The mixture was then formed into a transparent disk using a KBr-press in which an evacuated die is subjected to 12 kbar of pressure. The FT-IR spectra were recorded on a Perkin-Elmer Spectrum One FT-IR spectrometer in the region from 400 cm^{-1} to 4000 cm^{-1} in transmittance mode using eight scans at a resolution of 4 cm^{-1} .

7.3 X-ray diffraction on single crystals

X-ray crystallography is a very powerful tool to determine the detailed structure of molecules, whenever suitable crystals are available (Lippard, 1995: 81f). It is based on the diffraction of X-radiation from the regular three-dimensional array of atoms in the crystal. This diffraction can be conveniently thought of in terms of the reflection of a monochromatic beam of X-rays off a set of parallel planes of atoms in the crystal, with the conditions for such diffraction of the incident beam given by the Bragg law:

$$n\lambda = 2d \cdot \sin\theta \quad (7.1)$$

Here n is an integer that indicates the diffraction order (generally $n = 1$), λ is the wavelength of the X-ray beam, d is the distance between parallel lattice planes, and the angle θ is the so called Bragg-angle between the incident X-ray beam and the lattice plane, such that the angle between the incident and diffracted beams is 2θ .

The relative intensities of the beams diffracted by each of the large numbers of such planes from a typical crystal is related to the distribution of electron density (and thus to the molecular structure) within the unit cell of the crystal lattice by a process of Fourier transformation.

The X-ray crystal structure analyses for this dissertation were measured on two different diffractometers: a *STOE IPDS II* and *Bruker Smart Apex* of the companies Stoe and Bruker, respectively.

The radiation source was either a conventional sealed X-ray tube or a rotating anode, in both cases graphite-monochromated Mo-K α radiation ($\lambda = 0.71069 \text{ \AA}$) was used. The crystals used for the measurements were selected under an optical microscope and attached to a glass fibre on the goniometer head using perfluoropolyether oil, and cooled (to 180, 150 or 100 K, depending on the diffractometer) to prevent crystal decomposition by loss of lattice solvent. The crystal was then rotated through a small angle (0.3-1.3 $^\circ$) about an axis; during this rotation many reflections pass through the diffraction condition given by the Bragg law, and these reflections give rise to a pattern of small spots on the area detector. After readout of this frame, the detector is erased, and the process is repeated for the next small angle, until the crystal has been rotated through at least 180 $^\circ$. The unit cell is usually determined from the positions of indexed reflections from a small selection of all the frames recorded. The intensities of each reflection on each image can then be integrated to give raw intensities for each reflection **hkl**, and these intensities can be corrected semi-empirically for crystal absorption using SADABS (Sheldrick, 1996) to give the final dataset.

The structures were solved using direct methods, followed by full matrix least-squares refinement of the atomic parameters (coordinates and temperature factors) against F^2 (all data) using SHELXTL (Sheldrick, 2003), in which the residual wR_2 is minimised during the refinement. The residual factors R_1 and wR_2 are defined as:

$$R_1 = \frac{\sum ||F_o| - |F_c||}{\sum |F_o|}$$

$$wR_2 = \sqrt{\frac{\sum w(F_o^2 - F_c^2)^2}{\sum w(F_o^2)^2}}$$

where $|F_o|$ is the structure factor for a given reflection obtained from the raw data after collection, integration reduction and absorption correction. $|F_c|$ is the corresponding structure factor calculated from the structural model. The value w is the weight for each structure factor and depends on the accuracy with which the intensity of the corresponding reflection was measured.

w is defined as:

$$\frac{1}{w} = \sigma^2 F_0^2 + (aP)^2 + bP$$

where P is defined as:

$$P = \frac{\text{Max}(F_0^2, 0) + 2F_c^2}{3}$$

Normally the final value of wR_2 should be lower than 0.15 for a well refined structure.

Another important factor is the Goodness of Fit, S, which is defined as:

$$S = \sqrt{\frac{\sum w(F_0^2 - F_c^2)^2}{(n-p)}}$$

where n is the number of unique reflections and p is the total number of parameters refined. Values for S, which are not close to 1.0, indicate that the weighting scheme should be adjusted. If S is far from unity it indicates twinning problems or the wrong choice of space group. After the refinement R_1 is calculated from the "observed" data with intensity such that $F_o^2 \geq 2\sigma(F_o^2)$. Satisfactory refinement usually results in R_1 having a value lower than 0.05.

7.4 X-ray Powder diffraction

X-ray Powder diffraction (XRPD) is an analytical technique which is mainly used for phase identification of a crystalline material and can provide information on unit cell dimensions. It can be used to establish the purity of a bulk sample by comparison with the diffraction pattern simulated from the crystal structure determined from a single crystal; in this way it can be confirmed that the crystal used for the structural determination was representative of the bulk sample. In particular, when a series of compounds is synthesised that differ only in the rare earth ion (LnIII) used, XRPD can establish whether the complexes crystallise isomorphously, and are thus isostructural. One disadvantage is that significantly more sample is needed than in the case of single crystal X-ray studies. If the sample is not microcrystalline, it is necessary to grind it finely, to prevent any preferential orientation of the crystallites.

The sample is irradiated with a monochromatic X-ray beam (Cu-K α in the present study) and the diffracted intensity is measured as a function of the scattering angle 2theta.

7.5 Magnetic measurements

Magnetic susceptibility measurements were obtained using a Quantum Design MPMS-XL SQUID susceptometer with an external magnetic field of 7 T. The measurements were performed on polycrystalline samples.

The magnetic data were corrected for the diamagnetic contribution due to the sample holder as well as the diamagnetic contribution for the sample, which was calculated using Pascal's constants (Bain, 2008: 532ff).

7.6 Mössbauer spectroscopy

The Mössbauer spectra were acquired using a conventional spectrometer in the constant-acceleration mode equipped with a ^{57}Co source (3.7 GBq) in a rhodium matrix. Isomer shifts are given relative to $\alpha\text{-Fe}$ at room temperature. The polycrystalline sample was inserted in an Oxford Instruments Mössbauer-Spectromag 4000 Cryostat, which has a split-pair superconducting magnet system for applied fields up to 5 T, with the field of the sample oriented perpendicular to the γ - ray direction, while the sample temperature can be varied between 3.0 and 300 K. Spectra were fitted using the Normos Mössbauer fitting program.

7.7 Some magnetic parameters for lanthanides ions

Ln	config. Ln^{3+}	Ground state	Number of unpaired e^-	χT	Observed χT	g
La	$4f^0$	1S_0	0	0	0	-
Ce	$4f^1$	$^2F_{5/2}$	1	0.81	0.7-0.8	0.86
Pr	$4f^2$	3H_4	2	1.60	1.4-1.6	0.80
Nd	$4f^3$	$^4I_{9/2}$	3	1.64	1.5-1.6	0.73
Sm	$4f^5$	$^6H_{5/2}$	5	0.09	0.2-0.4	0.29
Eu	$4f^6$	7F_0	6	0	1.4-1.5	-
Gd	$4f^7$	$^8S_{7/2}$	7	7.88	7.8-8	2
Tb	$4f^8$	7F_6	6	11.81	11.3-12	1.5
Dy	$4f^9$	$^6H_{15/2}$	5	14.18	13.5-14	1.33
Ho	$4f^{10}$	5I_8	4	14.05	13.5-14.3	1.25
Er	$4f^{11}$	$^4I_{15/2}$	3	11.47	11-11.5	1.2
Yb	$4f^{13}$	$^2F_{7/2}$	1	2.58	2.3-3	1.14
Lu	$4f^{14}$	1S_0	0	0	0	-

Calculation of the g -factor for lanthanides:

$$g_{\text{Nd}^{3+}} = g_J \sqrt{J(J+1)} = 3.62^2$$

$$g_J^2 \cdot J(J+1) = 13.10$$

$$g^2 = \frac{13.10}{\frac{9(9+1)}{2(2+1)}}$$

$$g_{\text{Nd}^{3+}} = 0.73$$

Calculation of the expected χT values:

e.g. $[\text{Mn}^{\text{III}}_2\text{Dy}^{\text{III}}_4]$ complex

$$\mu_{\text{eff}}^2 = \sqrt{n_{\text{Mn}} \cdot S(S+1)g + n_{\text{Dy}} \cdot \mu_{\text{eff}}^2}$$

$$\mu_{\text{eff}} = \sqrt{2 \cdot \frac{4}{2} \left(\frac{4}{2} + 1 \right) 2 + 2 \cdot 10 \cdot 65^2} = \sqrt{24 + 226.85} = \sqrt{250.85}$$

$$\mu_{\text{eff}}^2 = 8\chi T$$

$$\chi T = \frac{250.85}{8} = 31.36 \text{ cm}^3 \text{ K mol}^{-1}$$

7.8 Synthetic approach

All starting materials apart from the lanthanide salts (Bünzli, 1989: 432ff) and manganese precursors were used as received without any further purification. The described manipulations were all performed under aerobic conditions.

7.9 Synthesis of precursor compounds

7.9.1 Manganese Precursor Compounds

7.9.1.1 $[\text{Mn}^{\text{III}}_2\text{Mn}^{\text{II}}_4\text{O}_2(\text{O}_2\text{CCMe}_3)_{10}(\text{py})_{2.5}] \cdot (\text{HO}_2\text{CCMe}_3)_{1.5} (1)$

To a mixture of $\text{Mn}(\text{CH}_3\text{COO})_2 \cdot 4\text{H}_2\text{O}$ (20 g, 81.61 mmol) and KMnO_4 (6.1 g, 38.6 mmol) was added 2,2-dimethylpropanoic acid (105 g, 1.03 mol). The mixture was heated at 300°C until the solution became colourless. Then the solution was cooled to 100°C and became slightly brown. Acetonitrile (180 mL) and pyridine (4 mL) were added and the mixture stirred for 5 minutes at 100°C. Afterwards the solution was left to cool to room temperature and a watch glass placed over the beaker to allow for slow crystallisation. After one day, red-brown crystals form and can be isolated by filtration. Further crystals can be harvested from the filtrate.

The air-dried products from all the batches were combined and dissolved in diethyl ether and the solution was then filtered. The filtrate was allowed to evaporate to dryness and dried under vacuum (Mereacre, 2008: 3577ff).

Selected IR data (KBr pellet):

$\tilde{\nu}$ = 2960.5 (s), 2927.1 (m), 2927.3 (m), 1692.2 (m), 1618.7 (m), 1591.6 (vs), 1570.5 (vs), 1482.9 (vs), 1458.7 (w), 1416.2 (vs), 1374.4 (s), 1359.4 (s), 1319.1 (w), 1229.3 (s), 1207.4 (m), 1030.2 (w), 1013.2 (w), 979.1 (w), 936.5 (w), 894.6 (w), 804.5 (w), 786.2 (w), 725.7 (w), 612.7 (s), 584.0 (m), 556.2 (m), 532.4 (w), 489.1 (w), 437.9 cm^{-1}

(v = very, s = strong, m = medium, w = weak, br = broad).

Elemental Analysis:

$C_{70}H_{117.5}Mn_6O_{25}N_{2.5}$ (1722.89 g/mol)

calculated: C 48.80, H 6.82, N 2.03;

found: C 48.53, H 6.99, N 1.88.

7.9.1.2 $Mn^{II}(CHCl_2COO)_3 \cdot 4H_2O$ (2)

A solution of dichloroacetic acid (10 mL) in water (50 mL) was heated to 100°C. $MnCO_3 \cdot xH_2O$ was added in small portions to the stirred mixture until no further foam formation was observed corresponding to the completion of the decarboxylation reaction. The mixture was filtered while still hot to isolate a clear solution from any unreacted $MnCO_3$. The resulting filtrate was evaporated to dryness.

Elemental Analysis:

$C_6H_3MnO_6Cl_6$ (438.72 g/mol)

calculated: C 16.43, H 0.68, N 0.00;

found: C 16.28, H 0.85, N 0.00.

7.9.1.3 $[Mn^{III}_8Mn^{IV}_4O_{12}(CH_3COO)_{12}(CHCl_2COO)_4] \cdot 4H_2O$ (3)

A solution of acetic acid (24 mL) and water (16 mL) was heated to 50°C. Then 1.5 g (3.92 mmol) $Mn(CHCl_2COO)_2 \cdot 4H_2O$ were added and dissolved completely, the solution cooled to room temperature, put in a petri dish and 0.24 g (1.52 mmol) $KMnO_4$ added with slow stirring for one minute. After this the petri dish was covered with a watch glass to allow for slow evaporation. Small black crystals were obtained after between one and three days.

Elemental Analysis:

$C_{32}H_{56}Mn_{12}O_{52}Cl_8$ (2215.19 g/mol)

calculated: C 17.35, H 2.53, N 0.00;

found: C 17.27, H 2.72, N 0.00.

7.9.2 Cobalt Precursor Compounds

7.9.2.1 $[Co^{II}_2(\mu-OH_2)(O_2CCMe_3)_4(HO_2CCMe_3)_4]$ (4)

$CoCO_3$ (4.0 g, 34 mmol) was treated with an excess of 2,2-dimethylpropanoic acid (20.0 g, 196 mmol) in the presence of water (3 mL) at 100°C for 24h, leading to dissolution of the carbonate salt. The solution was cooled to room temperature, MeCN (50 mL) was added and the mixture stirred briefly. The solution was filtered and cooled to 5°C, yielding pink crystals after one day. To increase the yield, the solution was then cooled to -18°C for two days to give a second crop of the cobalt pivalate compound. The second crop was collected by filtration, washed with cold MeCN and dried in a slow flow of N_2 (Aromí, 2003: 5142ff).

Elemental Analysis:

$C_{40}H_{78}Co_2O_{17}$ (948.90 g/mol)

calculated: C 50.63, H 8.29, N 0.00;

found: C 50.46, H 8.39, N 0.00.

7.9.2.2 $[Co^{III}_3(\mu_3-O)(O_2CCMe_3)_6(py)_3] \cdot O_2CCMe_3 \cdot H_2O \cdot 3.5HO_2CCMe_3$ (**5**)

4 (4 g, 4.2 mmol) was dissolved in pyridine (2 g, 25.3 mmol) and 2,2-dimethylpropanoic acid (20 g, 195.8 mmol) at 80°C.

Air was passed through the solution overnight, which changed colour from pink to brown and large dark brown crystals of $[Co^{III}_3(\mu_3-O)(O_2CCMe_3)_6(py)_3] \cdot O_2CCMe_3 \cdot H_2O \cdot 3.5HO_2CCMe_3$ were formed. The crystals were collected by filtration and washed with CCl_4 (Aromí, 2003: 5142ff).

Elemental Analysis:

$C_{67.5}H_{115}Co_3O_{23}N_3$ (1512.53 g/mol)

calculated: C 53.60, H 7.66, N 2.78;

found: C 53.61, H 7.74, N 2.74.

7.9.3 Iron Precursor Compounds

7.9.3.1 $[Fe^{III}_3O(O_2CCMe_3)_6(H_2O)_3]^+ [O_2CCMe_3] \cdot 2HO_2CCMe_3$ (**6**)

A slurry of $Fe(NO_3)_3 \cdot 9H_2O$ (10 g, 24.8 mmol) and 2,2-dimethylpropanoic acid (28.0 g, 274.0 mmol) was heated and maintained at 270°C over 2 h until the elimination of NO_2 stopped. Upon cooling to 100°C, ethanol (85 mL) and water (15 mL) were added slowly under stirring. Overnight, red-brown hexagonal prisms formed. These were isolated by filtration and recrystallised from a mixture of ethanol (50 mL) and water (10 mL). After 4 days the microcrystalline product was collected by filtration and washed with benzene and hexane and dried in vacuum leading to solvent-free **6**.

Elemental Analysis:

$C_{45}H_{90}Fe_3O_{22}$ (1149.71 g/mol)

calculated: C 47.01, H 7.80, N 0.00;

found: C 46.83, H 8.01, N 0.00.

7.9.3.2 $[Fe_6(O_2)(O_2)(O_2CCMe_3)_{12}(HO_2CCMe_3)_2]$ (**7**)

6 (0.6 g 0.58 mmol) were added to a mixture of THF (6 mL) and acetonitrile (6 mL). Then 20 drops of H_2O_2 (30%) were added to the stirred solution, followed by two further hours of stirring at room temperature. The turbid solution was then filtered and the microcrystalline product was dried in vacuum (Çelenligil-Çetin, 2000: 5838).

1H NMR (CD_2Cl_2): δ 8.19 (s, br, 18H, $(CH_3)_3CCO_2$), 6.94 (s, br, 72H, $(CH_3)_3CCO_2$), 6.25 (s, br, 18H, $(CH_3)_3CCO_2$), 1.29 (s, br, 18H, $(CH_3)_3CCO_2$).

Elemental Analysis:

$C_{70}H_{128}Fe_6O_{32}$ (1816.82 g/mol)

calculated: C 46.28, H 7.10, N 0.00;

found: C 46.55, H 7.29, N 0.00.

7.9.4 Lanthanide Precursor Compounds

7.9.4.1 $[Dy_2(O_2CCMe_3)_6(HO_2CCMe_3)_6] \cdot HO_2CCMe_3$ (**8**)

$Dy_2(O_2CCMe_3)_6(HO_2CCMe_3)_6 \cdot HO_2CCMe_3$ was prepared by a slight modification of a literature method (Fomina, 2004: 1349ff).

To a slurry of Dy_2O_3 (10 g, 26.81 mmol) in water a total of 10 mL of concentrated HNO_3 was added in small portions. Upon heating at 250°C a pale yellow solid was obtained. Then, 2,2-dimethylpropanoic acid (28 g, 274.0 mmol) was added and the mixture was heated at 200°C for one hour until the elimination of NO_2 stopped. After cooling the solution to 80°C, acetonitrile (180 mL) was added slowly and the mixture was stirred for a further two minutes. After this, the solution was cooled to room temperature and covered with a watch glass to allow slow crystallisation. The crystals were isolated by filtration and washed with acetonitrile.

Selected IR data (KBr pellet):

$\tilde{\nu} = 3435.5$ (sbr), 2963.1 (ms), 2930.6 (m), 2971.0 (w), 2066.9 (w, br), 1637.5 (s), 1546.4 (s), 1518.5 (s), 1486.1 (s), 1459.2 (m), 1431.9 (s), 1384.1 (s), 1363.8 (s), 1231.4 (m), 1032.7 (w), 902.3 (wm), 811.4 (wm), 790.8 (m), 610.9 (m), 559.8 (m) cm^{-1}

(v = very, s = strong, m = medium, w = weak, br = broad).

Elemental Analysis:

$C_{60}H_{114}Dy_2O_{24}$ (1646.66 g/mol)

calculated: C 47.41, H 7.59, N 0.00;

found: C 47.73, H 7.35, N 0.00.

7.10 Synthetic procedure for the described compounds

7.10.1 $[Mn^{II}_2La^{III}_2(hmp)_6(piv)_2(NO_3)_4] \cdot 2acetone$ (**9**)

$La(NO_3)_3 \cdot 6H_2O$ (0.029 g, 0.07 mmol) and hmpH (0.09 g, 0.82 mmol) were stirred in acetone (10 mL) at room temperature for 10 minutes. Then the mixture was stirred at boiling temperature for 3 minutes and **1** (0.07 g, 0.04 mmol) were added. The slurry was stirred at boiling temperature for further 5 minutes before it was allowed to cool down to room temperature. The dark black solution was filtered and sealed with Parafilm in which two tiny holes had been pierced. After 4 days well-formed dark brown crystals of **9**, suitable for X-ray crystallography had formed.

Yield: 0.034 g (17 % with respect to manganese)

Selected IR data (KBr pellet):

$\tilde{\nu}$ = 3414.9 (m), 2963.9 (w), 2925.0 (w), 2853.8 (w), 1715.0 (m), 1604.8 (s), 1568.5 (m), 1486.8 (s), 1467.7 (s), 1438.3 (s), 1403.0 (ms), 1384.8 (ms), 1362.3 (m), 1351.5 (ms), 1292.1 (s), 1222.4 (m), 1152.5 (m), 1059.1 (m), 1042.4 (s), 1029.7 (s), 1011.0 (mw), 897.0 (w), 819.9 (w), 760.4 (m), 567.1 (m) cm^{-1}
(v = very, s = strong, m = medium, w = weak, br = broad).

Elemental Analysis:

$\text{C}_{55}\text{H}_{72}\text{La}_2\text{Mn}_2\text{N}_{10}\text{O}_{25}$ (1660.90 g/mol)

calculated: C 39.77, H 4.37, N 8.43; (with solvent)

calculated: C 38.10, H 3.91, N 9.07; (without solvent)

found: C 38.96, H 4.01, N 8.99.

7.10.2 $\text{Mn}^{\text{III}}_4\text{La}^{\text{III}}_2(\mu_4\text{-O})(\mu_3\text{-O})(\text{hmp})_7(\text{OAc})(\text{DCAc})(\text{NO}_3)_5(\text{OH}_2)_{0.5}] \cdot 3\text{acetone}$ (10)

$\text{La}(\text{NO}_3)_3 \cdot 6\text{H}_2\text{O}$ (0.029 g, 0.07 mmol) and hmpH (0.09 g, 0.82 mmol) were stirred in acetone (10 mL) at room temperature for 15 minutes. Then the mixture was stirred at boiling temperature for 3 minutes and 0.04 g, (0.02 mmol) of **3** were added. The slurry was stirred at 70°C for further 5 minutes before it was allowed to cool to room temperature. The black solution was filtered and was kept sealed for 5 days to give well-formed black crystals of **10**.

Yield: 0.062 g (56 % with respect to manganese)

Selected IR data (KBr pellet):

$\tilde{\nu}$ = 3470.2 (s), 3414.5 (s), 3232.5 (wm), 2923.2 (w), 2845.9 (w), 1711.3 (wm), 1655.0 (w), 1637.6 (m), 1618.3 (m), 1569.4 (wm), 1537.9 (wm), 1474.8 (m), 1459.1 (m), 1438.5 (s), 1384.8 (s), 1365.0 (m), 1322.0 (ms), 1291.0 (s), 1223.0 (wm), 1157.7 (wm), 1065.4 (ms), 1044.0 (s), 819.3 (w), 764.2 (m), 721.8 (m), 670.9 (m), 621.0 (m), 566.4 (m), 474.6 (m) cm^{-1}
(v = very, s = strong, m = medium, w = weak, br = broad).

Elemental Analysis:

$\text{C}_{49}\text{H}_{54}\text{Mn}_4\text{La}_2\text{N}_{12}\text{O}_{29}\text{Cl}_2$ (1843.49 g/mol)

calculated: C 31.92, H 2.95, N 9.12; (with solvent)

calculated: C 28.78, H 2.17, N 10.07; (without solvent)

found: C 32.06, H 2.98, N 8.86.

7.10.3 $[\text{Mn}^{\text{III}}_2\text{Eu}^{\text{III}}_4(\mu_4\text{-O})_2(\text{hmp})_4(\text{pic})_2(\text{piv})_6(\mu\text{-N}_3)_2] \cdot 2\text{CH}_3\text{CN}$ (11)

$\text{EuCl}_3 \cdot 6\text{H}_2\text{O}$ (0.074 g, 0.20 mmol), hmpH (0.075 g, 0.69 mmol) and NaN_3 (0.05 g, 0.77 mmol) were dissolved in CH_3CN (15 mL). After 10 minutes stirring at room temperature, **1** (0.05 g, 0.029 mmol) was added. After a further two minutes of stirring at room temperature, KOH (0.05 g, 0.8 mmol) was added. The vial, in which the reaction took place, was closed completely but with one hole in the lid and stirred for 40 minutes at 70°C. The resulting dark brown solution was allowed to cool to room temperature and was filtered.

The vessel was closed with parafilm with five holes pierced into it to allow slow evaporation. After ten days, well-formed dark brown crystals appeared.

Yield: 0.012 g (6 % with respect to manganese)

Selected IR data (KBr pellet):

$\tilde{\nu}$ = 3395.6 (w, br), 2958.7 (m), 2927.2 (wm), 2901.6 (w), 2868.7 (w), 2081.1 (vs), 2036.8 (w), 1635.6 (s), 1611.4 (m), 1588.6 (s), 1568.9 (s), 1552.2 (m), 1528.7 (m), 1484.6 (s), 1458.7 (w), 1446.3 (m), 1426.9 (s), 1413.9 (ms), 1392.6 (m), 1375.4 (m), 1362.0 (m), 1341.0 (wm), 1288.0 (wm), 1226.6 (m), 1109.4 (wm), 1092.4 (m), 1049.4 (m), 1013.7 (w), 894.2 (w), 758.2 (m), 658.2 (m), 632.5 (m) cm^{-1}

(v = very, s = strong, m = medium, w = weak, br = broad).

Elemental Analysis:

$\text{C}_{70}\text{H}_{92}\text{Mn}_2\text{Eu}_4\text{O}_{22}\text{N}_{14}$ (2199.29 g/mol)

calculated: C 38.23, H 4.22, N 8.92; (with solvent)

calculated: C 37.44, H 4.09, N 7.94; (without solvent)

found: C 38.11, H 4.19, N 8.57.

7.10.4 $[\text{Mn}^{\text{III}}_2\text{Gd}^{\text{III}}_4(\mu_4\text{-O})_2(\text{hmp})_4(\text{pic})_2(\text{piv})_6(\mu\text{-N}_3)_2]\cdot 2\text{CH}_3\text{CN}$ (12)

The reaction was performed analogously to the synthesis of 11 but using 0.074 g (0.20 mmol) $\text{GdCl}_3\cdot 6\text{H}_2\text{O}$ in place of the $\text{EuCl}_3\cdot 6\text{H}_2\text{O}$.

Yield: 0.014 g (7 % with respect to manganese)

Selected IR data (KBr pellet):

$\tilde{\nu}$ = 3392.1 (w, br), 2959.7 (m), 2925.5 (w), 2902.6 (w), 2867.3 (w), 2080.1 (vs), 2037.4 (w), 1635.6 (s), 1612.6 (m), 1587.6 (s), 1567.3 (s), 1554.2 (m), 1527.4 (m), 1482.6 (s), 1458.7 (w), 1446.3 (m), 1427.9 (s), 1413.2 (ms), 1391.3 (m), 1376.6 (m), 1363.0 (m), 1342.0 (wm), 1289.0 (wm), 1226.6 (m), 1108.4 (wm), 1092.6 (m), 1049.3 (m), 1013.8 (w), 895.7 (w), 758.1 (m), 658.3 (m), 632.3 (m) cm^{-1}

(v = very, s = strong, m = medium, w = weak, br = broad).

Elemental Analysis:

$\text{C}_{70}\text{H}_{92}\text{Gd}_4\text{Mn}_2\text{O}_{22}\text{N}_{14}$ (2220.44 g/mol)

calculated: C 37.86, H 4.18, N 8.83; (with solvent)

calculated: C 37.07, H 4.05, N 7.86; (without solvent)

found: C 37.42, H 4.17, N 8.52.

7.10.5 $[\text{Mn}^{\text{III}}_2\text{Tb}^{\text{III}}_4(\mu_4\text{-O})_2(\text{hmp})_4(\text{pic})_2(\text{piv})_6(\mu\text{-N}_3)_2]\cdot 4\text{CH}_3\text{CN}$ (13)

The reaction was performed analogously to the synthesis of 11 but using 0.074 g (0.20 mmol) $\text{EuCl}_3\cdot 6\text{H}_2\text{O}$ in place of the $\text{EuCl}_3\cdot 6\text{H}_2\text{O}$.

Yield: 0.014 g (7 % with respect to manganese)

Selected IR data (KBr pellet):

$\tilde{\nu}$ = 3395.6 (w, br), 2958.7 (m), 2926.2 (w), 2901.6 (w), 2868.7 (w), 2081.1 (vs), 2036.8 (w), 1636.6 (s), 1611.4 (m), 1588.6 (s), 1568.9 (s), 1552.2 (m), 1528.7 (m), 1483.6 (s), 1457.7 (w), 1445.0 (m), 1426.9 (s), 1412.9 (ms), 1392.6 (m), 1375.6 (m), 1362.0 (m), 1341.0 (wm), 1288.0 (wm), 1227.6 (m), 1108.4 (wm), 1092.5 (m), 1049.7 (m), 1013.4 (w), 894.7 (w), 758.5 (m), 658.9 (m), 632.8 (m) cm^{-1}

(v = very, s = strong, m = medium, w = weak, br = broad).

Elemental Analysis:

$\text{C}_{74}\text{H}_{98}\text{Mn}_2\text{Tb}_4\text{O}_{22}\text{N}_{16}$ (2309.24 g/mol)

calculated: C 38.49, H 4.28, N 9.70; (with solvent)

calculated: C 36.96, H 4.04, N 7.84; (without solvent)

found: C 36.92, H 4.07, N 7.90.

7.10.6 $[\text{Mn}^{\text{III}}_2\text{Dy}^{\text{III}}_4(\mu_4\text{-O})_2(\text{hmp})_4(\text{pic})_2(\text{piv})_6(\mu\text{-N}_3)_2]\cdot 4\text{CH}_3\text{CN}$ (14)

$\text{Dy}(\text{NO}_3)_3\cdot 6\text{H}_2\text{O}$ (0.1 g, 0.22 mmol), hmpH (0.075 g, 0.69 mmol) and NaN_3 (0.05 g, 0.77 mmol) were dissolved in CH_3CN (15 mL). After 10 minutes stirring at room temperature, **1** (0.05 g, 0.029 mmol) was added. After a further two minutes of stirring at room temperature, KOH (0.05 g, 0.8 mmol) was added. The vial, in which the reaction took place, was closed completely but with one hole in the lid and stirred for 40 minutes at 70°C. The resulting dark brown solution was allowed to cool to room temperature and was filtered. The vessel was closed with parafilm with five holes pierced into it to allow slow evaporation. After one month, well-formed dark brown crystals appeared.

It was found that performing the same reaction with $\text{DyCl}_3\cdot 6\text{H}_2\text{O}$ (0.078 g, 0.2 mmol) gave crystals after only ten days and this procedure was adopted for the compounds made with the other lanthanides.

Yield: 0.022 g (11 % with respect to manganese)

Selected IR data (KBr pellet):

$\tilde{\nu}$ = 3400.2 (w, br), 2958.6 (m), 2925.9 (w), 2797.4 (w), 2082.2 (vs), 1637.1 (s), 1589.9 (s), 1569.9 (s), 1530.5 (m), 1483.7 (s), 1427.1 (s), 1413.0 (s), 1393.5 (m), 1375.9 (m), 1361.5 (m), 1227.5 (m), 1092.6 (m), 1050.0 (m), 895.0 (w), 757.7 (m), 632.5 (m) cm^{-1}

(v = very, s = strong, m = medium, w = weak, br = broad).

Elemental Analysis:

$\text{C}_{74}\text{H}_{98}\text{Mn}_2\text{Dy}_4\text{O}_{22}\text{N}_{16}$ (2323.54 g/mol)

calculated: C 38.25, H 4.25, N 9.65; (with solvent)

calculated: C 36.71, H 4.01, N 7.78; (without solvent)

found: C 37.22, H 4.08, N 7.97.

7.10.7 [Mn^{III}₂Ho^{III}₄(μ₄-O)₂(hmp)₄(pic)₂(piv)₆(μ-N₃)₂]₂·4CH₃CN (15)

The reaction was performed analogously to the synthesis of **11** but using 0.074 g (0.20 mmol) HoCl₃·6H₂O in place of the EuCl₃·6H₂O.

Yield: 0.010 g (5 % with respect to manganese)

Selected IR data (KBr pellet):

$\tilde{\nu}$ = 3396.1 (w, br), 2958.7 (ms), 2926.0 (m), 2901.6 (w), 2867.7 (w), 2081.0 (vs), 2036.8 (w), 1636.0 (s), 1612.4 (m), 1589.3 (s), 1568.7 (s), 1552.2 (m), 1528.3 (m), 1483.3 (s), 1457.1 (wm), 1445.3 (m), 1425.9 (s), 1411.3 (m), 1392.6 (m), 1375.6 (m), 1361.3 (m), 1341.4 (m), 1288.2 (wm), 1227.8 (m), 1108.2 (wm), 1092.1 (m), 1049.3 (m), 1013.1 (w), 894.8 (m), 758.2 (m), 658.9 (m), 632.5 (m) cm⁻¹

(v = very, s = strong, m = medium, w = weak, br = broad).

Elemental Analysis:

C₇₄H₉₈Mn₂Ho₄O₂₂N₁₆ (2333.26 g/mol)

calculated: C 38.09, H 4.23, N 9.60; (with solvent)

calculated: C 36.55, H 4.00, N 7.75; (without solvent)

found: C 37.03, H 4.11, N 8.44.

7.10.8 [Mn^{III}₂Er^{III}₄(μ₄-O)₂(hmp)₄(pic)₂(piv)₆(μ-N₃)₂]₂·4CH₃CN (16)

The reaction was performed analogously to the synthesis of **11** but using 0.076 g (0.20 mmol) ErCl₃·6H₂O in place of the EuCl₃·6H₂O.

Yield: 0.012 g (6 % with respect to manganese)

Selected IR data (KBr pellet):

$\tilde{\nu}$ = 3393.3 (w, br), 2958.7 (m), 2926.2 (w), 2901.6 (w), 2868.7 (w), 2081.1 (vs), 2036.8 (w), 1635.6 (s), 1612.4 (m), 1588.6 (s), 1568.9 (s), 1553.2 (m), 1528.7 (m), 1483.6 (s), 1456.7 (w), 1445.0 (m), 1427.9 (s), 1412.9 (ms), 1392.6 (m), 1375.2 (m), 1363.0 (m), 1341.0 (wm), 1287.0 (wm), 1227.6 (m), 1109.4 (wm), 1093.5 (m), 1048.4 (m), 1012.4 (w), 894.7 (w), 758.5 (w), 658.9 (w), 632.8 (w) cm⁻¹

(v = very, s = strong, m = medium, w = weak, br = broad).

Elemental Analysis:

C₇₄H₉₈Mn₂Er₄O₂₂N₁₆ (2342.58 g/mol)

calculated: C 37.94, H 4.22, N 9.57; (with solvent)

calculated: C 36.39, H 3.98, N 7.72; (without solvent)

found: C 37.12, H 4.21, N 9.43.

7.10.9 [Mn^{II}Mn^{III}₂Mn^{IV}Gd^{III}₃(μ₄-O)(μ₃-OH)₂(n-bdea)₃(piv)₉(N₃)(NO₃)] · MeCN (17)

1 (0.05 g, 0.03 mmol) and n-bdeaH₂ (0.05 g, 0.31 mmol) were dissolved in CH₃CN (15 mL) and stirred at room temperature for five minutes. Then Gd(NO₃)₃·6H₂O (0.049 g, 0.11 mmol) was added and the solution was stirred for further five minutes. After adding NaN₃ (0.01 g, 0.15 mmol), the vial, in which the reaction took place, was closed completely but with one hole in the lid and first stirred for 20 minutes at 70°C and then for further 20 minutes at boiling temperature. The nearly black solution was filtered and sealed with Parafilm with eight small holes pierced into it. After eight days, well-formed dark brown rectangular crystals appeared.

Yield: 0.09 g (9 % with respect to manganese)

Selected IR data (KBr pellet):

$\tilde{\nu}$ = 3431.5 (w, br), 2962.4 (m), 2931.8 (m), 2872.4 (wm), 2055.3 (ms), 1637.2 (s), 1616.4 (s), 1560.0 (ms), 1527.9 (m), 1484.3 (m), 1458.5 (m), 1427.6 (m), 1415.2 (m), 1376.4 (m), 1362.2 (m), 1316.7 (w), 1225.2 (m), 1074.7 (wm), 1031.4 (w), 898.2 (w), 619.8 (m), 478.0 (wm) cm⁻¹
(v = very, s = strong, m = medium, w = weak, br = broad).

Elemental Analysis:

C₇₁H₁₃₇Mn₄Gd₃N₈O₃₀ (2274.39 g/mol)

calculated: C 37.49, H 6.07, N 4.93; (with solvent)

calculated: C 37.11, H 6.05, N 4.39; (without solvent)

found: C 37.37, H 6.03, N 4.86.

7.10.10 [Mn^{II}Mn^{III}₂Mn^{IV}Dy^{III}₃(μ₄-O)(μ₃-OH)₂(n-bdea)₃(piv)₉(N₃)(NO₃)] · MeCN (18)

The reaction was performed analogously to the synthesis of **17** but using 0.05 g (0.11 mmol) Dy(NO₃)₃·6H₂O in place of the Gd(NO₃)₃·6H₂O.

Yield: 0.036 g (35 % with respect to manganese)

Selected IR data (KBr pellet):

$\tilde{\nu}$ = 3435.2 (w, br), 2962.1 (m), 2931.2 (m), 2872.8 (wm), 2055.8 (ms), 1637.8 (s), 1616.8 (s), 1560.9 (ms), 1528.1 (m), 1484.2 (m), 1459.2 (m), 1427.3 (m), 1415.0 (m), 1376.7 (m), 1362.4 (m), 1316.3 (w), 1225.9 (m), 1074.1 (wm), 1031.1 (w), 898.9 (w), 619.5 (m), 478.3 (wm) cm⁻¹
(v = very, s = strong, m = medium, w = weak, br = broad).

Elemental Analysis:

C₇₁H₁₃₇Mn₄Dy₃N₈O₃₀ (2290.14 g/mol)

calculated: C 37.24, H 6.03, N 4.89; (with solvent)

calculated: C 36.85, H 6.01, N 4.36; (without solvent)

found: C 37.12, H 6.00, N 4.81.

7.10.11 $[\text{Mn}^{\text{II}}\text{Mn}^{\text{III}}_2\text{Mn}^{\text{IV}}\text{Ho}^{\text{III}}_3(\mu_4\text{-O})(\mu_3\text{-OH})_2(\text{n-bdea})_3(\text{piv})_9(\text{N}_3)(\text{NO}_3)] \cdot \text{MeCN}$ (19)

The reaction was performed analogously to the synthesis of **17** but using 0.050 g (0.11 mmol) $\text{Ho}(\text{NO}_3)_3 \cdot 6\text{H}_2\text{O}$ in place of the $\text{Gd}(\text{NO}_3)_3 \cdot 6\text{H}_2\text{O}$.

Yield: 0.031 g (30 % with respect to manganese)

Selected IR data (KBr pellet):

$\tilde{\nu} = 3412.0$ (w, br), 3236.7 (m), 2960.8 (m), 2930.4 (m), 2872.1 (wm), 2056.6 (ms), 1638.1 (s), 1617.3 (s), 1561.2 (ms), 1527.8 (m), 1483.9 (m), 1459.4 (m), 1427.8 (m), 1415.1 (m), 1376.0 (m), 1362.0 (m), 1316.6 (w), 1226.4 (m), 1074.8 (wm), 1031.6 (w), 898.5 (w), 619.0 (m), 478.6 (wm) cm^{-1}
(v = very, s = strong, m = medium, w = weak, br = broad).

Elemental Analysis:

$\text{C}_{71}\text{H}_{137}\text{Mn}_4\text{Ho}_3\text{N}_8\text{O}_{30}$ (2297.43 g/mol)

calculated: C 37.12, H 6.01, N 4.88; (with solvent)

calculated: C 36.73, H 5.99, N 4.35; (without solvent)

found: C 37.02, H 5.93, N 4.74.

7.10.12 $\text{Mn}^{\text{II}}\text{Mn}^{\text{III}}_2\text{Mn}^{\text{IV}}\text{Er}^{\text{III}}_3(\mu_4\text{-O})(\mu_3\text{-OH})_2(\text{n-bdea})_3(\text{piv})_9(\text{N}_3)(\text{NO}_3) \cdot \text{MeCN}$ (20)

The reaction was performed analogously to the synthesis of **17** but using 0.051 g (0.11 mmol) $\text{Er}(\text{NO}_3)_3 \cdot 6\text{H}_2\text{O}$ in place of the $\text{Gd}(\text{NO}_3)_3 \cdot 6\text{H}_2\text{O}$.

Yield: 0.019 g (18 % with respect to manganese)

Selected IR data (KBr pellet):

$\tilde{\nu} = 3433.1$ (w, br), 2962.2 (m), 2932.4 (m), 2872.3 (wm), 2055.2 (ms), 1636.6 (s), 1616.7 (s), 1561.4 (ms), 1527.3 (m), 1484.1 (m), 1459.4 (m), 1427.2 (m), 1415.4 (m), 1376.2 (m), 1362.5 (m), 1316.1 (w), 1225.3 (m), 1074.3 (wm), 1031.0 (w), 898.8 (w), 619.9 (m), 478.4 (wm) cm^{-1}

(v = very, s = strong, m = medium, w = weak, br = broad).

Elemental Analysis:

$\text{C}_{71}\text{H}_{137}\text{Mn}_4\text{Ho}_3\text{N}_8\text{O}_{30}$ (2304.42 g/mol)

calculated: C 37.01, H 5.99, N 4.86; (with solvent)

calculated: C 36.62, H 5.97, N 4.33; (without solvent)

found: C 36.91, H 5.93, N 4.68.

7.10.13 $[\text{Mn}^{3.5}_4\text{Pr}^{\text{III}}_6\text{Li}_2(\mu_3\text{-O})_2(\mu_5\text{-CO}_3)_2(\text{n-bdea})_6(\text{piv})_{12}(\text{NO}_3)_2] \cdot 4\text{CH}_3\text{CN}$ (21)

A solution of **1** (0.2 g, 0.12 mmol) and n-bdeaH₂ (0.3 g, 1.86 mmol) in CH₃CN (20 mL) was stirred for five minutes at room temperature. $\text{Pr}(\text{NO}_3)_3 \cdot 6\text{H}_2\text{O}$ (0.38 g, 0.87 mmol) was added and stirred for a further five minutes.

After adding LiOH (0.1 g, 4.12 mmol) the solution was heated at 70°C for 40 minutes and then filtered. The filtrate was kept in a vial, closed with Parafilm with five holes pierced into it and allowed to evaporate slowly. After two days well-formed dark brown crystals appeared.

Yield: 0.117 g (53 % with respect to manganese)

Selected IR data (KBr pellet):

$\tilde{\nu}$ = 3433.1 (mbr), 2959.1 (ms), 2930.0 (m), 2867.6 (m), 1594.3 (m), 1559.6 (s), 1484.7 (s), 1459.4 (m), 1420.4 (s), 1399.8 (m), 1384.2 (s), 1374.4 (s), 1290.1 (w), 1225.5 (m), 1080.1 (m), 893.3 (m), 588.8 (m) cm^{-1}

(v = very, s = strong, m = medium, w = weak, br = broad).

Elemental Analysis:

$\text{C}_{118}\text{H}_{222}\text{Pr}_6\text{Li}_2\text{Mn}_4\text{N}_{12}\text{O}_{50}$ (3688.16 g/mol)

calculated: C 38.43, H 6.07, N 4.56; (with solvent)

calculated: C 37.49, H 6.01, N 3.18; (without solvent)

found: C 38.42, H 6.12, N 4.38.

7.10.14 $[\text{Mn}^{3.5}_4\text{Nd}^{\text{III}}_6\text{Li}_2(\mu_3\text{-O})_2(\mu_5\text{-CO}_3)_2(\text{n-bdea})_6(\text{piv})_{12}(\text{NO}_3)_2] \cdot 3\text{CH}_3\text{CN}$ (22)

The reaction was performed analogously to the synthesis of **21** but using 0.038 g (0.87 mmol) $\text{Nd}(\text{NO}_3)_3 \cdot 6\text{H}_2\text{O}$ in place of the $\text{Pr}(\text{NO}_3)_3 \cdot 6\text{H}_2\text{O}$.

Yield: 0.070 g (32 % with respect to manganese)

Selected IR data (KBr pellet):

$\tilde{\nu}$ = 3432.5 (w, br), 2959.1 (m), 2929.5 (m), 2867.2 (m), 1596.8 (s), 1560.5 (s), 1484.7 (s), 1460.4 (m), 1419.5 (ms), 1399.5 (m), 1384.3 (s), 1374.6 (ms), 1291.8 (w), 1225.3 (m), 1079.7 (m), 1031.0 (w), 893.7 (wm), 846.1 (w), 791.9 (w), 589.8 (wm) cm^{-1}

(v = very, s = strong, m = medium, w = weak, br = broad).

Elemental Analysis:

$\text{C}_{116}\text{H}_{219}\text{Nd}_6\text{Li}_2\text{Mn}_4\text{N}_{11}\text{O}_{50}$ (3667.10 g/mol)

calculated: C 37.93, H 6.17, N 4.19; (with solvent)

calculated: C 37.28, H 5.97, N 3.16; (without solvent)

found: C 37.66, H 6.18, N 3.99.

7.10.15 $\text{Mn}^{3.5}_4\text{Sm}^{\text{III}}_6\text{Li}_2(\mu_3\text{-O})_2(\mu_5\text{-CO}_3)_2(\text{n-bdea})_6(\text{piv})_{12}(\text{NO}_3)_2] \cdot 3\text{CH}_3\text{CN}$ (23)

The reaction was performed analogously to the synthesis of **21** but using 0.039 g (0.87 mmol) $\text{Sm}(\text{NO}_3)_3 \cdot 6\text{H}_2\text{O}$ in place of the $\text{Pr}(\text{NO}_3)_3 \cdot 6\text{H}_2\text{O}$.

Yield: 0.045 g (28 % with respect to manganese)

Selected IR data (KBr pellet):

$\tilde{\nu}$ = 3430.5 (m, br), 2959.0 (s), 2930.2 (s), 2867.8 (ms), 1629.9 (ms), 1600.5 (s), 1563.9 (s), 1484.9 (s), 1459.1 (ms), 1420.4 (s), 1399.2 (ms), 1374.6 (s), 1346.6 (s), 1296.0 (m), 1225.1 (ms), 1161.4 (w), 1080.0 (ms), 1032.1 (m), 982.3 (w), 894.3 (m), 845.6 (wm), 791.9 (m), 590.1 (m) cm^{-1}
(v = very, s = strong, m = medium, w = weak, br = broad).

Elemental Analysis:

$\text{C}_{116}\text{H}_{219}\text{Sm}_6\text{Li}_2\text{Mn}_4\text{N}_{11}\text{O}_{50}$ (3703.82 g/mol)
calculated: C 37.62, H 5.96, N 4.16; (with solvent)
calculated: C 36.90, H 5.91, N 3.13; (without solvent)
found: C 37.54, H 5.83, N 4.03.

7.10.16 $[\text{Mn}^{3.5}_4\text{Eu}^{\text{III}}_6\text{Li}_2(\mu_3\text{-O})_2(\mu_5\text{-CO}_3)_2(\text{n-bdea})_6(\text{piv})_{12}(\text{NO}_3)_2] \cdot 3\text{CH}_3\text{CN}$ (24)

The reaction was performed analogously to the synthesis of **21** but using 0.039 g (0.87 mmol) $\text{Eu}(\text{NO}_3)_3 \cdot 6\text{H}_2\text{O}$ in place of the $\text{Pr}(\text{NO}_3)_3 \cdot 6\text{H}_2\text{O}$.

Yield: 0.078 g (35 % with respect to manganese)

Selected IR data (KBr pellet):

$\tilde{\nu}$ = 3431.0 (w, br), 2959.2 (s), 2930.3 (s), 2867.6 (s), 1632.0 (s), 1603.0 (s), 1567.9 (s), 1485.1 (s), 1461.9 (s), 1419.6 (s), 1399.1 (s), 1375.1 (s), 1349.5 (s), 1297.4 (m), 1224.6 (s), 1161.6 (w), 1079.9 (ms), 1032.6 (m), 894.0 (m), 845.5 (wm), 791.7 (m), 590.5 (ms) cm^{-1}
(v = very, s = strong, m = medium, w = weak, br = broad).

Elemental Analysis:

$\text{C}_{116}\text{H}_{219}\text{Eu}_6\text{Li}_2\text{Mn}_4\text{N}_{11}\text{O}_{50}$ (3713.44 g/mol)
calculated: C 37.46, H 6.10, N 4.14; (with solvent)
calculated: C 36.80, H 5.90, N 3.12; (without solvent)
found: C 37.06, H 5.91, N 3.87.

7.10.17 $[\text{Mn}^{3.5}_4\text{Gd}^{\text{III}}_6\text{Li}_2(\mu_3\text{-O})_2(\mu_5\text{-CO}_3)_2(\text{n-bdea})_6(\text{piv})_{12}(\text{NO}_3)_2] \cdot 3\text{CH}_3\text{CN}$ (25)

The reaction was performed analogously to the synthesis of **21** but using 0.040 g (0.89 mmol) $\text{Gd}(\text{NO}_3)_3 \cdot 6\text{H}_2\text{O}$ in place of the $\text{Pr}(\text{NO}_3)_3 \cdot 6\text{H}_2\text{O}$.

Yield: 0.074 g (33 % with respect to manganese)

Selected IR data (KBr pellet):

$\tilde{\nu}$ = 3423.1 (w), 2959.3 (ms), 2903.8 (m), 2867.7 (m), 1632.9 (m), 1604.7 (s), 1570.0 (s), 1485.2 (s), 1420.6 (s), 1398.9 (m), 1384.2 (s), 1376.0 (s), 1298.9 (wm), 1224.9 (m), 1080.6 (m), 1033.1 (w), 894.7 (w), 590.8 (w) cm^{-1}
(v = very, s = strong, m = medium, w = weak, br = broad).

Elemental Analysis:

 $C_{116}H_{219}Gd_6Li_2Mn_4N_{11}O_{50}$ (3745.16 g/mol)

calculated: C 37.20, H 5.89, N 4.11; (with solvent)

calculated: C 36.48, H 5.84, N 3.09; (without solvent)

found: C 36.93, H 5.64, N 3.92.

7.10.18 $[Mn^{3.5}Tb^{III}_6Li_2(\mu_3-O)_2(\mu_5-CO_3)_2(n-bdea)_6(piv)_{12}(NO_3)_2] \cdot 3CH_3CN$ (26)

The reaction was performed analogously to the synthesis of **21** but using 0.040 g (0.88 mmol) $Tb(NO_3)_3 \cdot 6H_2O$ in place of the $Pr(NO_3)_3 \cdot 6H_2O$.

Yield: 0.131 g (58 % with respect to manganese)

Selected IR data (KBr pellet):

$\tilde{\nu} = 3414.7$ (s), 2958.7 (m), 2928.0 (m), 2867.1 (wm), 1637.0 (m), 1604.7 (s), 1570.7 (s), 1483.6 (ms), 1459.0 (m), 1425.4 (ms), 1400.0 (m), 1384.5 (s), 1300.7 (w), 1226.6 (m), 1080.7 (wm), 1033.9 (w), 896.2 (w), 592.0 (s), cm^{-1}
(v = very, s = strong, m = medium, w = weak, br = broad).

Elemental Analysis:

 $C_{116}H_{219}Tb_6Li_2Mn_4N_{11}O_{50}$ (3755.21 g/mol)

calculated: C 37.10, H 5.88, N 4.10; (with solvent)

calculated: C 36.38, H 5.83, N 3.09; (without solvent)

found: C 35.19, H 5.82, N 2.98.

7.10.19 $[Mn^{3.5}Dy^{III}_6Li_2(\mu_3-O)_2(\mu_5-CO_3)_2(n-bdea)_6(piv)_{12}(NO_3)_2] \cdot 3CH_3CN$ (27)

The reaction was performed analogously to the synthesis of **21** but using 0.040 g (0.88 mmol) $Dy(NO_3)_3 \cdot 6H_2O$ in place of the $Pr(NO_3)_3 \cdot 6H_2O$.

Yield: 0.152 g (67 % with respect to manganese)

Selected IR data (KBr pellet):

$\tilde{\nu} = 3433.5$ (w, br), 2959.3 (m), 2930.5 (m), 2868.4 (m), 1636.7 (wm), 1607.5 (s), 1571.2 (s), 1485.1 (s), 1459.8 (m), 1427.8 (ms), 1398.5 (m), 1384.6 (ms), 1348.6 (m), 1301.8 (w), 1225.1 (m), 1081.3 (m), 895.7 (w), 591.7 (m) cm^{-1}
(v = very, s = strong, m = medium, w = weak, br = broad).

Elemental Analysis:

 $C_{116}H_{219}Dy_6Li_2Mn_4N_{11}O_{50}$ (3776.66 g/mol)

calculated: C 36.89, H 5.84, N 4.08; (with solvent)

calculated: C 36.16, H 5.79, N 3.06; (without solvent)

found: C 35.66, H 5.68, N 3.10.

7.10.20 $[Mn^{3.5}Ho^{III}_6Li_2(\mu_3-O)_2(\mu_5-CO_3)_2(n-bdea)_6(piv)_{12}(NO_3)_2] \cdot 8CH_3CN$ (28)

The reaction was performed analogously to the synthesis of **21** but using 0.040 g (0.87 mmol) $Ho(NO_3)_3 \cdot 6H_2O$ in place of the $Pr(NO_3)_3 \cdot 6H_2O$.

Yield: 0.148 g (65 % with respect to manganese)

Selected IR data (KBr pellet):

$\tilde{\nu}$ = 3448.8 (m, br), 2959.7 (m), 2930.1 (wm), 2870.7 (wm), 1634.2 (s), 1608.0 (s), 1570.7 (s), 1484.8 (ms), 1460.5 (m), 1427.3 (ms), 1399.4 (m), 1384.5 (s), 1348.0 (m), 1305.3 (m), 1227.3 (m), 1080.4 (wm), 1035.0 (w), 896.9 (wm), 843.7 (w), 792.2 (w), 683.7 (w), 592.4 (wm) cm^{-1}

(v = very, s = strong, m = medium, w = weak, br = broad).

Elemental Analysis:

$\text{C}_{126}\text{H}_{234}\text{Ho}_6\text{Li}_2\text{Mn}_4\text{N}_{16}\text{O}_{50}$ (3996.50 g/mol)

calculated: C 37.87, H 5.90, N 5.61; (with solvent)

calculated: C 36.02, H 5.77, N 3.05; (without solvent)

found: C 36.86, H 5.88, N 4.12.

7.10.21 $[\text{Mn}^{3.5}_4\text{Y}^{\text{III}}_6\text{Li}_2(\mu_3\text{-O})_2(\mu_5\text{-CO}_3)_2(\text{n-bdea})_6(\text{piv})_{12}(\text{NO}_3)_2] \cdot 8\text{CH}_3\text{CN}$ (29)

The reaction was performed analogously to the synthesis of **21** but using 0.033 g (0.87 mmol) $\text{Y}(\text{NO}_3)_3 \cdot 6\text{H}_2\text{O}$ in place of the $\text{Pr}(\text{NO}_3)_3 \cdot 6\text{H}_2\text{O}$.

Yield: 0.008 g (4 % with respect to manganese)

Selected IR data (KBr pellet):

$\tilde{\nu}$ = 3423.2 (w, br), 2959.4 (m), 2930.2 (w), 2869.3 (w), 1609.8 (ms), 1572.1 (s), 1485.2 (s), 1459.2 (m), 1427.6 (s), 1399.4 (m), 1384.6 (ms), 1227.8 (w), 1082.7 (w), 897.0 (w), 866.0 (w), 592.0 (w) cm^{-1}

(v = very, s = strong, m = medium, w = weak, br = broad).

Elemental Analysis:

$\text{C}_{126}\text{H}_{234}\text{Y}_6\text{Li}_2\text{Mn}_4\text{N}_{16}\text{O}_{50}$ (3540.35 g/mol)

calculated: C 42.75, H 6.66, N 6.33; (with solvent)

calculated: C 41.13, H 6.59, N 3.49; (without solvent)

found: C 41.56, H 6.51, N 4.39.

7.10.22 $[\text{Fe}^{\text{III}}_4\text{Pr}^{\text{III}}_2(\mu_4\text{-O})_2(\text{n-bdea})_4(\text{piv})_4(\text{NO}_3)_2(\text{H}_2\text{O})_2] \cdot \text{MeCN}$ (30)

$\{\text{Fe}_3\}$ (**6**) (0.05 g, 0.04 mmol), n-bdeaH₂ (0.1 g, 0.62 mmol) and $\text{Pr}(\text{NO}_3)_3 \cdot 6\text{H}_2\text{O}$ (0.05 g, 0.11 mmol) were dissolved in acetonitrile (10 mL). The solution was stirred for 1 hour at boiling temperature under reflux. The obtained yellow solution is filtered off. After slow diffusion of acetone, brown nice shaped crystals were obtained after one day.

Yield: 0.031 g (58 % with respect to iron)

Selected IR data (KBr pellet):

$\tilde{\nu}$ = 3449.6 (w, br), 2961.2 (s), 2929.7 (s), 2898.7 (s), 2864.6 (s), 2692.1 (w), 1704.4 (m), 1584.3 (s), 1484.1 (s), 1461.9 (s), 1425.2 (s), 1384.2 (ms), 1376.7 (ms), 1359.5 (ms), 1295.8 (ms), 1228.0 (ms), 1100.8 (s), 1084.0 (s), 1030.0 (m), 1012.5 (m), 975.0 (wm), 900.1 (m), 819.2 (w), 787.8 (w), 781.8 (w), 734.0 (w), 619.0 (ms), 571.5 (m), 491.7 (m), 456.8 (m) cm^{-1}

(v = very, s = strong, m = medium, w = weak, br = broad).

Elemental Analysis:

$\text{C}_{54}\text{H}_{111}\text{Fe}_4\text{Pr}_2\text{N}_7\text{O}_{26}$ (1779.69 g/mol)

calculated: C 36.44, H 6.29, N 5.51; (with solvent)

calculated: C 35.92, H 6.26, N 4.83; (without solvent)

found: C 35.96, H 6.51, N 4.68.

7.10.23 $[\text{Fe}^{\text{III}}_4\text{Nd}^{\text{III}}_2(\mu_4\text{-O})_2(\text{n-bdea})_4(\text{piv})_4(\text{NO}_3)_2(\text{H}_2\text{O})_2]\cdot\text{acetone}$ (31)

The reaction was performed analogously to the synthesis of **30** but using 0.05 g (0.11 mmol) $\text{Nd}(\text{NO}_3)_3\cdot 6\text{H}_2\text{O}$ in place of the $\text{Pr}(\text{NO}_3)_3\cdot 6\text{H}_2\text{O}$.

Yield: 0.023 g (43 % with respect to iron)

Selected IR data (KBr pellet):

$\tilde{\nu}$ = 3449.6 (w, br), 2961.3 (s), 2929.6 (m), 2898.7 (m), 2864.9 (m), 1704.5 (m), 1585.0 (s), 1484.0 (s), 1464.8 (ms), 1425.4 (s), 1384.2 (m), 1376.8 (m), 1359.4 (m), 1296.7 (m), 1228.1 (m), 1101.1 (ms), 1084.1 (s), 1030.3 (wm), 899.9 (m), 819.1 (w), 787.5 (w), 781.6 (w), 735.9 (w), 616.9 (m) cm^{-1}

(v = very, s = strong, m = medium, w = weak, br = broad).

Elemental Analysis:

$\text{C}_{55}\text{H}_{114}\text{Fe}_4\text{Sm}_2\text{N}_6\text{O}_{27}$ (1803.38 g/mol)

calculated: C 36.63, H 6.37, N 4.66; (with solvent)

calculated: C 35.79, H 6.24, N 4.82; (without solvent)

found: C 35.46, H 6.43, N 4.50.

7.10.24 $[\text{Fe}^{\text{III}}_4\text{Sm}^{\text{III}}_2(\mu_4\text{-O})_2(\text{n-bdea})_4(\text{piv})_4(\text{NO}_3)_2(\text{H}_2\text{O})_2]\cdot\text{acetone}$ (32)

The reaction was performed analogously to the synthesis of **30** but using 0.05 g (0.11 mmol) $\text{Sm}(\text{NO}_3)_3\cdot 6\text{H}_2\text{O}$ in place of the $\text{Pr}(\text{NO}_3)_3\cdot 6\text{H}_2\text{O}$.

Yield: 0.023 g (43 % with respect to iron)

Selected IR data (KBr pellet):

$\tilde{\nu}$ = 3448.5 (w, br), 2961.2 (s), 2929.2 (m), 2898.5 (m), 2865.0 (m), 1704.4 (m), 1586.5 (s), 1483.9 (s), 1466.2 (ms), 1425.5 (s), 1384.5 (m), 1375.1 (m), 1359.7 (m), 1301.2 (m), 1228.3 (m), 1100.5 (ms), 1084.3 (s), 1031.5 (wm), 899.8 (m), 819.0 (w), 785.2 (w), 781.2 (w), 739.2 (w), 615.4 (m) cm^{-1}

(v = very, s = strong, m = medium, w = weak, br = broad).

Elemental Analysis:

$C_{55}H_{114}Fe_4Sm_2N_6O_{27}$ (1815.62 g/mol)

calculated: C 36.38, H 6.33, N 4.63; (with solvent)

calculated: C 35.54, H 6.19, N 4.78; (without solvent)

found: C 35.46, H 6.43, N 4.50.

7.10.25 $[Fe^{III}_4Eu^{III}_2(\mu_4-O)_2(n-bdea)_4(piv)_4(NO_3)_2(H_2O)_2] \cdot \text{acetone}$ (33)

The reaction was performed analogously to the synthesis of **30** but using 0.05 g (0.11 mmol) $Eu(NO_3)_3 \cdot 6H_2O$ in place of the $Pr(NO_3)_3 \cdot 6H_2O$.

Yield: 0.025 g (45 % with respect to iron)

Selected IR data (KBr pellet):

$\tilde{\nu} = 3448.5$ (w, br), 2961.2 (s), 2929.2 (m), 2898.5 (m), 2865.0 (m), 1704.4 (m), 1586.5 (s), 1483.9 (s), 1466.2 (ms), 1425.5 (s), 1384.5 (m), 1376.5 (m), 1359.7 (m), 1301.8 (m), 1228.3 (m), 1100.5 (ms), 1084.3 (s), 1031.5 (wm), 899.8 (m), 819.0 (w), 787.2 (w), 781.2 (w), 739.2 (w), 615.4 (m) cm^{-1}
(v = very, s = strong, m = medium, w = weak, br = broad).

Elemental Analysis:

$C_{55}H_{114}Fe_4Eu_2N_6O_{27}$ (1818.83 g/mol)

calculated: C 36.32, H 6.31, N 4.62; (with solvent)

calculated: C 35.47, H 6.18, N 4.77; (without solvent)

found: C 35.57, H 6.46, N 4.52.

7.10.26 $[Fe^{III}_4Gd^{III}_2(\mu_4-O)_2(n-bdea)_4(piv)_4(NO_3)_2(H_2O)_2] \cdot \text{acetone}$ (34)

The reaction was performed analogously to the synthesis of **30** but using 0.05 g (0.11 mmol) $Gd(NO_3)_3 \cdot 6H_2O$ in place of the $Pr(NO_3)_3 \cdot 6H_2O$.

Yield: 0.020 g (37 % with respect to iron)

Selected IR data (KBr pellet):

$\tilde{\nu} = 3448.2$ (w, br), 2961.0 (s), 2929.0 (m), 2898.1 (m), 2865.5 (m), 1704.8 (m), 1587.1 (s), 1484.1 (s), 1466.8 (ms), 1425.8 (s), 1384.8 (m), 1376.2 (m), 1359.2 (m), 1301.3 (m), 1228.5 (m), 1100.4 (ms), 1084.4 (s), 1031.7 (wm), 899.9 (m), 819.3 (w), 788.5 (w), 782.3 (w), 738.3 (w), 616.2 (m) cm^{-1}
(v = very, s = strong, m = medium, w = weak, br = broad).

Elemental Analysis:

$C_{55}H_{114}Fe_4Gd_2N_6O_{27}$ (1829.40 g/mol)

calculated: C 36.11, H 6.28, N 4.59; (with solvent)

calculated: C 35.26, H 6.15, N 4.74; (without solvent)

found: C 35.16, H 6.31, N 4.40.

7.10.27 [Fe^{III}₄Y^{III}₂(μ₄-O)₂(n-bdea)₄(piv)₄(NO₃)₂(H₂O)₂]· acetone (35)

The reaction was performed analogously to the synthesis of **30** but using 0.042 g (0.11 mmol) Y(NO₃)₃·6H₂O in place of the Pr(NO₃)₃·6H₂O.

Yield: 0.006 g (12 % with respect to iron)

Selected IR data (KBr pellet):

$\tilde{\nu}$ = 3449.1 (w, br), 2961.4 (s), 2929.6 (m), 2901.6 (m), 2865.7 (m), 1704.8 (m), 1588.5 (s), 1483.9 (s), 1426.3 (s), 1384.2 (m), 1376.5 (m), 1359.6 (m), 1307.3 (m), 1228.7 (m), 1102.9 (ms), 1084.9 (s), 1033.8 (wm), 900.1 (m), 819.4 (w), 787.2 (w), 781.1 (w), 744.9 (w), 616.9 (m) cm⁻¹

(v = very, s = strong, m = medium, w = weak, br = broad).

Elemental Analysis:

C₅₅H₁₁₄Fe₄Y₂N₆O₂₇ (1692.71 g/mol)

calculated: C 39.03, H 6.79, N 4.96; (with solvent)

calculated: C 38.21, H 6.66, N 5.14; (without solvent)

found: C 38.76, H 6.57, N 5.12.

7.10.28 [Fe^{III}₆(μ₃-O)₂(hmp)₆(piv)₆]²⁺[Eu^{III}(NO₃)₅]²⁻·2acetone (36)

{Fe₃} (**6**) (0.25 g, 0.24 mmol), hmpH (0.078 g, 0.71 mmol) and Eu(NO₃)₃·6H₂O (0.45 g, 1 mmol) were dissolved in acetone (20 mL). The solution was stirred for 30 minutes at 50°C and the resulting red solution is filtered. After ten hours three small crystals were obtained and isolated by filtration. One of these crystals was returned to the filtrate to yield red single crystals after four more hours.

Yield: 0.218 g (80.4 % with respect to iron)

Selected IR data (KBr pellet):

$\tilde{\nu}$ = 3429.8 (w, br), 2964.3 (m), 2930.2 (wm), 2906.5 (wm), 1712.7 (w), 1609.7 (m), 1562.7 (s), 1485.1 (s), 1427.8 (s), 1383.6 (s), 1364.6 (m), 1313.0 (s), 1290.2 (s), 1227.3 (m), 1156.7 (w), 1062.6 (m), 1046.9 (s), 1028.8 (m), 764.5 (m), 597.0 (ms), 553.1 (ms), 433.8 (m) cm⁻¹

(v = very, s = strong, m = medium, w = weak, br = broad).

Elemental Analysis:

C₇₅H₁₀₈Fe₆EuN₁₁O₃₈ (2258.75 g/mol)

calculated: C 39.88, H 4.82, N 6.82; (with solvent)

calculated: C 38.68, H 4.52, N 7.19; (without solvent)

found: C 39.07, H 4.65, N 6.96.

7.10.29 [Fe^{III}₆(μ₃-O)₂(hmp)₆(piv)₆]²⁺[Gd^{III}(NO₃)₅]²⁻·2acetone (37)

The reaction was performed analogously to the synthesis of **36** but using (0.45 g, 1 mmol) Gd(NO₃)₃·6H₂O in place of the Eu(NO₃)₃·6H₂O.

Yield: 0.233 g (85.8 % with respect to iron)

Selected IR data (KBr pellet):

$\tilde{\nu}$ = 3414.2 (sbr), 2961.7 (m), 2930.1 (m), 2916.3 (w), 2066.7 (w), 1713.9 (m), 1636.4 (ms), 1610.5 (s), 1561.5 (vs), 1484.8 (s), 1427.4 (s), 1383.7 (s), 1363.8 (s), 1313.0 (s), 1289.7 (s), 1227.3 (ms), 1156.4 (wm), 1062.1 (m), 1047.0 (s), 763.9 (m), 596.8 (s), 552.7 (s), 432.7 (m) cm^{-1}

(v = very, s = strong, m = medium, w = weak, br = broad).

Elemental Analysis:

$\text{C}_{75}\text{H}_{108}\text{Fe}_6\text{GdN}_{11}\text{O}_{38}$ (2264.03 g/mol)

calculated: C 39.79, H 4.81, N 6.81; (with solvent)

calculated: C 38.58, H 4.51, N 7.17; (without solvent)

found: C 38.83, H 4.64, N 6.95.

7.10.30 $[\text{Fe}^{\text{III}}(\mu_3\text{-O})_2(\text{hmp})_6(\text{piv})_6]^{2+}[\text{Dy}^{\text{III}}(\text{NO}_3)_6]^{2-} \cdot 2\text{acetone}$ (38)

The reaction was performed analogously to the synthesis of **36** but using 0.336 g (1 mmol) $\text{Dy}(\text{NO}_3)_3 \cdot 6\text{H}_2\text{O}$ in place of the $\text{Eu}(\text{NO}_3)_3 \cdot 6\text{H}_2\text{O}$.

Yield: 0.203 g (74.5 % with respect to iron)

Selected IR data (KBr pellet):

$\tilde{\nu}$ = 3414.4 (s), 2962.4 (m), 2930.1 (wm), 2906.2 (wm), 1713.9 (wm), 1637.7 (m), 1611.2 (s), 1562.0 (s), 1485.0 (s), 1427.7 (s), 1384.2 (s), 1364.0 (s), 1315.8 (s), 1289.7 (s), 1227.4 (m), 1156.6 (wm), 1062.1 (m), 1047.0 (s), 764.1 (m), 597.0 (ms), 552.9 (m), 433.0 (m) cm^{-1}

(v = very, s = strong, m = medium, w = weak, br = broad).

Elemental Analysis:

$\text{C}_{75}\text{H}_{108}\text{Fe}_6\text{DyN}_{11}\text{O}_{38}$ (2269.28 g/mol)

calculated: C 39.70, H 4.80, N 6.79; (with solvent)

calculated: C 38.49, H 4.49, N 7.16; (without solvent)

found: C 37.55, H 4.53, N 6.70.

7.10.31 $[\text{Fe}^{\text{III}}(\mu_3\text{-O})_2(\text{hmp})_6(\text{piv})_6]^{2+}[\text{Ho}^{\text{III}}(\text{NO}_3)_6]^{2-} \cdot 2\text{acetone}$ (39)

The reaction was performed analogously to the synthesis of **36** but using 0.338 g (1 mmol) $\text{Ho}(\text{NO}_3)_3 \cdot 6\text{H}_2\text{O}$ in place of the $\text{Eu}(\text{NO}_3)_3 \cdot 6\text{H}_2\text{O}$.

Yield: 0.224 g (82.2 % with respect to iron)

Selected IR data (KBr pellet):

$\tilde{\nu}$ = 3435.5 (sbr), 2961.6 (m), 2930.0 (wm), 2316.7 (w), 2066.8 (w), 1713.8 (ms), 1610.6 (s), 1561.6 (vs), 1484.7 (s), 1427.4 (s), 1383.4 (s), 1363.7 (s), 1317.5 (s), 1289.7 (s), 1227.4 (m), 1156.5 (wm), 1062.1 (m), 1047.0 (s), 763.9 (m), 596.8 (s), 552.7 (s), 432.4 (m) cm^{-1}

(v = very, s = strong, m = medium, w = weak, br = broad).

Elemental Analysis:

$C_{75}H_{108}Fe_6HoN_{11}O_{38}$ (2271.71 g/mol)

calculated: C 39.65, H 4.79, N 6.78; (with solvent)

calculated: C 38.44, H 4.49, N 7.15; (without solvent)

found: C 39.16, H 4.45, N 6.95.

7.10.32 $[Fe^{III}(\mu_3-O)_2(hmp)_6(piv)_6]^{2+}[Er^{III}(NO_3)_5]^{2-} \cdot 2acetone$ (40)

The reaction was performed analogously to the synthesis of **36** but using 0.339 g (1 mmol) $Er(NO_3)_3 \cdot 6H_2O$ in place of the $Eu(NO_3)_3 \cdot 6H_2O$.

Yield: 0.217 g (79.5 % with respect to iron)

Selected IR data (KBr pellet):

$\tilde{\nu} = 3468.6$ (sbr), 2962.1 (m), 1713.1 (ms), 1637.8 (m), 1611.0 (m), 1561.3 (ms), 1484.6 (m), 1427.2 (m), 1383.8 (m), 1364.1 (m), 1319.5 (m), 1289.8 (m), 1227.7 (wm), 1156.5 (w), 1062.1 (w), 1047.1 (m), 764.0 (w), 596.9 (m), 552.5 (m), 432.1 (m) cm^{-1}

(v = very, s = strong, m = medium, w = weak, br = broad).

Elemental Analysis:

$C_{75}H_{108}Fe_6ErN_{11}O_{38}$ (2274.04 g/mol)

calculated: C 39.61, H 4.79, N 6.78; (with solvent)

calculated: C 38.41, H 4.48, N 7.14; (without solvent)

found: C 38.95, H 4.52, N 6.88.

7.10.33 $[Co^{III}Pr^{III}(\mu_3-OH)_2(hmp)_4(piv)_8(\mu-N_3)_2(NO_3)_2] \cdot 2CH_3CN$ (41)

The reaction was performed analogously to the synthesis of **46** but using 0.095 g (0.22 mmol) $Pr(NO_3)_3 \cdot 6H_2O$ in place of the $Dy(NO_3)_3 \cdot 6H_2O$.

Yield: 0.016 g (12 % with respect to cobalt)

Selected IR data (KBr pellet):

$\tilde{\nu} = 3438.2$ (w, br), 2958.2 (m), 2928.6 (w), 2868.3 (w), 2076.3 (s), 1613.2 (wm), 1567.1 (s), 1552.8 (s), 1483.2 (s), 1465.8 (ms), 1422.2 (s), 1375.0 (m), 1358.0 (m), 1311.1 (m), 1228.3 (m), 1032.7 (wm), 894.0 (w), 546.9 (wm) cm^{-1}

(v = very, s = strong, m = medium, w = weak, br = broad).

Elemental Analysis:

$C_{68}H_{104}Co_2Pr_4N_{14}O_{28}$ (2247.13 g/mol)

calculated: C 36.35, H 4.66, N 8.72; (with solvent)

calculated: C 35.50, H 4.56, N 7.76; (without solvent)

found: C 36.24, H 4.72, N 8.63.

7.10.34 [Co^{III}₂Sm^{III}₄(μ₃-OH)₂(hmp)₄(piv)₈(μ-N₃)₂(NO₃)₂]₂·2CH₃CN (42)

The reaction was performed analogously to the synthesis of **46** but using 0.097 g (0.22 mmol) Sm(NO₃)₃·6H₂O in place of the Dy(NO₃)₃·6H₂O.

Yield: 0.014 g (10 % with respect to cobalt)

Selected IR data (KBr pellet):

$\tilde{\nu}$ = 3436.2 (w, br), 2958.9 (m), 2928.2 (w), 2868.9 (w), 2076.2 (s), 1613.9 (wm), 1567.3 (s), 1552.1 (s), 1483.6 (s), 1465.8 (ms), 1422.5 (s), 1375.6 (m), 1358.7 (m), 1311.9 (m), 1228.0 (m), 1032.7 (wm), 894.1 (w), 547.4 (wm) cm⁻¹
(v = very, s = strong, m = medium, w = weak, br = broad).

Elemental Analysis:

C₆₈H₁₀₄Co₂Sm₄N₁₄O₂₈ (2284.94 g/mol)

calculated: C 35.74, H 4.59, N 8.58; (with solvent)

calculated: C 34.90, H 4.48, N 7.63; (without solvent)

found: C 35.53, H 4.51, N 8.44.

7.10.35 [Co^{III}₂Eu^{III}₄(μ₃-OH)₂(hmp)₄(piv)₈(μ-N₃)₂(NO₃)₂]₂·2CH₃CN (43)

The reaction was performed analogously to the synthesis of **46** but using 0.098 g (0.22 mmol) Eu(NO₃)₃·6H₂O in place of the Dy(NO₃)₃·6H₂O.

Yield: 0.015 g (11 % with respect to cobalt)

Selected IR data (KBr pellet):

$\tilde{\nu}$ = 3415.0 (w, br), 2959.0 (m), 2928.0 (w), 2868.9 (w), 2077.2 (s), 1614.7 (wm), 1568.7 (s), 1552.6 (s), 1483.9 (s), 1466.9 (ms), 1422.9 (s), 1375.8 (m), 1359.1 (m), 1312.4 (m), 1286.4 (m), 1228.4 (m), 1032.8 (wm), 894.2 (w), 547.6 (wm) cm⁻¹
(v = very, s = strong, m = medium, w = weak, br = broad).

Elemental Analysis:

C₆₈H₁₀₄Co₂Eu₄N₁₄O₂₈ (2291.35 g/mol)

calculated: C 35.64, H 4.57, N 8.56; (with solvent)

calculated: C 34.79, H 4.47, N 7.61; (without solvent)

found: C 34.91, H 4.47, N 8.22.

7.10.36 [Co^{III}₂Gd^{III}₄(μ₃-OH)₂(hmp)₄(piv)₈(μ-N₃)₂(NO₃)₂]₂·2CH₃CN (44)

The reaction was performed analogously to the synthesis of **46** but using 0.099 g (0.22 mmol) Gd(NO₃)₃·6H₂O in place of the Dy(NO₃)₃·6H₂O.

Yield: 0.019 g (14 % with respect to cobalt)

Selected IR data (KBr pellet):

$\tilde{\nu}$ = 3434.4 (wb), 2958.9 (m), 2928.2 (w), 2868.3 (w), 2076.3 (s), 1613.4 (wm), 1567.3 (s), 1552.5 (s), 1483.2 (s), 1465.5 (ms), 1422.5 (s), 1375.6 (m), 1358.6 (m), 1311.2 (m), 1228.7 (m), 1032.4 (wm), 894.6 (w), 547.2 (wm) cm^{-1}
(v = very, s = strong, m = medium, w = weak, br = broad).

Elemental Analysis:

$\text{C}_{68}\text{H}_{104}\text{Co}_2\text{Gd}_4\text{N}_{14}\text{O}_{28}$ (2312.50 g/mol)
calculated: C 35.32, H 4.53, N 8.48; (with solvent)
calculated: C 34.46, H 4.43, N 7.54; (without solvent)
found: C 34.89, H 4.45, N 8.23.

7.10.37 $[\text{Co}^{\text{III}}_2\text{Tb}^{\text{III}}_4(\mu_3\text{-OH})_2(\text{hmp})_4(\text{piv})_8(\mu\text{-N}_3)_2(\text{NO}_3)_2] \cdot 2\text{CH}_3\text{CN}$ (45)

The reaction was performed analogously to the synthesis of **46** but using 0.099 g (0.22 mmol) $\text{Tb}(\text{NO}_3)_3 \cdot 6\text{H}_2\text{O}$ in place of the $\text{Dy}(\text{NO}_3)_3 \cdot 6\text{H}_2\text{O}$.

Yield: 0.015 g (11 % with respect to cobalt)

Selected IR data (KBr pellet):

$\tilde{\nu}$ = 3416.0 (w, br), 2958.7 (m), 2928.4 (w), 2868.2 (w), 2079.3 (s), 1614.5 (wm), 1576.1 (s), 1555.4 (s), 1483.2 (s), 1472.0 (ms), 1423.8 (s), 1384.1 (m), 1358.6 (m), 1311.4 (m), 1286.1 (m), 1228.3 (m), 1032.4 (wm), 895.2 (w), 549.3 (wm) cm^{-1}
(v = very, s = strong, m = medium, w = weak, br = broad).

Elemental Analysis:

$\text{C}_{68}\text{H}_{104}\text{Co}_2\text{Tb}_4\text{N}_{14}\text{O}_{28}$ (2319.20 g/mol)
calculated: C 35.21, H 4.52, N 8.46; (with solvent)
calculated: C 34.36, H 4.42, N 7.51; (without solvent)
found: C 34.61, H 4.41, N 7.92.

7.10.38 $[\text{Co}^{\text{III}}_2\text{Dy}^{\text{III}}_4(\mu_3\text{-OH})_2(\text{hmp})_4(\text{piv})_8(\mu\text{-N}_3)_2(\text{NO}_3)_2] \cdot 2\text{CH}_3\text{CN}$ (46)

$\text{Dy}(\text{NO}_3)_3 \cdot 6\text{H}_2\text{O}$ (0.1 g, 0.22 mmol), hmpH (0.075 g, 0.69 mmol) and NaN_3 (0.05 g, 0.77 mmol) were dissolved in CH_3CN (15 mL). After two minutes of stirring at room temperature, KOH (0.05 g, 0.8 mmol) were added. After further 10 minutes stirring at room temperature, $\{\text{Co}_2\}$ (**4**) (0.05 g, 0.029 mmol) was added. The vial, in which the reaction took place, was closed completely but with one hole in the lid and stirred for 20 minutes at 70°C. The resulting dark brown solution was allowed to cool to room temperature and was filtered. The vessel was closed with parafilm with five holes pierced into it to allow slow evaporation. After ten days, well-formed dark green-brown crystals appeared.

Yield: 0.018 g (13 % with respect to cobalt)

Selected IR data (KBr pellet):

$\tilde{\nu}$ = 3438.1 (wb), 2958.9 (m), 2928.2 (w), 2868.9 (w), 2076.2 (m), 1613.9 (w), 1567.3 (s), 1552.1 (ms), 1483.6 (ms), 1465.8 (m), 1422.5 (ms), 1375.6 (wm), 1357.7 (m), 1312.9 (m), 1228.4 (m), 1032.4 (wm), 894.2 (w), 546.4 (wm) cm^{-1}
(v = very, s = strong, m = medium, w = weak, br = broad).

Elemental Analysis:

$\text{C}_{68}\text{H}_{104}\text{Co}_2\text{Dy}_4\text{N}_{14}\text{O}_{28}$ (2333.50 g/mol)

calculated: C 35.00, H 4.49, N 8.40; (with solvent)

calculated: C 34.14, H 4.39, N 7.47; (without solvent)

found: C 35.12, H 4.52, N 8.44.

7.10.39 $[\text{Co}^{\text{III}}_2\text{Ho}^{\text{III}}_4(\mu_3\text{-OH})_2(\text{hmp})_4(\text{piv})_8(\mu\text{-N}_3)_2(\text{NO}_3)_2] \cdot 2\text{CH}_3\text{CN}$ (47)

The reaction was performed analogously to the synthesis of **46** but using 0.100 g (0.22 mmol) $\text{Ho}(\text{NO}_3)_3 \cdot 6\text{H}_2\text{O}$ in place of the $\text{Dy}(\text{NO}_3)_3 \cdot 6\text{H}_2\text{O}$.

Yield: 0.011 g (15 % with respect to cobalt)

Selected IR data (KBr pellet):

$\tilde{\nu}$ = 3435.4 (wb), 2958.4 (m), 2928.5 (w), 2868.2 (w), 2076.5 (m), 1613.3 (w), 1567.2 (s), 1552.4 (ms), 1483.6 (ms), 1465.4 (m), 1422.1 (ms), 1375.2 (wm), 1356.9 (m), 1312.3 (m), 1228.1 (m), 1032.0 (wm), 894.4 (w), 546.2 (wm) cm^{-1}

(v = very, s = strong, m = medium, w = weak, br = broad).

Elemental Analysis:

$\text{C}_{68}\text{H}_{104}\text{Co}_2\text{Ho}_4\text{N}_{14}\text{O}_{28}$ (2343.22 g/mol)

calculated: C 34.85, H 4.47, N 8.37; (with solvent)

calculated: C 34.00, H 4.37, N 7.43; (without solvent)

found: C 34.62, H 4.42, N 8.24.

7.10.40 $[\text{Co}^{\text{III}}_2\text{Er}^{\text{III}}_4(\mu_3\text{-OH})_2(\text{hmp})_4(\text{piv})_8(\mu\text{-N}_3)_2(\text{NO}_3)_2] \cdot 2\text{CH}_3\text{CN}$ (48)

The reaction was performed analogously to the synthesis of **46** but using 0.101 g (0.22 mmol) $\text{Er}(\text{NO}_3)_3 \cdot 6\text{H}_2\text{O}$ in place of the $\text{Dy}(\text{NO}_3)_3 \cdot 6\text{H}_2\text{O}$.

Yield: 0.013 g (9 % with respect to cobalt)

Selected IR data (KBr pellet):

$\tilde{\nu}$ = 3437.3 (mbr), 2958.5 (ms), 2928.0 (m), 2867.9 (wm), 2081.0 (vs), 1580.1 (vs), 1557.5 (s), 1483.9 (vs), 1425.0 (vs), 1406.1 (ms), 1375.8 (ms), 1358.0 (ms), 1314.2 (ms), 1286.8 (m), 1229.2 (ms), 1032.5 (m), 895.5 (w), 769.5 (m), 552.7 (w) cm^{-1}

(v = very, s = strong, m = medium, w = weak, br = broad).

Elemental Analysis:

$C_{68}H_{104}Co_2Er_4N_{14}O_{28}$ (2352.54 g/mol)

calculated: C 34.72, H 4.46, N 8.34; (with solvent)

calculated: C 33.86, H 4.35, N 7.40; (without solvent)

found: C 34.81, H 4.47, N 8.31.

8 Crystal structure data

For compounds for which only the unit cell was determined, only the cell parameters are given.

Compound	9	10
Empirical Formula	C ₅₅ H ₇₂ La ₂ Mn ₂ N ₁₀ O ₂₅	C ₅₅ H ₆₅ Cl ₂ La ₂ Mn ₄ N ₁₂
FW [g/mol]	1660.90	1966.67
Crystal System	monoclinic	monoclinic
Space Group	P2 ₁ /c	P 2 ₁ /c
a [Å]	12.0557(10)	16.7254(12)
b [Å]	13.7630(12)	21.3575(13)
c [Å]	21.6145(17)	23.5210(15)
α [°]	90	90
β [°]	98.734(9)	91.473(6)
γ [°]	90	90
Volume [Å ³]	3544.7(5)	8399.2(10)
Z	2	4
T [K]	298	150(2)
F (000)	1672	3916
D _c [Mg m ⁻³]	1.556	1.555
μ(Mo-Kα)[mm ⁻¹]	1.609	1.722
Diffractometer	STOE IPDS II	STOE IPDS II
Data Measured	22196	34174
Unique Data	6888	10254
R _{int}	0.0775	0.0783
Data with [I>2σ(I)]	3902	7720
Parameters	410	923
Restraints	22	210
wR ₂ (all data)	0.1600	0.2878
R ₁ ([I/σ>2σ])	0.0546	0.1030
S (all data)	0.984	1.066
Biggest diff. peak/hole	0.579/-1.343	1.162/-1.503

8 CRYSTAL STRUCTURE DATA

Compound	11	12
Empirical Formula	$C_{70}H_{92}Eu_4Mn_2N_{14}O_{22}$	$C_{70}H_{92}Gd_4Mn_2N_{14}O_{22}$
FW [g/mol]	2199.30	2220.44
Crystal System	monoclinic	monoclinic
Space Group	C2/c	C2/c
a [Å]	29.671(3)	29.7074(11)
b [Å]	14.2200(9)	14.2061(6)
c [Å]	21.663(2)	21.6628(7)
α [°]	90	90
β [°]	108.158(12)	108.147(3)
γ [°]	90	90
Volume [Å ³]	8684.8(13)	8687(7)
Z	4	
T [K]	200(2)	200(2)
F (000)	4352	
Dc [Mg m ⁻³]	1.682	
μ (Mo-K α)[mm ⁻¹]	3.201	
Diffractometer	STOE IPDS II	
Data Measured	24676	
Unique Data	8381	
Rint	0.1625	
Data with [$I > 2\sigma(I)$]	4544	
Parameters	506	
Restraints	0	
wR2 (all data)	0.1907	
R1 ($[I > 2\sigma]$)	0.1561	
S (all data)	0.963	
Biggest diff. peak/hole	1.596/-4.006	

8 CRYSTAL STRUCTURE DATA

Compound	13	14
Empirical Formula	$C_{74}H_{98}Tb_4Mn_2N_{16}O_{22}$	$C_{74}H_{98}Dy_4Mn_2N_{16}O_{22}$
FW [g/mol]	2309.24	2323.56
Crystal System	monoclinic	triclinic
Space Group	C2/c	$P\bar{1}$
a [Å]	19.7985(4)	19.5580(8)
b [Å]	21.0543(5)	20.7692(10)
c [Å]	24.4422(5)	24.0713(10)
α [°]	107.013(2)	106.861(3)
β [°]	91.141(2)	91.128(3)
γ [°]	102.002(2)	102.110(4)
Volume [Å ³]	9494(3)	9115.3(7)
Z		4
T [K]	200(2)	150(2)
F (000)		4576
D_c [Mg m ⁻³]		1.693
μ (Mo-K α)[mm ⁻¹]		3.580
Diffractometer		STOE IPDS II
Data Measured		63851
Unique Data		35822
R_{int}		0.0319
Data with $[I > 2\sigma(I)]$		25042
Parameters		2093
Restraints		79
wR_2 (all data)		0.1518
R_1 ($[I/\sigma > 2\sigma]$)		0.0560
S (all data)		0.984
Biggest diff. peak/hole		4.768/-3.311

Compound	15	16
Empirical Formula	$C_{74}H_{98}Ho_4Mn_2N_{16}O_{22}$	$C_{74}H_{98}Er_4Mn_2N_{16}O_{22}$
FW [g/mol]	2333.26	2342.58
Crystal System	triclinic	triclinic
Space Group	$P\bar{1}$	$P\bar{1}$
a [Å]	19.7379(6)	19.7532(5)
b [Å]	21.0014(6)	21.0178(6)
c [Å]	24.3715(6)	24.3038(8)
α [°]	106.954(3)	106.733(3)
β [°]	91.068(3)	90.953(3)
γ [°]	101.946(3)	102.078(3)
Volume [Å ³]	9420(4)	9417(4)
T [K]	200(2)	200(2)

8 CRYSTAL STRUCTURE DATA

Compound	17	18
Empirical Formula	$C_{71}H_{137}Gd_3Mn_4N_8O_{30}$	$C_{71}H_{137}Dy_3Mn_4N_8O_{30}$
FW [g/mol]	2274.39	2290.14
Crystal System	orthorhombic	orthorhombic
Space Group	Pbca	Pbca
a [Å]	13.4221(12)	13.4288(10)
b [Å]	26.739(2)	26.7203(19)
c [Å]	54.022(5)	53.932(4)
α [°]	90	90
β [°]	90	90
γ [°]	90	90
Volume [Å ³]	19388(3)	19352(4)
T [K]	293(2)	293(2)

Compound	19	20
Empirical Formula	$C_{71}H_{137}Ho_3Mn_4N_8O_{30}$	$C_{71}H_{137}Er_3Mn_4N_8O_{30}$
FW [g/mol]	2297.44	2304.42
Crystal System	orthorhombic	orthorhombic
Space Group	Pbca	Pbca
a [Å]	13.5875(3)	13.8035(5)
b [Å]	27.0030(6)	27.247(16)
c [Å]	54.4932(17)	54.8616(2)
α [°]	90	90
β [°]	90	90
γ [°]	90	90
Volume [Å ³]	19993.7(9)	20633(31)
Z	8	
T [K]	293(2)	293(2)
F (000)	9280	
D_c [Mg m ⁻³]	1.526	
μ (Mo-K α)[mm ⁻¹]	2.905	
Diffractometer	STOE IPDS II	
Data Measured	86663	
Unique Data	18211	
R_{int}	0.0887	
Data with [$I > 2\sigma(I)$]	10865	
Parameters	1024	
Restraints	170	
wR_2 (all data)	0.1094	
R_1 ($[I > 2\sigma]$)	0.0508	
S (all data)	0.960	
Biggest diff. peak/hole	0.861/-0.833	

8 CRYSTAL STRUCTURE DATA

Compound	21	22
Empirical Formula	$C_{118}H_{222}Pr_6Li_2Mn_4N_{12}O_{50}$	$C_{118}H_{222}Nd_6Li_2Mn_4N_{12}O_{50}$
FW [g/mol]	3688.18	3708.15
Crystal System	monoclinic	monoclinic
Space Group	$P 2_1/n$	$P 2_1/n$
a [Å]	19.1528(19)	19.1127(1)
b [Å]	15.2274(15)	15.5506(7)
c [Å]	26.697(3)	26.5793(1)
α [°]	90	90
β [°]	100.398(2)	100.927(6)
γ [°]	90	90
Volume [Å ³]	7658.1(13)	7756(10)
Z	2	
T [K]	100(2)	200(2)
F (000)	3748	
D_c [Mg m ⁻³]	1.599	
μ (Mo-K α)[mm ⁻¹]	2.268	
Diffractometer	Bruker Smart Apex	
Data Measured	48799	
Unique Data	14993	
R_{int}	0.0604	
Data with [$I > 2\sigma(I)$]	11495	
Parameters	905	
Restraints	88	
wR_2 (all data)	0.1156	
R_1 ($[I/\sigma > 2\sigma]$)	0.0497	
S (all data)	1.034	
Biggest diff. peak/hole	1.401/-1.230	

Compound	23	24
Empirical Formula	$C_{118}H_{222}Sm_6Li_2Mn_4N_{12}O_{50}$	$C_{118}H_{222}Eu_6Li_2Mn_4N_{12}O_{50}$
FW [g/mol]	3744.87	3754.49
Crystal System	monoclinic	monoclinic
Space Group	$P 2_1/n$	$P 2_1/n$
a [Å]	19.4126(7)	19.3683(8)
b [Å]	15.4350(4)	15.4191(4)
c [Å]	26.9611(1)	26.9509(1)
α [°]	90	90
β [°]	100.049(5)	100.177(5)
γ [°]	90	90
Volume [Å ³]	7954(7)	7922(8)
T [K]	200(2)	200(2)

8 CRYSTAL STRUCTURE DATA

Compound	25	26
Empirical Formula	$C_{116}H_{219}Gd_6Li_2Mn_4N_{11}O_{50}$	$C_{118}H_{222}Tb_6Li_2Mn_4N_{12}O_{50}$
FW [g/mol]	3745.16	3796.26
Crystal System	monoclinic	monoclinic
Space Group	$P 2_1/n$	$P 2_1/n$
a [Å]	19.0162(12)	19.2759(6)
b [Å]	15.2263(7)	15.3828(3)
c [Å]	26.6159(18)	26.7685(9)
α [°]	90	90
β [°]	99.851(5)	99.892(4)
γ [°]	90	90
Volume [Å ³]	7592.9(8)	7819.3(6)
Z	2	
T [K]	150(2)	200(2)
F (000)	3764	
D_c [Mg m ⁻³]	1.638	
μ (Mo-K α)[mm ⁻¹]	2.982	
Diffractometer	Bruker Smart Apex	
Data Measured	45981	
Unique Data	15461	
R_{int}	0.0636	
Data with [$I > 2\sigma(I)$]	11005	
Parameters	842	
Restraints	50	
wR_2 (all data)	0.1358	
R_1 ($[I/\sigma > 2\sigma]$)	0.0545	
S (all data)	0.979	
Biggest diff. peak/hole	1.135/-2.635	

8 CRYSTAL STRUCTURE DATA

Compound	27	28
Empirical Formula	$C_{116}H_{219}Dy_6Li_2Mn_4N_{11}O_{50}$	$C_{126}H_{234}Ho_6Li_2Mn_4N_{16}O_{50}$
FW [g/mol]	3776.66	3996.50
Crystal System	monoclinic	monoclinic
Space Group	$P 2_1/c$	$C2/c$
a [Å]	18.8860(16)	28.7327(5)
b [Å]	15.1696(13)	18.1269(4)
c [Å]	26.450(2)	34.4563(7)
α [°]	90	90
β [°]	99.472(1)	109.104(2)
γ [°]	90	90
Volume [Å ³]	7474.3(11)	16957(8)
Z	2	
T [K]	100(2)	200(2)
F (000)	3788	
D_c [Mg m ⁻³]	1.678	
μ (Mo-K α) [mm ⁻¹]	3.366	
Diffractometer	Bruker Smart Apex	
Data Measured	53361	
Unique Data	16577	
R_{int}	0.0476	
Data with [$I > 2\sigma(I)$]	13163	
Parameters	842	
Restraints	50	
wR_2 (all data)	0.1697	
R_1 ($[I/\sigma > 2\sigma]$)	0.0630	
S (all data)	1.110	
Biggest diff. peak/hole	4.250/-2.544	

8 CRYSTAL STRUCTURE DATA

Compound	29	30
Empirical Formula	$C_{126}H_{234}Li_2Mn_4N_{16}O_{50}Y_6$	$C_{54}H_{111}Pr_2Fe_4N_7O_{26}$
FW [g/mol]	3540.39	1779.72
Crystal System	monoclinic	triclinic
Space Group	C2/c	$P\bar{1}$
a [Å]	34.0806(17)	10.3828(10)
b [Å]	17.9812(7)	11.5447(11)
c [Å]	28.4767(12)	17.3466(17)
α [°]	90	97.505(11)
β [°]	109.219(4)	106.252(11)
γ [°]	90	97.510(11)
Volume [Å ³]	16478.2(13)	1948.3(3)
Z	4	1
T [K]	180(2)	200(2)
F (000)	7368	914
D_c [Mg m ⁻³]	1.427	1.517
μ (Mo-K α)[mm ⁻¹]	2.462	2.024
Diffractometer	STOE IPDS II	STOE IPDS II
Data Measured	16239	15445
Unique Data	16239	7061
R_{int}	0.0000	0.0611
Data with [$I > 2\sigma(I)$]	10674	5941
Parameters	857	419
Restraints	60	50
wR_2 (all data)	0.1533	0.1436
R_1 ($[I/\sigma > 2\sigma]$)	0.0641	0.0523
S (all data)	1.034	1.026
Biggest diff. peak/hole	0.467/-0.589	1.372/-2.755

8 CRYSTAL STRUCTURE DATA

Compound	31	32
Empirical Formula	$C_{55}H_{114}Nd_2Fe_4N_6O_{27}$	$C_{55}H_{114}Sm_2Fe_4N_6O_{27}$
FW [g/mol]	1803.38	1815.62
Crystal System	triclinic	triclinic
Space Group	$P\bar{1}$	$P\bar{1}$
a [Å]	10.3419(8)	10.2621(10)
b [Å]	11.6491(9)	11.6226(11)
c [Å]	17.3102(13)	17.2553(17)
α [°]	98.724(9)	98.746(11)
β [°]	105.332(9)	105.378(11)
γ [°]	95.201(9)	95.125(11)
Volume [Å ³]	1969.1(2)	1943.1(3)
Z		1
T [K]	200(2)	200(2)
F (000)		930
D_c [Mg m ⁻³]		1.552
μ (Mo-K α) [mm ⁻¹]		2.288
Diffractometer		STOE IPDS II
Data Measured		12582
Unique Data		7041
R_{int}		0.0456
Data with [$I > 2\sigma(I)$]		5693
Parameters		421
Restraints		36
wR_2 (all data)		0.1476
R_1 ($[I/\sigma > 2\sigma]$)		0.0552
S (all data)		1.016
Biggest diff. peak/hole		0.980/-2.297

8 CRYSTAL STRUCTURE DATA

Compound	33	34
Empirical Formula	$C_{55}H_{114}Eu_2Fe_4N_6O_{27}$	$C_{55}H_{114}Gd_2Fe_4N_6O_{27}$
FW [g/mol]	1818.84	1829.42
Crystal System	triclinic	triclinic
Space Group	$P\bar{1}$	$P\bar{1}$
a [Å]	10.2636(10)	10.2927(9)
b [Å]	11.6162(12)	11.5720(9)
c [Å]	17.2433(19)	17.2195(14)
α [°]	98.697(12)	98.481(10)
β [°]	105.296(12)	105.349(10)
γ [°]	94.982(12)	95.225(10)
Volume [Å ³]	1942.8(3)	1937.9(3)
Z	1	1
T [K]	200(2)	200(2)
F (000)	932	934
D_c [Mg m ⁻³]	1.555	1.568
μ (Mo-K α)[mm ⁻¹]	2.391	2.490
Diffractometer	STOE IPDS II	STOE IPDS II
Data Measured	11605	12594
Unique Data	6669	7054
R_{int}	0.1666	0.0288
Data with [$I > 2\sigma(I)$]	4014	5649
Parameters	421	421
Restraints	37	36
wR_2 (all data)	0.1810	0.1343
R_1 ($[I/\sigma > 2\sigma]$)	0.0664	0.0488
S (all data)	0.998	1.033
Biggest diff. peak/hole	0.951/-1.784	1.246/-1.794

8 CRYSTAL STRUCTURE DATA

Compound	35	36
Empirical Formula	$C_{55}H_{114}Y_2Fe_4N_6O_{27}$	$C_{75}H_{108}Fe_6EuN_{11}O_{38}$
FW [g/mol]	1692.74	2258.75
Crystal System	triclinic	monoclinic
Space Group	$P\bar{1}$	C2/c
a [Å]	10.2665(10)	27.248(13)
b [Å]	11.5663(11)	15.821(7)
c [Å]	17.1509(15)	26.412(11)
α [°]	98.376(11)	90
β [°]	105.369(11)	117.93(5)
γ [°]	95.339(11)	90
Volume [Å ³]	1924.2(3)	10060(11)
Z	1	
T [K]	200(2)	200(2)
F (000)	884	
D_c [Mg m ⁻³]	1.461	
μ (Mo-K α)[mm ⁻¹]	2.300	
Diffractometer	STOE IPDS II	
Data Measured	12040	
Unique Data	6926	
R_{int}	0.0507	
Data with [$I > 2\sigma(I)$]	4275	
Parameters	421	
Restraints	36	
wR_2 (all data)	0.1842	
R_1 ($[I/\sigma > 2\sigma]$)	0.0647	
S (all data)	0.990	
Biggest diff. peak/hole	1.244/-1.113	

8 CRYSTAL STRUCTURE DATA

Compound	37	38
Empirical Formula	$C_{75}H_{108}Fe_6GdN_{11}O_{38}$	$C_{75}H_{108}Fe_6DyN_{11}O_{38}$
FW [g/mol]	2264.07	2269.28
Crystal System	monoclinic	monoclinic
Space Group	C2/c	C2/c
a [Å]	26.920(4)	27.4001(2)
b [Å]	15.589(2)	15.7843(8)
c [Å]	26.079(4)	26.4138(2)
α [°]	90	90
β [°]	118.037(2)	117.005(9)
γ [°]	90	90
Volume [Å ³]	9660(2)	10178(1)
Z	4	
T [K]	100(2)	200(2)
F (000)	4636	
D_c [Mg m ⁻³]	1.557	
μ (Mo-K α)[mm ⁻¹]	1.641	
Diffractometer	Bruker Smart Apex	
Data Measured	29728	
Unique Data	10681	
R_{int}	0.0287	
Data with [$I > 2\sigma(I)$]	8726	
Parameters	573	
Restraints	78	
wR_2 (all data)	0.2063	
R_1 ($[I/\sigma > 2\sigma]$)	0.0762	
S (all data)	1.046	
Biggest diff. peak/hole	3.445/-1.936	

Compound	39	40
Empirical Formula	$C_{75}H_{108}Fe_6HoN_{11}O_{38}$	$C_{75}H_{108}Fe_6ErN_{11}O_{38}$
FW [g/mol]	2271.71	2274.04
Crystal System	monoclinic	monoclinic
Space Group	C2/c	C2/c
a [Å]	27.3588(2)	26.5943(16)
b [Å]	15.6478(9)	15.6322(5)
c [Å]	26.6457(2)	27.3747(16)
α [°]	90	90
β [°]	117.303(11)	117.326(6)
γ [°]	90	90
Volume [Å ³]	10136(17)	10110(9)
T [K]	200(2)	200(2)

8 CRYSTAL STRUCTURE DATA

Compound	41	42
Empirical Formula	$C_{68}H_{104}Pr_4Co_2N_{14}O_{28}$	$C_{68}H_{104}Sm_4Co_2N_{14}O_{28}$
FW [g/mol]	2247.15	2284.94
Crystal System	monoclinic	monoclinic
Space Group	C2/c	C2/c
a [Å]	24.109(3)	24.7100(2)
b [Å]	18.9152(15)	18.9670(9)
c [Å]	19.909(2)	20.2500(18)
α [°]	90	90
β [°]	94.553(9)	95.667(11)
γ [°]	90	90
Volume [Å ³]	8775.2(12)	9444(20)
Z	4	
T [K]	150(2)	200(2)
F (000)	4496	
D_c [Mg m ⁻³]	1.649	
μ (Mo-K α) [mm ⁻¹]	2.548	
Diffractometer	STOE IPDS II	
Data Measured	40134	
Unique Data	10828	
R_{int}	0.0285	
Data with $[I > 2\sigma(I)]$	9502	
Parameters	521	
Restraints	17	
wR_2 (all data)	0.1151	
R_1 ($[I/\sigma > 2\sigma]$)	0.0429	
S (all data)	1.062	
Biggest diff. peak/hole	0.952/-1.989	

8 CRYSTAL STRUCTURE DATA

Compound	43	44
Empirical Formula	$C_{68}H_{104}Eu_4Co_2N_{14}O_{28}$	$C_{68}H_{104}Gd_4Co_2N_{14}O_{28}$
FW [g/mol]	2291.35	2312.51
Crystal System	monoclinic	monoclinic
Space Group	C2/c	C 2/c
a [Å]	24.3688(7)	23.8887(19)
b [Å]	18.8564(7)	18.5208(15)
c [Å]	20.0951(5)	19.8980(16)
α [°]	90	90
β [°]	94.916(3)	94.608(1)
γ [°]	90	90
Volume [Å ³]	9199(8)	8775.2(12)
Z		4
T [K]	200(2)	100(2)
F (000)		4576
D_c [Mg m ⁻³]		1.750
μ (Mo-K α) [mm ⁻¹]		3.430
Diffractometer		STOE IPDS II
Data Measured		34328
Unique Data		10078
R_{int}		0.0351
Data with [$I > 2\sigma(I)$]		9078
Parameters		519
Restraints		15
wR_2 (all data)		0.0979
R_1 ($[I/\sigma > 2\sigma]$)		0.0342
S (all data)		1.083
Biggest diff. peak/hole		1.528/-0.520

8 CRYSTAL STRUCTURE DATA

Compound	45	46
Empirical Formula	$C_{68}H_{104}Tb_4Co_2N_{14}O_{28}$	$C_{68}H_{104}Dy_4Co_2N_{14}O_{28}$
FW [g/mol]	2319.20	2333.51
Crystal System	monoclinic	monoclinic
Space Group	C2/c	C 2/c
a [Å]	20.1179(5)	23.9666(12)
b [Å]	18.7135(4)	18.4531(11)
c [Å]	24.3414(6)	19.8875(9)
α [°]	90	90
β [°]	94.744(3)	94.621(4)
γ [°]	90	90
Volume [Å ³]	9132(6)	8766.8(8)
Z		4
T [K]	200(2)	150(2)
F (000)		4608
D_c [Mg m ⁻³]		1.768
μ (Mo-K α) [mm ⁻¹]		3.817
Diffractometer		STOE IPDS II
Data Measured		32628
Unique Data		10481
R_{int}		0.0264
Data with [$I > 2\sigma(I)$]		9004
Parameters		519
Restraints		15
wR_2 (all data)		0.1068
R_1 ($[I/\sigma > 2\sigma]$)		0.0398
S (all data)		1.051
Biggest diff. peak/hole		0.769/-2.239

8 CRYSTAL STRUCTURE DATA

Compound	47	48
Empirical Formula	C ₆₈ H ₁₀₄ Ho ₄ Co ₂ N ₁₄ O ₂₈	C ₆₈ H ₁₀₄ Er ₄ Co ₂ N ₁₄ O ₂₈
FW [g/mol]	2343.23	2352.55
Crystal System	triclinic	triclinic
Space Group	P $\bar{1}$	P $\bar{1}$
a [Å]	13.5562(10)	13.5725(14)
b [Å]	13.8969(10)	13.9107(15)
c [Å]	13.9677(10)	13.9731(14)
α [°]	84.951(1)	85.082(2)
β [°]	69.693(1)	69.662(2)
γ [°]	64.180(1)	64.198(2)
Volume [Å ³]	2215.2(3)	2220.4(4)
Z	1	1
T [K]	100(2)	100(2)
F (000)	1156	1160
D _c [Mg m ⁻³]	1.756	1.759
μ (Mo-K α) [mm ⁻¹]	3.975	4.182
Diffractometer	Bruker Smart Apex	Bruker Smart Apex
Data Measured	17365	12174
Unique Data	9739	9216
R _{int}	0.0160	0.0215
Data with [I > 2 σ (I)]	8861	7168
Parameters	524	524
Restraints	16	16
wR ₂ (all data)	0.0768	0.1256
R ₁ ([I/σ > 2σ])	0.0293	0.0476
S (all data)	1.049	1.009
Biggest diff. peak/hole	3.888/-0.921	5.411/-1.590

9 Bibliography

- (ABBAS, 2010: 8067ff) G. Abbas, Y. Lan, G. E. Kostakis, W. Wernsdorfer, C. E. Anson, A. K. Powell, *Inorg. Chem.*, **2010**, 49, 8067-8072.
- (ABU-NAWWAS, 2008: 198ff) A.-A. H. Abu-Nawwas, P. V. Mason, V. A. Milway, C. A. Muryn, R. J. Pritchard, Floriana Tuna, D. Collison, R. E. P. Winpenny, *Dalton Trans.*, **2008**, 198-200.
- (AIME, 1998: 19ff) S. Aime, M. Botta, M. Fasano, E. Terreno, *Chem. Soc. Rev.*, **1998**, 27, 19-29.
- (AKHTAR, 2009: 1698ff) M. N. Akhtar, Y. Lan, V. Mereacre, R. Clérac, C. E. Anson, A. K. Powell, *Polyhedron*, **2009**, 28, 1698-1703.
- (AKHTAR, 2009: 3502ff) M. N. Akhtar, Y.-Z. Zheng, Y. Lan, V. Mereacre, C. E. Anson, A. K. Powell, *Inorg. Chem.*, **2009**, 48, 3502-3504.
- (AKO, 2006: 2579ff) A. M. Ako, V. Mereacre, I. J. Hewitt, R. Clérac, L. Lecren, C. E. Anson, A. K. Powell, *J. Mater. Chem.*, **2006**, 16, 2579-2586.
- (AKO, 2006: 4926ff) A. M. Ako, I. J. Hewitt, V. Mereacre, R. Clérac, W. Wernsdorfer, C. E. Anson, A. K. Powell, *Angew. Chem. Int. Ed.*, **2006**, 45, 4926-4929.
- (AKO, 2006: 5048ff) A. M. Ako, I. J. Hewitt, V. Mereacre, R. Clérac, W. Wernsdorfer, C. E. Anson, A. K. Powell, *Angew. Chem.*, **2006**, 118, 5048-5051.
- (AKO, 2007: 756ff) A. M. Ako, O. Waldmann, V. Mereacre, F. Klöwer, I. J. Hewitt, C. E. Anson, H. U. Gudel, A. K. Powell, *Inorg. Chem.*, **2007**, 46, 756-766.
- (AKO, 2009: 544ff) A. M. Ako, V. Mereacre, R. Clérac, W. Wernsdorfer, I. J. Hewitt, C. E. Anson, A. K. Powell, *Chem. Commun.*, **2009**, 544-546.
- (ALBORÉS, 2009: 9366ff) P. Alborés, E. Rentschler, *Angew. Chem. Int. Ed.*, **2009**, 48, 9366-9370.
- (ALLEN, 1993: 31ff) F. H. Allen, O. Kennard, *Chem. Des. Autom. News*, **1993**, 8 (1), 31-37.

- (AMMALA, 2000: 1688ff) P. Ammala, J. D. Cashion, C. M. Kepert, B. Moubaraki, K. S. Murray, L. Spiccia, B. O. West, *Angew. Chem. Int. Ed.*, **2000**, 39, 1688–1690.
- (ANDRUH, 1993: 1616ff) M. Andruh, E. Bakalbassis, O. Kahn, J. C. Trombe, P. Porcher, *Inorg. Chem.*, **1993**, 32, 1616-1622.
- (ARMSTRONG, 1984: 3653ff) W. H. Armstrong, A. Spool, G. C. Papaefthymiou, R. B. Frankel, S. J. Lippard, *J. Am. Chem. Soc.*, **1984**, 106, 3653-3667.
- (AROMÍ, 2003: 5142ff) G. Aromí, A. S. Batsanov, P. Christian, M. Helliwell, A. Parkin, S. Parsons, A. A. Smith, G. A. Timco, R. E. P. Winpenny, *Chem. Eur. J.*, **2003**, 9, 5142-5161.
- (AROMÍ, 2006: 1ff) G. Aromí, E. K. Brechin, *Structure & Bonding*, **2006**, 122, 1–69.
- (AUBIN 1996: 7746ff) S. M. J. Aubin, M. W. Wemple, D. M. Adams, H.-L. Tsai, G. Christou, D. N. Hendrickson, *J. Am. Chem. Soc.*, **1996**, 118, 7746-7754.
- (BAGGIO, 2005: 8979ff) R. Baggio, R. Calvo, M. T. Garland, O. Peña, M. Perec, A. Rizzi, *Inorg. Chem.*, **2005**, 44, 8979-8987.
- (BAIN, 2008: 532ff) G. A. Bain, J. F. Berry, *J. Chem. Ed.*, **2008**, 85 (4), 532-536.
- (BAO, 2007: 2333ff) S. S. Bao, L. F. Ma, Y. Wang, L. Fang, C. J. Zhu, Y. Z. Li, L. M. Zheng, *Chem. Eur. J.*, **2007**, 13, 2333 – 2343.
- (BASKAR, 2010: 4747ff) V. Baskar, K. Gopal, M. Helliwell, F. Tuna, W. Wernsdorfer, R. E. P. Winpenny, *Dalton Trans.*, **2010**, 39, 4747–4750.
- (BATSANOV, 1988: 266ff) A. S. Batsanov, Yu.T. Struchkov, G. A. Timco, *Koord. Khim.*, **1988**, 14, 266.
- (BEATTIE, 1996: 2141ff) J. K. Beattie, T. W. Hambley, J. A. Kleptko, A. F. Masters, P. Turner, *Polyhedron*, **1996**, 15 (13), 2141-2150.
- (BENELLI, 1999: 4125ff) C. Benelli, M. Murrie, S. Parsons, R. E. P. Winpenny, *J. Chem. Soc., Dalton Trans.*, **1999**, 4125–4126.
- (BENELLI, 2002: 2369ff) C. Benelli, D. Gatteschi, *Chem. Rev.*, **2002**, 102, 2369–2387.

- (BINZ, 2006: 207202) B. Binz, A. Vishwanath, V. Aji, *Phys. Rev. Lett.*, **2006**, 96, 207202.
- (BISWAS, 2007: 1059ff) B. Biswas, S. Khanra, T. Weyhermüller, P. Chaudhuri, *Chem. Commun.*, **2007**, 1059–1061.
- (BLAKE, 1975: 193ff) A. B. Blake, L. R. Fraser, *J. Chem. Soc., Dalton Trans.*, **1975**, 193–197.
- (BLUME, 1967: 305ff) M. Blume, *Phys. Rev. Lett.*, **1967**, 18 (9), 305–307.
- (BOND, 1998: 1845ff) A. M. Bond, R. J. H. Clark, D. G. Humphrey, P. Panayiotopoulos, B. W. Skelton, A. H. White, *J. Chem. Soc., Dalton Trans.*, **1998**, 1845–1852.
- (BRECHIN, 2000: 389ff) E. K. Brechin, M. J. Knapp, J. C. Huffman, D. N. Hendrickson, G. Christou, *Inorg. Chim. Acta*, **2000**, 297, 389–399.
- (BRECHIN, 2005: 502ff) E. K. Brechin, E. C. Sanudo, W. Wernsdorfer, C. Boskovic, J. Yoo, D. N. Hendrickson, A. Yamaguchi, H. Ishimoto, T. E. Concolino, A. L. Rheingold, G. Christou, *Inorg. Chem.*, **2005**, 44, 502–511.
- (BRESE, 1991: 192ff) N. E. Brese, M. O'Keeffe, *Acta Cryst.*, **1991**, B47, 192–197.
- (BROOKER, 2002: 2080ff) S. Brooker, D. J. de Geest, R. J. Kelly, P. G. Plieger, B. Moubaraki, K. S. Murray, G. B. Jameson, *Dalton Trans.*, **2002**, 2080–2087.
- (BROWN, 1985: 244ff) I. D. Brown, D. Altermatt, *Acta Cryst.*, **1985**, B41, 244–247.
- (BROWN, 2006: 4497ff) D. A. Brown, N. J. Fitzpatrick, H. Müller-Bunz, A. T. Ryan, *Inorg. Chem.*, **2006**, 45, 4497–4507.
- (BÜNZLI, 1989: 432ff) J. C. G. Bünzli, G. R. Choppin, Editors. *Lanthanide Probes in Life, Chemical and Earth Sciences: Theory and Practice*, **1989**, 432.
- (CAO, 2008:1ff) C. Cao, S. Hill, H.-P. Cheng, *Phys. Rev. Lett.*, **2008**, Article 167206, 1–4.
- (CANESCHI, 1991: 5873ff) A. Caneschi, D. Gatteschi, R. Sessoli, A. L. Barra, L. C. Brunel, M. Guillot, *J. Am. Chem. Soc.*, **1991**, 113, 5873–5814.

- (CARLIN, 1986) R. L. Carlin, *Magnetochemistry*, **1986**, Springer-Verlag, Berlin.
- (ÇELENLİGİL-ÇETİN, 2000: 5838ff) R. Çelenligil-Çetin, R. J. Staples, P. Stavropoulos, *Inorg. Chem.*, **2000**, 39, 5838-5846.
- (CHEN, 2009: 808ff) F. Chen, W. Lu, Y. Zhu, B. Wu, X. Zheng, *J. Coord. Chem.*, **2009**, 62, Nr. 5, 808-816.
- (CHERKEZOVA-ZHELEVA, 2010) Z. Cherkezova-Zheleva, M. Shopska, I. Mitov, G. Kadinov, *Hyperfine Interactions*, **2010**, DOI 10.1007/s10751-010-0176-5.
- (CHRISTOU, 2000: 66ff) G. Christou, D. Gatteschi, D. N. Hendrickson, R. Sessoli, *MRS Bull.*, **2000**, 25, 66.
- (CHUDNOVSKY, 1988: 661ff) E. M. Chudnovsky, L. Gunther, *Phys. Rev. Lett.*, **1988**, 60 (8), 661-664.
- (CORNIA, 1996: 4414ff) A. Cornia, D. Gatteschi, K. Hegetschweiler, L. Hausherr-Primo, V. Gramlich, *Inorg. Chem.*, **1996**, 35, 4414-4419.
- (COSTES, 2002: 323ff) J. P. Costes, J. M. Clemente-Juan, F. Dahan, F. Nicodème, M. Verelst, *Angew. Chem. Int. Ed.*, **2002**, 41, 323-325.
- (COTTON, 1972: 185ff) S. A. Cotton, *Coordination Chemistry Reviews*, **1972**, 8, 185-223.
- (DE SA, 1991: 55) M. S. De Sa, C. A. C. Sequeira, *Corros. Prev. Control*, **1991**, 31, 55.
- (DUNAND, 1982: 570ff) A. Dunand, R. Gerdil, *Acta Cryst.*, **1982**, B38, 570-575.
- (DUNSKII, 1978: 131ff) V. F. Dunsii, Yu. V. Yatskov, *J. of Engineering Physics and Thermophysics*, **1978**, 34 (2), 131-136.
- (ENZ, 1986: 1765ff) M. Enz, R. Schilling, *J. Phys. C: Solid State Phys.*, **1986**, 19, 1765-1770.
- (EFTHYMIU, 2009: 3373ff) C. G. Efthymiou, C. Papatriantafyllopoulou, N. I. Alexopoulou, C. P. Raptopoulou, R. Boča, J. Mrozinski, E. G. Bakalbassis, S. P. Perlepes, *Polyhedron*, **2009**, 28, 3373-3381.
- (ELISEEVA, 2006: 4809ff) S. V. Eliseeva, M. Ryazanov, F. Gumy, S. I. Troyanov, L. S. Lepnev, J.-C. G. Bünzli, N. P. Kuzmina, *Eur. J. Inorg. Chem.*, **2006**, 4809-4820.

- (FAUS, 1994: 5535ff) J. Faus, M. Julve, F. Lloret, J. A. Real, J. Sletten, *Inorg. Chem.*, **1994**, 33, 5535-5540.
- (FLEURY, 2009: 2192ff) B. Fleury, V. Huc, L. Catala, P. Jegou, L. Baraton, C. David, S. Palacin, T. Mallah, *CrystEngComm*, **2009**, 11, 2192-2197.
- (FOMINA, 2004: 1349ff) I. G. Fomina, M. A. Kiskin, A. G. Martynov, et al., *Russ. J. Inorg. Chem.*, **2004**, 49 (9), 1349-1359.
- (FOGUET-ALBIOL, 2005: 4282ff) D. Foguet-Albiol, K. A. Abboud, G. Christou, *Chem. Commun.*, **2005**, 4282-4284.
- (FOGUET-ALBIOL, 2005: 897ff) D. Foguet-Albiol, T. A. O'Brien, W. Wernsdorfer, B. Moulton, M. J. Zaworotko, K. A. Abboud, G. Christou, *Angew. Chem. Int. Ed.*, **2005**, 44, 897-901.
- (GADE, 1998: 307ff) L. H. Gade, *Koordinationschemie*, **1998**, Wiley-VCH, Weinheim, 307-309.
- (GALLOWAY, 2008: 7438) K. W. Galloway, A. M. Whyte, W. Wernsdorfer, J. Sanchez-Benitez, K. V. Kamenev, A. Parkin, R. D. Peacock, M. Murrie, *Inorg. Chem.*, **2008**, 47, 7438-7442.
- (GATTESCHI, 2008: 1701ff) D. Gatteschi, L. Bogani, A. Cornia, M. Mannini, L. Sorace, R. Sessoli, *Solid State Sciences*, **2008**, 10, 1701-1709.
- (GÓMEZ-SEGURA, 2007: 3699ff) J. Gómez-Segura, J. Veciana, D. Ruiz-Molina, *Chem. Commun.*, **2007**, 3699-3707.
- (GORUN, 1987: 3337ff) S. M. Gorun, G. C. Papaefthymiou, R. B. Frankel, S. J. Lippard, *J. Am. Chem. Soc.*, **1987**, 109, 3337-3348.
- (GREENWOOD, 1971: 148ff) N. N. Greenwood, T. C. Gibb, *Mossbauer Spectroscopy*, Chapman and Hall, London, **1971**, 148-164.
- (GRUENWALD, 2009: 2109ff) K. R. Gruenwald, A. M. Kirillov, M. Haukka, J. Sanchizc, A. J. L. Pombeiro, *Dalton Trans.*, **2009**, 2109-2120.
- (GÜTLICH, 1970: 133ff) P. Gütllich, *Chemie in unserer Zeit, Physikalische Methoden in der Chemie: Mößbauer-Spektroskopie I*, **1970**, 4, 133-144.
- (HAKEN, 2006: 280ff) H. Haken, H. Wolf, *Molekülphysik und Quantenchemie*, **2006**, Springer, Berlin.

- (HE, 2005: 8285ff) F. He, M.-L. Tong, X.-M. Chen, *Inorg. Chem.*, **2005**, 44, 8285–8292.
- (HEGETSCHWEILER, 1992: 1299ff) K. Hegetschweiler, H. W. Schmalle, H. M. Streit, V. Gramlich, H.-U. Hund, I. Ernila, *Inorg. Chem.*, **1992**, 31(7), 1299-1302.
- (HEGETSCHWEILER, 1990: 3625ff;) K. Hegetschweiler, H. Schmalle, H. M. Streit, W. Schneider, *Inorg. Chem.*, **1990**, 29(18), 3625-3627.
- (HEROUX, 2009: 3541ff) K. J. Heroux, A. L. Rheingold, D. N. Hendrickson, *Eur. J. Inorg. Chem.*, **2009**, 3541–3544.
- (HUHEEY, 2003: 534ff) J. Huheey, E. Keiter, R. Keiter, *Anorganische Chemie*, 3.Auflage, **2003**, de Gruyter, Berlin, 534-544.
- (HULLIGER, 1994: 151ff) J. Hulliger, *Angew. Chem.*, **1994**, 106, 151-171.
- (ISHIKAWA, 2003: 8694f) N. Ishikawa, M. Sugita, T. Ishikawa, S.-Y. Koshihara, Y. Kaizu, *J. Am. Chem. Soc.*, **2003**, 125, 8694-8695.
- (ISHIKAWA, 2005: 2931ff) N. Ishikawa, M. Sugita, W. Wernsdorfer, *Angew. Chem. Int. Ed.*, **2005**, 44, 2931–2935.
- (ISHIKAWA, 2005: 3650f) N. Ishikawa, M. Sugita, W. Wernsdorfer, *J. Am. Chem. Soc.*, **2005**, 127, 3650-3651.
- (ISILAK, 2009:1102ff) S. Isilak, V. Mereacre, Y. Lan, C. E. Anson, A. K. Powell, *Aust. J. Chem.*, **2009**, 62, 1102–1107.
- (IUCR, 2006) <http://reference.iucr.org/dictionary/l>, (last modified 9 May **2006**, red 6 September 2010)
- (JAHN, 1937: 220ff) H. A. Jahn, E. Teller, *Proceedings of the Royal Society of London, Series A-Mathematical and Physical Sciences*, **1937**, 161, 220-235.
- (JAMBOR, 1998: 2549ff) J. L. Jambor, J. E. Dutrizac, *Chem. Rev.*, **1998**, 98, 2549–2585.
- (JOHN, 2005: 4486ff) D. John, W. Urland, *Eur. J. Inorg. Chem.*, **2005**, 4486-4489.
- (KAHN, 1993) O. Kahn, *Molecular Magnetism*, **1993**, Wiley-VCH, New York.

- (KAHN, 2000: 3413ff) M. L. Kahn, J.-P. Sutter, S. Golhen, P. Guionneau, L. Ouahab, O. Kahn, D. Chasseau, *J. Am. Chem. Soc.*, **2000**, 122, 3413-3421.
- (KAHN, 2002: 525ff) Kahn M. L. Kahn, R. Ballou, P. Porcher, O. Kahn, J.-P. Sutter, *Chem. Eur. J.*, **2002**, 8 (2), 525-531.
- (KAJIWARA, 2011: 196ff) T. Kajiwara, M. Nakano, K. Takahashi, S. Takaishi, M. Yamashita, *Chem. Eur. J.*, **2011**, 17, 196-205.
- (KAMBE, 1950: 48ff) K. Kambe, *J. Phys. Soc. Jpn.*, **1950**, 5, 48-51.
- (KASUYA, 1956: 45ff) T. Kasuya, *Progress of Theoretical Physics*, **1956**, 16, 45-57.
- (KISKIN, 2004: 734ff) M. A. Kiskin, I. G. Fomina, G. G. Aleksandrov, A. A. Sidorov, V. M. Novotortsev, Y. G. Shvedenkov, I. L. Eremenko, I. I. Moiseev, *Inorg. Chem. Comm.*, **2004**, 7, 734-736.
- (KITTEL, 1953) C. Kittel, *Introduction to solid state physics*, **1953**, Wiley, New York.
- (KLEIN, 1952: 65ff) M. Klein, *American Journal of Physics*, **1952**, 20(2), 65-71.
- (KLOSS, 1994) A. Kloss, *Geschichte des Magnetismus*, Berlin, Offenbach, VDE-Verlag, **1994**.
- (KLÖWER, 2009: 57ff) F. Klöwer, *Dissertation, Diethanolaminliganden in der Synthese von 3d und 3d/4f molekularen Magneten*, **2009**, 57-59.
- (KOIZUMI, 2007: 8445ff) S. Koizumi, M. Nihei, T. Shiga, M. Nakano, H. Nojiri, R. Bircher, O. Waldmann, S. T. Ochsenein, H. U. Güdel, F. Fernandez-Alonso, H. Oshio, *Chem. Eur. J.*, **2007**, 13, 8445 - 8453.
- (KURETI, 2003: 281ff) S. Kureti, K. Hizbullah, W. Weisweiler, *Appl. Catal. B: Environmental*, **2003**, 43, 281-291.
- (LAGET, 1998: 1533ff) V. Laget, C. Hornick, P. Rabu, M. Drillon, R. Ziessel, *Coord. Chem. Rev.*, **1998**, 178-180, 1533-1553.
- (LAM, 2003: 149ff) A. W.-H. Lam, W.-T. Wong, S. Gao, G. Wen, X.-X. Zhang, *Eur. J. Inorg. Chem.*, **2003**, 149-163.

- (LE BRIS, 2007: 80ff) J. Le Bris, L. G. Hubert-Pfalzgraf, S. Daniele, J. Vaissermann, *Inorg. Chem. Comm.*, **2007**, 10, 80–83.
- (LECREN, 2005: 11311ff) L. Lecren, W. Wernsdorfer, Y.-G. Li, O. Roubeau, H. Miyasaka, R. Clérac, *J. Am. Chem. Soc.*, **2005**, 127, 11311–11317.
- (LEGGETT, 1987: 1ff) A. J. Leggett, S. Chakravarty, A. T. Dorsey, M. P. A. Fisher, A. Garg, W. Zwerger, *Rev. Mod. Phys.*, **1987**, 59, 1–85.
- (LERMONTOVA, 2006: 5710) E. K. Lermontova, A. A. Selina, S. S. Karlov, A. V. Churakov, J. A. K. Howard, Y. F. Oprunenko, M. Y. Antipin, J. Sundermeyer, G. S. Zaitseva, *J. Organomet. Chem.*, **2006**, 691, 5710–5724.
- (LI, 2006: 6308ff) Y. Li, F.-K. Zheng, X. Liu, W.-Q. Zou, G.-C. Guo, C.-Z. Lu, J.-S. Huang, *Inorg. Chem.*, **2006**, 45, 6308–6316.
- (LIN, 2009: 9489ff) P.-H. Lin, T. J. Burchell, L. Ungur, L. F. Chibotaru, W. Wernsdorfer, M. Murugesu, *Angew. Chem. Int. Ed.*, **2009**, 48, 9489–9492.
- (MICKLITZ, 1989: 372ff) W. Micklitz, S. G. Bott, J. G. Bentsen, S. J. Lippard, *J. Am. Chem. Soc.*, **1989**, 111, 372–374.
- (LIPPARD, 1995: 81f) S. J. Lippard, J. M. Berg, *Bioanorganische Chemie*, **1995**, Spektrum, Akad. Verl., Heidelberg, 81–82.
- (LIS, 1980: 2042ff) T. Lis, *Acta Cryst.*, **1980**, B36, 2042–2046.
- (LIU, 1993: 4102ff) W. Liu, H. H. Thorp, *Inorg. Chem.*, **1993**, 32, 4102–4105.
- (LIU, 2004: 2280f) W. S. Liu, T. Q. Jiao, Y. Z. Li, Q. Z. Liu, M. Y. Tan, H. Wang, L. F. Wang., *J. Am. Chem. Soc.*, **2004**, 126, 2280–2281.
- (MABBS, 1973) F. E. Mabbs, D. J. Machin, *Magnetism and transition metal complexes*, **1973**, Chapman and Hall, London.
- (MALAESTEAN, 2010: 1990ff) I. L. Malaestean, M. Speldrich, A. Ellern, S. G. Baca, P. Kögerler, *Polyhedron*, **2010**, 29, 1990–1997.
- (MANSON, 2000: 1135ff) J. L. Manson, E. Ressouche, J. S. Miller, *Inorg. Chem.*, **2000**, 39, 1135–1141.

- (MEHANDJIEV, 2008: 413ff) D. Mehandjiev, P. R. Bontchev, *Jour. University Chem. Techn. and Metall.*, **2008**, 43 (4), 413-417.
- (MEREACRE, 2007: 9248f) V. M. Mereacre, A. M. Ako, R. Clérac, W. Wernsdorfer, G. Filoti, J. Bartolomé, C. E. Anson, A. K. Powell, *J. Am. Chem. Soc.*, **2007**, 129 (30), 9248-9249.
- (MEREACRE, 2008: 3577ff) V. Mereacre, A. M. Ako, R. Clérac, W. Wernsdorfer, I. J. Hewitt, C. E. Anson, A. K. Powell, *Chem. Eur. J.*, **2008**, 14, 3577-3584.
- (MEREACRE, 2009: 2524ff) V. Mereacre, A. M. Ako, M. N. Akhtar, A. Lindemann, C. E. Anson, A. K. Powell, *Helvetica Chimica Acta*, **2009**, 92, 2507-2524.
- (MEREACRE, 2009: 3551ff) V. Mereacre, D. Prodius, A. M. Ako, S. Shova, C. Turta, K. Wurst, P. Jaitner, A. K. Powell, *Polyhedron*, **2009**, 28, 3551-3555.
- (MEREACRE, 2010: 4918ff) V. Mereacre, M. N. Akhtar, Y. Lan, A. M. Ako, R. Clérac, C. E. Anson, A. K. Powell, *Dalton Trans.*, **2010**, 39, 4918-4927.
- (MEREACRE, 2010: 5293ff) V. Mereacre, Y. Lan, R. Clérac, A. M. Ako, I. J. Hewitt, W. Wernsdorfer, G. Buth, C. E. Anson, A. K. Powell, *Inorg. Chem.*, **2010**, 49, 5293-5302.
- (MILIOS, 2007: 2754f) C. J. Milios, A. Vinslava, W. Wernsdorfer, S. Moggach, S. Parsons, S. P. Perlepes, G. Christou, E. K. Brechin, *J. Am. Chem. Soc.*, **2007**, 129, 2754-2755.
- (MILLER, 1994: 385ff) J. S. Miller, A. J. Epstein, *Angew. Chem. Int. Ed.*, **1994**, 33, 385-415.
- (MILLER, 2000: 4392ff) J. S. Miller, *Inorg. Chem.*, **2000**, 39, 4392-4408.
- (MISHRA, 2005: 54ff) A. Mishra, W. Wernsdorfer, K. A. Abboud, G. Christou, *Chem. Commun.*, **2005**, 54-56.
- (MISHRA, 2005: 2086ff) A. Mishra, W. Wernsdorfer, S. Parsons, G. Christou, E. K. Brechin, *Chem. Commun.*, **2005**, 2086-2088.
- (MISHRA, 2006: 10197ff) A. Mishra, W. Wernsdorfer, K. A. Abboud, G. Christou, *Inorg. Chem.*, **2006**, 45, 10197-10206.

- (MISHRA, 2007: 602) S. Mishra, J. Zhang, L. G. Hubert-Pfalzgraf, D. Luneau, E. Jeanneau, *Eur. J. Inorg. Chem.*, **2007**, 602–608.
- (MISHRA, 2008: 1940ff) A. Mishra, Y. Pushkar, J. Yano, V. K. Yachandra, W. Wernsdorfer, K. A. Abboud, G. Christou, *Inorg. Chem.*, **2008**, 47, 1940–1948.
- (MORALES, 1997: 5461ff) M. P. Morales, C. J. Serna, F. Bødker, S. Mørup, *J. Phys.: Condens. Matter*, **1997**, 9, 5461–5467.
- (MORI, 2005: 2588ff) F. Mori, T. Ishida, T. Nogami, *Polyhedron*, **2005**, 24, 2588–2592.
- (MORRISH, 1965) A. H. Morrish, *The Physical Principles of Magnetism*, John Wiley and Sons, New York, **1965**.
- (MÖßBAUER, 1958: 124ff) R. Mößbauer: *Zeitschrift für Physik: Gammastrahlung in Ir191*, **1958**, 151, 124–143.
- (MUNTO, 2006: 2612ff) M. Munto, J. Gómez-Segura, J. Campo, M. Nakano, N. Ventosa, D. Ruiz-Molina, J. Veciana, *J. Mat. Chem.*, **2006**, 16, 2612–2617.
- (MURUGESU, 2004: 4766f) M. Murugesu, M. Habrych, W. Wernsdorfer, K.A. Abboud, G. Christou, *J. Am. Chem. Soc.*, **2004**, 126, 4766–4767;
- (MURUGESU, 2006: 613ff) M. Murugesu, A. Mishra, W. Wernsdorfer, K. Abboud, G. Christou, *Polyhedron*, **2006**, 25, 613–625.
- (NAYAK, 2008: 51ff) S. Nayak, Dissertation: *The Use of Coordination Chemistry Principles to Control Aggregation Processes of Metal Ions*, **2008**, 51–55.
- (NÉEL, 1948: 137ff) L. Néel, *Annales de Physique (Paris), Propriétés magnétiques des ferrites; Ferrimagnétisme et antiferromagnétisme*, **1948**, 3, 137–198.
- (O'CONNOR, 1982) C. J. O'Connor, *Prog. Inorg. Chem.*, **1982**, 29, 203.
- (OCZKO, 2005: 237ff) G. Oczko, P. Starynowicz, *Journal of Molecular Structure*, **2005**, 740, 237–248.
- (OERSTED 1820: 273ff) H. C. Oersted, Experiments on the Effect of a Current of Electricity on the Magnetic, *Annals of Philosophy*, **1820**, 273–276.

- (OTERO, 2009: 10107ff) G. Otero, E. Evangelio, C. Rogero, L. Vázquez, J. Gómez-Segura, J. A. M. Gago, D. Ruiz-Molina, *Langmuir*, **2009**, 25 (17), 10107–10115.
- (PARSONS, 1996: 1825ff) S. Parsons, G. A. Solan, R. E. P. Winpenny, C. Benelli, *Angew. Chem. Int. Ed.*, **1996**, 35, 1825-1828.
- (PILAWA, 1999: 191ff) B. Pilawa, *Ann. Phys.*, **1999**, 8, 191-254.
- (PILLAI, 2009: 1643ff) K. M. Pillai, M. Prat, M. Marcoux, *Int. J. of Heat and Mass Transfer*, **2009**, 52, 1643–1656.
- (POINTILLART, 2007: 1602ff) F. Pointillart, K. Bernot, R. Sessoli, D. Gatteschi, *Chem. Eur. J.*, **2007**, 13, 1602–1609.
- (RIEDEL, 1975: 413ff) E. F. Riedel, R. D. Wilett, *Solid State Communications*, **1975**, 16, 413-416.
- (RIEDEL, 2007: 246ff) E. Riedel, C. Janiak, T. M. Klapötke, H.-J. Meyer, *Moderne Anorganische Chemie*, 3.Auflage, **2007**, de Gruyter, Berlin, 246-249.
- (RIEDEL, 2007: 243) E. Riedel, C. Janiak, T. M. Klapötke, H.-J. Meyer, *Moderne Anorganische Chemie*, 3.Auflage, **2007**, de Gruyter, Berlin, 243.
- (RIVOIRARD, 2003: 622ff) S. Rivoirard, P. de Rango, D. Fruchart, J. Charbonnier, D. Vempaire, J. Alloys and Compounds, **2003**, 356–357, 622–625.
- (ROHDE, 2003: 2069ff) A. Rohde, W. Urland, *Z. Anorg. Allg. Chem.*, **2003**, 629, 2069-2071.
- (RUDERMANN, 1954: 99ff) M. A. Ruderman, C. Kittel, *Phys. Rev.*, **1954**, 96, 99-102.
- (RUIZ, 2008: 52ff) E. Ruiz, J. Cirera, J. Cano, S. Alvarez, C. Loose, J. Kortus, *Chem. Commun.*, **2008**, 52-54.
- (SAALFRANK, 2001: 2765ff) R. W. Saalfrank, I. Bernt, M. M. Chowdhry, F. Hampel, G. B. M. Vaughan, *Chem. Eur. J.*, **2001**, 7, Nr.13, 2765-2769.
- (SAALFRANK, 2005: 1149ff) R. W. Saalfrank, T. Nakajima, N. Mooren, A. Scheurer, H. Maid, F. Hampel, C. Trieflinger, J. Daub, *Eur. J. Inorg. Chem.*, **2005**, 1149–1153.
- (SCHEURER, 2010: 4784ff) A. Scheurer, A. M. Ako, R. W. Saalfrank, F. W. Heinemann, F. Hampel, K. Petukhov, K. Gieb, M. Stocker, P. Müller, *Chem. Eur. J.*, **2010**, 16, 4784–4792.

- (SCHRAY, 2010: 5185ff) D. Schray, G. Abbas, Y. Lan, V. Mereacre, A. Sundt, J. Dreiser, O. Waldmann, G. E. Kostakis, C. E. Anson, A. K. Powell, *Angew. Chem. Int. Ed.*, **2010**, 49, 5185–5188.
- (SCOTT, 2005: 6540ff) R. T. W. Scott, S. Parsons, M. Murugesu, W. Wernsdorfer, G. Christou, E. K. Brechin, *Angew. Chem. Int. Ed.*, **2005**, 44, 6540–6543.
- (SESSOLI, 1993: 141ff) R. Sessoli, D. Gatteschi, A. Caneschi, M. A. Novak, *Nature*, **1993**, 365, 141–143.
- (SESSOLI, 2003: 278ff) R. Sessoli, D. Gatteschi, *Angew. Chem.*, **2003**, 115 (3), 278–309.
- (SESSOLI, 2009: 2328ff) R. Sessoli, A. K. Powell, *Coord. Chem. Rev.*, **2009**, 253, 2328–2341.
- (SHELDRIK, 1996) G. M. Sheldrick, *SADABS (the Siemens Area Detector Absorption Correction)*, **1996**, University of Göttingen.
- (SHELDRIK, 2003) G. M. Sheldrick, *SHELXTL 5.1*, **2003**, Bruker AXS. Inc., Madison, WI 53719-1173, USA.
- (SHINODA, 1983) K. Shinoda, H. Kunieda, *Encyclopedia of Emulsion Technology*, **1983**, Dekker, New York, 5.
- (SHOVA, 2004: 292) S. Shova, D. Prodius, V. Mereacre, Y. A. Simonov, J. Lipkowski, C. Turta, *Inorg. Chem. Comm.*, **2004**, 7, 292–295.
- (SHRIVER, 2006: 606) D. F. Shriver, P. W. Atkins, T. L. Overton, J. P. Rourke, M. T. Weller, F. A. Armstrong, *Inorganic Chemistry*, 4th Edition, **2006**, Oxford University Press, Oxford, 606.
- (SLATER, 1930: 509ff) J. C. Slater, *Phys. Rev.*, **1930**, 35, 509–529.
- (SOLER, 2003: 1777ff) M. Soler, W. Wernsdorfer, K. A. Abboud, D. N. Hendrickson, G. Christou, *Polyhedron*, **2003**, 22, 1777–1782.
- (STAMATATOS, 2006: 4134ff) T. C. Stamatatos, K. A. Abboud, W. Wernsdorfer, G. Christou, *Angew. Chem. Int. Ed.*, **2006**, 45, 4134–4137.
- (STAMATATOS, 2008: 5006ff) T. C. Stamatatos, K. M. Poole, K. A. Abboud, W. Wernsdorfer, T. A. O'Brien, G. Christou, *Inorg. Chem.*, **2008**, 47, 5006–5021.

- (STAMATATOS, 2009: 3308ff) T. C. Stamatatos, G. Christou, *Inorg. Chem.*, **2009**, 48, 3308-3322.
- (STAMATATOS, 2010) T. C. Stamatatos, D. Foguet-Albiol, W. Wernsdorfer, K. A. Abbouda, G. Christou, *Chem. Commun.*, **2010**, DOI: 10.1039/C0CC01701A.
- (TAGUCHI, 2010: 199ff) T. Taguchi, W. Wernsdorfer, K. A. Abboud, G. Christou, *Inorg. Chem.*, **2010**, 49, 199-208.
- (TAGUCHI, 2010: 9131ff) T. Taguchi, M. S. Thompson, K. A. Abboud, G. Christou, *Dalton Trans.*, **2010**, 39, 9131-9139.
- (TAHER, 2010: 1ff) M. A. Taher, S. E. Jarelnabbi, B. E. Bayoumy, S. M. El-Medani, R. M. Ramadan, *Int. J. of Inorg. Chem.*, **2010**, Article ID 296215, 1-6.
- (TANG, 2006: 1729ff) J. Tang, I. Hewitt, N. T. Madhu, G. Chastanet, W. Wernsdorfer, C. E. Anson, C. Benelli, R. Sessoli, A. K. Powell, *Angew. Chem. Int. Ed.*, **2006**, 45, 1729-1733.
- (TASIOPOULOS, 2004: 2117ff) A. J. Tasiopoulos, A. Vinslava, W. Wernsdorfer, K. A. Abboud, G. Christou, *Angew. Chem. Int. Ed.*, **2004**, 43, 2117-2121.
- (TAUSCHEK, 1933) G. Tauschek, *Elektromagnetischer Speicher für Zahlen und andere Angaben*, patent DE 643803, **1933**.
- (TERAOKA 1995: L181ff) Y. Teraoka, S. Kagawa, W. F. Shangguan, *Appl. Catal. B: Environmental*, **1995**, 5, L181-L185.
- (THIAKOU, 2006: 2869ff) K. A. Thiakou, V. Bekiari, C. P. Raptopoulou, V. Psycharis, P. Lianos, S. P. Perlepes, *Polyhedron*, **2006**, 25, 2869-2879.
- (THOMAS, 1996:145ff) L. Thomas, F. Lioni, R. Ballou, D. Gatteschi, R. Sessoli, B. Barbara, *Nature*, **1996**, 383, 145-147.
- (TWIGG, 2007: 2ff) M. V. Twigg, *Appl. Catal.: Environmental*, **2007**, 70, 2-15.
- (UCHIDA, 2006: 359ff) M. Uchida, Y. Onose, Y. Matsui, Y. Tokura, *Science*, **2006**, 311, 359-361.
- (URBAIN, 1935: 2132) G. W. Urbain, P. Weiss, F. Trombe, *Compte Rendus*, **1935**, 200, 2132.

- (VERSCHUUR, 1993) G. L. Verschuur, *Hidden attraction: The Mystery and History of Magnetism*, Oxford University Press, Oxford **1993**.
- (VINCENT, 1989: 2086) J. B. Vincent, C. Christmas, H.-R. Chang, Q. Li, P. D. W. Boyd, J. C. Huffman, D. N. Hendrickson, G. Christou, *J. Am. Chem. Soc.*, **1989**, 111, 2086.
- (WALDMANN, 2007: 10035ff) O. Waldmann, *Inorg. Chem.*, **2007**, 46, 10035-10037.
- (WALDMANN, 2008: 3486ff) O. Waldmann, A. M. Ako, H. U. Güdel, A. K. Powell, *Inorg. Chem.*, **2008**, 47, 3486-3488.
- (WENGENMAYR 2002: 24ff) R. Wengenmayr, Max Planck Gesellschaft, *MaxPlanckForschung*, **2002**, 4, 24-31.
- (WERNSDORFER 2002: 416ff) W. Wernsdorfer, N. Aliaga-Alcaldet, D. N. Hendrickson, G. Christou, *Nature*, **2002**, 416, 406-409.
- (WANG, 2010: 7276ff) M. Wang, D.-Q. Yuan, C.-B. Ma, M.-J. Yuan, M.-Q. Hu, N. Li, H. Chen, C.-N. Chen, Q.-T. Liu, *Dalton Trans.*, **2010**, 39, 7276-7285.
- (WELLS, 1984) A. F. Wells, *Structural Inorganic Chemistry*, **1984**, 5th Ed., Oxford Science Publications, ISBN 0-19-855370-6.
- (WIBERG, 2007) N. Wiberg, E. Wiberg, A. Fr. Holleman, *Lehrbuch der Anorganischen Chemie*, 102. Auflage, **2007**, de Gruyter, Berlin.
- (WITTICK, 2006: 1534ff) L. M. Wittick, L. F. Jones, P. Jensen, B. Moubaraki, L. Spiccia, K. J. Berry, K. S. Murray, *Dalton Trans.*, **2006**, 1534-1543.
- (WOOD, 1998: 4149ff) R. M. Wood, G. J. Palenik, *Inorg. Chem.*, **1998**, 37, 4149-4151.
- (WU, 1998: 1913ff) R. Wu, M. Poyraz, F. E. Sowrey, C. E. Anson, S. Wocadlo, A. K. Powell, U. A. Jayasooriya, R. D. Cannon, T. Nakamoto, M. Katada, H. Sano, *Inorg. Chem.*, **1998**, 37, 1913-1921
- (XIANG, 2010: 4737ff) H. Xiang, Y. Lan, H.-Yong Li, L. Jiang, T.-B. Lu, C. E. Anson, A. K. Powell, *Dalton Trans.*, **2010**, 39, 4737-4739.
- (YANG, 2003: 1857ff) E.-C. Yang, N. Harden, W. Wernsdorfer, L. Zakharov, E. K. Brechin, A. L. Rheingold, G.

- Christou, D. N. Hendrickson, *Polyhedron*, **2003**, 22, 1857-1863.
- (YANG, 2007: 456f) C.-I. Yang, W. Wernsdorfer, G.-H. Lee, H.-L. Tsai, *J. Am. Chem. Soc.*, **2007**, 129, 456-457.
- (YI, 1998: 2243ff) T. Yi, S. Gao, B. Li, *Polyhedron*, **1998**, 17, 2243-2248.
- (YOSIDA, 1957: 893ff) K. Yoshida, *Phys. Rev.*, **1957**, 106, 893-898.
- (ZALESKI, 2004: 3912ff) C. M. Zaleski, E. C. Depperman, J. W. Kampf, M. L. Kirk, V. L. Pecoraro, *Angew. Chem. Int. Ed.*, **2004**, 43, 3912-3914.
- (ZELENKA, 1996: 3ff) P. Zelenka, W. Cartellieri, P. Herzog, *Appl. Catal.: Environmental*, **1996**, 10, 3-28.
- (ZENER, 1951: 403ff) C. Zener, *Phys. Rev.*, **1951**, 82, 403-405.
- (ZHANG, 2005: 1185ff) J. Zhang, L. G. Hubert-Pfalzgraf, D. Luneau, *Polyhedron*, **2005**, 24, 1185-1195.
- (ZHAO, 2010: 4911ff) X.-Q. Zhao, Y. Lan, B. Zhao, P. Cheng, C. E. Anson, A. K. Powell, *Dalton Trans.*, **2010**, 39, 4911-4917.
- (ZHENG, 2006: 165ff) Y.-Z. Zheng, M.-L. Tong, W.-X. Zhang, X.-M. Chen, *Chem. Commun.*, **2006**, 165-167.
- (ZHENG, 2008: 10813ff) Y.-Z. Zheng, Y. Lan, C. E. Anson, A. K. Powell, *Inorg. Chem.*, **2008**, 47, 10813-10815.

10 Affix

10.1 List of Abbreviations

ac	alternating current
BVSC	bond valence sum calculations
dc	direct current
D	zero-field splitting parameter
DCAc	dichloroacetate
dmmpH ₂	dimethoxymethylpyridine
h	hour
H	magnetic field
hepH	2-(Hydroxyethyl)pyridine
hmpH	2-(Hydroxymethyl)pyridine
HS	high spin
Hz	Hertz
IR	Infrared
K	Kelvin
m	mass
M	magnetisation
μ_B	bohr magneton
Me	methyl
MeOH	methanol
MeCN	acetonitrile
mL	milliliter
mmol	millimole
n-bdeaH ₂	<i>N</i> -n-Butyldiethanolamine
OAc	acetate
Oe	Øersted
pivH	pivalic acid
picH	picolinic acid
py	pyridine
SQUID	super-conducting quantum interference device
T	temperature
T	tesla
T _c	critical temperature
U _{eff}	effective energy barrier
V	volume
χ	molar magnetic susceptibility
χ'	in-phase magnetic susceptibility
χ''	out-of-phase magnetic susceptibility

10.2 List of figures

Figure 1: Overview of possible spin arrangements	7
Figure 2: Weiss-domains with Bloch-walls	8
Figure 3: The plot of magnetic susceptibility as a function of temperature for paramagnetic, ferromagnetic and antiferromagnetic materials.	8
Figure 4: Hysteresis loop of a hard (left) and a soft (right) ferromagnet with the hysteresis measured using the same sweep rate.	9
Figure 5: The plot of $1/\chi$ as a function of temperature for paramagnetic, ferromagnetic and antiferromagnetic materials.	9
Figure 6: Magnetic characteristic of an ideal ferrimagnet (left) and the plot of χT as a function of temperature for paramagnetic, ferromagnetic, antiferromagnetic and ferrimagnetic materials (right).	10
Figure 7: Bethe-Slater curve	11
Figure 8: super exchange using the example of MnO	12
Figure 9: Variation of the indirect exchange coupling constant, j , of a free electron gas in the neighbourhood point magnetic moment at the origin $r=0$.	12
Figure 10: Double-exchange of the d-electron of Mn ^{III}	13
Figure 11: Spin alignment in $[\text{Mn}_{12}\text{O}_{12}(\text{CH}_3\text{COO})_{16}(\text{H}_2\text{O})_4]$ (Caneschi, 1991: 5873ff).	15
Figure 12: Two potential diagram showing the relative positions of the zero-field split M_S levels of an $S_T = 10$ system and the energy barrier separating the $M_S = +10$ and the $M_S = -10$ states.	15
Figure 13: The magnetic hysteresis loops of Mn ₁₂ -Ac are shown at the indicated temperatures at a scan rate of 0.025 T/10 s (Thomas, 1996:145ff).	16
Figure 14: An example of ac susceptibility measurements as a function of temperature at different frequencies, and as a function of frequency at different temperatures: (a, c) in-phase and (b, d) out-of-phase signals of a Dy ₄ compound (Abbas, 2010: 8067ff).	17
Figure 15: An example of τ versus $1/T$ plot obtained from both temperature and frequency dependent ac susceptibility measurements under zero dc field of a Dy ₄ compound (Abbas, 2010: 8067ff).	18
Figure 16: d^4 high-spin Mn ^{III} configuration leading to Jahn-Teller distortion	22
Figure 17: Two possible arrangements of five electrons in octahedral environment	23
Figure 18: Some reported coordination modes of ligand n-bdeaH ₂ (mode I (Foguet-Albiol, 2005: 4282ff), mode II (Biswas, 2007: 1059ff), mode III (Le Bris, 2007: 80ff), mode IV (Saalfrank, 2005: 1149ff), mode V (Lermontova, 2006: 5710), mode VI (Foguet-Albiol, 2005: 897ff), mode VII (Mishra, 2007: 602), mode VIII (Mishra, 2007: 602), mode IX (Zhang, 2005: 1185ff), mode X (Le Bris, 2007: 80ff))	28
Figure 19: Coordination modes of ligand hmpH (Efthymiou, 2009: 3373ff; Stamatatos, 2009: 3308ff)	29
Figure 20: Common coordination modes of the carboxylate group.	30
Figure 21: Molecular structure of $[\text{Mn}_6\text{O}_2(\text{piv})_{10}(\text{py})_{2.5}]$	30
Figure 22: Molecular structure of Mn ₁₂ -DCA	31
Figure 23: Side view of the Mn ₁₂ -DCA cluster with the axial carboxylate groups in sight.	32
Figure 24: Molecular structure of Co ₂ -pivalate	33
Figure 25: Molecular structure of Co ₃ -pivalate	33
Figure 26: Molecular structure of precursor compound 6	34
Figure 27: Molecular structure of Fe ₆ -pivalate	35
Figure 28: Molecular structure of Dy ₂ -pivalate. H atoms and pivalates situated in the crystal lattice are omitted for clarity.	36
Figure 29: Molecular structure of $[\text{Mn}^{\text{III}}_2\text{La}^{\text{III}}_2(\text{hmp})_6(\text{piv})_2(\text{NO}_3)_4]$	41

Figure 30: Polyhedral representation along the c-axis of compound 9 with La polyhedra being violet and the Mn octahedra pink (left) and the metal core of 9. _____	42
Figure 31: Molecular structure of $[\text{Mn}^{\text{III}}_4\text{La}^{\text{III}}_2(\mu_4\text{-O})(\mu_3\text{-O})(\text{hmp})_7(\text{O}_2\text{CMe})(\text{O}_2\text{CCHCl}_2)(\text{NO}_3)_5(\text{OH}_2)_{0.5}]\cdot 3\text{acetone}$ with Jahn-Teller axes (turquoise). Organic hydrogen atoms and solvent molecules are omitted for clarity. _____	43
Figure 32: Crystal packing of 10 in the polyhedral representation, projected along the a axis. La polyhedra are yellow and the Mn octahedra are violet (left) and the metal core of 10. _____	44
Figure 33: The bicapped square antiprismatic coordination polyhedra around La(1) and La(2). _____	44
Figure 34: Structure of $[\text{Mn}^{\text{III}}_2\text{Mn}^{\text{II}}_2(\text{hmp})_6(\text{NO}_3)_4]\cdot 2\text{acetone}$. Organic hydrogen atoms and solvent molecules are omitted for clarity. _____	45
Figure 35: Temperature-dependence of the χT product under 0.1 T for compound 10. _____	49
Figure 36: Plot of magnetisation M vs. H (left) and M vs. H/T (right) between 2 K and 5 K for 10. The solid lines are to guide the eye. _____	49
Figure 37: Temperature-dependent ac susceptibilities of 10 from 1.8 K to 10 K under zero dc field at indicated frequencies. _____	49
Figure 38: Frequency-dependent ac susceptibilities of 10 from 1.8 K to 4 K under zero dc field at indicated frequencies. _____	50
Figure 39: Molecular structure of $[\text{Mn}^{\text{III}}_2\text{Dy}^{\text{III}}_4(\mu_4\text{-O})_2(\text{hmp})_4(\text{pic})_2(\text{piv})_6(\mu\text{-N}_3)_2]\cdot 4\text{CH}_3\text{CN}$ with Jahn-Teller axes (turquoise). Organic hydrogen atoms and solvent molecules are omitted for clarity. _____	51
Figure 40: The $\{\text{Mn}^{\text{III}}_2\text{Dy}^{\text{III}}_4(\mu_4\text{-O})_2\}$ core of 14 (left) and part of the structure of 14 in the polyhedral representation, projected along the b axis. All Dy polyhedra are yellow and the Mn octahedra are violet. _____	52
Figure 41: Distorted dodecahedron environment of Dy(1) and Dy(3), representing the coordination polyhedra of all four Dy ^{III} ions in 14. _____	52
Figure 42: Temperature-dependence of the χT product under 0.1 T for compound 11-15. _____	58
Figure 43: Plot of magnetisation M vs. H (left) and M vs. H/T (right) between 1.8 K and 8 K for 11. The solid lines are to guide the eye. _____	58
Figure 44: Plot of magnetisation M vs. H (left) and M vs. H/T (right) between 1.8 K and 8 K for 12. The solid lines are to guide the eye. _____	58
Figure 45: Plot of magnetisation M vs. H (left) and M vs. H/T (right) between 1.8 K and 8 K for 13. The solid lines are to guide the eye. _____	59
Figure 46: Plot of magnetisation M vs. H (left) and M vs. H/T (right) between 1.8 K and 8 K for 14. The solid lines are to guide the eye. _____	59
Figure 47: Plot of magnetisation M vs. H (left) and M vs. H/T (right) between 1.8 K and 8 K for 15. The solid lines are to guide the eye. _____	59
Figure 48: Plots of the in-phase and out-of-phase ac susceptibility for 13. _____	60
Figure 49: Molecular structure of $\text{Mn}^{\text{II}}\text{Mn}^{\text{III}}_2\text{Mn}^{\text{IV}}\text{Ho}^{\text{III}}_3(\mu_4\text{-O})(\mu_3\text{-O})_2(\text{n-bdea})_3(\text{N}_3)(\text{piv})_9(\text{NO}_3)$. Organic hydrogen atoms and solvent molecules are omitted for clarity. _____	61
Figure 50: View of the "basket"-like geometry (left) within the metal core (right). _____	61
Figure 51: View of the metal core with colour-marked butterfly cores. _____	62
Figure 52: The square antiprismatic coordination polyhedra around Ho(1) and Ho(2) and the triaugmented triangular prism of Ho(3). _____	62
Figure 53: Part of the structure of 19 in the polyhedral representation, projected along the b axis. Ho(1)-(3) polyhedra are yellow and the Mn octahedra are violet. _____	63
Figure 54: Temperature-dependence of the χT product under 1000 Oe for compound 18 and 19. _____	67

Figure 55: Plot of magnetisation M vs. H (left) and M vs. H/T (right) between 1.8 K and 8 K for 18. The solid lines are to guide the eye.	67
Figure 56: Plot of magnetisation M vs. H (left) and M vs. H/T (right) between 1.8 K and 8 K for 19. The solid lines are to guide the eye.	67
Figure 57: Molecular structure of $[\text{Mn}^{\text{IV}}_2\text{Mn}^{\text{III}}_2\text{Gd}^{\text{III}}_6\text{Li}_2(\mu_3\text{-O})_2(\mu_5\text{-CO}_3)_2(\text{n-bdea})_6(\text{piv})_{12}(\text{NO}_3)_2]\cdot 3\text{CH}_3\text{CN}$, 25. Organic hydrogen atoms and solvent molecules are omitted for clarity.	68
Figure 58: Left: Metal core of 25. Right: Part of the structure of 25 in the polyhedral representation, projected along the b axis. Gd(1)-(3) polyhedra are yellow, Mn octahedra are violet and Li tetrahedra are rose.	69
Figure 59: The coordination polyhedra around Gd(1), Gd(2) and Gd(3): square antiprism, dodecahedron and distorted bisdisphenoid.	69
Figure 60: Temperature-dependence of the χT product under 0.1T for compound 21-29.	79
Figure 61: Plot of magnetisation M vs. H (left) and M vs. H/T (right) between 1.8 K and 8 K for 21. The solid lines are to guide the eye.	80
Figure 62: Plot of magnetisation M vs. H (left) and M vs. H/T (right) between 1.8 K and 5 K for 22. Plots for 2 K were omitted, as the temperature problems occurred during the measurement. The solid lines are to guide the eye.	80
Figure 63: Plot of magnetisation M vs. H (left) and M vs. H/T (right) between 1.8 K and 8 K for 23. The solid lines are to guide the eye.	80
Figure 64: Plot of magnetisation M vs. H (left) and M vs. H/T (right) between 1.8 K and 8 K for 24. The solid lines are to guide the eye.	81
Figure 65: Plot of magnetisation M vs. H (left) and M vs. H/T (right) between 1.8 K and 8 K for 25. The solid lines are to guide the eye.	81
Figure 66: Plot of magnetisation M vs. H (left) and M vs. H/T (right) between 1.8 K and 8 K for 26. The solid lines are to guide the eye.	81
Figure 67: Plot of magnetisation M vs. H (left) and M vs. H/T (right) between 1.8 K and 8 K for 27. The solid lines are to guide the eye.	82
Figure 68: Plot of magnetisation M vs. H (left) and M vs. H/T (right) between 1.8 K and 5 K for 29. The solid lines are to guide the eye.	82
Figure 69: χT plot for compound 29. The line represents the best-fit calculated values.	82
Figure 70: Temperature-dependent ac susceptibilities of 27 below 10 K under zero dc field at indicated frequencies.	83
Figure 71: Frequency dependence of the in-phase (left) and out-of-phase (right) ac susceptibility as a function of the dc applied field and measured at 1.8 K for 27.	83
Figure 72: Frequency dependence in zero dc field of the in-phase (χ') and the out-of-phase (χ'') ac susceptibility component at 1.81 K and 2K for 27.	83
Figure 73: Temperature dependent catalytic oxidation of CO to CO ₂ by calcinated 27.	84
Figure 74: Molecular structure of the $[\text{Fe}^{\text{III}}_4\text{Pr}^{\text{III}}_2(\mu_4\text{-O})_2(\text{n-bdea})_4(\text{piv})_4(\text{NO}_3)_2(\text{H}_2\text{O})_2]\cdot \text{MeCN}$ aggregate in 30. Organic hydrogen atoms are omitted for clarity.	86
Figure 75: The distorted octahedral coordination polyhedron of the core (left) and dodecahedral environment around Pr ^{III} .	87
Figure 76: Core structure of compound 30.	87
Figure 77: View along the a-axis with the cluster aggregates shown as polyhedral representations. H atoms are omitted for clarity.	88
Figure 78: Enlarged view of the crystals obtained from slow diffusion with acetone (left) and methanol (right).	88
Figure 79: X-ray powder diffraction pattern of Fe ₄ Pr ₂ obtained by slow diffusion of acetone (green) and methanol (red).	89

Figure 80: Comparison of the IR of 30 (green) made with 6 as starting material and the product obtained from 7 as precursor compound (red).	89
Figure 81: Temperature dependence of the χT product for polycrystalline samples of compounds 30, 32 and 34 at 1000 Oe.	94
Figure 82: Plot of magnetisation (M) vs. H and H/T, respectively, between 2 K and 5 K for 30. The solid lines are to guide the eye.	95
Figure 83: Plot of magnetisation (M) vs. H and H/T, respectively, between 2 K and 5 K for 32. The solid lines are to guide the eye.	95
Figure 84: Plot of magnetisation (M) vs. H and H/T, respectively, between 2 K and 5 K for 34. The solid lines are to guide the eye.	95
Figure 85: The ^{57}Fe Mössbauer spectra for 30 at 3K in zero applied field and at 3 K in field of 5 T.	97
Figure 86: Molecular structure of the $[\text{Fe}^{\text{III}}_6(\mu_3\text{-O})_2(\text{hmp})_6(\text{piv})_6]_2 + [\text{Gd}(\text{NO}_3)_5]^{2-}$ aggregate in 37. Organic hydrogen atoms are omitted for clarity.	98
Figure 87: Left: View of the core of the Fe_6 cation. Right: View along the a-axis with the cluster aggregates shown as polyhedral representations. H atoms are omitted for clarity with Fe^{III} shown in brown colour and Gd^{III} in yellow colour.	99
Figure 88: Temperature dependence of the χT product for polycrystalline samples of compounds 37, 38, 39 and 40 at 1000 Oe (left) and 10000 Oe (right).	103
Figure 89: Plot of magnetisation (M) vs. H and H/T, respectively, between 2 K and 8 K for 36. The solid lines are to guide the eye.	103
Figure 90: Plot of magnetisation (M) vs. H and H/T, respectively, between 2 K and 8 K for 37. The solid lines are to guide the eye.	103
Figure 91: Plot of magnetisation (M) vs. H and H/T, respectively, between 2 K and 8 K for 38. The solid lines are to guide the eye.	104
Figure 92: Plot of magnetisation (M) vs. H and H/T, respectively, between 2 K and 8 K for 39. The solid lines are to guide the eye.	104
Figure 93: Plot of magnetisation (M) vs. H and H/T, respectively, between 2 K and 8 K for 40. The solid lines are to guide the eye.	104
Figure 94: Molecular structure of $[\text{Co}^{\text{III}}_2\text{Dy}^{\text{III}}_4(\text{hmp})_4(\text{piv})_8(\text{N}_3)_2(\text{NO}_3)] \cdot 2\text{CH}_3\text{CN}$. Atoms marked with primes are inversion-center-generated. Organic hydrogen atoms and solvent molecules are omitted for clarity.	106
Figure 95: Side view (core only) of the tetranuclear core with the flanking Co^{III} showing the coplanarity in the Dy_4 core of 46.	106
Figure 96: Views of the inner coordination polyhedra of 46 showing the square antiprism coordination of $\text{Dy}(1)$ and the three-face centred trigonal prism stereochemistry about $\text{Dy}(2)$.	107
Figure 97: Core view of compound 46.	107
Figure 98: Temperature dependence of the χT product for polycrystalline samples of compounds 42-48 at 1000 Oe.	115
Figure 99: Plot of magnetisation (M) vs. H and H/T, respectively, between 1.8 K and 8 K for 42. The solid lines are to guide the eye.	116
Figure 100: Plot of magnetisation (M) vs. H and H/T, respectively, between 1.8 K and 8 K for 43. The solid lines are to guide the eye.	116
Figure 101: Plot of magnetisation (M) vs. H and H/T, respectively, between 1.8 K and 8 K for 44. The solid lines are to guide the eye.	116
Figure 102: Plot of magnetisation (M) vs. H and H/T, respectively, between 1.8 K and 8 K for 45. The solid lines are to guide the eye.	117
Figure 103: Plot of magnetisation (M) vs. H and H/T, respectively, between 1.8 K and 10 K for 46 up to 9T. The solid lines are to guide the eye.	117
Figure 104: Plot of magnetisation (M) vs. H and H/T, respectively, between 1.8 K and 8 K for 47. The solid lines are to guide the eye.	117

Figure 105: Plot of magnetisation (M) vs. H and H/T, respectively, between 1.8 K and 8 K for 48. The solid lines are to guide the eye.	118
Figure 106: Temperature dependence of the in-phase (χ') and the out-of-phase (χ'') ac susceptibility components at different frequencies for 46.	118
Figure 107: Zero dc field ac susceptibility measurements for 46 as a function of the frequency at different temperatures in-phase (left) and out-of-phase signals (right).	119
Figure 108: Ac susceptibility measurements for 46 as a function of the frequency at different temperatures in-phase (left) and out-of-phase signals (right) with an applied dc field of 600 Oe.	119
Figure 109: Plot of relaxation time (τ) vs. $1/T$ using ac $\chi''M$ data for complex 46. The solid line is the fit of the data to the Arrhenius equation.	120

10.3 List of tables

Table 1: Typical ranges for χ (Riedel, 2007: 243).	4
Table 2: Selected bond lengths for 10.	46
Table 3: Selected bond angles for 10.	47
Table 4: Magnetic data summarised from the dc measurements. ^a taking into account a g factor of Mn metal ions of 2.	48
Table 5: Summary of selected cell parameters.	54
Table 6: Selected bond lengths for 11.	54
Table 7: Selected bond angles for 11.	55
Table 8: Selected bond lengths for 14.	55
Table 9: Selected bond angles for 14.	55
Table 10: Magnetic data summarised from the dc measurements. ^a taking into account a g factor of Mn metal ions of 2.	57
Table 11: Summary of selected cell parameters of 17, 18, 19 and 20 selected at RT.	64
Table 12: Selected Bond lengths for 19.	64
Table 13: Selected bond angles for 19.	65
Table 14: Magnetic data summarised from the dc measurements. ^a taking into account a g factor of Mn metal ions of 2.	66
Table 15: Selected cell parameters for compounds 21-29.	72
Table 16: Selected bond lengths for 21.	72
Table 17: Selected bond angles for 21.	73
Table 18: Selected bond lengths for 25.	74
Table 19: Selected bond angles for 25.	74
Table 20: Selected bond lengths for 27.	75
Table 21: Selected bond angles for 27.	76
Table 22: Selected bond lengths for 29.	76
Table 23: Selected bond angles for 29.	77
Table 24: Magnetic data summarised from the dc measurements. ^a taking into account a g factor of Mn metal ions of 2.	79
Table 25: Summary of selected cell parameters.	90
Table 26: Selected bond lengths for 30.	90
Table 27: Selected bond angles for 30.	91
Table 28: Selected bond lengths for 32.	91
Table 29: Selected bond angles for 32.	91
Table 30: Selected bond lengths for 33.	91
Table 31: Selected bond angles for 33.	92
Table 32: Selected bond lengths for 34.	92

Table 33: Selected bond angles for 34.	92
Table 34: Selected bond lengths for 35.	92
Table 35: Selected bond angles for 35.	93
Table 36: Magnetic data summarised from the dc measurements. a taking into account a g factor of FeIII metal ions of 2.	93
Table 37: Summary of selected cell parameters.	100
Table 38: Selected bond lengths for 37.	100
Table 39: Selected bond lengths for 37.	100
Table 40: Magnetic data summarised from the dc measurements. a taking into account a g factor of FeIII metal ions of 2.	102
Table 41: Summary of selected cell parameters.	108
Table 42: Selected bond lengths for 41.	109
Table 43: Selected bond angles for 41.	109
Table 44: Selected bond lengths for 44.	109
Table 45: Selected bond angles for 44.	110
Table 46: Selected bond lengths for 46.	110
Table 47: Selected bond angles for 46.	111
Table 48: Selected bond lengths for 47.	111
Table 49: Selected bond angles for 47.	112
Table 50: Selected bond lengths for 48.	112
Table 51: Selected bond angles for 48.	112
Table 52: Magnetic data summarised from the dc measurements.	113

11 Acknowledgments

Finally I want to say some words from my side, from my heart. This thesis is the summary of my results which I found over the last three years.

Over the last three years until today science was and still is a big part of my life. Although this thesis illustrates and summarises the scientific development of my topic it does not illustrate my personal development. I did not only have to learn a lot of things regarding scientific issues but also regarding interpersonal aspects and myself.

The list of people, who assisted, supported and guided me over the past years and helped me to arrive where I am today, is very long and I wish to thank everybody who was involved in the development of this work.

However, I wish to dedicate special thanks to some people, who made this thesis possible and without them this thesis would not be like it is today:

I wish to cordially thank Prof. Annie K. Powell and Dr. Rodolphe Clérac (alphabetic order). Despite certain problems both helped me a lot and without their strong will and patience I would not have been able to do my PhD. Both of you should know, that I am ineffable thankful for this opportunity and for your efforts to help me. It is something that I will always remember you for.

I wish to express my heartfelt thanks to my mentors Valeriu and Denis. We had many discussions and I learnt so much from them. It was an indescribable fortune to get to know these two Moldavians! I will never forget anything you did for me! Yes, Denis, you have to be crazy to get crystals, mâi!

Numerous X-ray measurements, including the refinement afterwards were done by Dr. Chris Anson, the crystallographer of the Powell group. I wish to thank him cordially for the help over the past three years and especially for the corrections of this thesis.

The magnetic measurements were generated in Germany and France. Therefore I wish to thank anybody who was involved and was not mentioned yet: Yanhua Lan, Margot Kalisz and Kartik Mondal.

Vielmals danken möchte ich Gertraud Amschlinger für ihre Unterstützung bezüglich administrativer Aufgaben, ihr offenes Ohr und ihrer äusserst lieben Art. Ausserdem möchte ich hiermit auch die Chance nutzen, mich bei Herr Lehmann zu bedanken, dem Techniker des AK Powell.

Je veux rendre grâce aussi à Marie-Christine Gauthier de Bordeaux pour sa compréhension et son aide avec l'administration en France.

For the corrections and the formatting I wish to thank Elly, who helped me regarding numerous issues and encouraged me many times.

Big thanks concern also Prof. Peter Weinberger from Austria, who became meanwhile a real friend. I appreciate the discussions with him, his ideas and motivating words.

I also want to say thank you for the nice cooperation with Andreas Pacher from the group of Sven Kureti, who was responsible for the catalytic experiments. Additionally I wish to thank the following people for giving me advice or any other support: H.R., Tobias Schenk, Karolina Chovolou, Simon Hildebrandt, Ramona Winkler, Patrizia Lo Piccolo, Dirk Schray, Sven Pfirrmann, Roberta Bomparola, sokie.de and all my friends.

Schlussendlich möchte ich noch meinen Eltern danken. Ihr habt es mir ermöglicht zu studieren und letztendlich seid ihr auch dafür verantwortlich, dass ich meine Dissertation anfertigen konnte. Während der gesamten Zeit habt ihr mich unterstützt und mich zu dem gemacht, was ich heute bin. Danke!

“Es sind die vorgefassten Meinungen, die es den Völkern so schwer machen, einander zu verstehen, und die es ihnen so leicht machen, einander zu verachten.”

Romain Rolland (1866-1944),
frz. Schriftsteller.

12 Conference contributions

1st Karlsruhe-Strasbourg bilateral meetings on progress in Supramolecular Chemistry, June 9th 2008, Strasbourg (France).

Poster presentation at MOLMAT 2008: 3rd International Symposium on Molecular Materials based on Chemistry, Solid State Physics, Theory and Nanotechnology, July 8-11th 2008, Toulouse (France) named HETERO-METALLIC COMPLEXES FUNCTIONING AS SINGLE-MOLECULE MAGNETS.

2nd Karlsruhe-Strasbourg bilateral meetings on progress in Supramolecular Chemistry, December 5th 2008, Karlsruhe (Germany).

Poster presentation at FIGIPAS 2009: Meeting in Inorganic Chemistry, July 1-4th 2009, Palermo (Italy) named MOLECULAR ENGINEERING OF MAGNETIC COMPLEXES: THE CASE OF $S_T = 83/2$ Mn_{19} -AGGREGATE.

1st International Summer School Karlsruhe – Dublin: Coordination Chemistry approaches to new multifunctional materials, October 16-18th 2009, Karlsruhe (Germany).

Poster presentation at MOLMAT 2010: 4th International Conference on Molecular Materials, July 5-8th 2010, Montpellier (France) named NEW HETEROMETALLIC 3*d*-4*f* MAGNETIC COMPLEXES.

150th Anniversary Weltkongress Chemie - Progress and Challenges in Chemistry, September 3-4th 2010, Karlsruhe (Germany).

Oral Presentation at the 2nd KIT PhD Symposium 2010, September 30th 2010, Karlsruhe (Germany) named NEW HETEROMETALLIC 3*d*-4*f* MAGNETIC COMPLEXES.

Oral Presentation at the 3rd SchaulnsLand Symposium 2010, November 26-29th 2010, Freiburg (Germany) named STRUCTURE AND MAGNETIC PROPERTIES OF UNUSUAL ASYMMETRIC 3*d*-4*f* COMPLEXES.